University of Sussex

The Distant, Dusty Universe: Finding Star-Forming Galaxies with the Herschel Space Observatory

Charlotte Louise Clarke

Submitted for the degree of Doctor of Philosophy

University of Sussex

May 2016

Declaration

I hereby declare that this thesis has not been and will not be submitted in whole or in part to another University for the award of any other degree.

Galaxy catalogues produced in chapter 2 were created for the second HerMES data release. The companion paper to this release was published in Monthly Notices of the Royal Astronomical Society in 2014 and titled *HerMES: point source catalogues from Herschel-SPIRE observations II* with lead author L. Wang.

The galaxy catalogue produced, and the method of production in chapter 4 will be first described in a paper submitted to Monthly Notices of the Royal Astronomical Society in 2015 with lead author K. Pitchford, with references to this thesis.

All catalogues produced are publicly available at `hedam.lam.fr/HerMES/`.

Signature:

Charlotte Louise Clarke

UNIVERSITY OF SUSSEX

Charlotte Louise Clarke, Doctor of Philosophy

The Distant, Dusty Universe:
Finding Star-Forming Galaxies with the Herschel Space Observatory

Summary

The formation and growth of galaxies through star formation is an unsolved problem in astrophysics. Emission from galaxies in the far-infrared is known to be strongly correlated with obscured star formation and makes up a significant fraction of the cosmic infrared background. The Herschel Space Observatory was designed to cover the wavelengths where this background peaks and gave an unprecedented view of the Universe at this part of the electromagnetic spectrum.

This thesis uses observations conducted for the Herschel Multi-tiered Extragalactic Survey (HerMES) by the Herschel Space Observatory's SPIRE instrument to catalogue sources of far infrared emission at 250μm, 350μm and 500μm which will allow models of galaxy evolution to be constrained. Source detection and extraction is performed with both blind and prior-driven algorithms on two newly constructed maps and, for the first time, on the largest of the HerMES' maps, HeLMS. Modifications are made to the algorithms to compensate for cirrus contamination. The accuracy and completeness of both algorithms are assessed and compared.

In addition, emission from a galaxy across the three SPIRE bands is known to be strongly correlated. The extent of the covariance between the SPIRE images is explored using Principal Component Analysis, finding that up to 95% of the variance in the SPIRE maps can be explained by one linear combination of the three SPIRE bands. This new projection of data could allow previously unfeasible multi-dimensional probability of deflection analyses to be performed through a reduction of the data dimensionality.

Looking forward, the *Herschel* Extragalactic Legacy Project (HELP) will be using *Herschel* observations from both HerMES and the H-ATLAS collaboration to create homogenous, multi-wavelength data products. In the final chapter, a comparison between datasets to test the homogeneity was undertaken, leading to a preliminary recalculation of the HerMES angular correlation function, a result that has been in contention between collaborations.

Catalogues created as part of this thesis are available at hedam.lam.fr/HerMES/.

Acknowledgements

They say “it takes a village” to raise a child and, whilst this thesis is only half the weight of a newborn baby, it took about the same number of people support, guide, teach and drag me through it. Whilst I can’t name everyone in this gratuitously long list, know that you are all appreciated more than you realise.

The largest thanks extends to my supervisor, Seb Oliver, who is both a fantastic scientist and mentor - without his encouragement (read: prying my fingers off the doorframe one at a time) I never would have had half the experiences and opportunities I had. I hope we can continue collaborating on all manner of ideas in future, and I especially hope I can continue accusing you of being a spy on a regular basis.

Stephen Wilkins and Stephen Serjeant have my thanks for being wonderful, patient examiners and fantastic scientists to aspire to be like in both their work and as inclusive members and mentors within the scientific community.

I thank the entire HerMES and now HELP teams at Sussex and further afield, in particular Lingyu Wang, Marco Viero, Anthony Smith, Isaac Roseboom and Jillian Scudder. Without your work and advice (both on and off the job) my own work would have been insurmountable and I am extremely grateful to you all. Naomi, Sorour, and Steven - I salute you, comrades in arms. Our team is best team.

The Astronomy Centre’s staff and students are all the most wonderful people and I already miss you all. It?s always been a community of PhD students and I hope that continues - I am watching you all ;). Kathy Romer, Peter Thomas, Darren Baskill and Ilian Iliev receive massive thanks for their intensive professional support, advice and tea. Thank you to Phil for having the same birthday.

A massive thank you to all my teachers but especially Mrs Cook, Mr Kent, Dr Macintosh, Mrs Fish, Dr Longstaff and Tim Evans for their sacrifices, expert teaching and encouragement to get me here. Best wishes to 7-7 and the sixth form crew and to Steph, Carla (Jim’s Predicament forever), Lel, Aaron and Arnika (I made half-good on it, Hubble’s Constant’s in here at least!). To the Imperial crew: potato smilies, Tuesday night curly fries, Wilson House, BSG, F1 and unicorns all the way. To Nic and Maria, I cannot thank you

enough for your friendship, I hope endless desserts will show my love!

Maxx, Alex and Beth: you and our friendship mean so much to me. I hope to continue supporting you the same way you have supported me. Bunmother away!

The final thank yous are for my family and partner. Peter Hurley's support was unwavering throughout the tumultuous latter half of writing ("Worse things happen at sea"). You have the patience of a saint and I may owe you some chores. My sister, Kelsey, the best sister in the world by a long way, thank you for being you, you make everything better. To Nanny Glenda, Nanny Gladys and Grandad Fred and my entire family - thank you for encouraging me throughout school and keeping me grounded. I hope you like it! To Grandad Vic and Uncle Dave, I did it! I miss you.

And finally, Mum and Dad: I love you so much I made a book about galaxies for you, and this time they're not chocolate bars hanging out of the dining room window. I hope this will educate you on the differences, this revenge has been in the works since 1997. Volume two will cover Milky Ways, Starbursts and Mars Bars. Exam is in three weeks. Good luck.

Official Acknowledgements

Herschel is an ESA space observatory with science instruments provided by European-led Principal Investigator consortia and with important participation from NASA.

This research has made use of:

- the NASA/IPAC Extragalactic Database (NED) which is operated by the Jet Propulsion Laboratory, California Institute of Technology, under contract with the National Aeronautics and Space Administration.
- Astropy, a community-developed core Python package for Astronomy Astropy Collaboration et al. (2013).
- APLpy, an open-source plotting package for Python hosted at http://aplpy.github.com
- "Aladin sky atlas" developed at CDS, Strasbourg Observatory, France (Bonnarel et al., 2000; Boch & Fernique, 2014)
- TOPCAT & STIL: Starlink Table/VOTable Processing Software (Taylor, 2005)

Funding in this thesis was provide by STFC studentship ST/J5007-7X/1

"It's Dust."

Something in the way he said it made Lyra imagine dust with a capital letter, as if this wasn't ordinary dust. The reaction of the Scholars confirmed her feeling, because Lord Asriel's words caused a sudden collective silence, followed by gasps of incredulity.

- Philip Pullman, The Golden Compass

Contents

List of Tables

List of Figures

Chapter 1

Introduction

1.1 Early Observations and Cosmology

Our understanding of the Universe at the start of the 20th century was very different to today. The received wisdom then was that the Universe was an unchanging void, the largest structures being stars or small groups of stars. The Universe obeyed the *Cosmological Principle*, first postulated by Isaac Newton. It states that on the largest scales the Universe will appear the same wherever an observer is in the Universe. To fulfil this the Universe must be homogenous and isotropic. Homogeneity ensures that wherever an observer is in the Universe their particular patch will contain a similar statistically representative sample of the Universe as another observer would see. Isotropy means that the Universe looks the same in every direction to an observer, that there is no preferred direction in the Universe for physical laws. Implicit in the Cosmological Principle Newton postulated is that the Earth is not in a special place in the Universe.

Observations at the time supported the cosmological principle on scales of a few hundreds of light years, with the Universe thought to be full of stars. Stars are observed as point-like structures and are numerous, but even over a millennium ago observations of faint, fuzzy blobs or nebulae were recorded by Persian astronomer Al-Sufi. Like the Milky Way, a stripe of faint light across the sky that was reasoned to arise from unresolved stars, these nebulae were thought to be relatively small groups of stars much like open clusters of resolved stars like the Pleiades, clouds made of gas or individual nebulous stars. The invention of the telescope quickly added many more of these diffuse structures to catalogues. Spectral observations by Huggins in 1864 of nebulae demonstrated two-thirds had a spectrum consistent with many stars and a third consistent with gas. The nebulae then represented two distinct populations of galaxies.

1.1.1 Fuzzy Blobs to Galaxies

Observations of Cephid-variable (CV) stars were able to place constraints on distances within the nearby Universe. These stars pulsate rapidly on the order of a few days to months and their luminosity changes with the size of the star. There is a strong correlation between these stars' luminosity and period, meaning that the ratio between apparent magnitude and the predicted absolute magnitude from the period of the star can be used to calculate the distance to the star using the inverse square law.

This work in distance calculations sparked The Great Debate in 1920 between Harlow Shapley and Heber Curtis. Shapley believed his work on CV stars constrained the size of the Milky Way to be larger than previously thought and thus all nebulae were part of the Milky Way. For distance calculations to the Andromeda "Nebula" to be correct, the Universe would have to be on the order of hundreds of millions of light years across, which seemed impossible at the time. Curtis believed a subset of nebulae were outside the Milky Way as "Island Universes" a term coined by Immanuel Kant in 1755. The idea of a fraction of nebula being separate to the Milky Way was floated in science literature as early as 1750 by Thomas Wright in "an original theory or new hypothesis of the Universe" who deduced that the Milky Way was a gravitationally bound disk of stars and other nebulae might be the same. It did not gain traction in the community before the The Great Debate.

Shapely won the debate at the time, although it was not long before Curtis was vindicated. In 1924 Edwin Hubble found CV stars in some star-like nebulae, including the Andromeda "Nebula" and calculated the distance to be far larger (on the order of a million light years away) than contemporary estimates of the size of the Milky Way (then 300,000 light years in diameter). Andromeda and similar nebulae were then understood to be gravitationally bound groups of billions to trillions of stars far outside our own Milky Way, and were collectively known as galaxies.

Hubble went on to classify galaxies to deduce their evolution. Hubble's "Tuning-Fork" diagram categorised galaxies by their ellipticity, the strength of a central bar of stars within the galaxy and the tightness of any spiral arms, postulating that galaxies changed from formless structures to highly structured disks. Nowadays, studies of galactic dynamics have shown almost the opposite from Hubble's study. How galaxies grow and develop over time is an unanswered question in astronomy. This thesis contributes to the growing body of knowledge attempting to explain the Universe as we see it.

1.1.2 Big Bang

Five years after Hubble's paradigm shifting publication, in 1929 he again caused waves by calculating recessional velocities of galaxies as a function of distance using the light-curves of CV stars. The magnitude of the CV star is related to the period of pulsation for CV stars and can be used to calculate a distance. Hubble also used the concept of redshift to determine the speed of recession of galaxies. Light emitted from a source moving relatively to an observer will appear to be of a lower or higher frequency dependent on the direction of motion of the source. The fraction of change of the wavelength relative to the rest frame wavelength is known as the the redshift z and is also an expression of the recessional velocity as a fraction of the speed of light in a vacuum.

Hubble found that the recessional velocity of a galaxy increased with distance, implying that (for the most part) galaxies were all moving away from each other and therefore the Universe was expanding in all directions. Hubble calculated the rate of expansion as 500km/s/Mpc, a value now known as Hubble's constant $H_0 = v/d$, although with improved measurements this value is now in the region of 70km/s/Mpc. Coupled with Albert Einstein's publication presenting General Relativity in 1915, describing gravity as a property arising from the warping of space-time through interactions with matter and energy, space was now seen, not as a static void, but a dynamic entity of the Universe itself. In 1931 George Lemaître cemented this view by reasoning that if the Universe is expanding it must have been smaller at one point in the past. Taking this further, the Universe would have been extremely small at one point and expanded outwards over time. The Universe could have had a beginning. Steady-state proponent Fred Hoyle disagreed with Lemaître's conclusion of a possible beginning and supposedly publicly disparaged the hypothesis as the "Big Bang" theory. Whether the phrase was said with contempt or not is disputed, but the name has since stuck.

The combination of the finite speed of light and redshift allow astronomers to calculate how long light has been travelling from observed galaxies. This is important as the lifetime of astronomical objects and events are often far longer than a human lifetime or even the human species as a whole and thus watching a single galaxy evolve is not possible. Finding the ages and other observational properties of galaxies allows a statistical understanding of the evolution of galaxies.

1.1.3 Accelerated Expansion

More recently, the dynamics of this expansion have been studied with other measures such as supernova, using the relationship between the measure of how quickly the supernova fades (the light curve) and the apparent brightness of the event. Like CV stars, supernova can help measure cosmological distances. They are rarer but much brighter than CV stars and so can be seen at greater distances. Riess et al. (1998) were attempting to map the recent expansion history of the Universe to see how Hubble's "constant" changed over time. The team expected to find Hubble's constant decreasing over time to show that mass in the Universe was "tugging" on spacetime, causing a deceleration in the expansion. Instead they found the opposite, that the Universe's expansion was accelerating. To achieve this expansion, the field equations constructed by Einstein to describe General Relativity could be modified to include a cosmological constant, interpreted as the vacuum energy density of space itself. When originally constructed, the cosmological constant was added as as fudge to maintain a static equilibrium in the Universe, although was removed upon Hubble's discovery of an expanding, dynamic Universe. The discovery of the accelerated expansion of the Universe put the cosmological constant back in and the unknown property of the Universe giving rise to this acceleration was given the name Dark Energy. Calculations showed approximately 70% of the energy content of the Universe can be attributed to Dark Energy.

1.1.4 Origins of the Cosmic Microwave Background

If the Universe was once far smaller and more dense, there should be signatures of this history found in the present day state of the Universe. The early Universe must have contained high energy radiation in the form of photons (packets of light energy) and electrons and protons in the form of plasma. The photons were scattered in the plasma by electrons and thus could not travel great distances, and any atoms that formed were almost instantaneously broken apart by a high energy photon. As the Universe expanded the light was redshifted by the expansion of space itself, reducing the energy of the photons to a point where they were not energetic enough to break part the atoms. The electrons and protons were then able to come together to form hydrogen (and other elements with calculable proportions) in a process known as recombination. As the atoms were neutrally charged, the photons could not interact with them and therefore these photons continued to pass through the Universe unimpeded, effectively making the Universe transparent to light at these lower energy levels. This process is known as photon decoupling, and if one

could find these photons, they could be traced back to the surface of last scattering at around the time of recombination.

In 1964, Andrei Doroshkevich and Igor Novikov derived that this background radiation should be detectable and present in the microwave to radio part of the electromagnetic spectrum, and was dubbed Cosmic Microwave Background Radiation (CMB). At the same time, Arno Penzias and Robert Woodrow Wilson were looking for microwave signals from clouds of gas and dust to map the Milky Way with the Holmdel Horn Antenna at Bell Labs. They detected a hiss across the entire sky that had no reasonable explanation and could not be removed from their data, going as far as to kill the pigeons nesting in the horn under the assumption that they were causing the interference. The hiss persisted however, and upon publishing in 1965 became the first reported detection of the CMB.

Since then, further space experiments mapping the entire sky with COBE, WMAP and most recently Planck have shown this emission (after subtracting foregrounds and compensating for relative motions of the Earth around the Sun and galaxy) to be a pure blackbody spectrum corresponding to a temperature of 2.73K, with fluctuations in the tens of μK. The fluctuations are related to the density of the Universe when the photons were last scattered. More dense regions would recombine later and so the temperature of the photons free-streaming from these areas would be marginally higher than other regions.

1.1.5 Structure Formation and Halos

The fluctuations in density at early times were also the seeds for structure formation. Small fluctuations created areas with stronger gravitational fields which caused matter to accrete and these density instabilities to grow. The majority of matter is dark matter, matter that only interacts gravitationally. Baryonic matter then falls into the gravitational wells caused by these dark matter structures. The large-scale structures, as traced by observable matter, form a spider-web-like structure of sheets, filaments, knots and voids. Surveys of galaxies in the local Universe by the Sloan Digital Sky Survey (SDSS, Alam et al. (2015)) have confirmed this "swiss cheese"-like, yet regular structure. These observations are confirmation of the Universe's adherence to the Cosmological Principle, just on a larger scale than assumed 100 years previously.

Cosmological computer simulations are often used to model the Universe. They include matter that interacts gravitationally only, representing dark matter, and sometimes matter that in addition follows thermodynamical laws and other sub-grid physical mod-

els representing baryonic matter. Sub-grid models used in cosmological simulations to approximate behaviour at unresolved scales in the simulation e.g. the number of stars formed in a region of dense matter or the formation of black holes. Sometimes instead of baryonic physics (which is far more time expensive than a pure dark matter simulation), physical models fitted to observations, semi-analytic models (SAMS), are used to "paste" galaxies onto the dark matter. The most used of these simulations is the Millennium Simulation (Springel et al., 2005) created with GADGET-2 (Springel, 2005) that consists of a dark matter simulation and with either the L-galaxies (Croton et al., 2006; De Lucia et al., 2006) or GALFORM (Bower et al., 2006) SAM overlaid. These simulations show that galaxies form in regions of dense dark matter and support observations pointing to the existence of dark matter, (e.g. the higher than expected rotational velocities of stars at the edge of galaxies).

Galaxy formation models refer to the dense region of dark matter as a 'halo'. It is onto these dark matter halos that baryonic matter accretes and forms galaxies. Dark matter halos are specifically defined as the region and mass contained within a radius within which the average density is X times the critical density of the Universe (density at which the Universe is flat), where X is typically 200. This is often defined as the virial radius. With this particular definition halos are necessarily symmetrical, although there are ways to define them asymmetrically. In dark matter simulations particles representing masses of dark matter can be grouped if the distance between two particles is less than a specified length. This is a Friends-of-Friends linking algorithm (Einasto et al., 1984) and is how haloes are defined in the Millennium simulation.

In summary, current cosmological observations of the Universe follow the ΛCDM or standard model of the Universe. That is, both dark energy and cold dark matter (dark matter that travels at sub-relativistic speeds) both influence the on-going expansion of the Universe. The latest Planck cosmological parameters (Planck Collaboration, 2015) are $H_0 = h{\cdot}100\text{km/s/Mpc} = 67.8{\pm}0.9$ km/s/Mpc for the Hubble constant, $\Omega_b h^2 = 0.0226{\pm}1\%$ and $\Omega_c h^2 = 0.1186 \pm 2\%$ for the mass energy fractions of baryonic and cold dark matter. As fractions of the total mass-energy of the Universe this corresponds to 5%, 26% and 69% attributed to baryonic matter, dark matter and dark energy respectively. The best estimate of the age of the Universe is 13.799 ± 0.038 billion years.

1.2 Star Formation

Baryonic matter does not collapse uniformly onto a dark matter halo. Small fluctuations in density grow and form structures across all scales within the halo. One such structure at the range on the order of tens of parsecs wide are giant molecular clouds (GMCs) (Mo et al., 2010). These objects are dense, with molecular hydrogen densities $n_{H_2} \approx 100\text{cm}^{-3}$, orders of magnitude above the density of ionised hydrogen in other regions of the interstellar medium (ISM). Denser regions of the ISM are able to efficiently cool through molecular line emission. The higher density of gas and dust increases the likelihood of interaction between hydrogen ions. H_2 is believed to be formed from the recombination of two hydrogen atoms catalysed by the surface of a dust grain. Molecules like H_2 and carbon monoxide (CO) can be collisionally excited then radiatively de-excite, removing energy from the cloud. As the cloud continues to gravitationally collapse the probability of interaction increases and the cloud continues to cool. Across a wide range of densities GMCs are approximately 10K in temperature and far colder than other regions of the ISM that are at temperatures greater than 1000K.

Gravitational collapse within a clump cannot be prevented by thermal emission alone when the mass reaches a threshold mass. In the case of an idealised isothermal sphere of gas in pressure equilibrium with the surrounding region, this is the Bonner-Ebert mass, (Bonnor, 1956).

$$M_{\text{BE}} = 1.182 \frac{c_s^3}{(G^3\rho)^{1/2}} \tag{1.1}$$

where G is the gravitational constant, ρ the gas density and c_s the sound speed within the gas. For clumps (protostellar cores) with $M > M_{\text{BE}}$ the free-fall time (i.e. time the cloud will take to collapse under gravitational effects only) is on the order a few to ten million years. However magnetic fields and turbulence within the gas and dust prevent clouds from collapsing at this minimum time, with times estimated at hundreds of times longer than this. As the cloud collapses, material from the surrounding GMC is accreted and the mass grows.

Eventually the core of the cloud struggles to cool. As the density increases the collisions between molecules become more frequent, the energies higher and the photons released during deexcitation are of a high enough energy that the gas is no longer transparent to them. The energy becomes trapped in the gas and the further gravitational compression in the core due to infalling material continues to heat the gas, causing H_2 to dissociate. Eventually temperature and pressures are high enough that nuclear fusion occurs in the centre, forming a new star. The star will shine for a length of time dependent on its initial

mass. The light from these new stars can be observed in the optical and UV range.

1.2.1 Connection Between Dust, Star Formation and the Infrared

Star formation is not a 100% efficient process, with only 1% of the GMC mass content converted to stars in one free-fall time (Zuckerman & Evans, 1974). As a result, newly-formed stars are often enveloped in the same clouds of gas and dust they are made from and their light obscured. The UV and optical light is scattered and absorbed by this gas envelope, causing the gas and dust to heat up in regions near new stars (the closest regions become ionised HII regions) and the emission is reprocessed into the infrared. The emission spectrum resembles a modified black-body in the far-infrared, incorporating the marginally reflective nature of dust. The mid-infrared emission is dominated by rotational and vibrational emission lines from PAHs (Poly-cyclic Aromatic Hydrocarbons) from dust in the GMCs. Therefore the infrared emission of a GMC can give information on the level of obscured star formation. Given that gas is a requirement for star formation, there must be a calculable relationship between the two. An empirical relation is given as the Kennicutt-Schmidt law,

$$\dot{\Sigma}_* \propto \Sigma_{\rm gas}^N \tag{1.2}$$

that the rate of change of stellar mass per unit area (or the specific star formation rate, sSFR) is proportional to the surface density of gas to some power N. For starburst galaxies, the relationship between the star formation rate and infrared luminosity is given as

$$SFR\,(M_\odot/\mathrm{yr}^{-1}) = 1.7 \times 10^{-10} \mathrm{L_{FIR}}\,(\mathrm{L}_\odot) \tag{1.3}$$

as derived in Kennicutt (1998). Such relationships exist for other wavelengths and will constrain star formation rates at varying timescales (See Wilkins et al. (2012) for a discussion on the connection between the unobscured star-formation rate and the UV continuum). Therefore one can infer a *physical* property of a galaxy such as the star formation rate from an *observable* like the luminosity, and models of galaxy formation and evolution can be constrained. There are caveats, however. This relationship assumes a perfect correlation between the two variables when empirically, even accounting for observational error, this relationship will not hold exactly. Further, the assumption that all infrared emission is from star-formation is incorrect. Warmed interstellar dust not within a star-forming region will also emit IR and the amount of dust will be dependent on the age of the galaxy rather than current star formation rates.

1.2.2 A Note on Other Sources of Infrared Emission

As noted above not all far infrared light from galaxies is linked to star formation. In the local Universe over half of the infrared luminosity in quiescent galaxies originates in the thermal emission from ISM unrelated to star formation. The dust has been heated by starlight from older instead of recently created stars (Lonsdale Persson & Helou, 1987; Sodroski et al., 1997). This trend has also been noted out to redshifts $z < 1.4$ (Salim et al., 2009). Dust can also be heated by active galactic nuclei within galaxies. The material accreted by the AGN emits X-rays in the process which heat up the surrounding dust torus. This in turn reradiates into the infrared. X-ray sources have been shown to contribute approximately 15% to the far-infrared (Barger et al., 2001) and 15-25% in the mid-infrared (Fadda et al., 2002). Careful SED fitting to the AGN portion of the spectra can account for the proportion of the infrared luminosity contributed by AGN activity and prevent over estimations of the star formation rate.

1.2.3 Cosmic Star Formation History

Stars within galaxies have not formed at a consistent rate over time. Lilly et al. (1996) show the co-moving luminosity density increases by over an order of magnitude with redshift out to $z = 1$ within the UV, implying a higher degree of unobscured star formation was needed to maintain that luminosity at earlier times. Madau et al. (1996) takes this picture out to $z = 4$, demonstrating that $z > 2$ the star formation rate density decreases with redshift. A rest-frame UV study of unobscured star formation such as work using Hubble Space Telescope data with GOODS (Great Observatories Origins Deep Survey) Dahlen et al. (2007) has shown the peak of star formation at $z < 2$ with star formation an order of magnitude lower in the current epoch. Bouwens et al. (2012) mirrors this result probing at far deeper redshifts in rest-frame UV than previous studies including tentative results at $z = 10$. The shape of cosmic star formation history is well-defined in this result, with the peak around $z = 2$ current star formation rates similar to those reported at $z = 8$.

This picture is mirrored with obscured star formation observations in the mid-infrared from the like of Chary & Elbaz (2001) showing a peak plateau of star formation at $0.8 < z < 1$. More recently, Magnelli et al. (2011) has shown with prior source extraction on Spitzer data that infrared measures of the star formation history of the Universe show a similar picture, namely a plateau at $z = 2$ and a decline in more recent times. More recently Burgarella et al. (2013) (figure 1.1) use far infrared and UV emission to constrain star formation at $0 < z < 4$, finding the peak of obscured and unobscured cosmic star

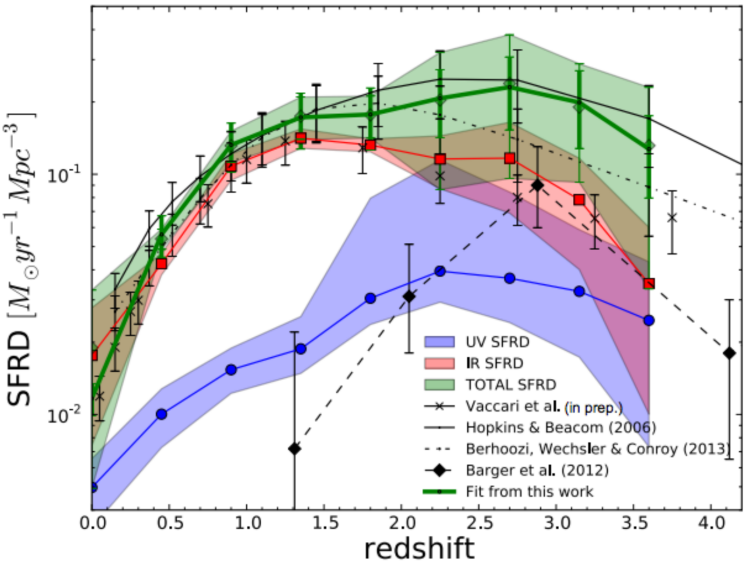

Figure 1.1: Evolution of the cosmic star formation rate density with redshift as presented in figure 4 of Burgarella et al. (2013). The figure shows the plateau in star formation around $z = 2.5$ and how this has declined by over a factor of ten to present day. The importance of including multi-wavelength studies is highlighted by demonstrating that the star formation rates calculated from IR (obscured) and UV (unobscured star formation) differ and complement each other. Reproduced with permission from Astronomy & Astrophysics, © ESO.

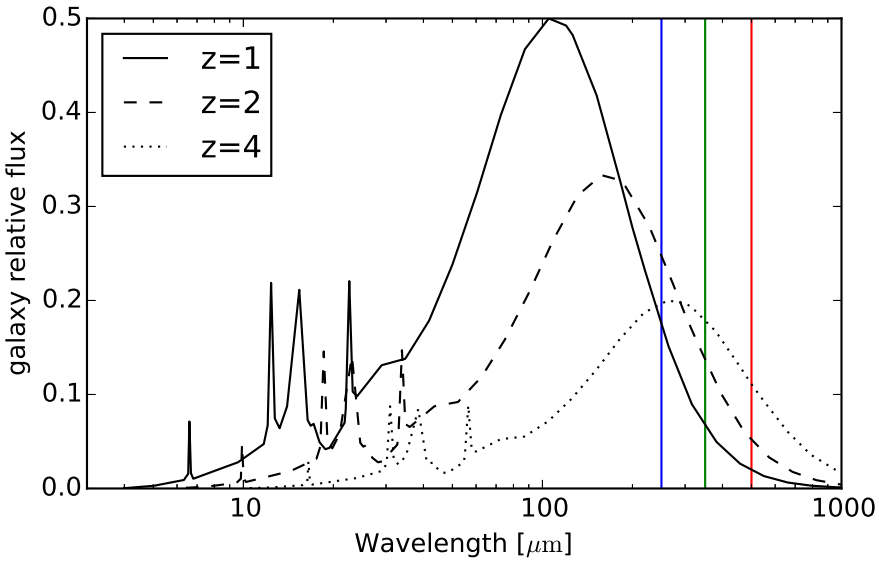

Figure 1.2: Demonstration of negative k-correction across the *Herschel*-SPIRE bands using the M82 SED. Whilst at other wavelengths the observed flux of a galaxy drops with increasing redshift, the observed flux remains relatively constant across the *Herschel*-SPIRE bands.

formation to be $2 < z < 2.5$. The authors emphasise the importance of multi-wavelength approaches to determine physical results like star formation rates of galaxies and therefore the impact far-infrared observations had on this particular area. A more recent study (Driver et al., 2016) of the cosmic spectral energy distribution across the near past (0.3-2.4 Gyr) using the Galaxy And Mass Assembly Panchromatic Data Release (GAMA-PDR) has also shown the energy budget of galaxies has dropped to three-fifths over this time period. Whist this is not a full calculation of the star formation history of the Universe, the change in energy budget is a proxy for star formation. Research therefore is in agreement that star formation reached a peak between $2 < z < 2.5$ and is now in decline, and more on these studies and the field of research can be read in Hopkins & Beacom (2006) and Madau & Dickinson (2014).

1.2.4 Negative k-Correction

Far infrared observations of the SEDs of star forming galaxies have one particular advantage: k-correction. k-correction is a compensation applied to observations to account for the (usually diminishing) effect redshift has on the amplitude of an SED. It is the correction applied to photometric observations to calculate what the rest-frame flux would be of a galaxy. As the spectrum is stretched by a factor of $(1 + z)$ to higher redshifts, the

observed intensity of the spectrum also falls proportional to $((1+z)D_L)^2$ (with D_L the luminosity distance) and so must also be k-corrected. Due to this redshift-induced attenuation, a galaxy can quickly become undetectable at higher redshifts. Figure 1.2 shows the change in the SED with redshift. In the mid-infrared, the sharp features originating from poly-cyclic aromatic hydrocarbon emission fade at higher redshifts. However, at particular wavelengths like at those longer than the wide peak in the SED in the far infrared, the peak itself is stretched through these wavelengths at high redshifts. Even though the intensity of the spectrum has fallen, the flux within the far-infrared (indicated by the SPIRE wavelengths in the figure) remains relatively constant. Therefore a galaxy can be observed across a wide range of redshifts with the same instrument. This is referred to as negative k-correction. Observations from the Herschel Space Observatory in particular benefits from this effect.

1.3 The Cosmic Infrared Background, Galaxies and Other Sources

The build up of observed infrared emission from galaxies over time forms what is known as the Cosmic Infrared Background (CIB). The CIB forms around half of the emission making up the extragalactic background light (EBL) from mechanisms associated with structure formation within the Universe, peaking at 150μm. Figure 1.3 shows the EBL as a function of wavelength with the *Herschel* coverage included, showing observations from the telescope can probe the peak of the CIB and thus find which populations of galaxies are the main contributors to the CIB.

It is not just extragalactic sources contributing to the infrared background. Figure 1.4 gives the contribution to the observed CIB from many sources and shows again which wavelengths the *Herschel* Space Observatory covers. The cosmic microwave background is the main significant contributor at very far-infrared wavelengths and as previously discussed is a relic of the Big Bang with a perfect blackbody emission spectrum at $T = 2.73$K and thus not of a galactic origin and is known to have low power on small scales. Untangling this emission from other sources is a particular problem for data from the Planck satellite (Planck Collaboration et al., 2014).

Emission from the ISM in our own galaxy (galactic cirrus) is a particular problem. The emission does not come from solely star forming regions but all across the sky, especially concentrated across the galactic plane. The structure is not uniform at any scale and

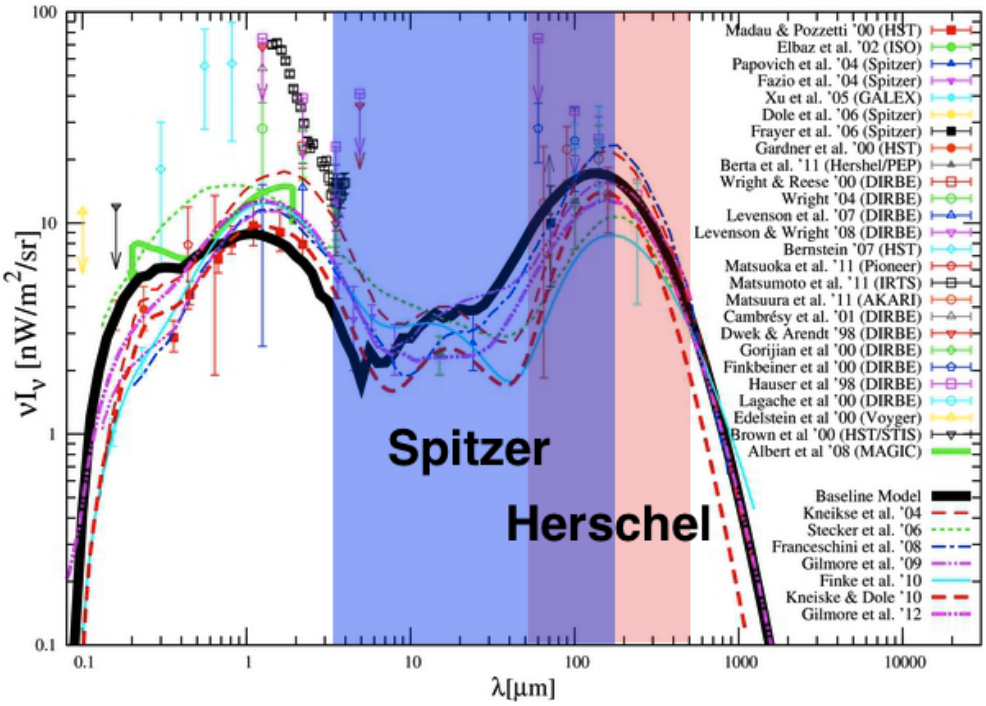

Figure 1.3: The extragalactic background light as measured from many observations and models as presented in figure 7 of Inoue et al. (2013) (reproduced by permission of the AAS). Wavelengths associated with instruments have been added for this thesis. The subject of this thesis, the *Herschel* Space Observatory, covers the peak of the cosmic infrared background.

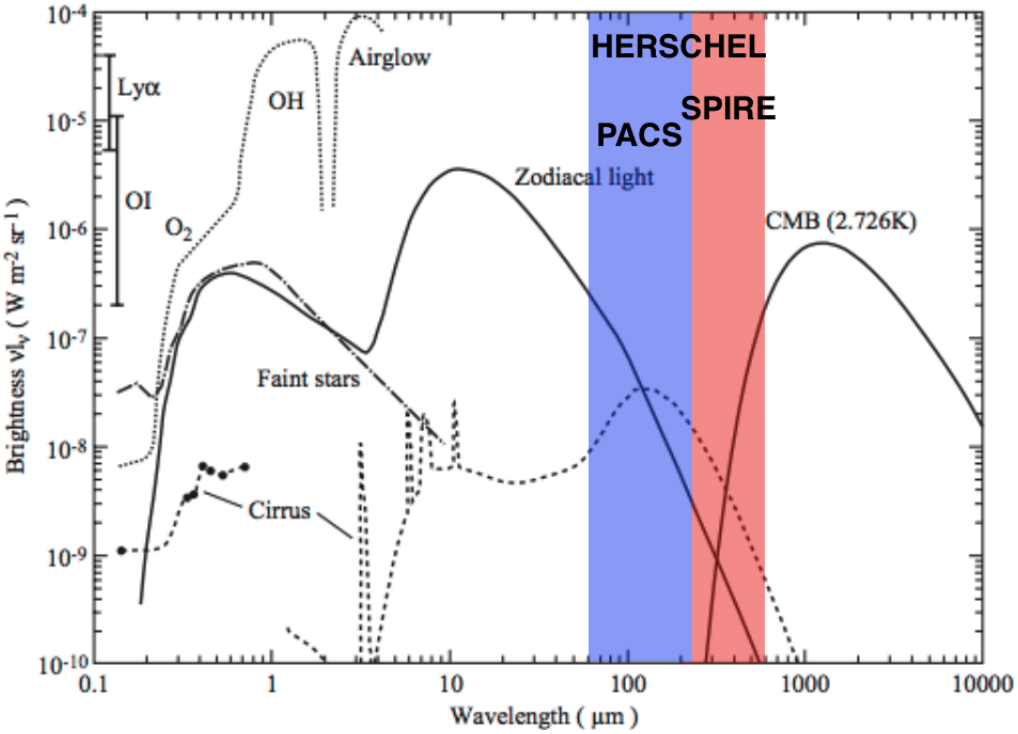

Figure 1.4: The relative contributions to the cosmic infrared background that is not related to galaxies outside the Milky Way. Figure adapted from figure 1 in Leinert et al. (1998) (Reproduced with permission from Astronomy & Astrophysics, © ESO) and figure 4.2 in Valtchanov (2014) to include the Herschel Space Observatory coverage.

thus has different intensities point-to-point (Neugebauer et al., 1984a). Broadly however the emission peaks at 100μm and correlates across the bands so the contribution to the infrared background can be constrained. Extragalactic survey fields are constructed to avoid areas of high cirrus contamination and thus reduce the impact on calculations such as the cosmic infrared background energy budget.

Zodiacal light is the main contaminant at mid-infrared wavelengths, arising from thermal emission from dust and gas in our own Solar System or scattered sunlight off this dust. This also includes the infrared light from asteroids in the Solar System; sunlight is absorbed by asteroids in an amount dependent on the albedo of the surface and the energy reemitted in the infrared (Sykes, 1988). Zodiacal light is brightest in the plane of the Solar System, increasing in intensity towards the Sun, and is fairly uniform in structure unlike galactic cirrus.

Finally there is airglow. This is diffuse emission from the upper atmosphere caused by for example interactions of molecules with cosmic rays or recombination of atoms after molecules are dissociated by sunlight. Airglow is dominant in the near infrared and, as it is an atmospheric effect, is not observed by space telescopes (Glass, 1999).

Observations of the CIB and far-infrared emission in general also suffer from attenuation effects. Molecules within our atmosphere like water absorb infrared infrared light, blocking effective observations of particular wavelengths corresponding to rotational and vibrational lines especially in the spectrum of these molecules. Infrared telescopes are best placed at high altitude with dry weather, although the possibility of poor weather cannot be ruled out and so space is the very best place for an infrared telescope for observations.

1.4 History of Infrared Astronomy

This section gives details about infrared facilities discussed in this thesis including the titular *Herschel* Space Observatory. Where relevant, major discoveries and examples of legacy surveys conducted on the telescopes are given. As this thesis is performing source detection and extraction, techniques used to find galaxies in these legacy surveys are also explained.

1.4.1 Infrared Discovery and the First Instrumentation

Wavelengths of light beyond the visible were first discovered in the early 1800s by William Herschel. Dubbed *infrared*, it was first 'observed' as a temperature rise in a thermometer placed alongside the red light of a rainbow split by a prism. This indicated the existence

of light that was beyond the red end of the human-visible spectrum.

The detection of infrared light relied on thermocouples and Crook's radiometers ('light mill') until the invention of the bolometer in 1878 by Samuel Pierpont Langley. A bolometer measures the increase in temperature of a substance otherwise kept at a fix temperature when light is absorbed. From there the energy impinged can be calculated and then the brightness of an object at a known wavelength inferred. The invention of cryogenically cooled systems in the 1950s was a further breakthrough for infrared astronomy, allowing instruments to be kept cool and preventing the infrared radiation from the instrument itself (the thermal noise) to be picked up by the bolometer.

1.4.2 The Earliest Facilities

In 1969 the 2-micron Sky Survey (Neugebauer & Leighton, 1969) was produced, an infrared star catalogue produced at Mount Wilson in California, USA. More than 5000 stars were catalogued with fluxes at 2.2 and 0.84μm and cross correlated to a number of optical star catalogues. The authors found stars that were brightest in the infrared, hinting that the Universe at infrared wavelengths could be far richer than previously thought.

The first space missions were rocket-bourne telescopes (as opposed to future orbiting telescopes) developed by the US Air Force Cambridge Research Laboratory (Walker, 1975), carrying broadband photometers covering the 3-5μm, 8-14μm and 16-24μm wavelengths. Whilst more difficult than ground-based observations, rockets can get the telescope high enough to reduce the attenuating effect of the atmosphere on the infrared signal. The longer wavelengths allowed for the identification of cooler objects such as proto-stellar sources (a collapsing cloud of gas and dust that will form a star), proto-planetary nebulae (formed through the mass lost during the late-time evolution of a star) and HII regions (cool regions of mainly ionised atomic hydrogen ionised by UV radiation from newly formed stars) (Price & Walker, 1976; Price, 1977; Price et al., 1983).

1.4.3 Selected Ground-Based Facilities

From the earlier short-term missions the next telescope facilities were ground-based. NASA's IRTF (Infrared Telescope Facility) and UKIRT (the UK infrared Telescope) observatories were both constructed on Mauna Kea. This was to take advantage of the unprecedented seeing (air masses flowing from the Pacific Ocean are extremely stable, reducing atmospheric interference) and the lack of overcast skies (due to the elevation).

Opened in 1979 IRTF has a 3m mirror and currently covers the 0.8-25μm wavelength

range with a number of instruments. IRTF was developed to track the Voyager missions and has since been heavily involved in planetary science, recently understanding the composition of Saturn's Moon Titan's atmosphere (Penteado et al., 2005; Kostiuk et al., 1997) and impacts on Jupiter (Baines et al., 2013), with extragalactic contributions such as studying PAH features in AGN hosts to find previously unobserved star formation (Rodríguez-Ardila & Viegas, 2003).

UKIRT was opened the same year as IRTF but with a slightly larger 3.8m mirror and covers the 0.8-5μm range. In 2005 UKIRT began a systematic study of the extragalactic sky with UKIDSS (the UKIRT infrared Deep Sky Survey, Lawrence et al. (2007)) as a successor to 2MASS, (Two-Micron All Sky Survey, Skrutskie et al. (2006)) a survey that catalogued galaxies, brown dwarfs and low-mass stars in the 1.25-2.17μm range at two separate facilities in different hemispheres. Whilst UKIRT alone cannot observe the entire sky, UKIDSS was a deeper survey and had twelve times the volume of 2MASS. The survey was designed as a legacy survey, with regions selected to contain other wavelengths for a complete multi-wavelength understanding of galaxies. Some of these fields (e.g. UDS, Ultra-deep Survey) are used in the Herschel Multi-tiered Extragalactic Survey (HerMES) which is extensively discussed in this thesis.

At far infrared wavelengths, the James Clerk Maxwell Telescope's SCUBA 2 instrument (Holland et al., 2013) on Mauna Kea has filters at 450μm and 850μm. The mirror is 15m in diameter, over 4 times wider than the Herschel Space Observatory's (below) bringing greater resolution than previous instruments at these far infrared wavelengths. Surveys like the SCUBA-2 Cosmology Legacy Survey (S2CLS, Geach et al. (2013)) have imaging in mostly northern hemisphere legacy fields like AKARI-NEP, COSMOS and UDS. SCUBA-2's overlap with Herschel bands and better resolution allows the better identification of sources and understanding of source blending.

The Atacama Pathfinder EXperiment (APEX) in Chile is a 12m telescope also at altitude, although covering the Southern Sky as opposed to Mauna Kea's northern sky coverage. The Large APEX Bolometer Camera (LABOCA) instrument (Siringo et al., 2009) covers 870μm and was originally constructed as a path-finder for ALMA, the Atacama Large Millimeter Array.

1.4.4 Selected Space-Based Facilities

The first space-based observatory to perform a full-sky survey at infrared wavelengths was IRAS, the Infrared Astronomical Satellite (Neugebauer et al., 1984b), launched in

1983 and covering wavelengths 12-100μm. Early results were spectacular and touched all areas of astrophysics (Neugebauer et al., 1984a), from finding a higher than expected dust content for comets to extended emission of dust in the interstellar medium (Low et al., 1984) and the Solar System (Sykes, 1988). The interstellar medium was shown to have an unexpected filamentary geometry. Distant galaxies extremely bright in the infrared were discovered, again far brighter than previously thought (Soifer et al., 1984) and not very bright in the optical (Houck et al., 1985). Those bright galaxies are known as Ultra-Luminous Infrared Galaxies or ULIRGs and are currently defined as galaxies with infrared luminosities $L_{8-1000\mu m} \geq 10^{12} L_{\odot}$ and are considered rare objects.

The Infrared Space Observatory (ISO, Kessler et al. (1996)), launched 1995, had an improved cryogenic system and IR detector technology and so was able to probe further into the infrared from 2.5 to 240μm. ISO did not perform an all-sky survey, instead selecting some 30,000 sources and providing far better images, with up to 1000 times better sensitivity and 100 times better angular resolution than IRAS. The largest open time survey conducted was ELAIS, (European Large Area ISO Survey, Oliver et al. (2000)), covering 20 sq. deg. and probing (then) high redshift objects at $z \approx 1$ (Serjeant et al., 2004). The survey number counts (the number of galaxies as a function of flux, Serjeant et al. (2000), Efstathiou et al. (2000)) found good agreement with confusion limited number counts from the Hubble Deep Field found with a deeper ISO survey and IRAS number counts at the bright end. This implied that a population of dusty, star forming galaxies makes up a significant fraction of the cosmic infrared background.

NASA's Spitzer Space Telescope (Werner et al., 2004), launched in 2003 and originally observed in the 3.5-160μm wavelength range. The liquid helium coolant was exhausted in 2009 and since then Spitzer has operated in a warm-mode, only observing in wavelengths 3.6μm and 4.5μm with the IRAC (infrared Array Camera) as these these wavelengths are less affected by the thermal emission of the telescope. Amongst the legacy surveys performed when the telescope was fully operational was the SWIRE survey (Spitzer Wide-Area Infrared Extragalactic Survey, Lonsdale et al. (2003)), covering 65 sq. deg., finding millions of sources including sources at $z > 2$. The fields chosen overlapped with previous regions to increase the multi-wavelength data available. The maps from Spitzer are at a high enough resolution that individual galaxies are resolved well enough to be a valuable resource for observations at longer wavelengths by providing cross-identifications and map offset calibrations.

Designed to probe deeper than IRAS and across a wider range of wavelengths, the

AKARI mission (Murakami et al., 2007; Ishihara et al., 2010; Doi et al., 2012) launched in 2006 performed another 'all-sky' survey (99% coverage), this time across 2-180μm. Some areas of the sky were visited multiple times to provide extremely deep maps and catalogues (Matsuhara et al., 2006) to compare to other surveys, for example Clements et al. (2011) specifically extract sources found in Spitzer maps within the AKARI Deep Field South (ADF-S) region to examine the number counts. It is this type of work that facilitates multi-wavelength studies across legacy fields.

Soon after, the Wide-field Infrared Survey Explorer (WISE, Wright et al. (2010)) was launched, again performing an all-sky survey although in four bands from 3.4 to 22μm, probing the near and mid-infrared more completely than AKARI. Over half a billion sources, from bright regions of nearby galaxies to point source-like extragalactic sources were identified.

As a precursor to the *Herschel*-SPIRE instrument, the BLAST (Balloon-borne Large Aperture Submillimeter Telescope, Pascale et al. (2008)) was launched in 2005 and 2006 from Sweden and Antarctica respectively, observing at 20μm, 350μm 500μm. Whilst still within the Earth's atmosphere, the telescope hung from a balloon and rode high-altitude winds to be above the majority of the attenuating atmosphere. BLAST observations of extragalactic skies include the South Ecliptic Pole field (Valiante et al., 2010), Extended Chanda Deep Field South (Chapin et al., 2011), and GOODS-south (Devlin et al., 2009), the latter finding that over half the extragalactic background must arise from sources at $z \geq 1.2$.

1.5 Herschel Space Observatory

FIRST (Far InfraRed and Submillimetre Telescope) was chosen in 1993 to be a cornerstone mission for the European Space Agency's Horizon 2000 long-term science plan. Renamed to the Herschel Space Observatory, (Pilbratt et al., 2010) *Herschel* was launched in 2009 with liquid helium coolant that depleted in 2013, giving almost four years of spectacular new results. To be far removed from the infrared light that an Earth-orbiting telescope would be exposed to, *Herschel* (and its sibling microwave telescope Planck) were positioned at Lagrangian Point 2, a gravitationally stable point in the Earth-Sun orbit in the "shadow" of the Earth. With the largest mirror in space at 3.5m across and the focal plane cooled to 1.4K, *Herschel* was able to produce high resolution maps in the mid-far infrared and confusion limited maps in the far infrared (the ability to detect sources is governed by the blending between sources as opposed to the instrumental noise). These

improvements provide the best ever view of the far-infrared to submillimetre end of the infrared spectrum. The spectral range 55-672μm was covered by the observatory from three instruments. Two combined direct detection cameras and medium resolution spectrometers PACS (Photodetector Array Camera and Spectrometer, Poglitsch et al. (2010)) and SPIRE (Spectral and Photometric Imaging REceiver, Griffin et al. (2010)) and a high resolution spectrometer HIFI (Heterodyne Instrument for the Far-Infrared, de Graauw et al. (2010)).

1.5.1 HIFI and PACS

HIFI covers the wavelength range of 240-625μm and 157-213μm with seven receivers at very high resolution, with an on-sky resolution of 13-40 arcseconds (comparable with the SPIRE instrument's point source function's (PSF's) full-width half maximums (FWHMs)), and a spectral resolution of 0.02-0.7 km/s. The signal is processed with heterodyning, mixing the incoming signal with another produced by the telescope to create a signal at a lower and therefore more manageable frequency. HIFI results include the detection of different spin isomers of water molecules throughout the planet-forming disk around star TW Hydrae; these molecules form at different temperatures indicating the material in the disk does not remain at a fixed radius (Hogerheijde et al., 2011). PACS covered a different frequency range of 60-210μm in three bands (although observing only two at once, 160μm with 70μm or 100μm) and a spectral resolution of 150-200 km/s. Pixel sizes are 3.2, 3.2 and 6.4 arcsec with FWHM of 5.6, 6.8 and 11.3 arcsec respectively. Comparing to Spitzer, the MIPS instrument has a FWHM of 18.6" at 70μm, meaning PACS has a three-times improvement on the angular resolution of the sky at these wavelengths and less likely to suffer from source confusion. The PEP (PACS Evolutionary Probe, Lutz et al. (2011)) was one of the largest guaranteed time surveys on the PACS instrument, covering many of the same legacy fields as the complementary survey HerMES with the SPIRE instrument (below, chapter 2). The survey aims to further understanding of galaxy evolution with the now better resolved PACS wavelengths providing amongst other things better estimates of star formation rates.

1.5.2 SPIRE

This thesis uses almost exclusively data and results from the SPIRE photometry instrumentation. SPIRE reaches the far-infrared wavelengths with photometric filters centred on 250, 350 and 500μm and the FTS (Fourier Transform Spectrometer) optimised for 200-

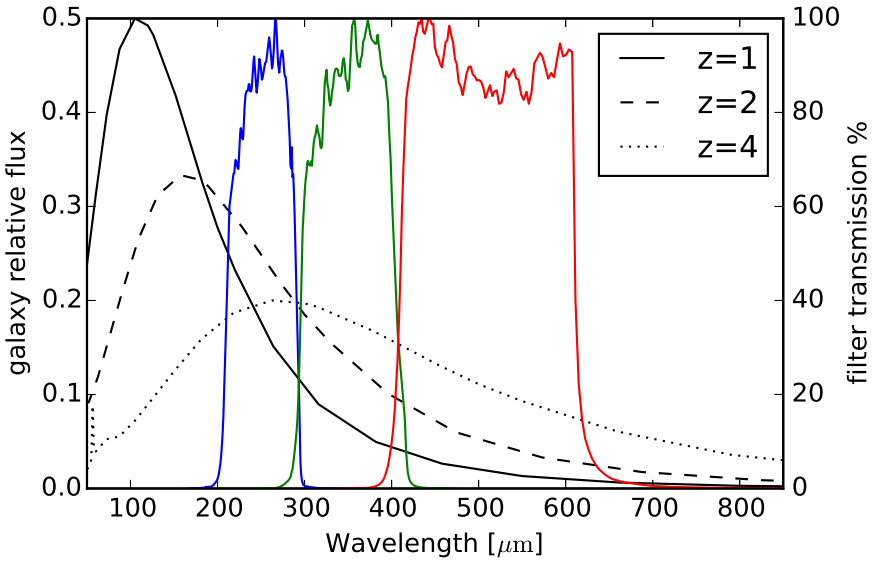

Figure 1.5: The three SPIRE filters centred on 250, 350 and 500μm. Super-imposed are SEDs representing M82 at different redshifts. Due to the change in shape of SED with redshift, higher redshift galaxies experience negative k-correction and thus the high redshift sources are still relatively bright.

400μm (Valtchanov, 2014). Standard image pixel sizes from the photometer are of 6, 10 and 14 arcsec with PSF FWHMs of 18.15, 25.15 and 36.3 arcsec. The FWHMs are broader than those of SCUBA-2, although this is due to JCMT's larger mirror that is currently unfeasible for a space mission. From the primary to final, light reflects from eight different mirrors to the detector. Before reaching the detectors the light passes through the filters, constructed from metal mesh filters (Ade et al., 2006) and shown in figure 1.5.

The arrays have 139, 88 and 43 bolometers (with an additional 4, 1 and 1 dead bolometers) in a hexagonal pattern for the 250, 350 and 500μm arrays. Each detector has a feedhorn directing light to the detector, preventing the majority of stray light from reaching the detector. The arrays are kept at a working temperature of 1.3K by the liquid helium coolant, reducing the impact of thermal emission from the array itself on the observations. The detectors are bolometers, consisting of an absorber of silicon nitride and a thermometer of germanium. The temperature rise in the absorber is due to impacting photons is monitored by the thermometer and the response recorded as the signal. Additional temperature fluctuations from dark bolometers are also recorded to provide some measure of the instrumental noise background and any temperature drifts (Valtchanov, 2014).

Observations are scheduled as Astronomical Observation Requests (AORs) which in-

clude the position, size, number of scan repeats to perform and the scan mode. *Herschel* can observe with SPIRE in parallel mode simultaneously (30 arcsec/s) with two PACS bands or SPIRE only at nominal (30 arcsec/s) or fast (60 arcsec/s) speeds. In the majority of large maps, the maps are constructed from cross-linked scans, scans at approximately ninety degrees to each other. Due to the hexagonal pattern of the detectors, the scan directions are at a +/-42 degree angle to the pattern to ensure the best coverage by the detectors. As AORs for large maps can consist of many scans, the telescope orientation will change over time thus asymmetries in the telescope beam at a particular pixel will be blurred.

Further information on HerMES (Herschel Multi-tiered Extragalactic Survey), a legacy survey conducted with *Herschel* is discussed in the next chapter.

1.6 Source Detection and Extraction Techniques

To understand the evolution of populations galaxies, emission from galaxies must be first identified within telescope data. This thesis will be doing just that, finding emission from galaxies in *Herschel*-SPIRE data as part of the HerMES collaboration. The techniques used to separate signals from galaxies within the data collected will vary telescope to telescope. Below are some common techniques used by the above surveys to put the HerMES source detection and extraction algorithms within a wider context. The source detection and extraction methods used by HerMES on the Herschel Space Observatory are detailed in the next chapter.

The IRAS point source catalogue was constructed from the data stream itself, with a square wave filter applied to the data and sources defined as where the signal peaks above the zero-point level. Each peak was compared to an idealised peak expected from a noiseless source to estimate a flux value (Beichmann, 1985). The IRAS Faint Source Survey (Moshir et al., 1992) went deeper than previous point-source catalogues by filtering all data streams with the shape of the point source, then co-adding the data streams to detect sources previously undetectable.

Both ISO (Héraudeau et al., 2004) and Spitzer surveys (Lonsdale et al., 2004; Shupe et al., 2008) perform source extraction using SExtractor (Bertin & Arnouts, 1996). SExtractor is a popular blind source extraction tool designed for optical images that primarily consist of extended sources. To find sources it thresholds an image, assigning pixels above the threshold to a source and below to a background. If there are fluctuations across the area of pixels assigned to a source (i.e. if sources are marginally blended), the

code breaks the region up into many sources (Holwerda, 2005). The photometry can be estimated in a number of ways. In this case aperture photometry was used, which is the addition of flux assigned to pixels within a defined radius around the centre of the source. Both ISO and Spitzer methods using the Lari method (Lari et al., 2001) to remove glitches caused by cosmic rays on the detector, relying on the detector's transient response to charged particles to flag and remove their effect on the signal. Source extraction is then performed on the cleaned maps using the IDL '*find*' command, selecting pixels above a threshold and fitting centroid shapes to the peaks.

AKARI's detection and extraction method is similar. Sources are extracted from images composed of two subsamples of scans using SEXTRACTOR. Signals above a threshold are registered and if confirmed in both data subsets are passed along to be photometrically determined on the entire image. This way erroneous signals from cosmic rays are excluded.

Sources are found with MDET, developed from the Szalay et al. (1999), comparing the likelihoods of a pixel lying on a blank background against the probability the pixel represents the peak of a source, accepting or rejecting a source with a certain number of sigma. All bands are considered at the same time. Positions of accepted sources are passed to WPHOT, and photometry is determined by fitting the PSF at all positions simultaneously. This multipart and simultaneous band fitting photometry is in contrast to single band detections provided by the likes of SEXTRACTOR.

For BLAST and JCMT images, the source detection algorithm performs a noise-weighted convolution of the map with the telescope PSF, finding peaks within this convolved map and fitting the PSF to the flux map to ascertain the photometry (Devlin et al., 2009; Geach et al., 2013). This is a maximum likelihood method of blind source detection and extraction and is expanded on in chapter 2 as a similar algorithm is used for *Herschel*-SPIRE data.

The LABOCA Extended Chandra Deep Field South Survey (LESS, Weiß et al. (2009)) is a survey on the APEX telescope using the LABOCA instrument, finding 126 submm galaxies at 870μm over a region of 30×30 arcmin^2. The sources are detected and extracted using a false detection rate algorithm (Hopkins et al., 2002) performed on the noise-weighted convolution of the map. The false detection rate is used as a parameter for the algorithm instead of a signal-to-noise ratio. At the same time as sources are found and removed on the map, negative peaks caused by the noise in the map are also recorded. These negative peaks are assumed to have positive spurious peaks associated with them and are used to estimate the probability of the number of spurious sources within the

current catalogue. This sets the minimum signal-to-noise ratio of the maps.

1.7 Thesis Summary

This introduction has placed the work of this thesis in the wider context of the modern understanding of cosmology and astronomy. The current definition of the standard model, ΛCDM, and the observations leading up to its establishment were given. Large-scale structure formation and the formation of galaxies within dark matter halos was explained as well as the mechanism behind star formation and its link to infrared emission. Observations in the infrared therefore can be linked to physical properties of galaxies which in turn can be used to infer the evolutionary history of galaxies. In addition the history of infrared astronomy was given, including modern observational facilities as well as the source detection methods in the data from each facility. The *Herschel* Space Observatory instrumentation and in particular the SPIRE instrument was outlined.

The value of far-infrared catalogues of galaxies to astrophysics is therefore obvious. With the *Herschel* Space Observatory providing such a large amount of data, finding galaxies and quantifying the accuracy of positional and flux estimates within those catalogues will allow astronomers to constrain astrophysical models of galaxy evolution through measures of obscured star formation.

In Chapter 2, the goals of the HerMES collaboration and recent results are described. The map making pipeline and source detection and extraction algorithms developed for *Herschel*-SPIRE maps within HerMES are explained. Two source extraction methods were used; a blind source detection and extraction method known as SUSSEXtractor and a second combination of the source detection software STARFINDER with a prior-driven algorithm DESPHOT to extract fluxes. For this thesis, the source detection and extraction algorithms are used on two maps newly constructed for the second HerMES data release, the uniform CDFS-SWIRE and Lockman-SWIRE fields. The raw number counts of the catalogues constructed from these algorithms are compared to draw comparisons between the two detection techniques.

Chapter 3 forms part of and extends the work of Wang et al. (2014), quantifying the completeness of catalogues as well as the positional and flux accuracies for four HerMES fields at different depths using a source injection technique. These results are used to compare the success of the source detection and extraction softwares at varying depths and to provide guideline corrections for astronomers using these catalogues. The paper itself uses simulated maps with realistic number counts to calculate the catalogue completeness

and accuracies. Both the source injection and full simulation results are compared to highlight which method is best in different situations.

Chapter 4 is devoted to the extraction of sources within the HeLMS field, a shallow 270 sq. deg. field that has extensive cirrus contamination. The cirrus structure within the field is explored to find whether this cirrus is fractal in nature and follows the same scaling laws as shown in statistically representative studies of galactic cirrus. The STARFINDER/DESPHOT pipeline is modified to cope with the increased size of the map and the aggressive filtering used to remove cirrus. This catalogue is the first publicly available for the HeLMS field and contains over 80,000 galaxies. The completeness and accuracy of the catalogues are assessed with source injection and the effect of randomly distributing the sources.

A different research area is covered in the chapter 5, looking at map-based approaches of distilling information from the three SPIRE maps. There is strong covariance between all three SPIRE wavelengths that is not often exploited. Using Principal Component Analysis (PCA) a transformation can be performed on the maps to find the linear combination of the maps that captures the most covariance. PCA is performed in a variety of different ways to find the best re-projection of the data for different situations. This data transformation can be used as a way to capture covariance between bands in probability of deflection analysis.

Finally, chapter 6 outlines an ongoing investigation into discrepancies between results from the HerMES and H-ATLAS collaborations. There is a discrepancy between the clustering measurements from both collaborations, particularly at 250μm. To identify where this difference may arise the map creation pipelines are discussed and quantified through stacking on 24μm sources. The catalogue creation processes are also compared. The angular correlation function is also recalculated for HerMES sources with the updated catalogues, using full simulations to calculate a first approximation to the transfer function for SUSSEXtractor and STARFINDER/DESPHOT source extraction techniques. Further work would look to calculating the angular clustering on H-ATLAS sources to find the clustering of HerMES sources across a variety of scales.

This work has covered a number of areas of research in the far-infrared, from detecting emission from galaxies to deriving scientific results from the *Herschel*-SPIRE maps and catalogues.

Chapter 2

Catalogues from the HerMES Second Data Release

This first chapter acts a secondary introduction chapter introducing HerMES, the *Herschel* Multi-tiered Extragalactic Survey, and the particular data reduction pipelines used to create the maps and catalogues from data from *Herschel*-SPIRE. These particular pipelines have been used for this thesis to create new galaxy catalogues for two fields for the second HerMES data release, available on HeDaM [hedam.lam.fr/HerMES/], and to create simulated images mimicking *Herschel*-SPIRE observations for the companion paper to this catalogue, Wang et al. (2014). The catalogues created are contrasted to each other to highlight the difference in performance in the two different source detection extraction algorithms used, SUSSEXtractor and STARFINDER/DESPHOT. This chapter leads into chapter 3 where the objective performance of both source extraction techniques is assessed using a technique called source injection.

2.1 HerMES: The *Herschel* Multi-tiered Extragalactic Survey

There were a number of key guaranteed time projects proposed for the *Herschel* mission proposed in the planning stage that were selected as legacy projects. HerMES, the *Herschel* Multi-tiered Extragalactic Survey (Oliver et al., 2012), was given the most amount of time on *Herschel*, with 900 hours and covering an area of 100 sq. deg with the SPIRE and PACS instruments, and 270 sq. deg. in one shallow field (HeLMS) with SPIRE alone. The broad science goal of the survey was to provide insight into galaxy evolution using far-infrared wavelengths.

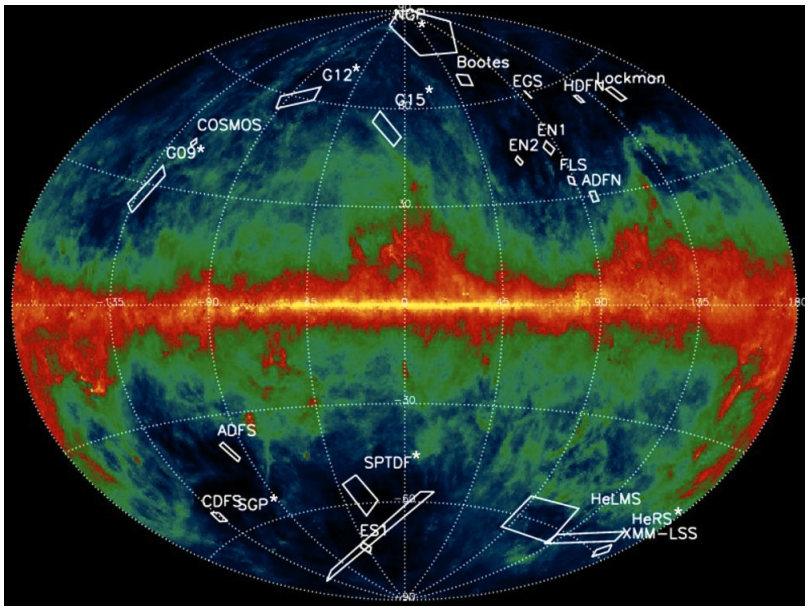

Figure 2.1: The locations and approximate footprints of many HerMES fields shown in galactic plane projection on top of IRAS dust maps. The warmer the colours the more intense the galactic cirrus emission. HerMES fields were placed to avoid the bulk of this galactic emission. This figure was produced by the HELP collaboration as discussed in a later chapter and so also includes fields from other surveys as indicated by asterisks.

To diversify the possible science results varying field sizes and depths were selected. The smaller fields reach a greater depth than the wider fields with many scan repeats and the shallower, wider fields have fewer scans contributing towards the final image. This leads to the so-called tiered "wedding-cake" design of the survey, ranging from the so-named Level-1 cluster fields of 0.08 sq. deg. to Level 6 region of XMM-LSS-SWIRE at 19 sq. deg. with HeLMS as the only Level 7 field. Fields were designed to sample a broad range of redshifts and luminosities of galaxies, the smaller fields reaching deeper to find fainter galaxies, and the wider, shallower fields finding the brighter, rarer objects. Binning by redshift and luminosity, the survey was designed to find 75 galaxies in each $\Delta \log L = 0.5$ times Δz=0.2 bin, between redshifts $0 \geq z \geq 3$. At 250μm, the luminosity depths were approximated at $z = 2$ to be $2 \times 10^{12} L_{\odot}$ for deep fields like COSMOS, to $1 \times 10^{13} L_{\odot}$ in HeLMS using the Lagache et al. (2003) models. Table 2.1 gives the names, AOR (astronomical observing request) numbers as well as the sizes and number of scans for all HerMES fields. Bolded field names are discussed in some capacity in this thesis. Many of these fields are so-called legacy fields that include data at other wavelengths from past surveys. This allows multi-wavelength science to be conducted, with examples given below.

Set	Level	Target	Mode	$\Omega_{\rm good}(\rm deg^2)$	Scan num.
1	CD	Abell 2218	Sp. Nom.	0.10	100
2	CD	Abell 1689	Sp. Nom.	0.08	48
3	CD	MS0451.6-0305	Sp. Nom.	0.08	48
4	CS	RXJ13475-1145	Sp. Nom.	0.08	48
5	CS	Abell 1835	Sp. Nom.	0.08	48
6	CS	**Abell 2390**	Sp. Nom.	0.08	48
7	CS	**Abell 2219**	Sp. Nom.	0.08	48
8	CS	Abell 370	Sp. Nom.	0.08	48
9	CS	MS1358+62	Sp. Nom.	0.08	48
10	CS	Cl0024+16	Sp. Nom.	0.08	48
11	CH	MS1054.4-0321	Sp. Nom.	0.16	16
12	CH	RXJ0152.7-1357	Sp. Nom.	0.16	16
13	L1	GOODS-S	Sp. Nom.	0.35	76
14	L2	**GOODS-N**	Sp. Nom.	0.55	30
15	L2	ECDFS	Sp. Nom.	0.58	19
22	L2	**COSMOS**	Sp. Nom.	2.82	8
17	L3	Groth Strip	Sp. Nom.	0.60	7
18	L3	Lockman-East ROSAT	Sp. Nom.	0.57	7
18B	L3	Lockman-East Spitzer	Sp. Nom.	1.40	7
19	L3	**Lockman-North**	Sp. Nom.	0.65	7
23	L4	UDS	Sp. Nom.	2.02	7
24	L4	VVDS	Sp. Nom.	2.02	7
22B	L5	COSMOS HerMES	Sp. Nom.	4.38	4
27	L5	**CDFS SWIRE**	Sp. Fast	11.39	20
28	L5	**Lockman SWIRE**	Sp. Fast	17.37	2
28B	L5	**Lockman SWIRE**	Sp. Fast	7.63	2
29	L5	EGS HerMES	Parallel	2.67	7
30	L5	**Bootes HerMES**	Parallel	3.25	5
31	L5	ELAIS N1 HerMES	Parallel	3.25	5
32	L5	XMM VIDEO1	Parallel	2.72	4
32B	L5	XMM VIDEO2	Parallel	1.74	4
32C	L5	XMM VIDEO3	Parallel	2.73	4

Cont.

Set	Level	Target	Mode	$\Omega_{\rm good}(\rm deg^2)$	Scan num.
33	L5	**CDFS SWIRE**	Parallel	10.89	5
34	L5	**Lockman SWIRE**	Parallel	16.08	4
39B	L5	ELAIS S1 VIDEO	Parallel	3.72	4
35	L6	ELAIS N1 SWIRE	Parallel	12.28	2
36	L6	XMM-LSS SWIRE	Parallel	18.87	2
37	L6	Bootes NDWFS	Parallel	10.57	2
38	L6	ADFS	Parallel	7.57	2
39	L6	ELAIS S1 SWIRE	Parallel	7.86	2
40	L6	**FLS**	Parallel	6.71	2
41	L6	ELAIS N2 SWIRE	Parallel	7.80	2
42	L7	**HeLMS**	Sp.Fast	270	2

Table 2.1: The set, standard name, scan mode, area of the field and number of scans. Each set has a corresponding number of AORs and the AOR lists are given below. Bolded field names are fields that are explicitly discussed in some capacity in this thesis.

The type of science possible was very much dependent on the confusion noise of the maps. The *Herschel* telescope beam is much wider than similar generation optical and near-infrared telescopes. Galaxies that are resolvable in the optical and near-infrared with SDSS or Spitzer may in the *Herschel* maps occupy the same telescope beam or even pixel, becoming unresolved point sources that are heavily blended together. Thus catalogues produced on *Herschel* maps are considered catalogues of *sources* rather than galaxies as one cannot assume that the extracted flux can be attributed to only one galaxy. Due to the number of distant galaxies emitting in the infrared across the sky the background to the map can be thought of as consisting of light from many galaxies instead of a flat black background. The combination of blended sources and a background consisting of a fluctuation of sources contributes to uncertainty in the determination of a source's flux. This is referred to as the confusion noise and is a hard limit on the detectability of sources.

Above the confusion noise (constrained by Nguyen et al. (2010) at 5σ=24.0, 27.5, 30.5mJy at 250, 350, and 500μm respectively) catalogues of sources can be constructed by finding peaks in the map corresponding to the shape of the instrument's point spread function (PSF) scaled to the flux of the source. These catalogued sources allow population statistics to be calculated. Stacking on known sources (Béthermin et al., 2012) to find average fluxes for unresolved sources or direct analysis on the map with a model of the

number counts (Glenn et al., 2010) enabled the number counts to reach down to 2mJy and to account for over 50% of the CIB from known sources alone. Viero et al. (2013) find galaxies of mass $9.5\log(M/M_{\odot})$ to $10\log(M/M_{\odot})$ contribute the most to the CIB at 250μm by simultaneously stacking sources binned on e.g. mass and colour to prevent biasing by flux from nearby sources.

Fields were chosen for the wealth of ancillary data already present. This allowed a matching between HerMES sources to spectroscopic redshifts (spec-zs) or to enable the determination of photometric redshifts (photo-zs) using the multi-wavelength data available by fitting model spectral energy distributions (SEDs). SEDs for HerMES sources were determined by combining SPIRE and PACS data from the PEP (PACS Evolutionary Probe, Lutz et al. (2011)) survey in Elbaz et al. (2010), and more recently in Huang et al. (2014). These photometric results were fitted to empirical templates in Rowan-Robinson et al. (2010) providing evidence for a cold dust component to the SED. These template fits would allow the determination of a redshift distribution for obscured star-forming galaxies. Given the redshift and the *Herschel* fluxes, the infrared luminosity of a source can be determined and thus the time evolution of the infrared luminosity function found as in Vaccari et al. (2010) and Eales et al. (2010b) showing strong evolution out to $z \approx 1$. More recently, Gruppioni et al. (2013) combine HerMES and PEP data to confirm that the infrared luminosity function evolves out to $z = 1$, flattens between $1 < z < 3$ and drops off after $z = 3$, consistent with the peak of star formation occurring at $z = 2$.

The link between star formation and environment could also be explored in wide fields that cover a broad range of densities. As the most massive halos are more strongly clustered (Kaiser, 1984) and there is strong correlation between the mass of a dark matter halo and a hosted galaxy, determining the clustering of HerMES sources and therefore the clustering of star-forming galaxies will give clues as to the type of environment that hosts a star forming galaxy. The smplitude of clustering at particular scales will also determine whether star formation occurs in the largest galaxies within central halos or smaller, orbiting galaxies in the sub-halos. Cooray et al. (2010) found the brighter HerMES sources were in dark matter halos above $(5 \pm 4) \times 10^{12} M_{\odot}$, with contributions towards both the 1-halo and 2-halo clustering strengths. These results are in contention with H-ATLAS, (Eales et al., 2010a) another *Herschel* legacy project, finding no clustering strength at 250μm (Maddox et al., 2010). A follow-up study by Mitchell-Wynne et al. (2012) constrained the redshift distribution $N(z)$ of sources in the Böotes field. The correlation function was cross-correlated with ancillary data in the near infrared to constrain the redshift

distribution but in the process found a clustering strength less than Cooray et al. (2010) at 250μm in the process. This discrepancy is still unresolved.

With such a wide area covered by HerMES, rare objects can also be discovered. Colour-cutting the catalogues and maps (choosing sources or pixels that have a ratio between two wavelengths greater than some value) to select sources that are extremely red and therefore more distant was performed by Dowell et al. (2014) and found the extreme object HFLS3. HFLS3 was followed up with a variety of telescopes (Riechers, 2013) and was spectroscopically confirmed at $z = 6.34$. This was at the time considered the most distant unlensed star forming galaxy then identified, and its star formation rate (SFR) then calculated at approximately $3000 M_{\odot}\mathrm{yr}^{-1}$. At those star formation rates an object would be rare enough that current galaxy formation models would not tolerate finding more than a few similar objects (Riechers, 2013). Subsequent follow-up observations (Cooray et al., 2014) have found that the system is lensed and have revised the star formation rate to $1320 M_{\odot}\mathrm{yr}^{-1}$. Whilst this is not a paradigm-shifting value, these rarer systems are still of great value for galaxy evolution models.

Distant objects can also be found through gravitational lensing as with HFLS3. Extremely high mass galaxies or galaxy clusters strongly warp space-time around them, forcing light from objects behind them to change path as they pass through the gravitational field, allowing the otherwise hidden object to be observed. The lensed object is magnified and can be multiply imaged dependent on the alignment of the lens and object, aiding identification of lensed sources. Lensed sources allow us to probe further in redshift and/or to fainter sources. Wardlow et al. (2013) identified 13 lensed source candidates across the L2-6 fields with nine confirmed in telescope follow-ups on the Hubble Space Telescope or W. M. Keck Observatory. In addition over a hundred sources were flagged within the Lockman fields as being potential lensed sources by Rowan-Robinson et al. (2014) using SED template fits to photometry.

The diverse scientific results above all utilise data products created by the HerMES telescope data processing teams and will be the subject of discussion for the rest of this chapter and chapter 3. To process the telescope data, the HerMES team was divided into four, PMAP and PCAT to process the PACS maps and catalogues respectively, and SMAP and SCAT for the SPIRE data. The majority of the work in this thesis falls within the SCAT team's remit, with work in this chapter directly contributing to the HerMES second data release (Wang et al., 2014). The SMAP process is also described below as simulation maps were made using the pipeline for this and a later chapter and a comparison between

the HerMES and H-ATLAS map-making process is made in chapter 6. The PMAP and PCAT processes are not discussed in this thesis.

2.2 Map Creation

During an observation scan, the photons reflected by *Herschel*'s mirror onto the bolometers are absorbed and increase the temperature as the telescope scans the sky. The data obtained from the bolometers is referred to as "time-ordered data" or TOD as it exists as a one dimensional stream of data separated by scan and detector number. This data needs to be turned into an image of the sky (map) to work with HerMES source detection algorithms. HerMES uses the standard HIPE (Herschel Interactive Processing Environment, Ott (2010), Valtchanov (2014)) pipeline for part of the map reconstruction then uses an algorithm developed by the SMAP team to create the final maps (Viero et al., 2013; Levenson et al., 2010)).

2.2.1 HIPE

HerMES maps are constructed from two different pipelines. The first processing from level 0.5 to 1 product was done using HIPE, the *Herschel* Interactive Processing Environment. Whilst this timeline processing was not explored in this thesis, the main algorithms are summarised below for context and completeness.

The first step is to remove electrical crosstalk. Electrical crosstalk is interference with signals from individual detectors, for example a signal in one detector inducing a signal in another. A cross-talk removal matrix is recorded for each SPIRE photometer array, noting the relative induction introduced by each bolometer and thus providing a linear decomposition of each data stream from each bolometer as a function of the signal from all bolometers. From there the signals can be decoupled and the signal from each bolometer understood independently.

Deglitching is performed. Glitches are caused by cosmic rays hitting a detector, increasing the temperature rapidly and spiking the signal. If propagated through the map they appear as a very bright streak that dims in the direction of the scan. The timelines are first analysed for these sharp peaks through a kappa-sigma function. Kappa-sigma clipping is a way of identifying data in the timeline that is drawn from a different population distribution as the background. In this case, it is a method of finding signals in the timeline that are much higher or lower than expected, many standard deviations away from the mean. First, the mean and standard deviation of all values of the data are found.

The mean is subtracted off and pixels within a range of $\kappa\sigma$ are found. $\kappa = 5$ as standard within the pipeline. Then the mean and standard deviation of the new sample are found again and the criteria reapplied. This is iterated 100 times or until the mean changes by a fraction of $< 1.0 \times 10^{-10}$. Then all pixels outside that value are flagged to be masked or replaced with white-noise representative of the mean and sigma derived from the last iteration. Cosmic ray glitches typically only effect one bolometer at a time.

Other glitches can be removed, these include cooler-burps which are longer lasting deviations from the signal than cosmic rays. The temperature of the bolometer array constantly increases as the focal plane is exposed to the sky, this is known as temperature drift. Thermistors on the focal plane act to monitor this increase in temperature which can be used to subtract off the temperature drift from the timeline. Cooler-burps and are an atypical increase in temperature of the focal plane (i.e. all the bolometers) that cannot be taken into account with a standard temperature drift correction. The resultant is a paler then darker stripe across the map as the gradient of the temperature drift correction is far steeper or shallower than required, an example is shown in figure 2.2.

The electrical response of the signal is filtered with a low-pass filter to remove small scale fluctuations in the signal not caused by an in-sky signal. As filtering can cause aberrations, an electrical filter correction is applied by dividing by the corresponding transfer function. Units of the detector are then converted into flux density; the response of each detector is slightly different and non-linear and further discussed by Griffin et al. (2013).

The SMAP team have their own filter to remove the low frequency noise of less than 1Hz associated with temperature drifts and a stricter glitch detector. Therefore during the above pipeline the TOD is not corrected for temperature drifts.

2.2.2 SMAP Algorithm

The second stage is to make the level-one data into maps. HIPE has its own map making process, the Naïve mapper. In this algorithm, the TODs from each obsID are stitched together to form a continuous data stream and a temperature drift correction is applied. The median value is subtracted from the timelines to speed up the convergence of the iterative mapmaker described below. Whilst the instruments are kept at an extremely steady temperature by the liquid helium coolant system, small fluctuations in temperature are introduced exposing the detectors to light. There are two thermistors on the focal plane, exposed to the same light as the bolometers. These thermistors (and any masked

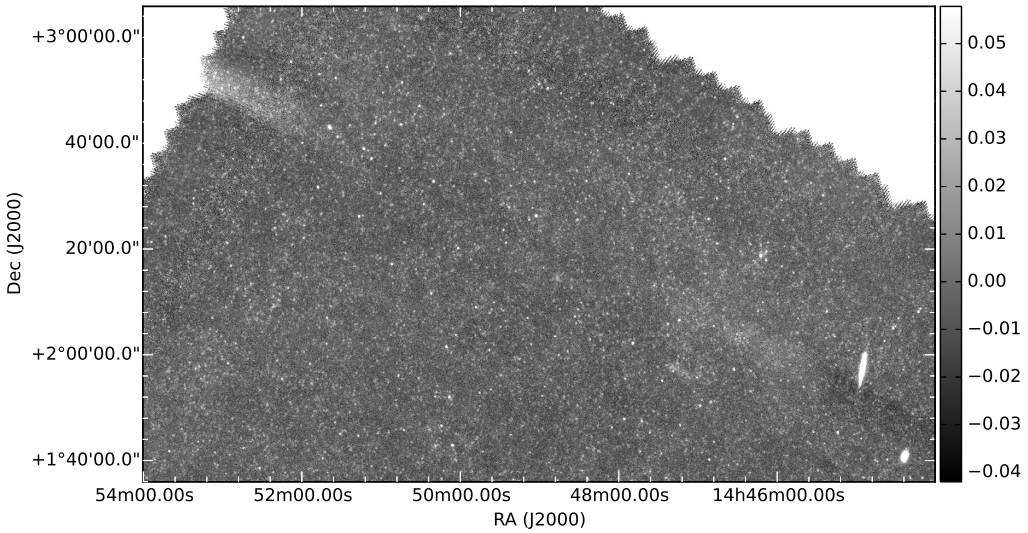

Figure 2.2: An image of the 250μm GAMA15 field (a H-ATLAS collaboration field, see chapter 6) in mJy/beam showing an unaccounted for temperature drift. The flux associated with the temperature drift has been incorrectly subtracted towards the edge of the map, showing the surface brightness increasing due to the erroneous temperature rise. The white region on the bottom-right is a foreground barred spiral galaxy NGC 5746.

bolometers) can track the μK fluctuations in temperature. Averaging the thermistors, (or, in cases where a cosmic ray has hit a thermistor and this has been noted, just using one value) allows a subtraction to be made to the bolometer response. The specifics of this algorithm ensure all the scans are mean subtracted. NB, as of writing, no absolute calibration has been calculated for the *Herschel* maps that would add a true background to these maps, so mean subtraction is a reasonable way to present the data. These temperature drifts are responsible for 1/f noise in the data. 1/f noise is noise with a power inversely proportional to the frequency of the noise and can be correlated across detectors. Removing these temperature drifts accounts for the majority of 1/f noise in the map. (Levenson et al., 2010).

Binning in the SMAP pipeline is performed differently. A *weighted* mean is constructed instead. The signal on the sky, S can be described as

$$S_{dsj} = g_d M(x_{dxj}, y_{dxj}) + P^n_{ds} + N_{dsj} \tag{2.1}$$

where d is an individual detector, s a scan and j a time sample. This signal can be described as the gain on a detector g, $M(x_{dsj}, y_{dsj})$ the sky brightness at a detector at a particular scan and time sample. P^n_{ds} is an order-n polynomial baseline offset that will be calculated iteratively, N is the noise.

The initial sky map $M^0(x_{dsj}, y_{dsj})$ is set to zero with gains set to 1.0. In each step of the iteration, either the gains are held constant or P^n_{ds}, with each alternate step in the iteration switching between either the gains or polynomial fit to the scans and detectors allowed to vary. Both g and P are determined by minimising the residual variance between the model and map between steps.

Then a weighted mean is constructed

$$M^i(x,y) = \frac{\sum_{dsj} w^i_{ds}(S_{dsj} - P^{ni}_{ds})/g^i_d}{\sum_{dsj} w^i_{ds}} \tag{2.2}$$

In other words, the value of the flux at a time sample that has been binned into a pixel is the weighted sum of the signal minus the background subtraction divided by the gain for each detector and scan. At this point the polynomial P^n_{ds} is chosen to minimise the residual value between the current and previous iteration of the map such that the residual map R is given as

$$R^i_{dsj} = S_{dsj} - g^i_d[M^{i-1}(x_{dsj}, y_{dsj}) + P^{ni}_{sd}] \tag{2.3}$$

The weights w^j_{ds} are the inverse variance of the residual of the timeline

$$w^i_{ds} = 1/\frac{1}{N}\sum_{j=1}^{N}(R^i_{dsj})^2 \tag{2.4}$$

where N is the number of samples in scan S, and the weights are normalised to sum to 1. Thus scans that have a low variance in the residual are weighted more highly.

From this a noise map can be calculated using these residual variances and expressed in terms of the weight of each sample as

$$\sigma^j(x,y) = (\sum_{dsj} w^j_{ds})^{-1/2} \tag{2.5}$$

In other words, the noise represents the standard propagation of errors as calculated from the variances of of samples on individual pixels in the residual map.

The order of polynomial P^n to fit will depend on the size of the map. This polynomial will be calculated and subtracted off for each scan and detector. Therefore the best fit polynomial will depend on the length of a scan. Smaller fields with be $n = 2$ up to $n = 3$ for the widest HerMES fields. The level 7 field HeLMS's map was an exception and was created using SANEPIC (Patanchon et al., 2008).

From the sky map M and baseline fit P^n fits, a model for what each detector sees can be constructed. This is set to occur after ten iterations to ensure values are close to their final value. Any detector that varies 10σ from this model (i.e. is glitched) is removed from subsequent iterations and therefore the final map-making process.

Also occurring after ten iterations is a calculation of map offset. Each AOR is stacked with *Spitzer* MIPS 24μm sources. Sources within these catalogues are known to an accuracy of < 1 arcsec by checking against 2MASS sources in the same fields so are a valid measure of offset. The centre of a 2D Gaussian fit is recorded and each offset and glitched detector is noted for the remaining iterations.

Each map is produced with an image map in units of Jy/beam, an error map again in units of Jy/beam, a coverage map in units of seconds and for some datasets a flag extension that flags regions in the map with a binary mask, 0 for no coverage, 1 for coverage in scans in one direction, and 2 for "central" scans. This final flag extension will be removed from all maps for the final data release.

Jackknife maps are also constructed by dividing the data into two sets after the parameters for equation 2.1 have been determined. They are labelled "ang" for data divided by scan orientation, "bolo" for division by bolometer number, and "half" by dividing the data by time. Some maps will not have enough data per pixel to do division by time or bolometer. Further, dividing by scan direction means only the overlapping regions can be examined. Nested maps do not have jackknife maps released. Jackknife maps are useful for noise estimation, as a way of estimating errors during data extraction on maps, and for map validation - glitches or cosmic rays that pass through detection algorithms can be caught by eye and scans or detectors removed in further reruns of the maps-making software.

2.2.3 SMAP Simulation Pipeline

Simulations are an integral part of testing astrophysical models. Models that produce galaxy catalogues must be able to recreate the observations they were derived on when run through simulations of telescope pipelines. Simulated images and catalogues provide a controlled way to test the performance of data reduction pipelines by giving a known input to measure outputs against. The process of creating simulated *Herschel* SPIRE images is given below when a simulated catalogue of fluxes and possible positions is given.

The input catalogue or *truth catalogue* is given as a series of fluxes at different wavelengths spanning the SPIRE bands. The fluxes are converted to Jy and are put into an array representing the sky at a size equivalent of 2 arcsec^2 length per pixel, far smaller than the final SPIRE product maps. Any fluxes found to be in the same pixel are summed. The array is then convolved with a Gaussian representation of the telescope beam (discussed below) which produces a *sky*, a true representation of the simulated catalogue on the sky

given the PSF.

The SMAP team have developed an algorithm to transform a simulated sky into a SPIRE photometer timeline, and then allow the entire SMAP data reduction to be performed. The timeline simulator is given a HerMES field to mimic, so the same depth, scan masking and scan pattern can be used. $1/f$ noise to represent temperature fluctuations and Gaussian noise can be optionally applied. The full iterated pipeline is run again, finding the baseline subtraction to remove the $1/f$ noise. This simulation pipeline was able to show SMAP's $1/f$ noise removal worked very well (Levenson et al., 2010). Jackknife maps are also produced either by scan orientation, scan number or bolometer number. The resultant products are referred to as simulated maps, and any catalogues generated are output catalogues.

2.3 Point Spread Function

The point spread function (PSF) of a map relates to the response of a telescope. It is the resultant clean image produced when a point source - a source where the angular size is small enough that it cannot be resolved - that has been shaped through the particular optical set up from primary mirror to interaction with the bolometers. Due to the limited angular resolution of the *Herschel*-SPIRE bands, the pixels sizes in the standard data reduction pipeline for the 250, 350 and 500μm bands are 6, 10 and 14 arcsec, however as the sample rate of the HerMES maps are higher the SMAP team create maps at 6, 8.333 (25/3) and 12 arcsec. To understand the *Herschel*-SPIRE PSF, Neptune was observed. Neptune was observed at an angular diameter of 2.4 arcsec and as such is unresolved by SPIRE. Neptune is a bright object with a well-understood SED, making it they perfect candidate to study the beam. Figure 2.3 shows the PSF to a precision of 1arcsec in the 250μm filter and 2.4μm arcsec at 500μm normalised to a 1 Jy peak, a far higher pixel resolution than the standard maps.

Even when the beam is well constrained, due to many factors within the telescope affecting the PSF (mirror distortion, struts holding the secondary mirror, scan direction) it is extremely difficult to model. To that end, a Gaussian approximation of the beam is used in source extraction of full-width half maximum (FWHM) 18.15, 25.15 and 36.3 arcsec for the 250, 350 and 500μm maps respectively, approximately three times longer than one pixel length in the SMAP maps. Figure 2.3 shows the residual of the Neptune beam and the Gaussian fit. Clearly visible is the asymmetrical nature of the beam and the second lobes, caused by the diffraction pattern of the beam. The residuals are a maximum

5% away from the true beam.

2.3.1 NB using Neptune fit

Whilst Gaussian fits of the PSF with the above FWHMs seems appropriate, it is important to note that the PSF is dependent on the colour of the source detected. The transmission S of filters associated with each band are non-uniform across the typically broad spectral passband they cover ($d\lambda$). Neptune is a comparatively blue source across the bands, as such the PSF will be different for a redder source, such as a dusty galaxy at redshift $z = 2$ or higher that may have an SED angled differently across the transmission spectrum of the filter. The adjustment for the beam has been calculated in Griffin et al. (2013). In the model, the modified beam is given as:

$$P_{mod}(\theta, \nu, \nu_{eff}) = \max \begin{cases} P_{inner}(\theta/(\nu/\nu_{eff})^{\gamma} \\ P_{outer}(\theta) \end{cases} \tag{2.6}$$

with P the standard PSF, ν as the frequency, θ the angular scale of the beam, and γ the spectral index of the beam. The inner shape of the beam changes with the spectral slope of the SED, with redder sources experiencing a broader PSF.

Whilst many black-box source detection techniques allow for a non-Gaussian beam to be used and so the true beam from the standard pipeline could be used, HerMES maps are formed from many scans in different orientations. Given the nature of the coverage, every pixel has its own contribution from different scans with different orientations. This means every pixel has its own representative PSF corresponding to the number and orientation of scans. Whilst it is hypothetically possible to take this information into account when performing source extraction as the number of scans and orientation is known, it is beyond the scope of this thesis to do this. Gaussian fits to sources will be considered adequate with at the maximum 5% difference in the beam as shown in 2.3.

2.4 Source Detection and Extraction

Flux in *Herschel* maps arises from far-infrared sources and in HerMES maps, the flux comes primarily from cooler dust in galaxies. However, *Herschel*'s SPIRE instrument is unable to resolve very distant HerMES sources into galaxies, only showing point-sources. Combine that with confusion between sources due to the signal from sources overlapping and it is not simple to untangle what source (or portion of flux density from a source)

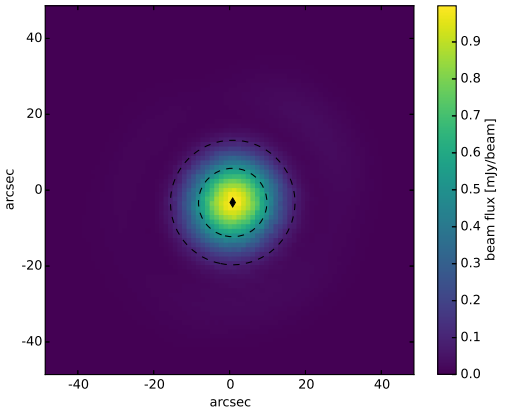

(a) 250μm beam

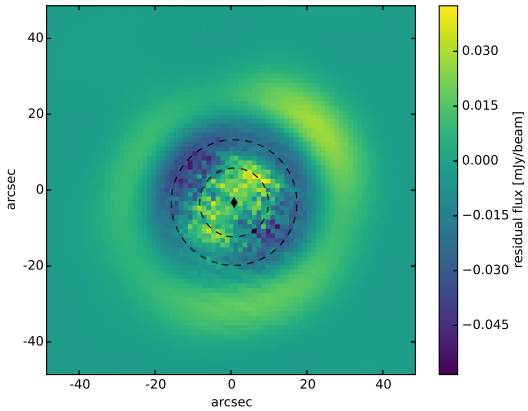

(b) 250μm beam residual

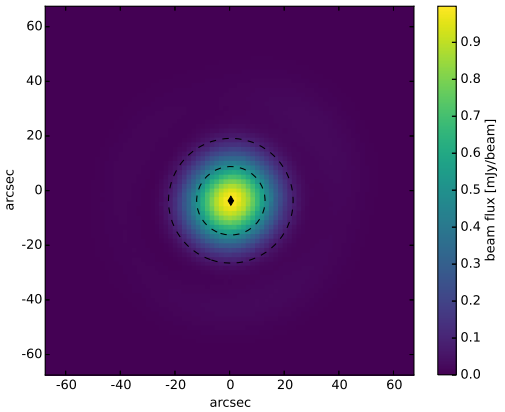

(c) 350μm beam

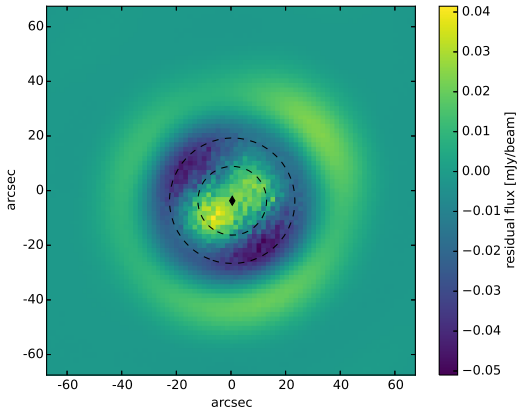

(d) 350μm beam residual

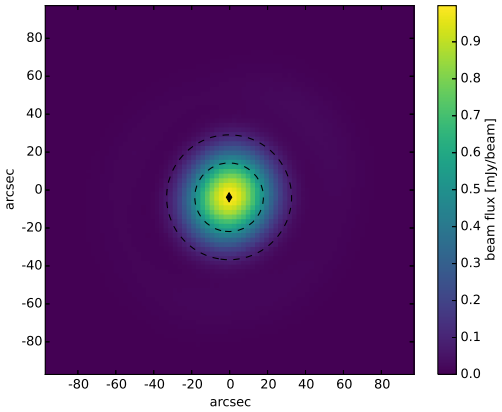

(e) 500μm beam

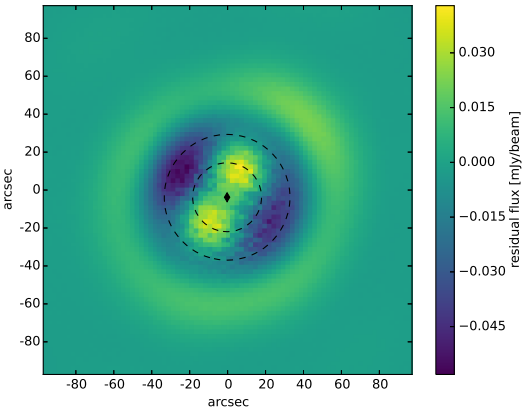

(f) 500μm beam residual

Figure 2.3: The *Herschel*-SPIRE beams as determined from observations of Neptune. Overlaid are contours of the Gaussian fit used in source extraction showing 0.5 and 0.1 times the peak value. Also shown are the residuals of the beam and Gaussian fit, clearly showing the asymmetrical lobes.

is associated with which galaxy. One must therefore be careful to distinguish between a *Herschel* source and flux from a galaxy.

As part of the HerMES second data release (DR2) new fields were constructed from combining AORs, nesting fields to create extremely deep regions. Whilst source extraction was performed on the nested fields, it was noted within the collaboration that data users may want wide maps with uniform coverage. Therefore source extraction in addition had to be run on the updated, wider maps. These were CDFS-SWIRE and Lockman-SWIRE.

The rest of this chapter will discuss the source detection and extraction methods employed on these new data sets and will provide some comparisons between the catalogues to be expanded on in the next chapter.

2.4.1 SUSSEXtractor

The simplest source detection and extraction method of the two used by HerMES is SUSSEXtractor, a Bayesian peak-finding algorithm. Bayesian statistics is a way to use "prior" information about the variable of interest to guide the solution to a model or hypothesis H with parameters θ given data D. Bayes' theorem is a given as

$$P(\theta|D,H) = \frac{P(D|\theta,H)P(\theta,H)}{P(D|H)} \tag{2.7}$$

where $P(\theta,H)$ is so-called prior information available about the parameters θ e.g. whether the solution is non-negative, approximate orders of magnitudes, or a Gaussian distribution. $P(D|\theta,H)$ is the likelihood of the data given θ and the hypothesis H. $P(D|H)$ is the probability of the data given the hypothesis, and as θ is the variable, this Bayesian Evidence term is a constant. SUSSEXtractor uses Bayes' theorem by analytically calculating the likelihood function and assuming a prior model for the source fluxes.

The likelihood can be given as $L \propto \exp\frac{-\chi^2}{2}$ calculated from the χ^2 fit of the model to the map given as

$$\chi^2 = \sum_{i=1}^{N_{\text{pixels}}} \left[\frac{d_i - m(\theta)_i}{\sigma_i}\right]^2 \tag{2.8}$$

where $m(\theta)_i$ is the modelled value of the ith pixel given the parameters θ, σ is the Gaussian instrumental noise associated with that pixel. The value under the summation sign therefore is a residual weighted by the noise, the lower the noise the higher the weight.

The model consists of a linear sum

$$m_i = SP_i + B \tag{2.9}$$

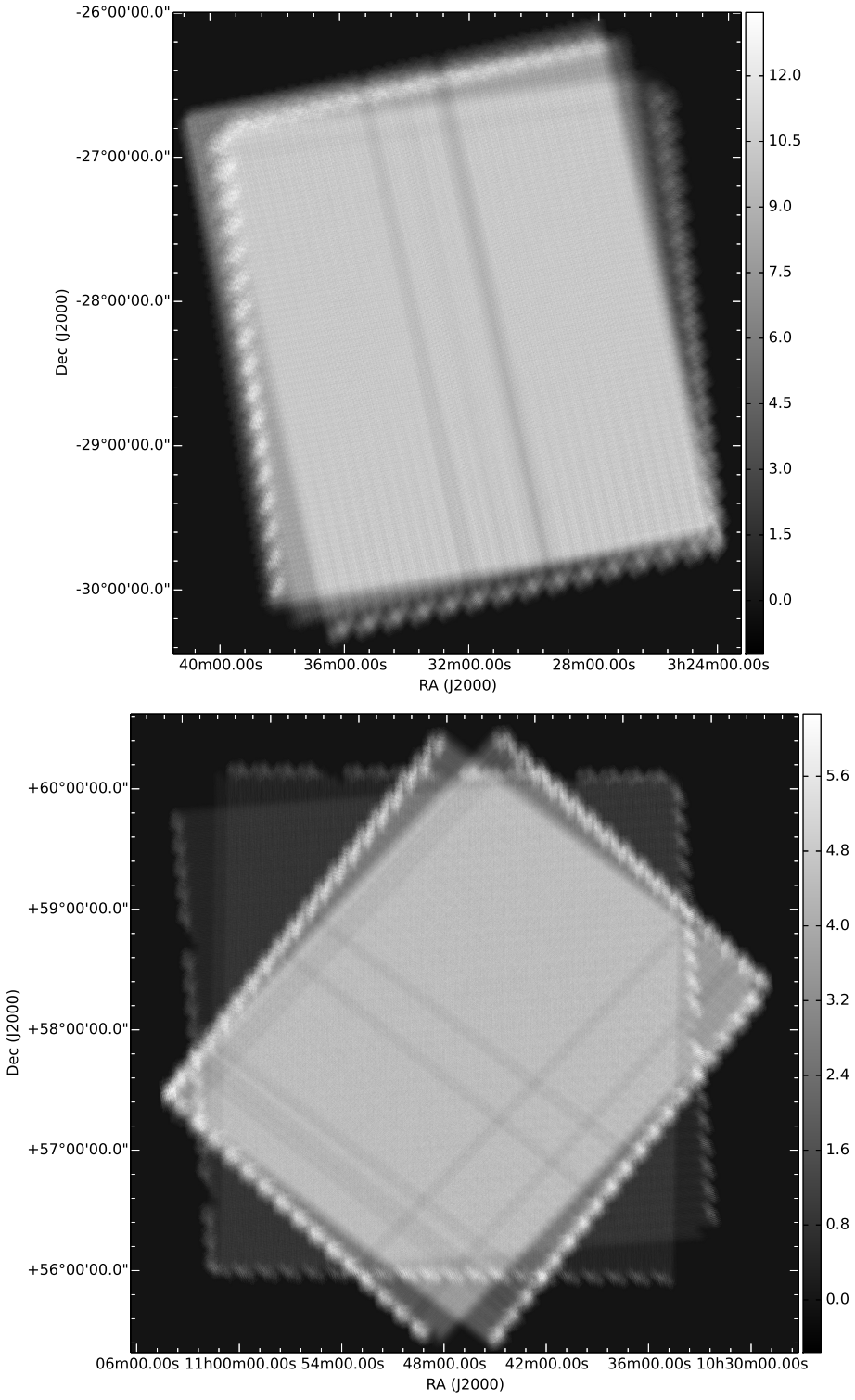

Figure 2.4: Coverage maps for the 250μm combined ECDFS and Lockman-SWIRE fields released as part of DR2. Clearly visible are the deeper regions made from overlapping AOR sets. CDFS is the deeper field. These maps were made to increase the depth in these wide scans.

where P_i is the PSF or matched filter at pixel i, B a uniform background and S the source flux density given as

$$S = \sum_{i=1}^{N_{\rm pixels}} \frac{d_i P_i}{\sigma_i^2} \Big/ \sum_{i=1}^{N_{\rm pixels}} \frac{P_i^2}{\sigma_i^2} \tag{2.10}$$

where d_i is a map pixel, P_i the matched filter chosen in SUSSEXtractor in lieu of the PSF. For one source on a white-noise background, this matched filter will be the PSF. However in deep maps with many confused sources the optimal filter will be narrower than the beam. Maps were divided into "deep" (Level 1 and 2 maps) and "shallow" (all other depths). The model used is a flat-prior, one that is equal across all parameter space and is essentially an uninformative prior. Therefore no assumptions are made about the parameters (i.e. no assumptions are made about the fluxes).

In this case the best function to smooth with (i.e. the matched filter) was an approximated beam, the central 5×5 pixels of a Gaussian of width 18.15, 25.15 and 36.3 arcsec at pixel sizes 6, 25/3 and 12 arcsec, the standard SMAP beam and pixel sizes. For shallow maps, the image and error were first convolved with the 5x5 kernel specified above. Each pixel is compared to the pixels surrounding it to locate maxima candidates in the image. Each approximate position is cut out and, using the intensities of the neighbouring pixels to infer how to move the peak through interpolation, the position of the source is located within the central pixel. The flux of the central pixel is the maximum likelihood estimate of the flux, i.e. the value of the flux that will minimise the χ^2. In the case of deep fields, the peaks are located first, then the smoothing is performed with a 3×3 kernel to estimate the fluxes at each pixel. Deep fields are less noisy and therefore one would hope to recover more sources. However, smoothing the map with a kernel will reduce the resolution of the image, blending sources together. This identification first, smoothing second is considered a reasonable compromise.

The instrumental errors for the source are given as

$$\sigma_S = 1 \sqrt{\sum_{i=1}^{N_{\rm pixels}} \frac{P_i^2}{\sigma_i^2}} \tag{2.11}$$

i.e. the variance of a source is the inverse of convolution of the matched filter squared with the inverse of the variance. This is calculated from the maximum likelihood solution in Serjeant et al. (2003). This is only the instrumental error however, there is an additional component from the confusion noise, the noise due to variance in the unresolved background (see section 3.4 for more details). The smoothed map at pixel j, S_j is used to

calculate the total error σ_{total} as

$$\sigma_{\rm total} = \sqrt{\frac{\sum_j (S_j - {\rm median}(S_j))^2}{N}} \tag{2.12}$$

the sum is restricted to pixels with $S_j <$median(S_j) and N is the number of pixels within that selection. Given the calculation of the instrumental noise across the entire map above, the median instrumental noise is taken ($\sigma_{\rm instrumental} = {\rm median}(\sigma_{S,j})$) and the confusion noise is calculated as

$$\sigma^2_{\rm confusion} = \sigma^2_{\rm total} - \sigma^2_{\rm instrumental} \tag{2.13}$$

and the total noise for each source is given as

$$\sigma_{\rm S,total} = \sqrt{\sigma^2_{\rm S,instrumental} + \sigma^2_{\rm confusion}} \tag{2.14}$$

2.4.2 STARFINDER

STARFINDER is a source finding algorithm designed for stellar fields. Sources do not have to be isolated to be found by STARFINDER, but instead the algorithm attempts to untangle flux from neighbouring sources so flux is not double counted. The algorithm is iterative, finding sources at lower and lower signal-to-noise (SNR, flux over the error in flux). A flux map, error map and PSF are given (the Gaussian PSF as above). SMAP standard products are given in Jy/beam and Starfinder requires units of Jy/pix. Each map is therefore divided by the beam area in pixels/beam, calculated as beamArea $= \pi \cdot {\rm FWHM}^2/(4 \ln 2)$.

STARFINDER identifies pixels above a specified signal to noise ratio, given as, for each iteration, an SNR of 7 down to 1.1 in increments of 0.1. A region of the flux map is cut out (150×150 pixels), and the area surrounding the pixels passing the SNR threshold is searched for a peak, returning a source position if the fit to the beam is above a specified minimal correlation coefficient (set to 0.7). The rest of the cutout is used for background estimation. The average beam to search with can be adjusted with each iteration by considering the fits to the sources. Each source is subtracted from the map, and the algorithm begins again with the minimum source SNR reduced to the next specified value.

STARFINDER is developed to deblend sources but the ideal image to deblend would be crowded stellar field like a globular cluster or open star cluster; many sources are found in a dense region surrounded by a relatively less dense or lower flux area. The hopefully large number of fluxless pixels around the galaxy allow a background estimation to be performed accurately. However in these HerMES fields this is not the case as the entire field is full of sources. So whilst STARFINDER is a good way to find sources, the

background estimation will be inappropriate. Background values are typically a few mJys either side of zero flux, which for many sources can be a large fraction of the flux.

Given a noisy, shallow map however, fewer pixels will pass through the first signal to noise cut. This means many fainter sources would be undetected that could be picked up by SUSSEXtractor. Further, STARFINDER will pass many pixels that sit on a high background (e.g. from cirrus) through the first stage of the algorithm, leading to an artificial increase in source density in these regions.

2.4.3 DESPHOT

Given the positions from STARFINDER, DESPHOT (Deblended SPIRE PHOTometry) will use these position as prior information to simultaneously fit scaled Gaussians representing the beam to the map at these positions.

DESPHOT models the image **d** as

$$\mathbf{d} = \sum_{i=1}^{n} \mathbf{P}_i f_i + \delta + B \tag{2.15}$$

with **P** representing the point spread function on an 11×11 grid, normalising the peak to one to represent a 1mJy/beam source. $\mathbf{P}_i$ is the PSF at source i, f_i is the flux density of source i, δ the noise and B the background which we set to zero for the first pass of this two-stage iterative process. We wish to solve for the vector of fluxes $\hat{f}$ in a maximum likelihood scheme and this is solved as:

$$\hat{\mathbf{f}} = (A^T N_d^{-1} A)^{-1} A^T N_d^{-1} d \tag{2.16}$$

A is the pointing matrix, representing m pixels by n sources, showing the contribution in pixel j from source i. $N_d =< \delta\delta^T >$ is the covariance matrix between the image pixels which is assumed to be diagonal, i.e. N_d is formed from the error map, representing the instrumental noise in each pixel as a function of coverage t, $\sigma_{\mathrm{inst}^2/\mathrm{t}}$. The pixels are not independent as as previously established, the flux binned to each pixel is from individual scans that have had a baseline subtracted. However, this is believed to be a small effect compared to the instrumental noise itself and this therefore ignored. To solve, DESPHOT utilises the LASSO algorithm (Tibshirani, 1996; Ter Braak et al., 2010). LASSO is an iterative method, and assumes at first all values in $\hat{f}$ are zero. LASSO will then try switching on a source and assigning a value to it that has the largest possibility of reducing the chi-squared fit between the data and model, whilst attempting to minimise the number of sources switched on to prevent over fitting. Further, LASSO is primed with a non-

negative prior as fluxes are physically positive. This algorithm will therefore solve the system using the fewest sources possible up to an acceptable tolerance level.

The background, ignored in the first iterative process, needs to be taken into account. As the background is made up of unresolved sources and almost entirely sources uncorrelated with the sources in the prior list, the background can be treated independently. The residual map R is calculated as

$$R = d - \sum_{i}^{n} P_i f_i \tag{2.17}$$

and the background B found as the y-intercept of a linear fit between the residual map and a map of beams of sources of flux 1. Only pixels surrounding or containing a known source are considered to prevent undetected sources from contributing to the background estimation. The background is then subtracted from d and then the algorithm rerun.

The code optionally searches for more sources of a Gaussian nature in the residual map using the IDL FIND command contained in the IDL astro library. FIND creates an (optionally elliptical) Gaussian PSF, takes a user specified intensity threshold and image and finds sources with an algorithm modified from the DAOPHOT tool (Stetson, 1987). These sources were not released with the catalogues; often these sources are found very close to neighbouring sources in the prior flux list and often the very faintest sources are turned off by the LASSO algorithm. This particular step in the algorithm is useful when the prior list is developed from data from another wavelength and does not contain every detectable source within the image being analysed and thus it is reasonable to expect bright, extra sources in the residual map.

The instrumental noise for each source is calculated as

$$\sigma = \sqrt{\mathrm{diag}(\mathrm{A^T N_d^{-1} A})^{-1}} \tag{2.18}$$

i.e. treating the errors as uncorrelated by taking the diagonal of the matrix multiplications. This does not take into the confusion noise which is calculated with a different method to SUSSEXtractor Smith et al. (2012a). In DESPHOT, the standard deviation of the residual map is found and the error map subtracted off in quadrature:

$$\sigma^2_{\mathrm{conf}} = \sigma^2_{\mathrm{res}} - \sigma^2_{\mathrm{pix}} \tag{2.19}$$

with σ_{pix} as the error map with a value per pixel. This effectively removes an average measure of the instrumental noise in each pixel. For a source, the total noise is then given as

$$\sigma^2_{\mathrm{tot}} = \sigma^2_i + \sigma^2_{\mathrm{conf}} \tag{2.20}$$

as in Smith et al. (2012a).

2.4.4 Map Segmentation

There are computational issues with the DESPHOT method, however. The larger or deeper the map, the higher the number of sources and therefore the larger the matrix to invert. Having upwards of 30,000 sources in a map like COSMOS would therefore be very difficult to manage. Therefore the map has to be broken up. A simple tiling scheme with a surrounding buffer region would allow a faster run time, however this ignores that, especially in shallower maps, some sources are completely isolated. Therefore the maps are segmented into smaller regions. The segmentation is a three step process. Pixels above a signal-to-noise ratio of one are recorded. This value is deemed appropriate to split the maps by as STARFINDER will only flag sources that are peaked on pixels of SNR=1.1 at the very least. An SNR=1 also implies that the flux in those pixels are from the background, confused sources only. The pixel closest to the bottom-left corner of the map is taken and neighbouring pixels are flagged as being as the same region. When the segment can grow no further, these pixels are recorded. Sources that lie on this region are flagged as belonging to the appropriate segment and a new region is started. When the algorithm is run, a rectangular array is cut-out of the map and a mask applied to pixels that do not belong on that segment. The code is rerun. The segmentation is repeated in the second run with the background subtracted - with maps with positive background more sources will be isolated in the second run as the resultant map's flux is reduced.

2.5 Contribution to the Second Data Release

2.5.1 Comparison of Number Density of Sources

Prior to the second HerMES data release in late 2013, the collaboration had decided to combine map data together to create shallow fields that included deep data. For example, CDFS-SWIRE field contains the GOODS-S and ECDFS regions and Lockman-SWIRE the Lockman-North and Lockman-East-ROSAT regions. Catalogues were produced for these so-called "nested" regions, but within internal discussion it was decided that further catalogues would need to be produced on the widest datasets only as any analysis on a wide area that used population statistics such as densities or a clustering correlation function would be hard to do with a heterogeneous dataset like catalogues produced from the nested fields. As a contribution for this thesis, catalogues from SUSSEXtractor and STARFINDER/DESPHOT for both the Lockman-SWIRE and CDFS-SWIRE shallow fields were produced and compared. CDFS-SWIRE is marginally deeper than Lockman-

Catalogue	number of sources			density of sources [/sq.deg.]		
	250μm	350μm	500μm	250μm	350μm	500μm
CDFS-SWIRE SUSSEXtractor	30552	19172	8320	2376	1491	647
CDFS-SWIRE DESPHOT	19169	28178	11096	1491	2191	862
Lockman-SWIRE SUSSEXtractor	32396	20987	8240	1642	1064	417
Lockman-SWIRE DESPHOT	18681	24903	8265	947	1262	418

Table 2.2: Density of source found in CDFS-SWIRE and Lockman-SWIRE above SNR=5. Field variations are due to the different depths. Whilst STARFINDER is designed for source-finding within crowded fields, SUSSEXtractor's matched filter is more successful at 250μm, detecting a greater number of sources.

SWIRE but still considered shallow by SUSSEXtractor and thus the same smoothing kernel is applied.

SUSSEXtractor and STARFINDER/DESPHOT were both run on the combined maps of CDFS-SWIRE AORs 27 and 33, and Lockman-SWIRE 28 and 28B. In addition, band-merged catalogues were created using the 250μm blind catalogue from STARFINDER as prior positions in DESPHOT across all three bands. The Spitzer 24μm prior so-called X-ID catalogues were not produced. In all, on the order of tens of thousands of sources were detected and extracted with a signal-to-noise ratio of 5 and above, with exact values in table 2.2. Given the areas of the combined fields are 12.86 and 19.73 sq. deg. for CDFS-SWIRE and Lockman-SWIRE respectively, this gives the number of sources per sq. deg. also in table 2.2. Figure 2.5 and 2.6 show the total number of sources in 0.04 sq. deg. regions. From the table and figures, it is immediately apparent that STARFINDER is locating more sources in the 350μm and 500μm maps compared to SUSSEXtractor. This is no surprise when considering that STARFINDER is designed to run on crowded fields iteratively, and so is likely to uncover more sources through its iterations. SUSSEXtractor on the other hand is (for these wider fields) modified to work on shallow fields and so may not find a faint source near a brighter one for example. This trend is reversed at 250μm however, with SUSSEXtractor's matched filter untangling peaks of sources more successfully than DESPHOT's simultaneous fitting of flux.

Figures 2.7 and 2.8 show the median signal-to-noise ratio (SNR) of the sources binned to 0.04 sq. deg. As with the number of sources, the SNR should not be correlated to any foreground structure in the maps, although if bright sources are clustered there should be some structure visible in these regions. The median is used as opposed to the

mean to prevent any extremely bright sources from skewing the result. The median SNR found with SUSSEXtractor is higher than DESPHOT. This implies that, even though STARFINDER/DESPHOT find more sources, the extra sources must be at a lower flux on average than those found with SUSSEXtractor (section 2.5.2). DESPHOT can fit extremely low fluxes to the map if the LASSO algorithm allows for it, and so this difference is not surprising.

2.5.2 Comparison of the Raw Number Counts

A direct comparison between the source fluxes shows some stark differences between the two algorithms. Subfigures a and b in figures 2.9, 2.10 and 2.11 show for all sources the recorded photometry in DESPHOT against SUSSEXtractor. The catalogues were matched to be within two pixel lengths of each other. Given that the maps were constructed such that the pixels were approximately a third of the FWHM of the beam, this places the sources within the same beam and so are very likely to be the same source. Immediately apparent is the lack of agreement between the fluxes, especially at low flux. Sub 40mJy at 250μm especially and more gradually at all fluxes in the 350μm and 500μm bands is a strong under-prediction of flux by DESPHOT. Whilst, as indicated by the coloured density of points in subplots a and b in figures 2.9 to 2.11 the fluxes of the majority of sources are close to parity, many are underestimated by DESPHOT or overestimated by SUSSEXtractor. This is true in both fields so is not field specific.

The difference between these two source extraction methods is explainable. To determine this the sources are split into samples determined by the number of sources in a segment in the DESPHOT routine. Subfigures c and d in figures 2.9, 2.10 and 2.11 show the match between fluxes given only one source on a segment, that is, a source surrounded by pixels with SNR=1 and as such DESPHOT's only degree of freedom is the flux of one source. The match between the two algorithms is extremely strong. However, when taking into account segments with 1, 2 and 3 sources on, as in subfigures e and f in figures 2.9, 2.10 and 2.11 that parity quickly drops, dropping further when all sources are considered. In segments with many sources, these sources are "chained" together in islands and so are blended to some degree. Therefore STARFINDER is more likely to detect the sources in the crowded regime. DESPHOT then can apportion the flux across the blended sources. SUSSEXtractor on the other hand struggles to detect blended sources and therefore the flux assigned to those sources that are detected will be much higher than DESPHOT as there is no other source to apportion the flux to. The more sources within a region, the

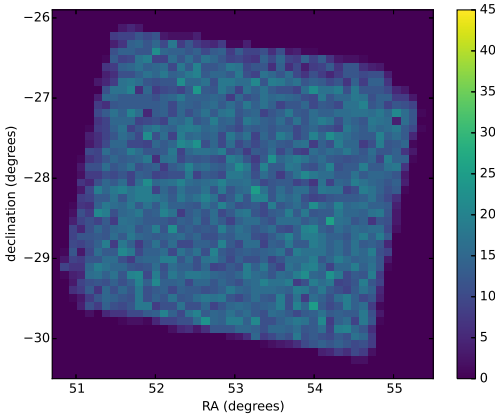

(a) DESPHOT 250μm

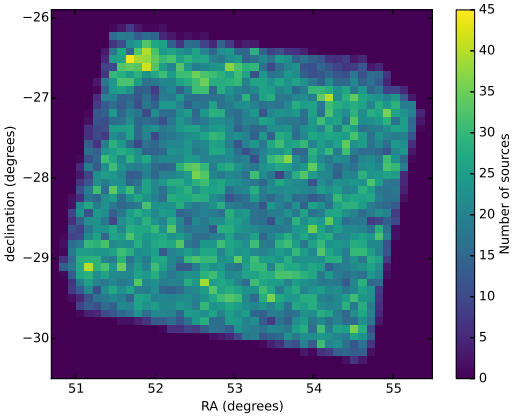

(b) SUSSEXtractor 250μm

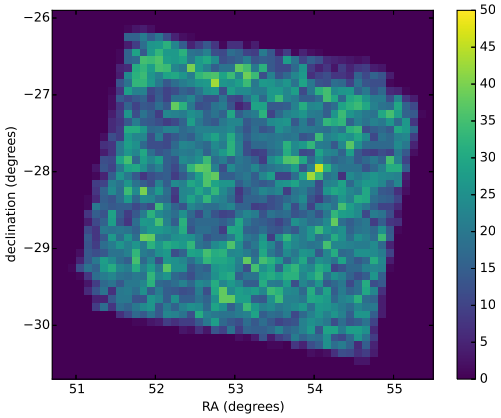

(c) DESPHOT 350μm

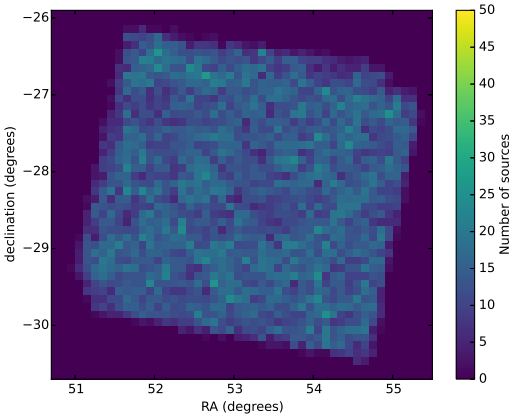

(d) SUSSEXtractor 350μm

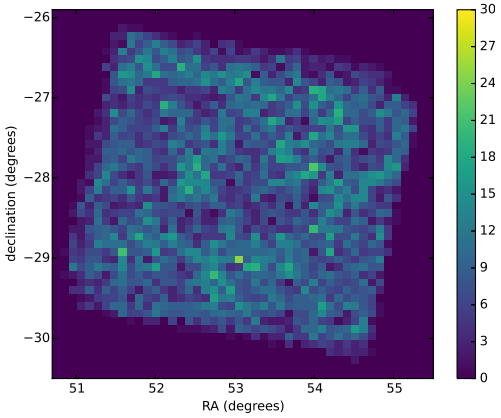

(e) DESPHOT 500μm

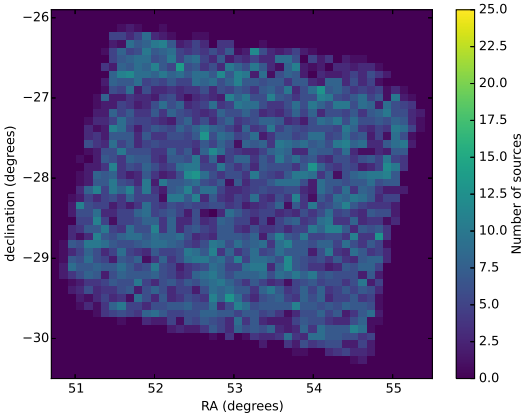

(f) SUSSEXtractor 500μm

Figure 2.5: Comparison of the number of sources across the map for SUSSEXtractor and CDFS-SWIRE. There are consistently a larger number of sources found with the STARFINDER/DESPHOT pipeline

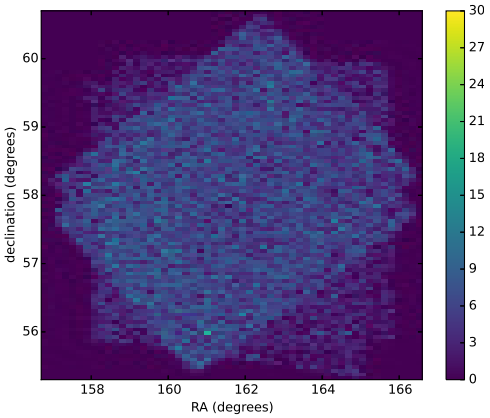

(a) DESPHOT 250μm

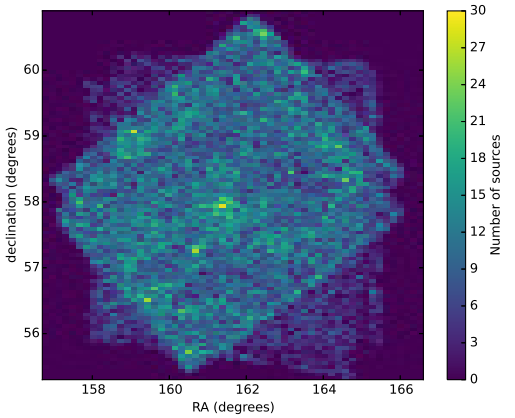

(b) SUSSEXtractor 250μm

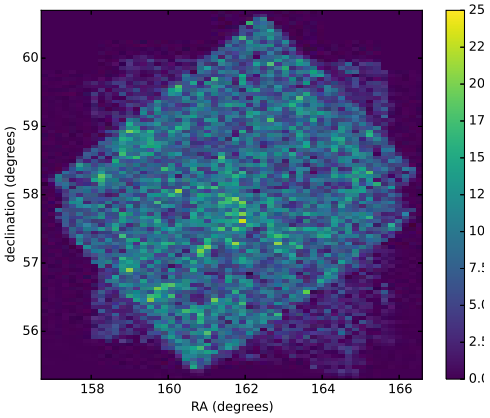

(c) DESPHOT 350μm

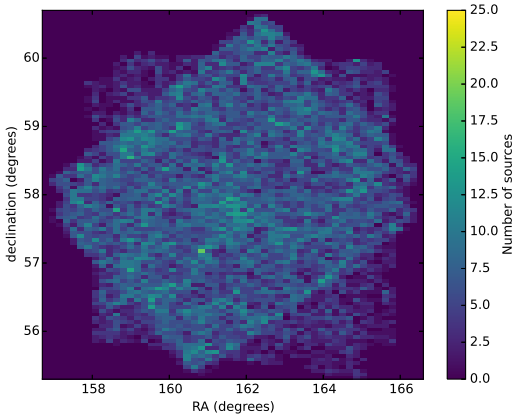

(d) SUSSEXtractor 350μm

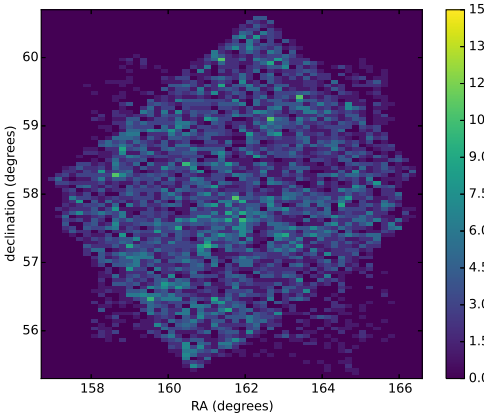

(e) DESPHOT 500μm

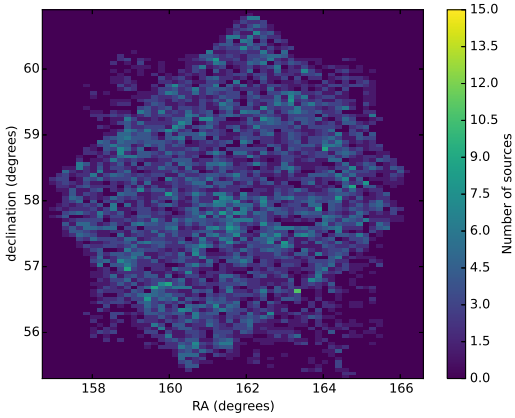

(f) SUSSEXtractor 500μm

Figure 2.6: Comparison of the number of sources across the map for SUSSEXtractor and Lockman-SWIRE. There are consistently a larger number of sources found with the STARFINDER/DESPHOT pipeline

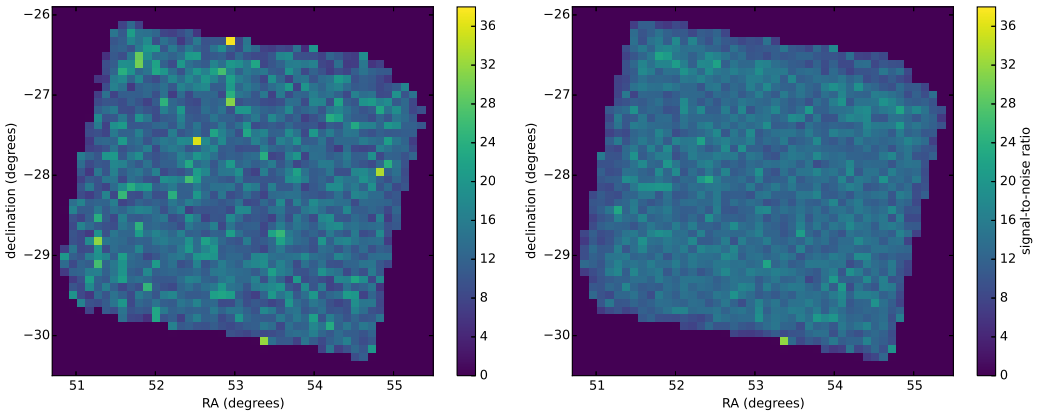

(a) DESPHOT 250μm

(b) SUSSEXtractor 250μm

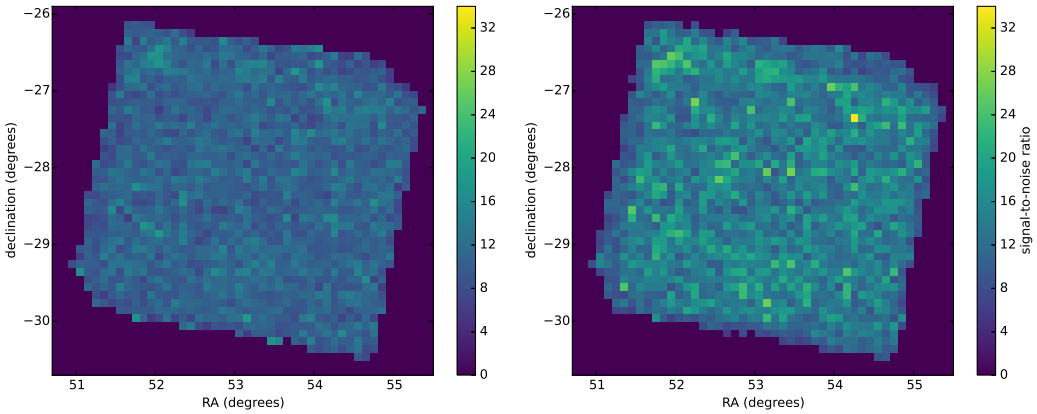

(c) DESPHOT 350μm

(d) SUSSEXtractor 350μm

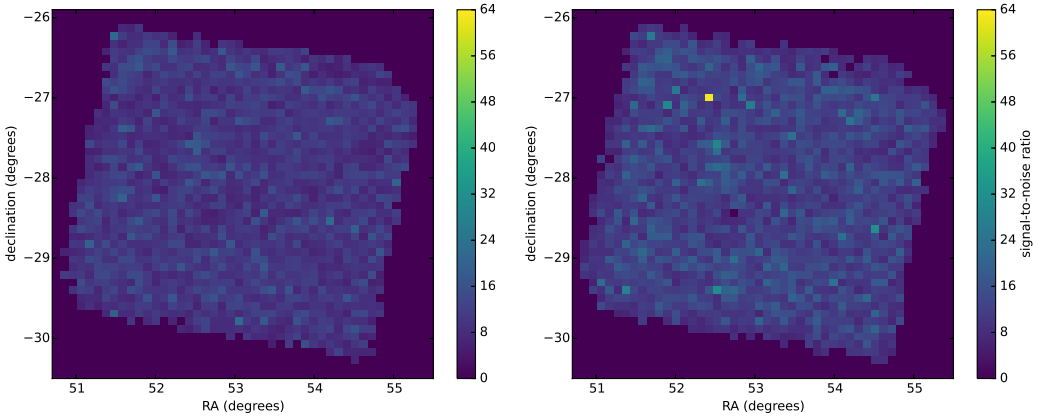

(e) DESPHOT 500μm

(f) SUSSEXtractor 500μm

Figure 2.7: Comparison of the median signal to noise value for sources across the map for SUSSEXtractor and CDFS-SWIRE. The signal-to-noise is consistently higher in SUSSEXtractor catalogues implying that whilst DESPHOT finds more sources they are fainter.

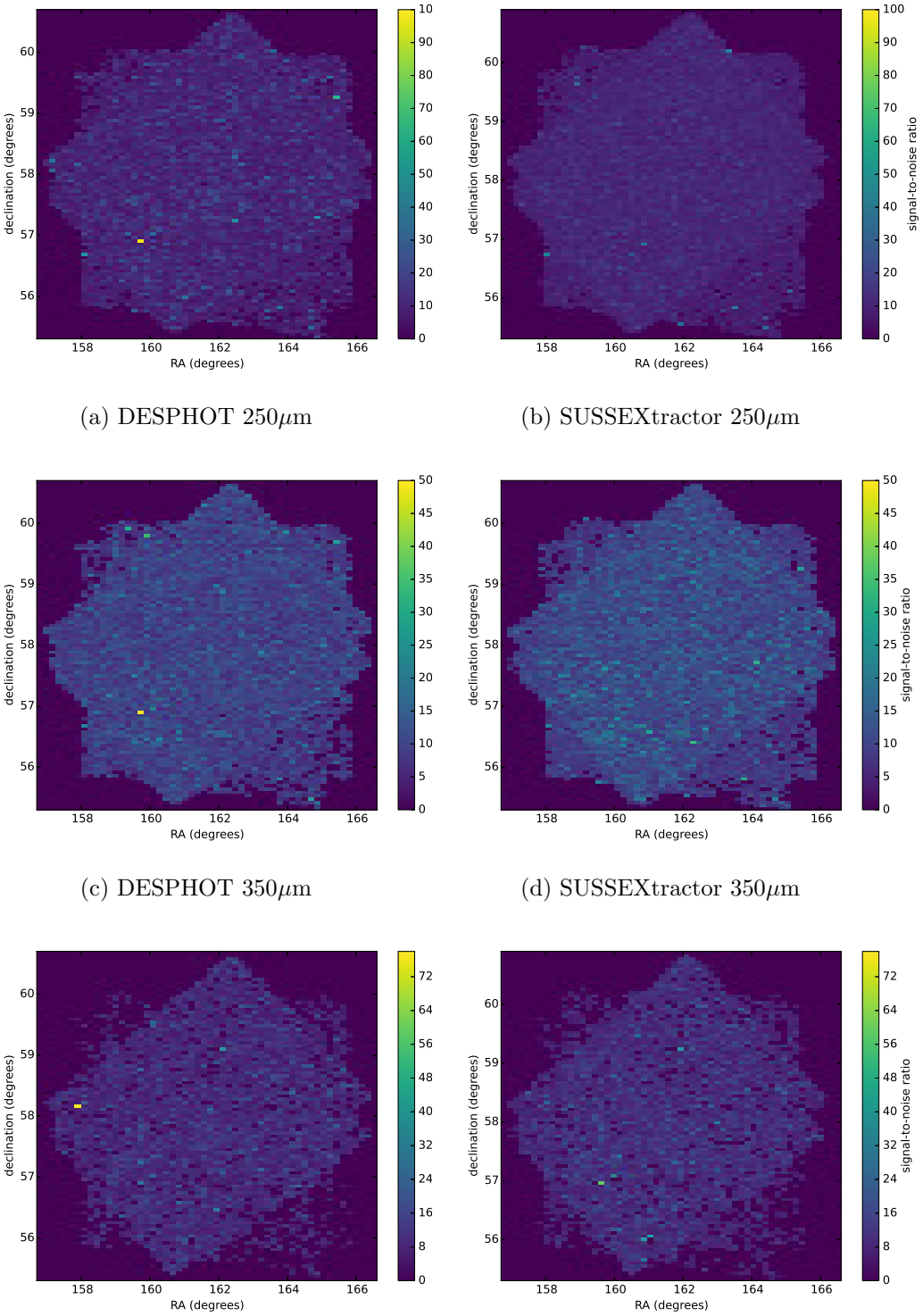

(a) DESPHOT 250μm

(b) SUSSEXtractor 250μm

(c) DESPHOT 350μm

(d) SUSSEXtractor 350μm

(e) DESPHOT 500μm

(f) SUSSEXtractor 500μm

Figure 2.8: Comparison of the median signal to noise value for sources across the map for SUSSEXtractor and Lockman-SWIRE. The signal-to-noise is consistently higher in SUSSEXtractor catalogues implying that whilst DESPHOT finds more sources they are fainter.

more likely the SUSSEXtractor fluxes will be overestimated for the few sources detected. Therefore source detection within a crowded regime like *Herschel*-SPIRE does require special consideration due to the confusion.

The number of sources as a function of flux varies dependent on which source extraction algorithm is used. To demonstrate this more clearly, the differential number counts are shown in figure 2.12, that is the number of sources between flux S and $S + dS$ per sq. deg. as dn/dS. The area is calculated from the number of pixels with flux in the image timsed by the length of a pixel squared. There is no additional weighting change for pixels that have a different coverage, e.g. for pixels associated with areas that have far fewer scans and thus are likely to have less sources on them, so there may be a fractional difference between the number counts of the two fields that is not only due to cosmic variance. The shift in the number of sources is greatest sub 40mJy in the 250μm map and there is an over prediction of the number of sources by DESPHOT above 20mJy by approximately a quarter and a half a decade across all fluxes in the 350μm and 500μm respectively.

In the 500μm especially, the amplitude of the number counts is higher at fainter fluxes with DESPHOT and higher for brighter sources for SUSSEXtractor. The sources are more blended at 500μm and thus the differences between the fluxes found by the two source extraction methods will be greatest.

Another issue is whether the turnover in the number counts between 10 and 50mJy is real. The source counts are often modelled as a power law (Condon, 1974) for the simplest solution, and if that was the case the turn over would not be real and instead should continue upwards. However, the source counts must turn over at some point - if the source counts stayed above power law trend greater than $\propto S^{-2}$ the number of sources contributing to the extragalactic background would diverge (Glenn et al., 2010). At a more physically motivated level, there is a finite volume in the visible Universe with galaxies forming in dark matter halos above a minimum mass; halo masses smaller than this minimum are unable to host a galaxy as the gas in them is unable to cool sufficiently to form stars (Shang et al., 2012). Therefore the number counts do not continue as a the same power-law to smaller fluxes but are instead governed by the halo mass function and galaxy formation models dictating a minimum halo mass for galaxy formation. Viero et al. (2013) fit the halo model of Shang et al. (2012) to the HerMES data, describing a simple model between dark matter halo and sub-halo mass and infrared luminosity. These luminosities can be converted to a flux with a spectral energy distribution model, in this case a grey body approximation to the dust emission in the far-infrared. At the

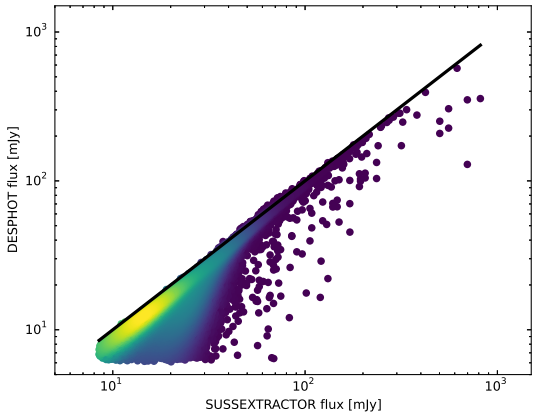

(a) CDFS-SWIRE all sources

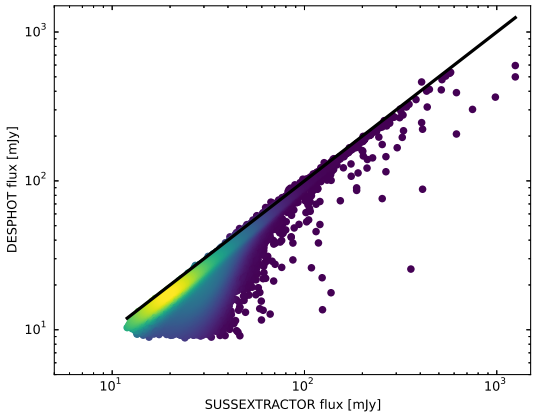

(b) Lockman-SWIRE all sources

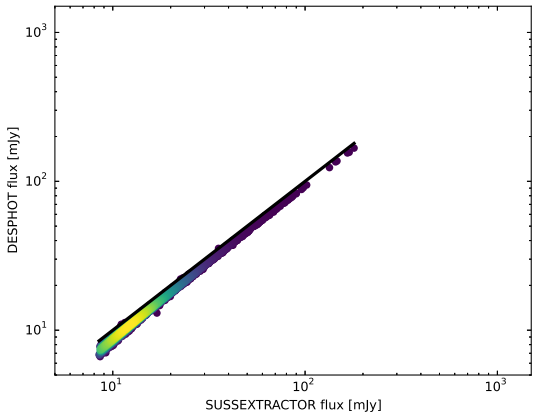

(c) CDFS-SWIRE segment size = 1

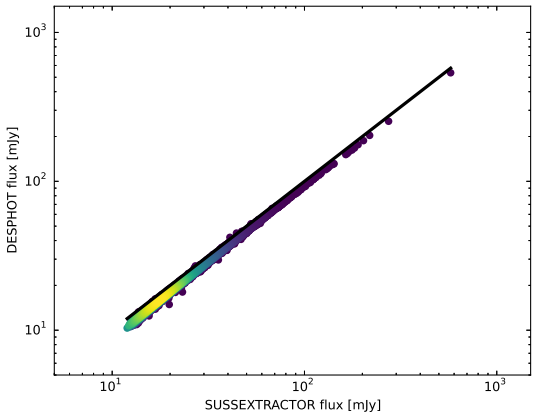

(d) Lockman-SWIRE segment size = 1

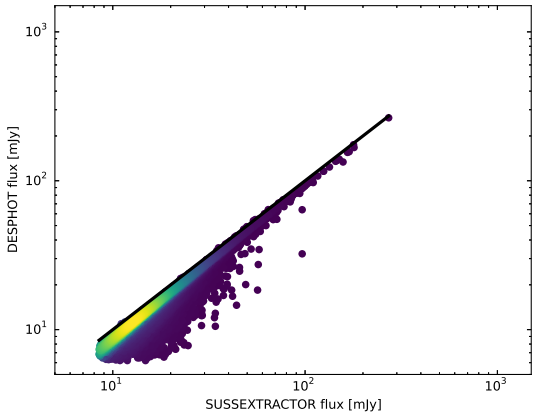

(e) CDFS-SWIRE segment size ≤ 3

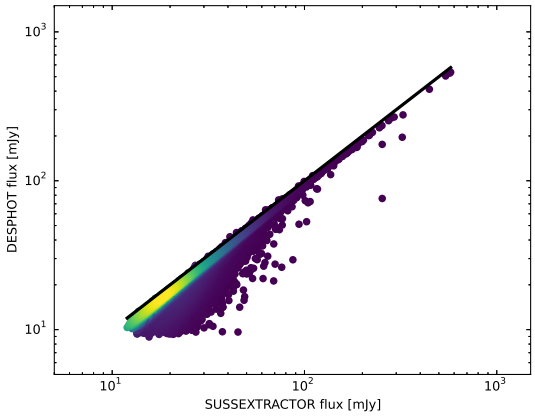

(f) Lockman-SWIRE segment size ≤ 3

Figure 2.9: Comparison of the photometry for CDFS-SWIRE and Lockman-SWIRE for the 250μm band. SUSSEXtractor overpredicts fluxes in crowded regions. The colour is an indication of density of sources (lighter is denser). The black line shows where the fluxes are equal.

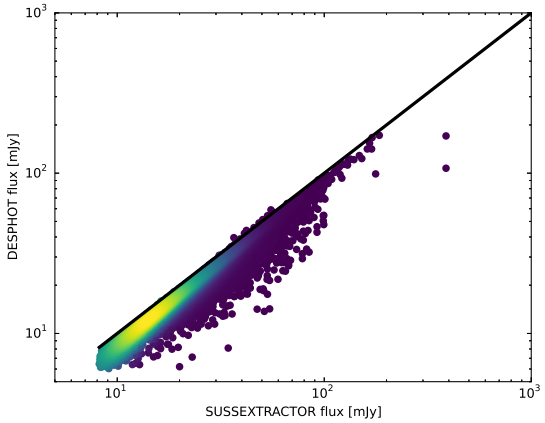

(a) CDFS-SWIRE all sources

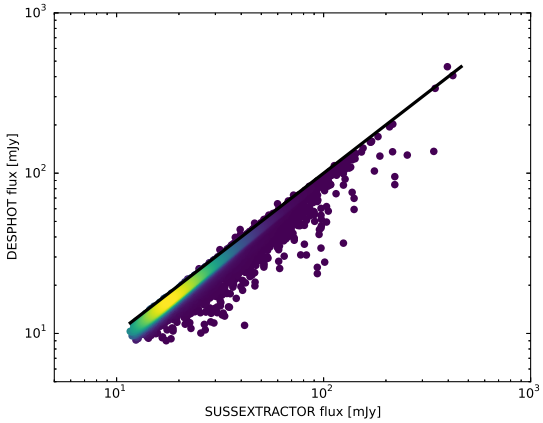

(b) Lockman-SWIRE all sources

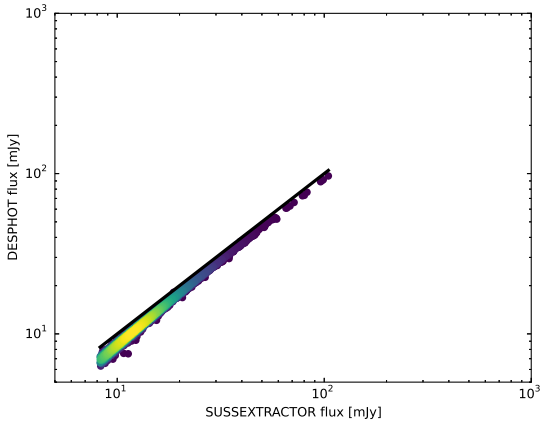

(c) CDFS-SWIRE segment size = 1

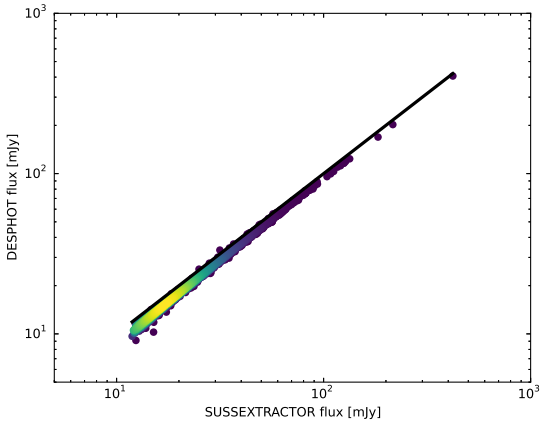

(d) Lockman-SWIRE segment size = 1

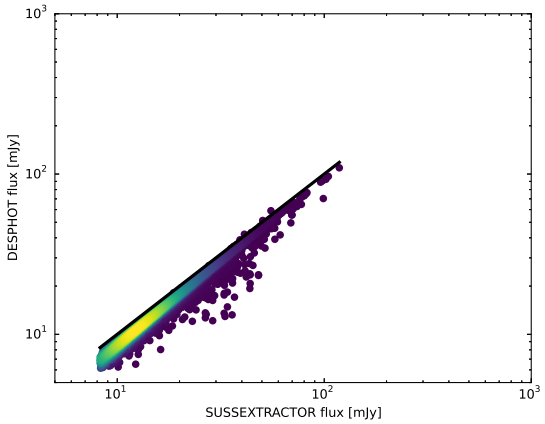

(e) CDFS-SWIRE segment size ≤ 3

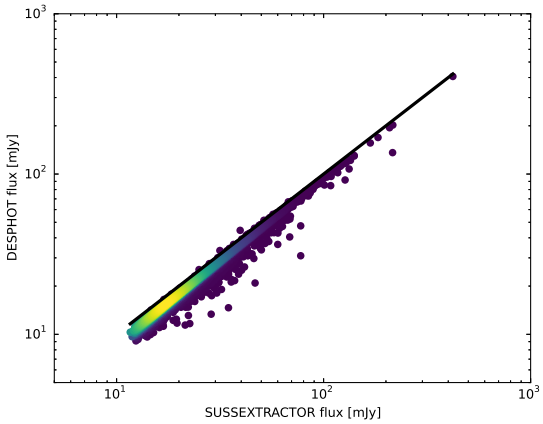

(f) Lockman-SWIRE segment size ≤ 3

Figure 2.10: Comparison of the photometry for CDFS-SWIRE and Lockman-SWIRE for the 350μm band. The colour is an indication of density of sources (lighter is denser). The black line shows where the fluxes are equal.

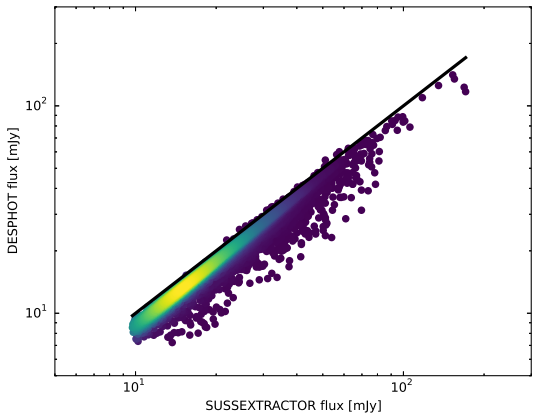

(a) CDFS-SWIRE all sources

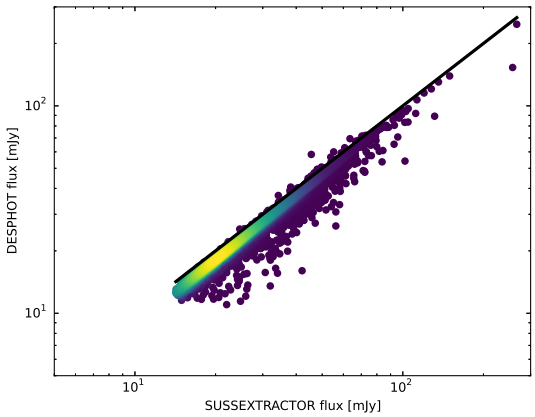

(b) Lockman-SWIRE all sources

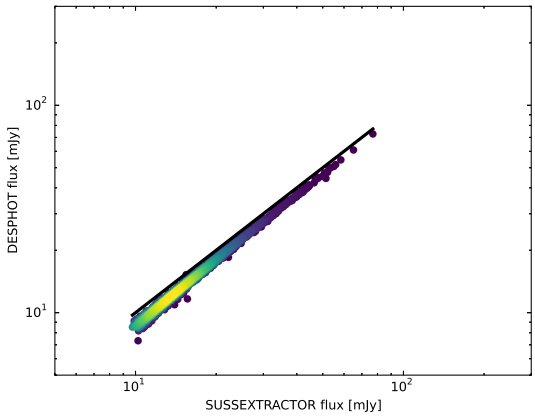

(c) CDFS-SWIRE segment size = 1

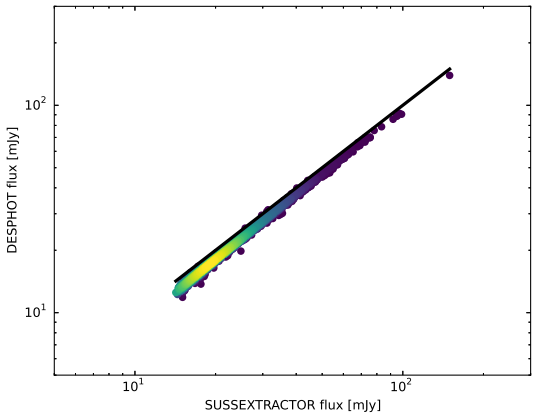

(d) Lockman-SWIRE segment size = 1

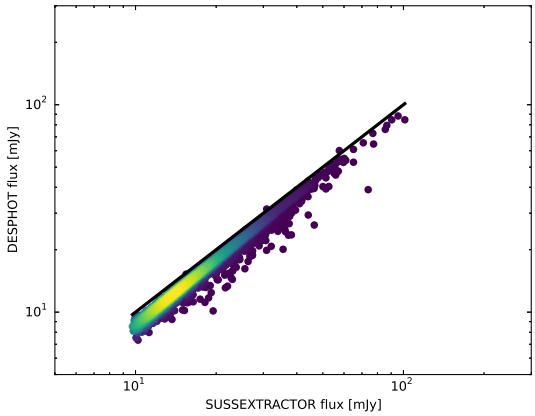

(e) CDFS-SWIRE segment size ≤ 3

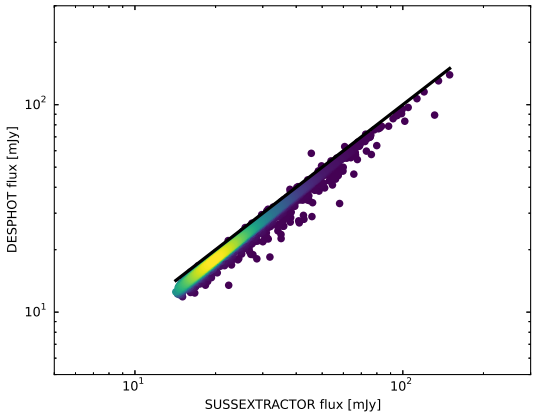

(f) Lockman-SWIRE segment size ≤ 3

Figure 2.11: Comparison of the photometry for CDFS-SWIRE and Lockman-SWIRE for the 500μm band. The colour is an indication of density of sources (lighter is denser). The black line shows where the fluxes are equal.

highest masses, feedback from many supernova suppresses star formation and so there is a downturn of luminosities at the highest halo masses. Given the constraints at these two halo mass extremes, there is a peak halo mass to form infrared luminous galaxies of $12.1 \pm 0.5 \log \mathrm{M}_{\odot}$ found in Viero et al. (2013) corresponding to a flux of order 30mJy at $z = 2$, and the turn-over in the number counts occurs at approximately 5mJy. The turnover in the raw differential number counts shown in this chapter occurs much later than the values calculated the models which hints at the incompleteness of the raw catalogue at fainter fluxes.

The differential number counts are often difficult to interpret given the range in N. Figure 2.13 show the Euclidean normalised differential number counts. This is a transformation of the number counts to what would be expected to be found if we inhabited a static Euclidean Universe and acts as a way to "straighten" the plot. The number of sources N at a particular luminosity within a volume described by distance r can be expressed as $N \propto r^3$. The luminosity of a source is not what is observed however, it is the flux. The flux S of a source varies with radius r as $S \propto r^{-2}$. Substituting for r gives $N \propto S^{-3/2}$. As we're dealing with differential counts, this is modified to $dN/dS \propto S^{-5/2}$. Thus, $S^{5/2} dN/dS = \text{const}$. Also included in the figures are the number counts from Béthermin et al. (2012) and Glenn et al. (2010) for a comparison to published results. These results are given as a guide and the results presented in this chapter have not been corrected for e.g. incompleteness (undetected sources) as the other results have.

The Glenn et al. (2010) number counts have been derived from the P(D) of the maps (discussed in section 3.4), effectively using the histogram of pixels as a function of flux, combined with a model for the number counts and the noise. By iterating the convolution of the model with the noise and telescope beam and against the pixel distribution of the map a parameters for a source model can be fit. This study finds fluxes down 2mJy, below the confusion limit of the maps and below the detection threshold for source extraction (e.g. for SUSSEXtractor in CDFS at 250μm this is 10mJy). Glenn et al. (2010) also detect a break in the power law of the model fit between 10mJy and 20mJy much like the break present in the raw number counts. The number counts are able to describe $64 \pm 14\%$ of the cosmic infrared background at 250μm, $60 \pm 20\%$ at 350μm and $43 \pm 12\%$ at 500μm.

The Béthermin et al. (2012) counts have been derived from a combination of source extraction and stacking on the maps again down to a flux of 2mJy. Using the Spitzer 24μm catalogue as a prior catalogue, sources are found in the SPIRE maps above a flux of 20mJy. Below 20mJy the photometric catalogue associated with the 24μm sources is

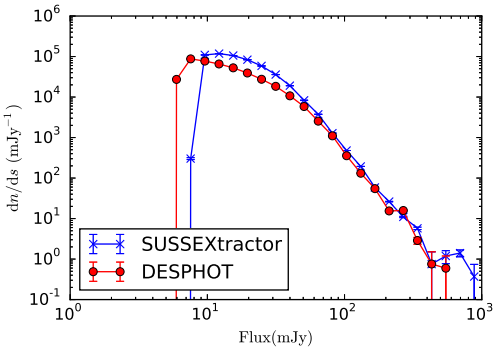

(a) CDFS-SWIRE 250μm

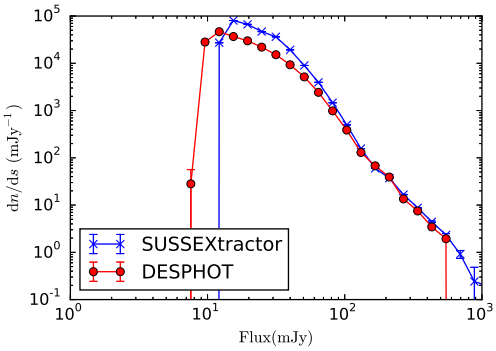

(b) Lockman-SWIRE 250μm

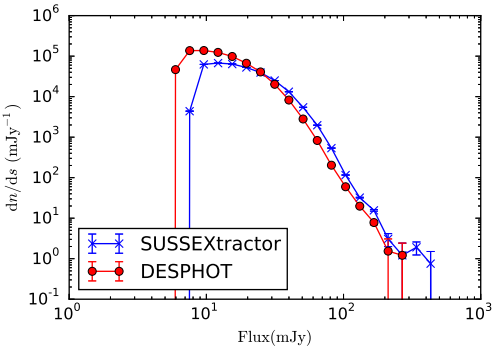

(c) CDFS-SWIRE 350μm

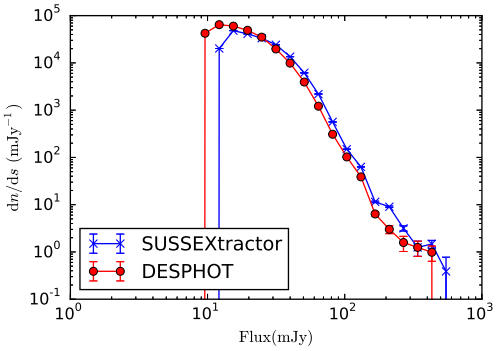

(d) Lockman-SWIRE 350μm

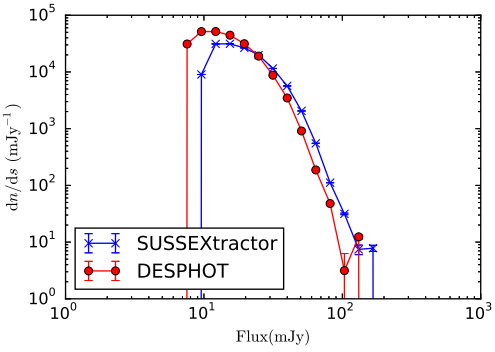

(e) CDFS-SWIRE 500μm

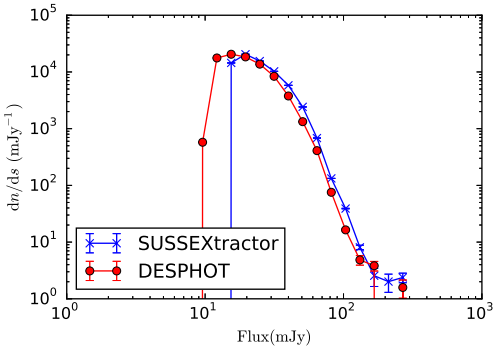

(f) Lockman-SWIRE 500μm

Figure 2.12: Comparison of the differential number counts CDFS-SWIRE and Lockman-SWIRE produced by SUSSEXtractor and DESPHOT. Especially notable is the under prediction of sources at higher fluxes by DESPHOT due to flux from bright sources being attributed elsewhere.

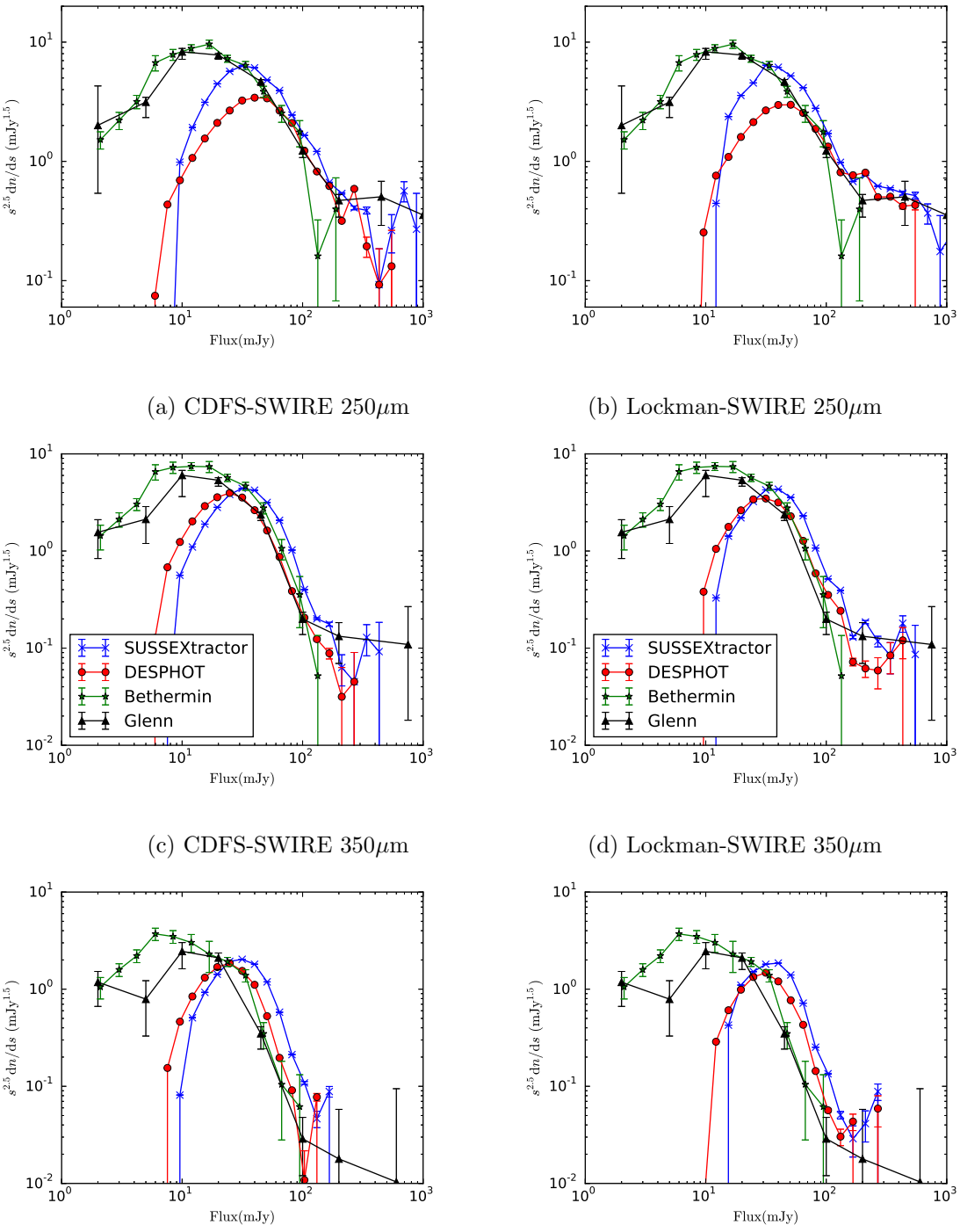

(a) CDFS-SWIRE 250μm

(b) Lockman-SWIRE 250μm

(c) CDFS-SWIRE 350μm

(d) Lockman-SWIRE 350μm

(e) CDFS-SWIRE 500μm

(f) Lockman-SWIRE 500μm

Figure 2.13: Comparison of the Euclidean normalised number counts CDFS-SWIRE and Lockman-SWIRE produced by SUSSEXtractor and DESPHOT. Also plotted are the results from Béthermin et al. (2012)'s stacking analysis and Glenn et al. (2010) P(D) analysis. These published counts have been corrected for completeness and so will not match the raw catalogue counts.

used to bin the Spitzer sources and a stacking analysis (cutting out the map around a set of sources to form a stamp and averaging the stamps pixel by pixel) is used to find the typical flux value of these sources within the GOODS-N and COSMOS fields, effectively allowing the number of sources at these lower fluxes to be constrained.

There is a strong difference between the number counts calculated within this chapter and the published ones for three main reasons. Source clustering due to large-scale structure in general will cause a difference in number counts due to source flux boosting as many sources group together, in Glenn et al. (2010) this is found to be 10% difference at its worst. Source blending due to the beam size is the biggest issue between the two source extraction algorithms and is the cause of the main difference between all three bands at bright fluxes, with 500μm being most strongly affected and therefore the least similar to the published results. Finally and most substantially, incompleteness of the catalogue will have an effect. This is corrected for in the published results and no such corrections have been applied on these raw counts.

2.6 Conclusions

This chapter has focussed on finding galaxies with two different algorithms within source-confused far-infrared images. The data originates from the *Herschel* Space Observatory's SPIRE instrument and was obtained as part of the *Herschel* Multi-tiered Extragalactic Survey (HerMES) consortium. HerMES was awarded the most time of the key projects on *Herschel* with the observing strategy to obtain images of extragalactic fields at primarily the SPIRE wavelengths of 250μm, 350μm and 500μm with, for some fields, additional parallel observations with PACS at 70μm and 160μm. HerMES fields were chosen to be legacy fields, fields with ancillary data from the optical, radio and near- and mid-infrared, and were constructed in such a way as to limit the contamination from galactic cirrus.

The main problem to overcome when constructing source catalogues with *Herschel*-SPIRE data is source blending. With beams of FWHM 18.15 arcsec to 36.3 arcsec the flux of neighbouring sources will blend together; thus peaks found with *Herschel*-SPIRE data are referred to as sources and not galaxies as their flux has not been yet attributed to an optically (or otherwise) identified galaxy counterpart.

Whilst software has been produced by the *Herschel* team for processing telescope data into maps and catalogues (HIPE, the *Herschel* Interactive Processing Environment), the HerMES consortium had developed its own algorithms. SMAP, the map-making team in-part use HIPE but the construction of maps from time-line data is performed with

a different algorithm that improves on surface-brightness estimates at each pixel from HIPE's naïve map-maker, and more aggressively filters the correlated $1/f$ noise from the timeline data.

There were two source extraction algorithms developed specifically for the HerMES maps. The first, SUSSEXtractor, is a blind source detector and extractor. The second method is a combination of STARFINDER, an algorithm developed for crowded stellar fields and used for source detection, and DESPHOT, a prior-driven simultaneous photometric algorithm for source extraction.

As part of the HerMES second data release and paper by Wang et al. (2014), both of the above source extraction methods were run on new maps constructed by adding wide-field scans together, Lockman-SWIRE and CDFS-SWIRE. This chapter compares the source density of sources across the maps, the typical signal-to-noise ratio and the raw number counts. The number counts from the two fields are extremely similar, demonstrating little variance caused by cosmic variance of source counts, a benefit of the extremely large areas *Herschel* could cover for survey fields. The median signal to noise ratio is again consistent enough across the map to not show any correlation bin to bin that could be indicative of large-scale fluctuations across the map not being removed and the number density of sources. The exact nature of this distribution of sources in the HerMES field is preliminarily explored in chapter 6 by examining the two-point correlation function of sources within Lockman-SWIRE and the smaller FLS field.

The fluxes from SUSSEXtractor and DESPHOT are compared and a strong correlation found at bright fluxes. At fainter fluxes the attributed flux is over predicted by SUSSEXtractor. This discrepancy is linked to the number of sources on a segment within the DESPHOT algorithm which in turn is an indication of the density of sources. SUSSEXtractor does not deblend sources very well, and therefore the flux from any sources that are undetected in the map contribute to neighbouring sources. As STARFINDER can identify sources closer together, this misattribution of flux is less likely to occur.

The initial comparison of source detection and extraction algorithms is extended in the next chapter to go beyond a relative comparison, comparing instead to simulations and therefore actual positions and fluxes of sources.

Chapter 3

The Completeness and Accuracy of HerMES' Source Detection and Extraction Algorithms

The previous chapter outlined the source detection and extraction algorithms SUSSEXtractor and STARFINDER/DESPHOT used in the HerMES consortium, and contrasted results from real catalogues generated from the algorithms. This chapter quantifies the accuracy of the source position and flux estimations using source injection. The completeness (probability of detection) is also calculated as a function of source flux. These quantities are calculated for four fields at different depths and for both source extraction algorithms. The confusion noise from the maps is also estimated and compared to previous HerMES results. This work extends the completeness and accuracy comparisons in Wang et al. (2014) which uses simulations of the sky instead of source injections. The results from this chapter are compared to the quantities found in the paper and recommendations are given as to the suitability of each completeness and accuracy curve in different regimes or possible use cases.

3.1 Estimating Completeness and Accuracy of SUSSEXtractor with Source Injection

Calculating the completeness function using only the maps available requires a technique known as source injection. With this method, a grid of sources at a particular flux is laid over the map (figure 3.1). The source detection and extraction algorithm is run over the map and output sources are matched to the known position of the grid sources. The frac-

tion of recovered sources is recorded. This is repeated at many flux values. The resultant curve gives the probability of detecting sources at a given flux value and this curve can be used to correct results such as number counts.

3.1.1 Process of Source Injection

The method used mirrors Smith et al. (2012a) which is summarised here for context. In the case of *Herschel* data, the maps are constructed from timelines. The grid of sources was injected into the timeline of the data and the maps reprocessed. Grid spacing was determined to be small enough to allow a lot of sources on the map, but far enough apart to keep sources from blending. The separation was also not a whole number of pixels to prevent detection biases from using perfectly centred injected beams. The separation was 113.387 arcsec for maps in parallel scan mode and 340.161 arcsec for fast scan maps. Flux densities used for the injected sources are 1, 2, 3, 4, 7, 10, 20, 30, 40, 70, 100, 200, 300, 400, 700, 1000 and 4000 mJy. Ideally, sources would be placed in the map and retrieved one at a time. This method was however considered prohibitive in time and computational costs.

For each iteration of maps, the catalogue from the original maps are matched to within a FWHM of the positions of injected sources and 50%-200% of the injected source flux density. Any sources that match are discarded from the injected catalogue and from further analysis as these would artificially boost the completeness of the catalogue.

The remaining sources in the injected catalogue are matched with sources in the output catalogue from each flux density, again a match is recorded only if the output source fluxes are 50%-200% of the injected source flux density. From this matched catalogue, catalogue completeness and accuracy for flux density and position can be calculated.

This is not the only approach to determining the completeness. Simulated catalogues and maps can be used as in the published results of Wang et al. (2014), shown and compared to in section 3.5.

3.1.2 Completeness Function

The ability to find sources in maps is dependent on both the flux of a source and the source's environment. A source in an empty map (a universe with one point-source-like galaxy) will hypothetically be detectable at any flux by these source detectors (without instrumental noise). However, the detectability of the source will be dependent on the

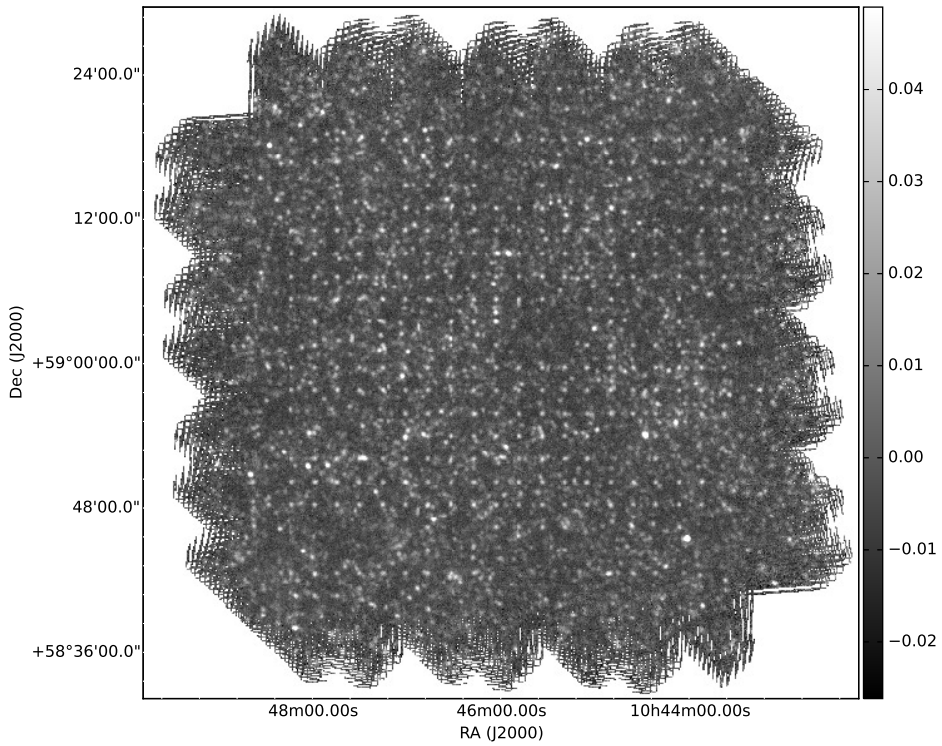

(a) 40mJy grid

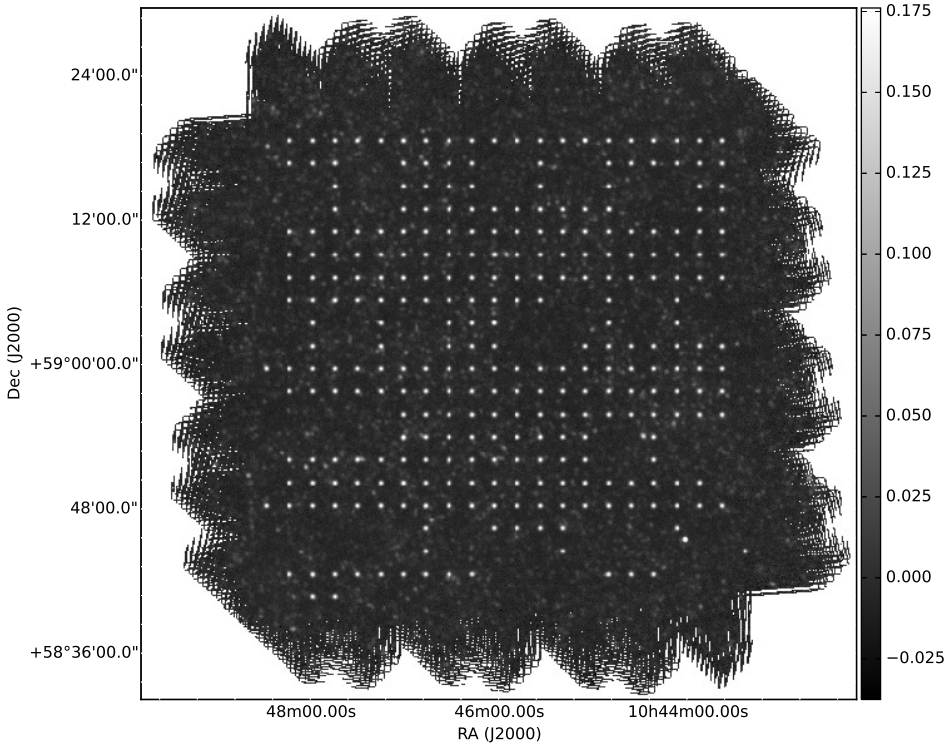

(b) 200mJy grid

Figure 3.1: Two source injected maps created in the Lockman-North region displayed in mJy/beam. By eye the 200mJy sources are far more visible than the 40mJy sources, demonstrating that the completeness will change as a function of flux.

flux of nearby sources and instrumental noise. The probability of detecting a source will increase as noise decreases (exposure time increases) and will increase with the source's flux. "Completeness" C is defined as the probability of detecting a source of a flux S and can be characterised by the generalised logistic function (Richards' curve (Richards, 1959)) such as:

$$C(S) = A + \frac{K - A}{(1 + Qe^{(-B(S-M))})^{1/\nu}} \tag{3.1}$$

where A and K are the lower and upper asymptotes of the curve respectively and B is the growth rate. The value of ν affects which asymptote the maximum growth occurs at. M is an offset to the central value of S and Q controls the steepness of the curve. For extremely low fluxes we would expect the source extractors to not find any sources and at high fluxes we expect to recover all of the sources. Whilst the minimum asymptote should be zero in an ideal case, fits are a lot better if this lower parameter is free to fall negative, i.e. returning a flux at which no more sources are found as opposed to asymptotically tending towards 0 detections. This is realistic as at extremely faint fluxes (e.g 0.1mJy) there is no possibility of detecting a source given the finite instrumental noise in the map. Q and ν are set to 1 to reduce the number of parameters in the fit and are not often used in completeness calculations (Smith et al., 2012a; Wang et al., 2014; Viero et al., 2014) This reduces the completeness function to

$$C(S) = A + \frac{A - 1}{(1 + e^{(-B(S-M))})} \tag{3.2}$$

The completeness function is calculated at each flux density value and is the fraction of sources matched to the input grid of sources after the spurious matches with the real catalogue are removed (figure 3.2). The errors were calculated using a binomial distribution; assuming C as a probability and n the total number of injected sources, the binomial mean is given as $\mu = nC$ variance $\sigma^2 = nC(1 - C)$. Plotted are the 32 and 68 percentiles as error bars. The results from L2-COSMOS, L4-Lockman-North, L5-Lockman-SWIRE and L6-XMM-LSS-SWIRE from the SUSSEXtractor catalogues are plotted with results tabulated in table 3.1.

Generally the steepness B is similar in each field but the offset is different and dependent on depth. COSMOS is the deepest, approximately 60% complete at 10mJy. In contrast, L5-Lockman-SWIRE is only 10% complete. L6-XMM-LSS-SWIRE is more complete than L5-Lockman-SWIRE. Both L5-Lockman-SWIRE and L6-XMM-LSS-SWIRE have the same number of scans (table 2.1) but were observed in different scan modes.

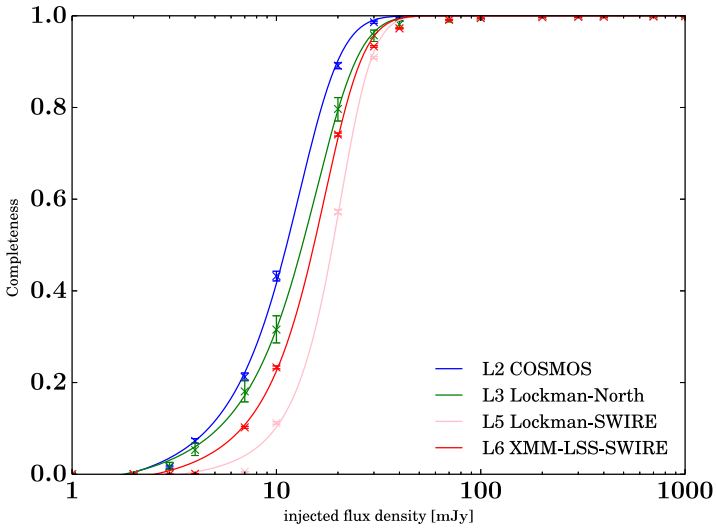

(a) 250μm

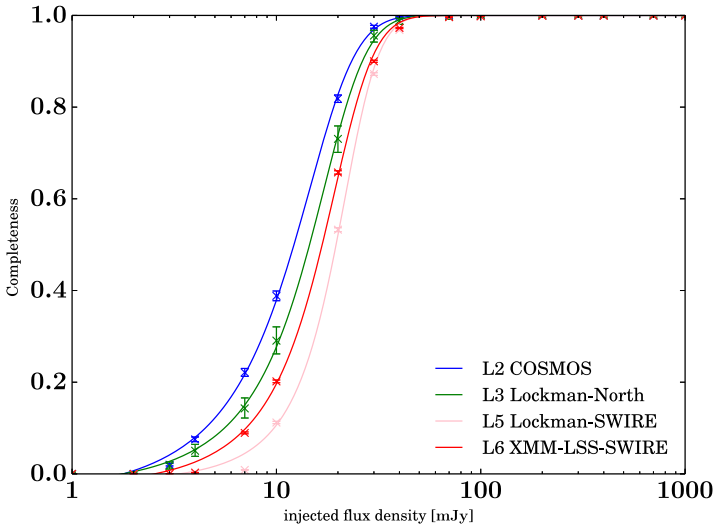

(b) 350μm

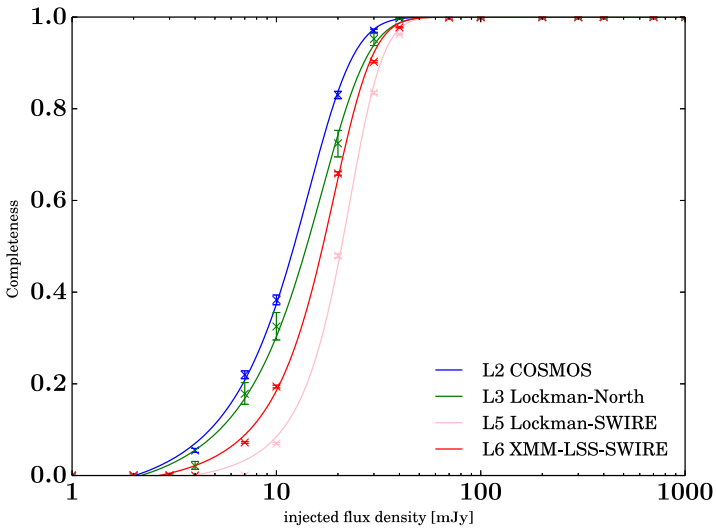

(c) 500μm

Figure 3.2: Completeness curves for four levels of scans. Crosses represent data with 1σ error bars and lines best fits.

Field	Band	Mean Noise (μJy/beam)	0% (mJy)	90% (mJy)	B	A(mJy)	M(mJy)
COSMOS	250	4.67	1.84	19.95	0.243 ± 0.010	10.275 ± 0.203	-0.130 ± 0.203
	350	4.55	1.77	25.13	0.185 ± 0.007	10.322 ± 0.033	-0.206 ± 0.027
	500	5.44	2.03	24.61	0.194 ± 0.010	10.511 ± 0.397	-0.192 ± 0.033
Lockman-North	250	4.44	1.78	26.22	0.192 ± 0.006	12.124 ± 0.228	-0.138 ± 0.016
	350	4.46	1.76	27.78	0.178 ± 0.005	13.232 ± 0.233	-0.130 ± 0.015
	500	5.12	2.17	28.01	0.162 ± 0.010	11.945 ± 0.642	-0.205 ± 0.050
Lockman-SWIRE	250	9.73	3.40	29.40	0.218 ± 0.011	18.520 ± 0.261	-0.037 ± 0.011
	350	9.57	3.34	31.55	0.192 ± 0.009	19.113 ± 0.290	-0.048 ± 0.012
	500	11.5	3.86	33.89	0.188 ± 0.010	20.502 ± 0.310	-0.045 ± 0.012
XMM-LSS-SWIRE	250	6.14	2.51	27.51	0.203 ± 0.010	14.447 ± 0.331	-0.090 ± 0.019
	350	5.99	2.52	29.40	0.175 ± 0.007	15.707 ± 0.327	-0.100 ± 0.017
	500	7.14	2.65	29.19	0.183 ± 0.008	15.985 ± 0.325	-0.087 ± 0.017

Table 3.1: Parameters of the completeness function (equation 3.2) for source positions extracted with SUSSEXtractor. Fixed to maximise at 1. In all cases the minimum M is consistent with 0 as expected.

The results show as expected that the parallel-mode performs a lot better (as the sample rate double that of fast-scan) with 50% completeness at 18.5mJy and 14.4mJy for L5-Lockman-SWIRE and L6-XMM-LSS-SWIRE respectively at 250μm. Despite this difference, as L5-Lockman-SWIRE's completeness curve is steeper, the completeness at 90% is 29.4mJy and 27.5mJy respectively.

The first data release Smith et al. (2012a) give 100% completeness at 30mJy. This value still holds within the errors, with ninety percent of sources identified by this flux in all but the Lockman-SWIRE 500μm, although 35mJy would be a more robust measure if absolute completeness was required.

3.1.3 Positional Accuracy

For each matched source, the mean offset in RA and dec for each field are found as a function of flux in figures 3.3 and 3.4. The 1σ values are plotted as dotted lines. In all cases above 30mJy there is no systematic positional offset for sources. This is to be expected as the maps are calibrated by stacking on 24μm sources which are known to be accurate to <1 arcsecond. At lower fluxes the mean appears to deviate from 0 offset, however the error on the mean at these lower fluxes is larger due to incompleteness and is consistent with zero.

The 1σ values as plotted are broader for a different reason, namely that at low fluxes, sources are more likely to be confused with neighbouring sources. Whilst a flux peak may not be identified in the original map as it would be too faint (and therefore not excluded in the matching as a spurious detection against the injected grid), in the injected map the additional grid source can boost a flux peak that will be located in an incorrect position. Determining the position of sources at fainter fluxes is therefore more liable to error. The reduction in the 1σ errors at higher flux is due to the increased signal-to-noise ratio of the sources and thus their position can be more accuracy ascertained. Encouragingly, all measurements are consistent with zero offset.

Pixel sizes are 6, 25/3, 12 arcseconds wide, and these were chosen so the FWHM was approximately three pixels. With that in mind, the accuracy of positions at each band can be compared. In the 500μm map at 30mJy, 1σ values are within a pixel offset in both RA and dec. Generally, the deeper maps outperform the shallower across all bands. In all cases, the worst performance in accuracy is <10 mJy sources.

Any lack of accuracy in the position of fainter sources has implications for any stacking or averaging performed. If a low flux sample catalogue is chosen, any stacked signal will

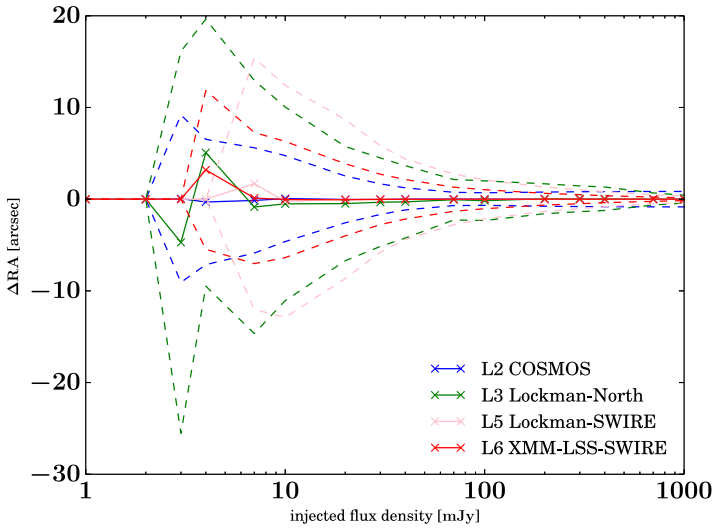

(a) 250μm

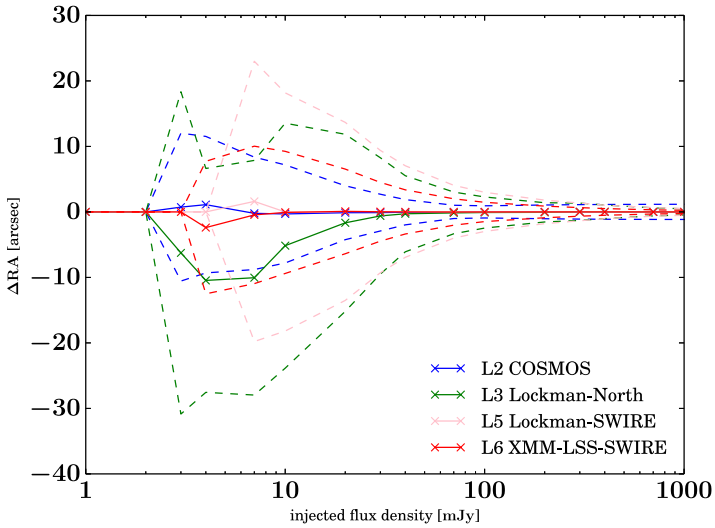

(b) 350μm

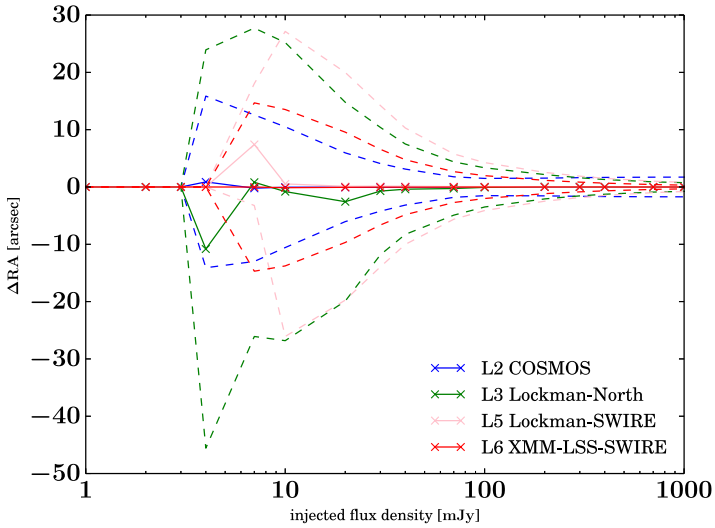

(c) 500μm

Figure 3.3: Offset in RA for four levels of scans. Crosses represent data with dashed lines as 1σ error bars. Solid lines join data points to guide the eye.

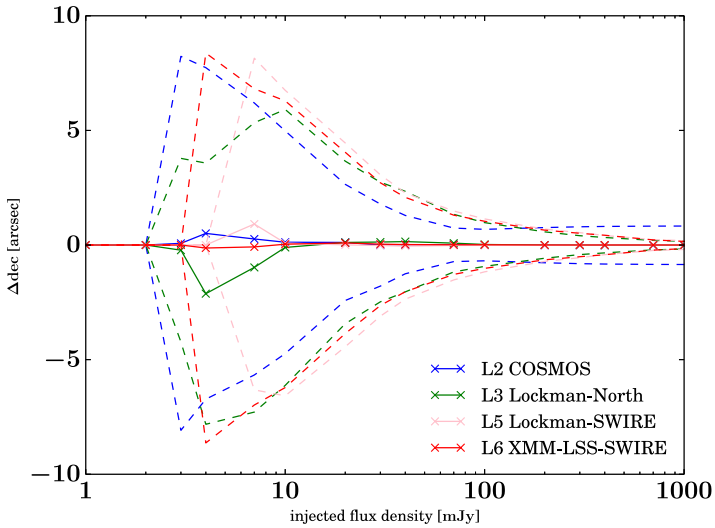

(a) 250μm

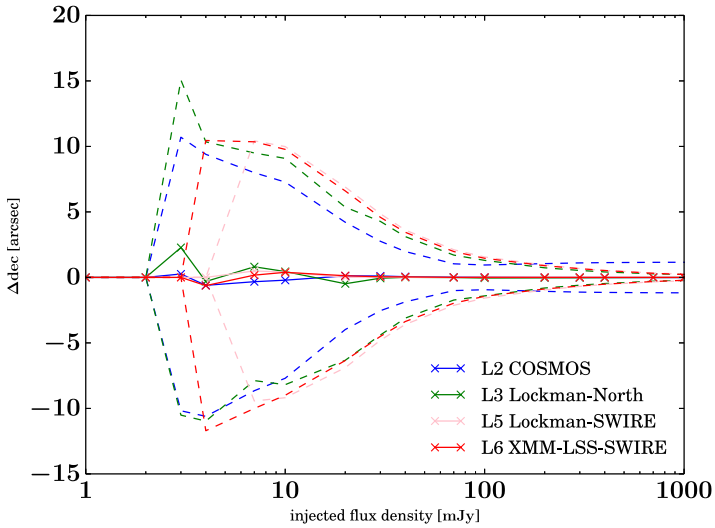

(b) 350μm

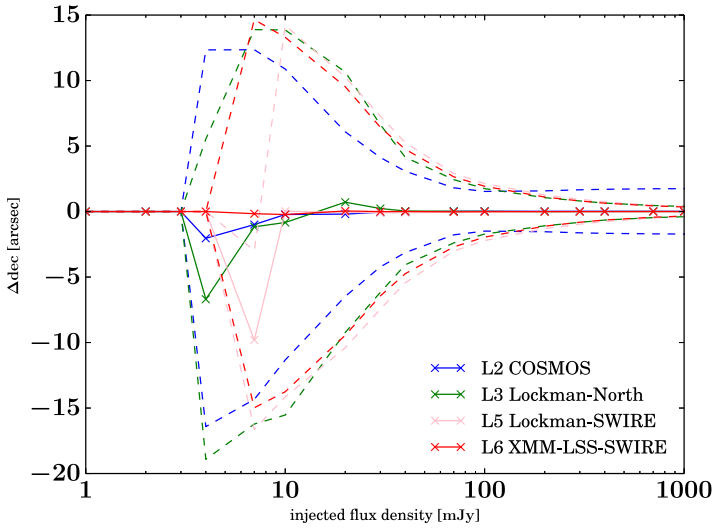

(c) 500μm

Figure 3.4: Offset in declination for four levels of scans. Crosses represent data with dashed lines as 1σ error bars. Solid lines join data points to guide the eye.

be far broader than sources stacked at higher fluxes, weakening a signal if a known beam size is used in analysis. Thankfully stacking on maps is usually performed with samples of galaxies from other, better resolved wavelengths. Whilst there is no evidence for a systematic offset at these low fluxes, stacking or using fluxes found in maps with a prior catalogue created at another wavelength at better resolution is the recommended method for low-flux sources.

3.1.4 Flux accuracy

Figure 3.5 shows the ratio $\log_{10}(S_{\rm recovered}/S_{\rm injected})$ for all matched sources. Immediately apparent is the over-prediction of flux of at a maximum factor of $10^{0.3}$ or 2 for the smallest fluxes. This limit is imposed by the flux cut for spurious sources, only sources that meet a flux tolerance of a ratio between 0.5 and 2 will make the cut. This is implying faint sources are indeed being significantly affected by a background or confusion between neighbouring sources. Sources are systematically boosted to higher fluxes and therefore are unreliable at very low flux.

In addition, Eddington biasing, the bias causing the detection of sources with flux scattered upwards by noise and the non-detection of sources scattered downwards, plays a significant role in over-predicting the fluxes. Note, whilst a real source of 10mJy in the 250μm map could be detected in Lockman-SWIRE, the recovered flux on average will be close to 20mJy which in this measure of completeness is a completely different flux bin. The implication is that a naïve attempt to correct any measure of e.g. the number counts by dividing through by the completeness curve will only lead to an over-estimation of sources at low flux density. However, this flux boosting effect readily drops even in Lockman-SWIRE and a 20mJy source in the 250μm map will only be boosted to approximately 22mJy, and so will not interfere with any 30mJy cuts made to the catalogue.

This flux boosting continues until a reversal at between 10-30mJy where the fluxes are then under-predicted. The under-predictions are not as severe as the over-predictions for lower fluxes, the worst case being a 20mJy source in the 250μm map being detected at an average of 15mJy in COSMOS. The under-prediction is most pronounced for COSMOS, the deepest field. This is contrary to common-sense as one would expect the best data to give the best flux estimates. However deeper maps will have more resolvable flux peaks, and therefore more sources at lower flux and more flux to be mis-attributed to the wrong sources. It is likely the missing flux from these sources has been shared amongst nearby true lower flux sources. Further, the deep maps like COSMOS have been filtered

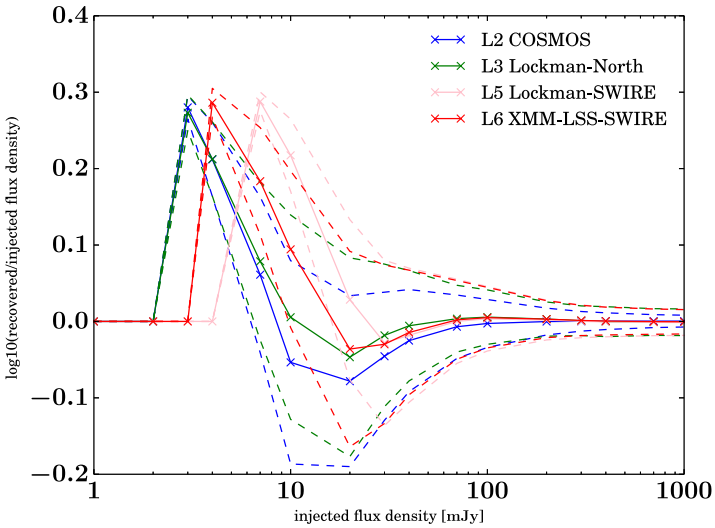

(a) 250μm

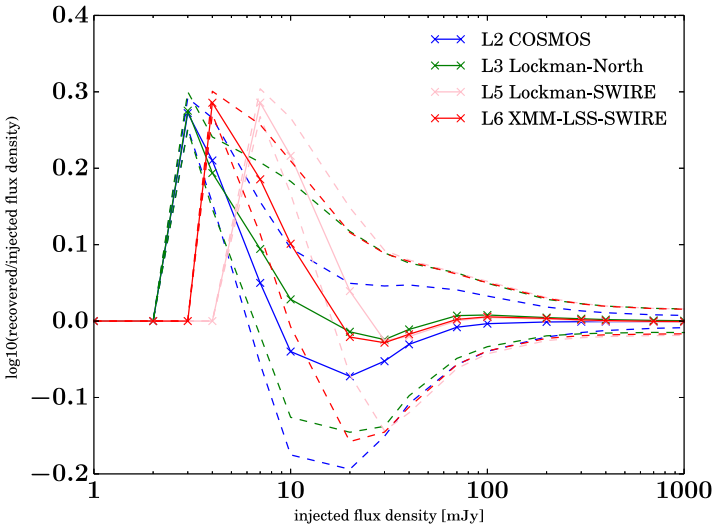

(b) 350μm

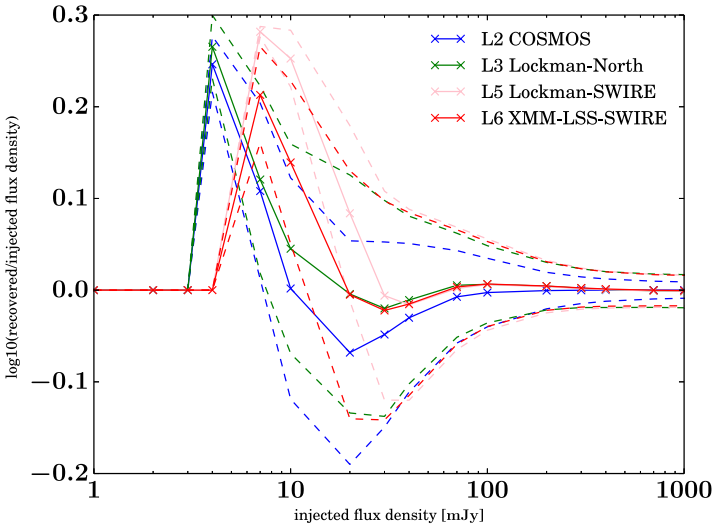

(c) 500μm

Figure 3.5: Flux accuracy curves for four levels of scans. Crosses represent data with dashed lines as 1σ error bars. Solid lines join data points to guide the eye.

differently, with a 3×3 peak PSF acting as a matched filter. This could also provide a contribution to the under-prediction in flux at all wavelengths. Both the under and over prediction of fluxes have a knock-on effect for the number counts, increasing the number counts artificially for sources between 10 and 20 mJy.

In all cases there is a turnover again in flux accuracy at 20mJy that settles very close to a ratio of 1 at 70mJy and is flat for sources above 100mJy in all fields and bands. This shows that for very high fluxes and signal-to-noise, the flux of sources can be detected accurately. If the fluxes in a field need to be rescaled therefore (e.g. due to a calibration error), fluxes above 100mJy would be appropriate to match to. As a caveat however, there are very few non-local sources in a real distribution above 100mJy (the errorbars here being small because a large number of artificial sources were injected) so caution must be exercised.

3.2 Number Counts

Number counts dn/ds/area per field and band are given in Figure 3.6. All fields at all bands have a strong agreement from 30mJy onwards up to 100mJy. This is encouraging as it shows that regardless of scan mode or number of scans the raw number counts do have agreement. The difference in turnover position between fields is dependent on the depth of the field. Further, from observations made looking at flux accuracy, the turnover point is not the point at which the number counts become reliable as low fluxes are boosted and higher fluxes are suppressed around the peak of the number counts. The counts are steep, and therefore Gaussian instrumental noise will be more likely to push sources from a lower to higher flux and be detected (Eddington biasing).

The bright end of the number counts varies between fields (and does not exist in the smaller Lockman-North) due to the limited size of the fields. Whilst HerMES fields were deliberately chosen to sample a large range of cosmological environments, the smallest fields are not wide nor deep enough to prevent biasing from cosmic variance. Further, whilst we have established that the flux density of the very brightest sources will have been accurately determined in the map, it is not known whether the flux should be attributed to a single galaxy or multiple neighbouring or aligned galaxies. Number counts from the LABOCA instrument on the APEX telescope at 870μm (Johansson et al., 2011) imply that many of these sources can be broken up, effectively steepening the counts further. New results from Bussmann et al. (2015) show with ALMA imaging 70% of *Herschel* sources can be broken into multiple counterparts, with over half of sources experiencing

amplification by lensing by a foreground galaxy.

3.3 Estimating Completeness and Accuracy of STARFINDER and DESPHOT with Source Injection

In this section, the completeness, positional and photometric accuracy is assessed for the STARFINDER/DESPHOT pipeline. The same source injected maps from the previous section with SUSSEXtractor is used to ensure consistency.

Each map is run through the STARFINDER and DESPHOT pipelines to produce a catalogue of fluxes. Not every datapoint is reported however. The grid separation is small enough and sources at bright fluxes bright enough that the signal to noise ratio of pixels is on average many times higher than the original map. This leads to the map segmentation algorithm in DESPHOT returning an error as the centre of even the shallowest maps turns into one giant segment with too many sources. With these large, artificial number of sources DESPHOT can often hang as LASSO cannot find a robust solution and instead returns zero for many fluxes. This means completeness estimates would be extremely poor and not representative of the detectablilty of sources at those particular fluxes.

For that reason the completeness and positional accuracy from the STARFINDER maps are reported rather than the final product. This is a reasonable assumption as the positions from STARFINDER are used as priors in DESPHOT. Further, every source detected by STARFINDER should be assigned a flux value by DESPHOT.

To note, this assessment of the completeness and positional accuracy of this pipeline using only the source detections will not necessarily work in cases where positional priors from another wavelength are used. Even in cases where a strong correlation between the two bands are expected (like 24μm and SPIRE fluxes, Elbaz et al. (2010)), DESPHOT will not assign a flux to every source in a dense prior catalogue. LASSO instead will preferentially turn sources off to prevent over-fitting. In this case therefore, the completeness and positional accuracy should be assessed only on those sources assigned a flux by DESPHOT. This caveat does not apply to the catalogues in this chapter as the positional priors has been created from the same map.

3.3.1 Positional Accuracy and Completeness

Figures 3.7 and 3.8 show the difference in RA and dec in each field and band between input grid positions and the matched output catalogue. As with SUSSEXtractor, the average

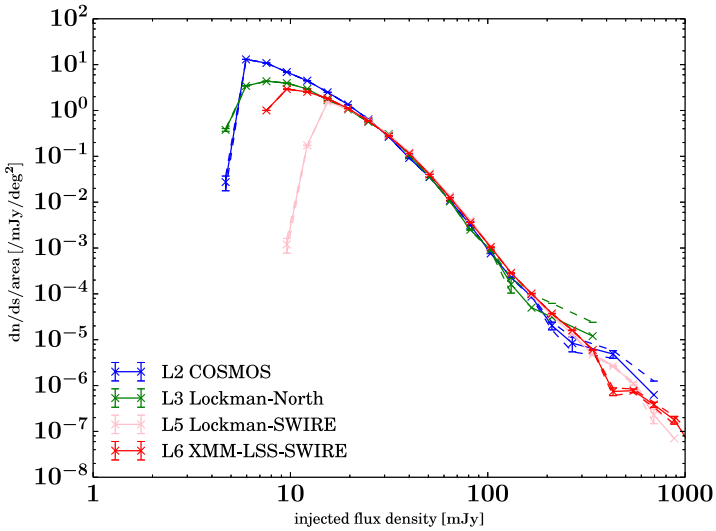

(a) 250μm

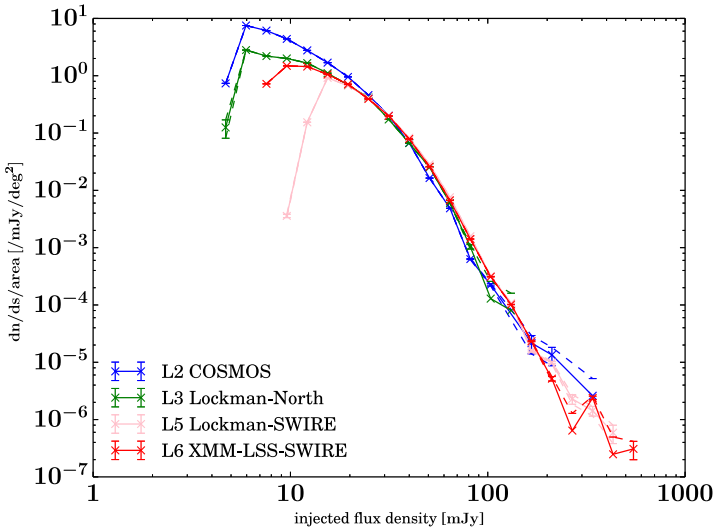

(b) 350μm

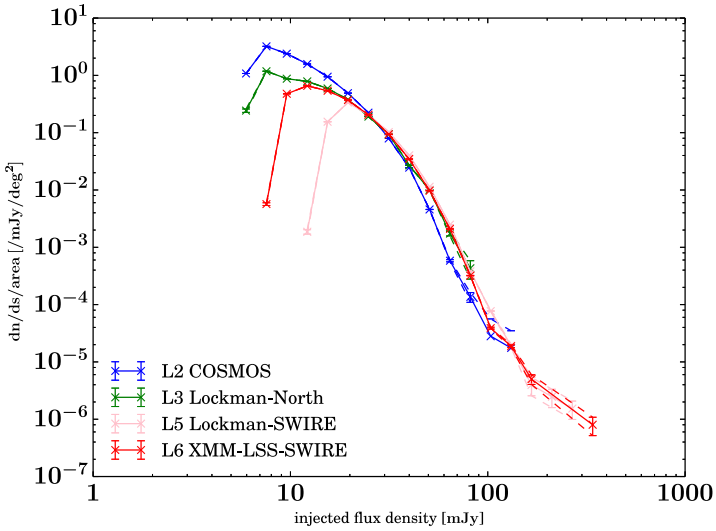

(c) 500μm

Figure 3.6: Raw number counts for all four catalogues found with SUSSEXtractor Crosses represent data with 1σ error bars. Solid lines join data points to guide the eye.

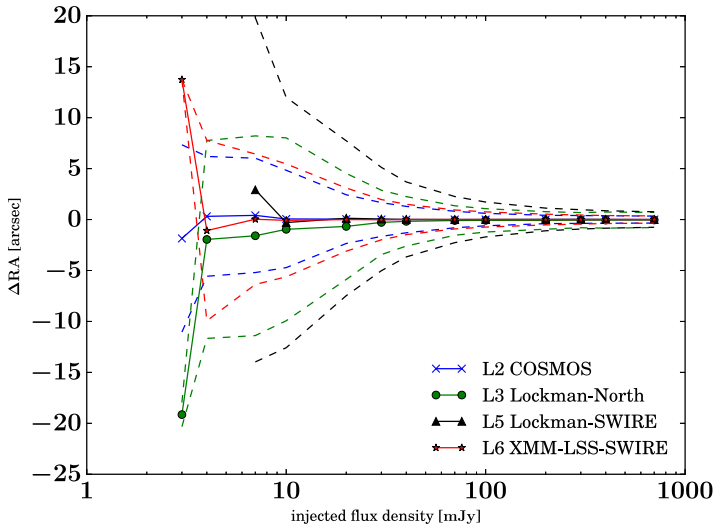

(a) 250μm

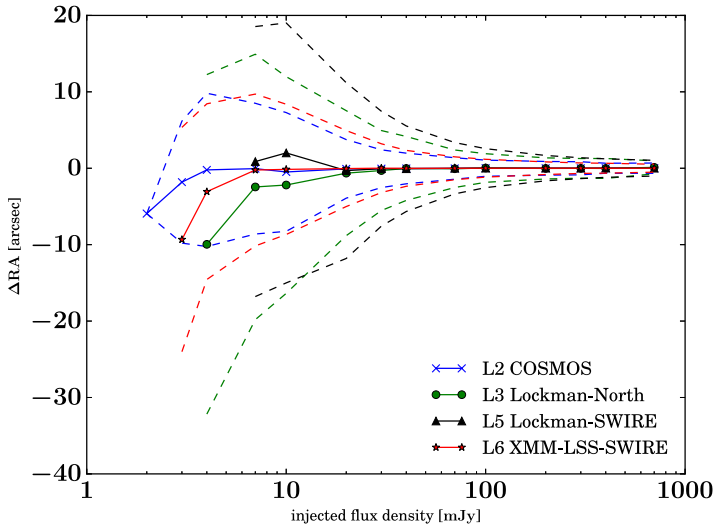

(b) 350μm

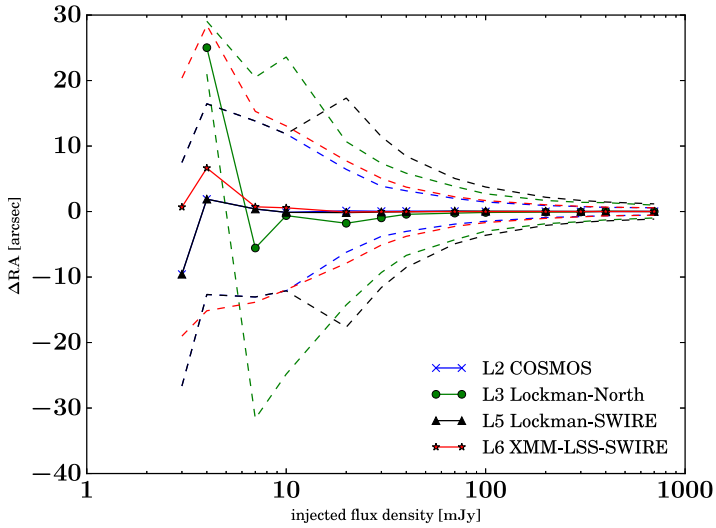

(c) 500μm

Figure 3.7: STARFINDER RA positional accuracy for four levels of scans. Points represent data with dashed lines as 1σ error bars. Solid lines join data points to guide the eye.

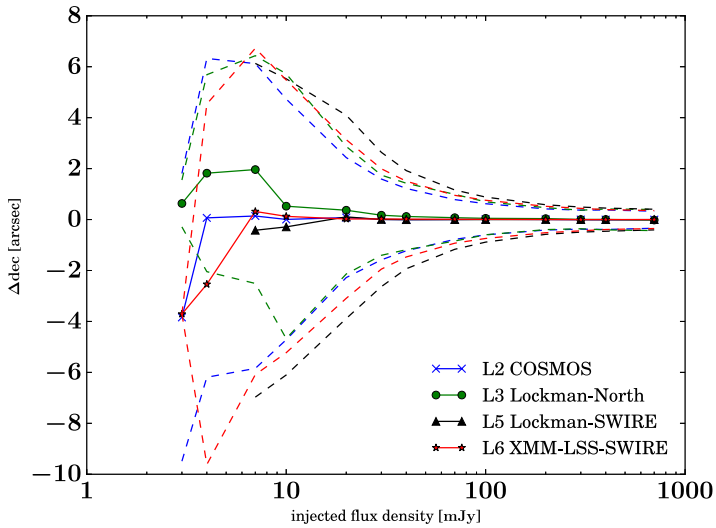

(a) 250μm

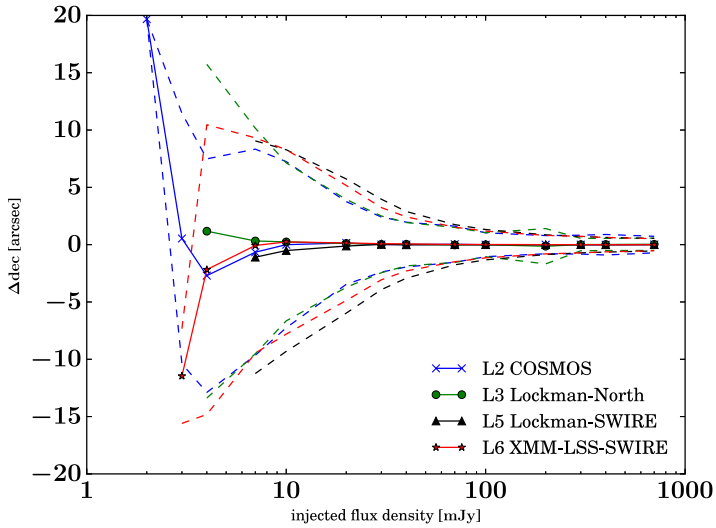

(b) 350μm

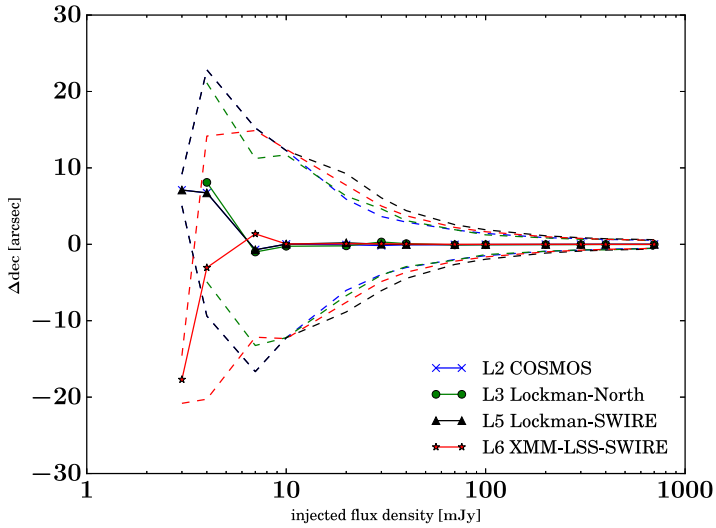

(c) 500μm

Figure 3.8: STARFINDER declination positional accuracy for four levels of scans. Points represent data with dashed lines as 1σ error bars. Solid lines join data points.

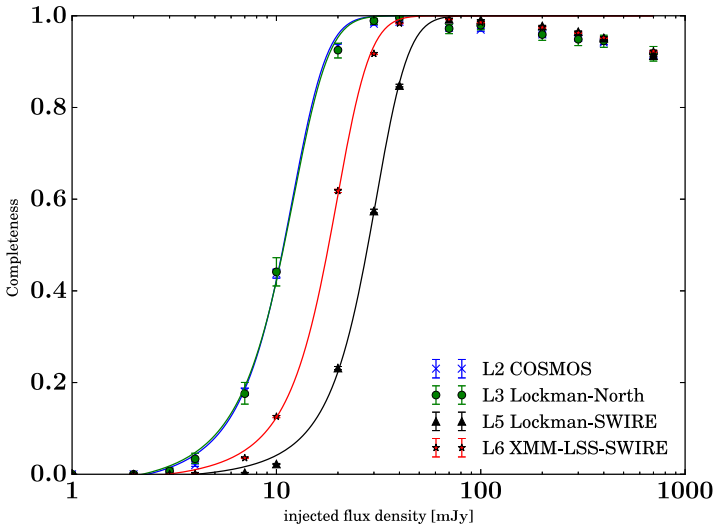

(a) 250μm

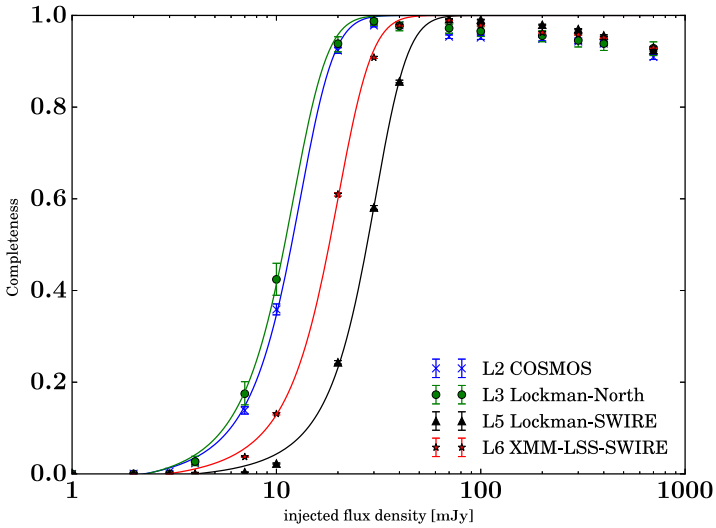

(b) 350μm

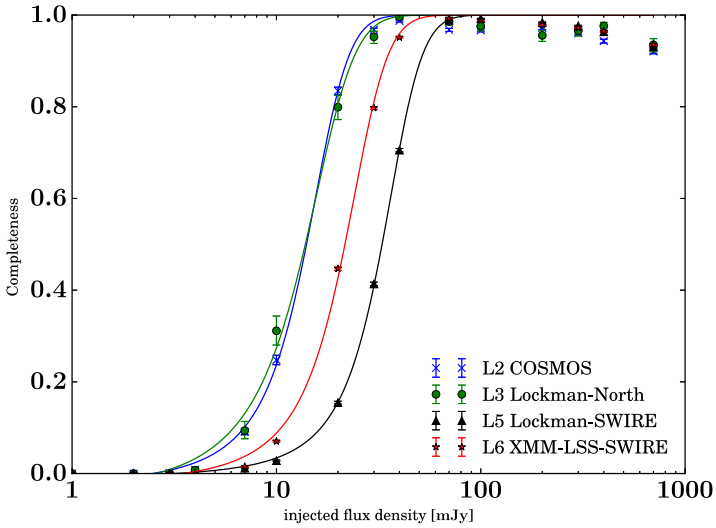

(c) 500μm

Figure 3.9: Starfinder completeness curves for four levels of scans. Points represent data with 1σ error bars. Solid lines show the line of best fit.

Field	Band	0% (mJy)	90% (mJy)	B	A(mJy)	M(mJy)
COSMOS	250	2.31	18.89	0.340 ± 0.074	10.503 ± 0.471	-0.062 ± 0.050
	350	2.22	19.43	0.319 ± 0.067	11.550 ± 0.620	-0.051 ± 0.046
	500	2.45	24.30	0.266 ± 0.033	13.673 ± 0.651	-0.051 ± 0.034
Lockman-North	250	2.19	19.01	0.324 ± 0.066	10.519 ± 0.481	-0.068 ± 0.050
	350	2.27	18.94	0.340 ± 0.072	10.640 ± 0.462	-0.059 ± 0.047
	500	2.56	25.62	0.219 ± 0.026	13.007 ± 0.737	-0.102 ± 0.05
Lockman-SWIRE	250	4.04	49.61	0.146 ± 0.016	27.632 ± 0.805	-0.032 ± 0.022
	350	4.02	48.85	0.146 ± 0.014	27.314 ± 0.725	-0.034 ± 0.021
	500	3.32	60.43	0.123 ± 0.011	37.467 ± 0.671	-0.027 ± 0.017
XMM-LSS-SWIRE	250	2.93	28.95	6.219 ± 0.027	17.672 ± 0.662	-0.040 ± 0.029
	350	2.93	29.23	0.208 ± 0.026	17.701 ± 0.701	-0.046 ± 0.031
	500	3.48	36.05	0.170 ± 0.016	21.087 ± 0.656	-0.050 ± 0.024

Table 3.2: Parameters of the completeness function (equation 3.2) for source positions extracted with STARFINDER. Fixed to maximise at 1. In all cases the minimum M is consistent with 0 as expected.

offset is zero; the discrepancy at low fluxes is well within the 1σ errors and still consistent with zero. The standard deviation of the offset becomes tighter at higher fluxes as the profile of the signal from the source becomes better resolved by STARFINDER. From the 1σ errors, SUSSEXtractor detects the position of sources better at 500μm, and not as well at as STARFINDER 250μm in all fields.

Figure 3.9 shows the completeness as a function of field, band and flux is a different picture. The percentage of recovered sources does increase as a function of flux as expected, and the deeper fields find more sources at lower fluxes than the shallower two. There is however a prominent turnover in the STARFINDER completeness; at the brightest fluxes the number of recovered sources decreases. Naïvely this is counterintuitive as the brightest fluxed should be the most detectable. However, it is likely STARFINDER is struggling to simultaneously fit extremely bright sources with the background estimation; a background box of 150 pixels squared is used around the source, with the residual flux used to calculate a background level. As previously stated, STARFINDER was designed for crowded stellar fields with the majority of pixels at zero flux. In the case of an injected grid of sources at the same unnaturally high flux the background estimation will suffer and could result in STARFINDER rejecting sources due to a perceived lack of correlation between the source profile and map. As there are extremely few sources at 500mJy and above in HerMES images it is unlikely that this turnover in the completeness would be present in the real catalogues.

The completeness as found with STARFINDER reaches 90% completeness later than SUSSEXtractor. For example, L5-Lockman-SWIRE reaches 90% completeness at 50, 49 and 60mJy as opposed to 29, 32 and 34mJy at 250, 350 and 500μm respectively. The performance of STARFINDER in the fields with the highest instrumental noise is worse than SUSSEXtractor. With the deepest field L2-COSMOS however, STARFINDER is complete at lower fluxes than SUSSEXtractor. This is also the case for L3-Lockman-North.

3.3.2 Flux Accuracy

Figure 3.10 shows the flux accuracy and errors on the mean (as opposed to 1σ errors) for DESPHOT. The flux accuracy results for DESPHOT are difficult to compare against different fields and with SUSSEXtractor. At very low flux the number of sources detected make finding the mean ratio between input and output fluxes difficult. As more sources cannot be injected into the map to increase the detected number of sources due to the

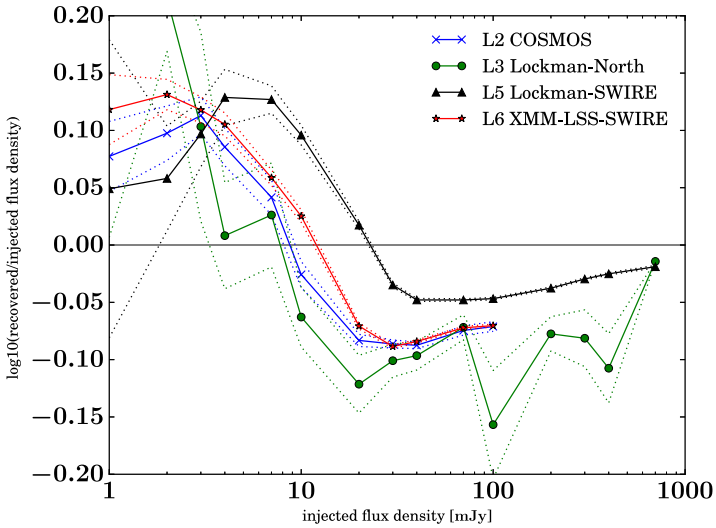

(a) 250μm

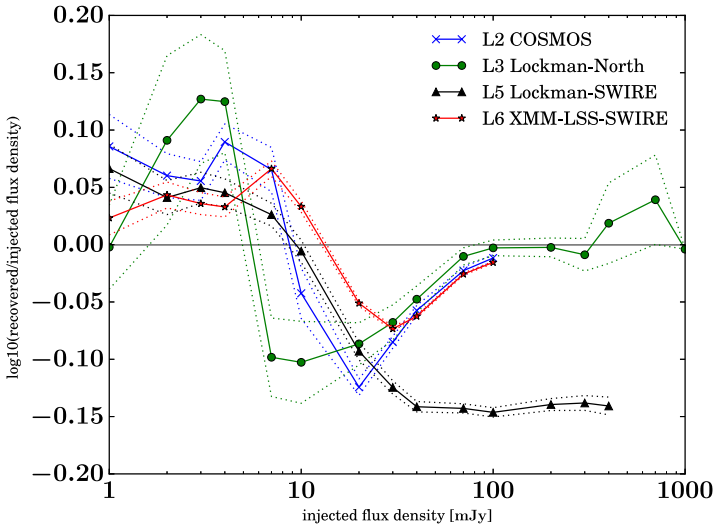

(b) 350μm

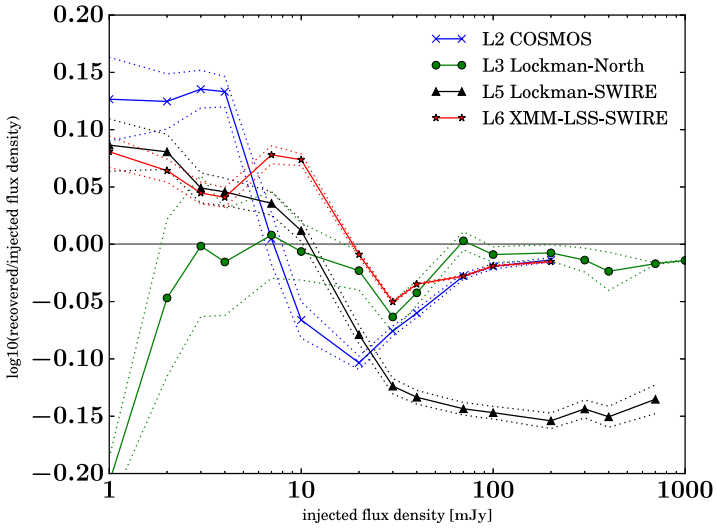

(c) 500μm

Figure 3.10: Flux accuracy curves from DESPHOT for four levels of scans. Points represent data with dotted lines as 1σ error bars. Solid lines join data points.

required separation between them, rerunning the source extraction with the grid injected at different positions would be one way to increase this accuracy.

At higher fluxes determining this flux ratio should become easier as the completeness increases, however the artificially bright number counts of sources within the map make map segmentation difficult. Some segments become too large, the matrix inversion cannot be conducted and so fluxes are reported as zero. Thus the flux ratio can deviate from zero. This is a particular issue for Lockman-SWIRE at 350μm and 500μm that converge to ratios of $10^{-0.15}$ or 70%. With the information available combined with the earlier direct comparison between Lockman-SWIRE and CDFS-SWIRE, the fluxes do appear to be underestimated across all bands until approximately 50mJy, when the flux estimate levels off. There is not an over reporting at low flux as with SUSSEXtractor as STARFINDER and the second pass of DESPHOT is able to find sources closer together than SUSSEXtractor, thus sharing flux between sources to better fit the model to the map.

3.4 Instrumental and Confusion Noise Measurements

Each catalogue contains information about a source's photometry, the error in that photometry as calculated from the instrumental noise and the total error in the source including the confusion noise. The first error calculation uses the error maps provided in the data, which are themselves constructed from instrumental noise calculations within the data reduction pipelines as a function of coverage. As previously, there a number of ways to calculate the confusion noise and both SUSSEXtractor and the STARFINDER/DESPHOT pipelines have their own methods, with SUSSEXtractor using the variance of the fluxes below the median value in the map, and DESPHOT fitting a linear model of the residual map against the exposure time of each pixel to find the variance in the flux when the exposure time tends to infinity.

The original, analytical calculation of confusion noise is given in Condon (1974) as a discussion on probability of deflection analysis in the radio as a function of the (resolved and unresolved) source counts and telescope beam as

$$\sigma^2_{conf} = \int_0^{x_{conf}} x^2 d\bar{n} \tag{3.3}$$

with x as $Sf(\theta, \phi)$, S the source flux, $f(\theta, \phi)$ a description of the telescope beam as a function of angular separation between points θ and rotation ϕ normalised to a peak of 1. x_{conf} represents the confusion limit, the flux at which a source would be unresolved on a background of confused sources. $d\bar{n}$ is the mean number of sources giving a flux density

profile of $x = Sf$ between a flux density profile of x and $x + dx$ is given as

$$d\bar{n} = \int_{x}^{x+dx} n\left[\frac{x}{f(\theta,\phi)}\right]\frac{d\Omega}{f(\theta,\phi)}dx \tag{3.4}$$

with $d\Omega$ the infinitesimal solid angle and n the differential source counts. In the case of $n = kS^{-\gamma}$, as is a common representation of source counts in the radio $d\bar{n}$ becomes Gaussian and therefore the mean equals the variance, making the equation 3.3 valid in this regime. In the case of *Herschel*-SPIRE data, source counts cannot be approximated by one simple power law (Oliver et al., 2010; Clements et al., 2010) although multiple broken power laws are used in Glenn et al. (2010).

However, the true source counts will not fit a power-law at bright scales - most source count models in recent years have not used a power-law model (Glenn et al., 2010; Johansson et al., 2011). The telescope beam is not analytical either, as previously discussed. Confusion noise estimations must therefore be made from the map directly. This leads to a problem: estimations of the confusion noise (and probability of deflection analysis) derived on the map directly are not just based on the source counts and beam. As discussed in Chapter 1 the observed far infrared sky consists of more than extragalactic sources. The interstellar medium, dust in the Solar System and from transient objects, cool stars in Milky Way, the cosmic microwave background and the telescope itself all contribute in some way.

Zodiacal light, infrared emission from dust within the Solar System, has peak emission in the mid-infrared and does contribute in the far-infrared, albeit a small amount. The dust has as very uniform structure and therefore does not contain the bright arcsecond scale fluctuations necessary to contribute to source confusion - if only present at large scales and therefore a smooth background, the zodiacal emission can be removed with filtering (Ott, 2010). Large scale uniform fluctuations like that from zodiacal emission have already been removed in the map-making pipeline and so this emission will not contribute to the final map.

Asteroids are point-source objects and therefore can contribute to foreground emission. The contribution to confusion noise from asteroids was modelled as part of the *Herschel* Confusion Noise Estimator's analysis; using the known positions and motions of asteroids from start of January 2000 to end of December 2012, and applying Standard Thermal Model Lebofsky et al. (1986) applied to calculate the flux of these objects, an estimate was made both of the number density of sources reaching a threshold flux and the confusion noise to a 0.5 by 0.5 arcmin resolution across the entire sky. The peak of confusion noise was non-negligible, but was located in the direction of the anti-solar point.

Fortuitously, *Herschel*'s observations were restricted away from the anti-solar point, with a solar aspect angle between approximately 60 to 120 degrees (Valtchanov, 2014) so the *Herschel* Confusion Noise Estimator ignores the asteroid contribution.

The Cosmic Microwave Background does contribute to the far infrared, however the fluctuations are not detectable by *Herschel*-PACS and *Herschel*-SPIRE as the signal is dominated by emission from galaxies. The Planck satellite, constructed to observe the entire sky and resolve the Cosmic Microwave Background observed in the sub-mm/microwave bands at wavelengths 300 to 3000μm. Whilst Planck overlaps with the *Herschel*-SPIRE wavelengths the CMB peaks at 1063μm, much longer than SPIRE's bands.

The main contributor to far-infrared fluctuations not from extragalactic sources is the interstellar medium in the Milky Way. The dust in low density HI clouds emits at a peak wavelength of 100μm at a typical temperature of 20K (Low et al., 1984). The structure of the emission resembles cirrus clouds within our own atmosphere and thus is referred to as galactic cirrus. It has power on all scales and has been shown to be fractal in nature (this will be discussed in depth in chapter 4). Cirrus emission has a strong contribution to the SPIRE bands, and the impact on confusion noise is carefully considered with observations and models (HCNE, Valtchanov (2014)). HerMES fields are carefully positioned to reduce the impact of cirrus in observations and as such the contribution of cirrus to the flux in most fields is minimal (section 3.6 shows where this is not the case). With this significant contribution not from the sources themselves, the confusion noise calculated directly from the map must either take into account the cirrus emission with some form of subtraction during the source extraction stage, or explicitly define the confusion noise and calculated confusion limit to include the cirrus emission. Using the probability of deflection analysis from Condon (1974) to iterate down to the number counts from the map (like Glenn et al. (2010)) must take into account the cirrus to be reliable.

With the above in mind, a third method has calculated the confusion and instrumental noise for HerMES maps on the Science Demonstration Phase data, which uses a different method from the source extraction algorithms, in Nguyen et al. (2010). If cirrus contamination has not been taken into account, the increase in variance caused by the cirrus will be folded into the confusion noise estimation as there are no strong assumptions made about the number counts.

Herschel-SPIRE maps with the 1/f noise noise removed can be represented as

$$d_i = f_i + n_i \tag{3.5}$$

with d_i a pixel in the map, f_i the true flux of the sky at that pixel and n_i a noise value

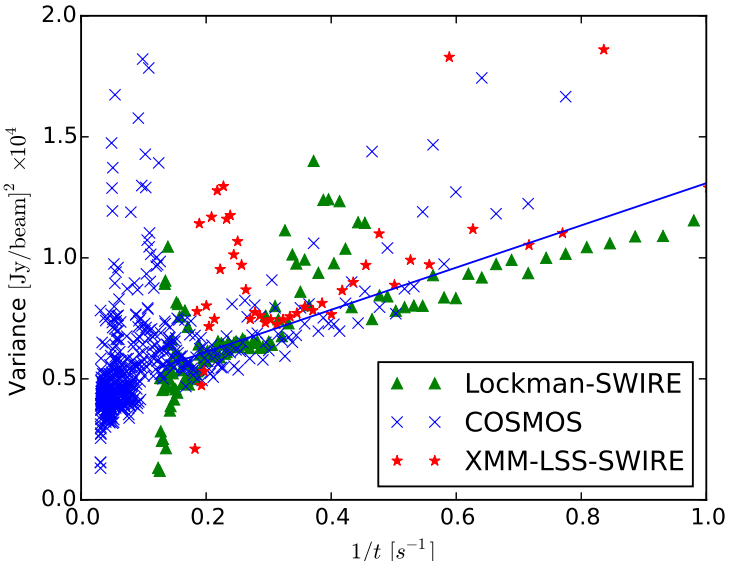

Figure 3.11: A linear fit of the variance of pixels against the inverse of the exposure time for 250μm maps. In equation 3.6 the intercept is the square of the confusion noise and the gradient the square of the instrumental noise.

drawn from a distribution representing uncorrelated instrumental noise. The error in the map is therefore the sum in quadrature of the errors of these values, namely

$$\sigma_d^2 = \sigma_{conf,i}^2 + \sigma_{inst,i}^2 \tag{3.6}$$

with σ_{inst}^2 the variance in the Gaussian the instrumental noise is drawn from at pixel i and $\sigma_{conf,i}^2$ the variance of the underlying flux in the map at pixel i. In this case, the confusion noise is treated and interpreted as a global constant that does not vary with i, representing the intrinsic underlying distribution of flux density and therefore the source counts of far-infrared galaxies. Note: in, for example, a field centred on a galaxy cluster with many bright galaxies would be expected to have a much larger confusion noise. Therefore cluster fields are not used in this calculation of the confusion noise.

The instrumental noise does vary on a pixel by pixel basis; the more times a point in the sky represented by a pixel is visited by the telescope, the more scans are taken and therefore the average calculated flux will be closer to the truth. The variance of the instrumental noise at pixel i is inversely proportional to exposure time t in the *Herschel*-SPIRE maps. This proportionality follows from the linear relationship of the bolometer response with the signal (Swinyard et al., 2010).

The instrumental noise and the variance in the map can be rewritten as

$$\sigma_d^2 = \sigma_{conf}^2 + \sigma_{inst}^2/t_i \tag{3.7}$$

This means the variance in the map is a linear sum, a function of $1/t_i$ with σ^2_{inst} as the gradient and σ^2_{conf} as the y-intercept, which is intuitive as the variance in the map should only be from source variance when the exposure time tends to infinity.

Nguyen et al. (2010) used the Lockman-SWIRE, GOODS-N and Lockman-North SDP data to calculate the confusion noise, the calculation is repeated here with Lockman-SWIRE and add the deep COSMOS and shallow XMM-LSS field. Lockman-North is contained within the footprint of the Lockman-SWIRE field so the data is not included here to ensure the same area of the sky is not used twice. XMM-LSS contains nearby galaxies that resolve as extended objects; these sources are not masked as they form part of the flux in the map and therefore part of the confusion noise in the map, so to remove them would be to report a lower confusion noise. Each pixel is binned by exposure time and the variance of that bin taken. These measures of the variance are then plotted against $1/t$ and the linear fit of equation 3.7 made. The calculation is run on the three maps together (but with each field's pixels binned separately) to ensure a wide range of exposure times.

Table 3.3 gives the updated results for the confusion and instrumental noises and lists the early Nguyen et al. (2010) and Rigby et al. (2011) results from HerMES and H-ATLAS respectively (H-ATLAS instrumental noises are not quoted as they're not given in mJy/beam/s$^{-0.5}$). The H-ATLAS confusion noise is calculated as $\sqrt{\sigma^2_{\rm map} - \langle\sigma^2_{\rm inst}\rangle}$ where $\sqrt{\sigma^2_{\rm map}}$ the variance of the map and $\langle\sigma^2_{\rm inst}\rangle$ the expectation variance of the instrumental noise. Despite the difference in calculation, the published results have good agreement. The HerMES values are all within $1-\sigma$ of each other (with the exception of the 350μm confusion noise within 2σ). However the updated 250μm and 350μm results are in contention with the H-ATLAS results, this could be a result of the different calculation methods. Even with the improvements made in the map making process from the science demonstration phase to the second data release the confusion noise and measured instrumental noise are not expected to change.

3.5 Assessing Completeness and Accuracy with Full Simulations

The DESPHOT pipeline could be modified to be more accommodating of the difficulties associated with grids of bright sources, however with too many modifications and exceptions the calculated accuracies would not reflect the actual pipeline. Using full simulations,

band	confusion noise (mJy/beam)			instrumental noise (mJy/beam/$s^{0.5}$)	
	this work	Nguyen '10	Rigby '11	this work	Nguyen '10
250	6.6 ± 0.2	5.8 ± 0.3	5.3 ± 0.4	9.3 ± 0.4	8.5 ± 0.4
350	7.2 ± 0.2	6.3 ± 0.4	6.4 ± 0.4	9.3 ± 0.6	9.4 ± 0.5
500	6.8 ± 0.1	6.8 ± 0.4	6.7 ± 0.5	11.0 ± 0.2	13.3 ± 0.7

Table 3.3: Confusion and instrumental noise calculations calculated on COSMOS, Lockman-SWIRE and XMM-LSS-SWIRE compared to the values calculated in Science Demonstration Phase in Nguyen et al. (2010).

where the flux of every source in the pipeline is known and the fluxes reflect the number counts of the real data, removes the need for pipeline modifications. The work outlined below includes methods and results modified and developed by other collaborators for the Wang et al. (2014) paper. The simulated maps were created and source extraction performed using existing pipelines by this author. The catalogue was matched using a Bayesian framework by a collaborator. The comparison between source injection and full simulations has been produced for this thesis.

3.5.1 Creating Full Simulations

Instead of a grid of injected sources (which, as shown in section 3.3 can break the DESPHOT pipeline), a set of realistic end-to-end simulations were created and used instead. This has the benefit of not biasing the maps with excess flux and can contain realistic clustering and therefore confusion noise.

The simulations are created from the Béthermin et al. (2011) models. These models use two populations of SED templates, a cold, dusty set and a starburst and those representing starburst galaxies. The starburst templates exhibit evolution with luminosity, the brighter galaxies having a warmer dust component. These SEDs from Lagache et al. (2004) are used to fit a parametrised luminosity function to the *Herschel* number counts in Glenn et al. (2010), H-ATLAS number counts in Clements et al. (2010) and a number of other far-infrared number counts from other instruments and luminosity functions calculated in the mid-infrared. The model also corrects the number counts for gravitational lensing.

The simulated images constructed as follows:

- A power spectra is created from the one and two-halo power spectra to create a proxy for a density map.

- The power-spectra is transformed to real-space "density map" on a grid of pixels 2 by 2 arcsecs in area and is normalised to be between 0 and 1.
- The sources are divided into batches of 1000, and a random number between 0 and 1 drawn.
- The sources are then randomly assigned pixels with a "density" greater than the random number. This will lead to an excess of sources and therefore flux within these high density regions.
- The flux of the sources assigned to a particular pixel is then summed.
- This "hitmap" of fluxes convolved with a Gaussian beam of FWHM 18.15, 25.15 or 36.3 arcsec for the 250μm, 350μm or 500μm simulation respectively.

The resultant image is a *sky* and is representative of the truth. The sources are assigned to 2 arcsec square pixels and convolved rather than each source's beam being interpolated to sub-arcsecond accuracy to speed up the creation of the maps. Therefore there will be many sources assigned to the same pixel and thus indistinguishable. However only 2% of the sources would be above 10mJy, the majority of other sources would form the unresolvable background of sources and contribute to he confusion noise. This sky is then transformed into a map by using the simulation software outlined in section 2.2.3. Each map is then run through the SUSSEXtractor and STARFINDER/DESPHOT software and subject to the same signal-to-noise cuts as the real catalogues.

3.5.2 Matching the Truth and Output Catalogues

Matching the truth and output catalogues is difficult when many true sources can contribute to an output flux, with differences in position. The algorithm used attempts to reflect that difficulty by allowing the matching of more than one source to the output catalogue by going beyond using a simple matching radius. Thus this method follows the method of Chapin et al. (2011).

Each possible pairing between input and output source flux is given a likelihood ratio LR a likelihood of the sources being associated dependent on the flux different $\Delta S = S_{in} - S_{out}$ and separation r. This is expressed as

$$\mathrm{LR}(\Delta S, r) = \frac{q(\Delta S) f(r)}{\rho(\Delta S) 2\pi r} \tag{3.8}$$

where $2\pi r$ represents the number density of sources found in area $r\,dr$ and $f(r)$ the probability distribution function between the input and output catalogues as a function of

offset i.e. the excess probability of finding a source at radius r above a random probability. Analogous to these positional probability measures are $\rho(\Delta S)$, the PDF of random matches as a function flux difference and $q(\Delta S)$ the PDF of true matches. Assuming a Gaussian beam, $f(r)$ is a Rayleigh profile

$$f(r) = \frac{r}{\sigma_r^2} \exp(-r^2/2\sigma_r^2) \tag{3.9}$$

with σ_r determined from fitting the residual of matching the histogram of positional offsets as a function of offset between the input and output catalogue and the linear scaled counts at $2\pi r$. Many output sources will be a sum in flux of multiple sources (Chapin et al. (2011) finds BLAST sources are often a blend of three objects or more) and so there will be an excess of truth source counts near the observed source. To find $\rho(\Delta S)$, the output list of fluxes is randomised and the number of matches at ΔS recorded. $q(\Delta S)$ first find the number of matches at ΔS between the input and output catalogues within an optimised search radius (i.e. the radius at which the number of true matches drops to near-zero and as such all matches at this radius are found. Then the lists are randomised again, the counts made and the subtraction between the total and random matches as a function of ΔS given to find $q(\Delta S)$.

The function 3.8 allows a calculation of likelihood ratio of the association of the sources between every source in the input and output catalogue. A randomised set of likelihood ratios calculated from a input and randomised output catalogue gives an indication of the spurious number of matches. This also gives an indication of the false identification rate as a function of LR ratio and can provide a sensible cut-off for the matches used in the matching metrics. The minimum likelihood ratio is defined at which 10% of matches are spurious at that likelihood ratio.

From this analysis, rather than a series of source injection grids rerun many times, a representative simulation can be run once and a careful matching performed between input and output catalogues acknowledging the extensive source confusion.

3.5.3 Comparison of Injection and Simulation Methods

Figures 3.12 and 3.13 show the completeness curves for COSMOS and Lockman-SWIRE for SUSSEXtractor and STARFINDER and comparing the results from the source injection and full simulations. There is a better consistency between the injection and simulation STARFINDER mean results in COSMOS than the SUSSEXtractor results. At brighter fluxes, whilst the mean completeness calculated with the injection and simulation

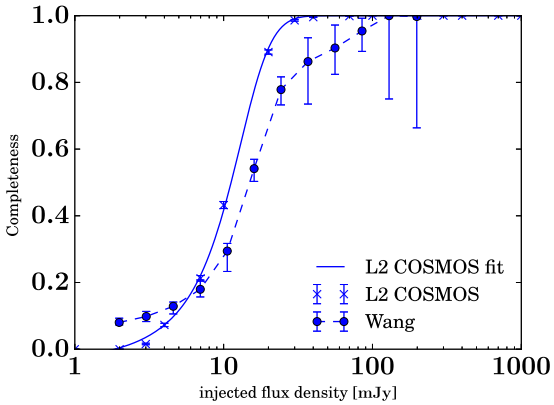

(a) SUSSEXtractor 250μm

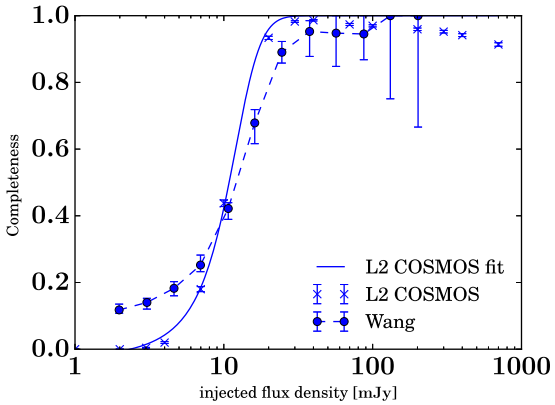

(b) STARFINDER 250μm

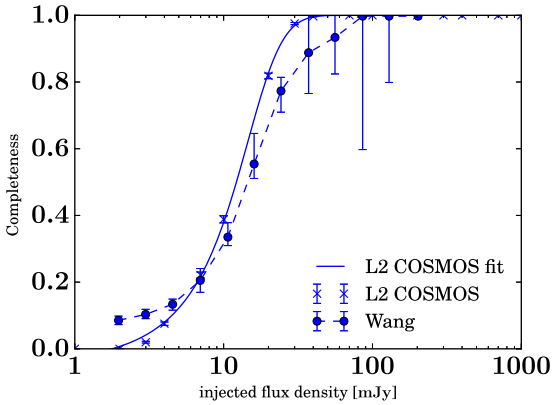

(c) SUSSEXtractor 350μm

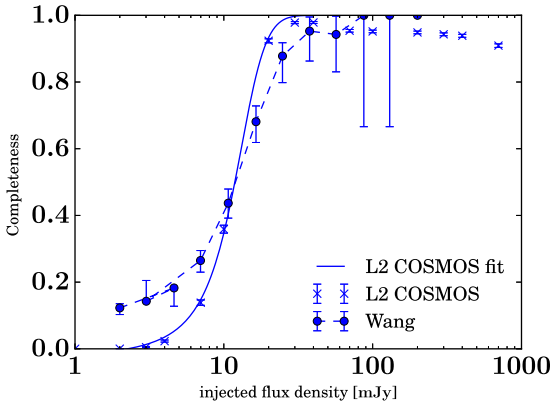

(d) STARFINDER 350μm

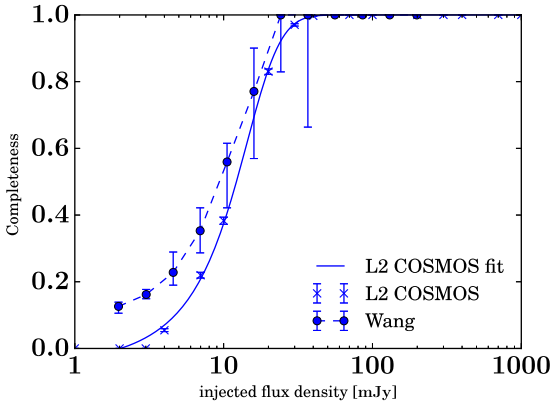

(e) SUSSEXtractor 500μm

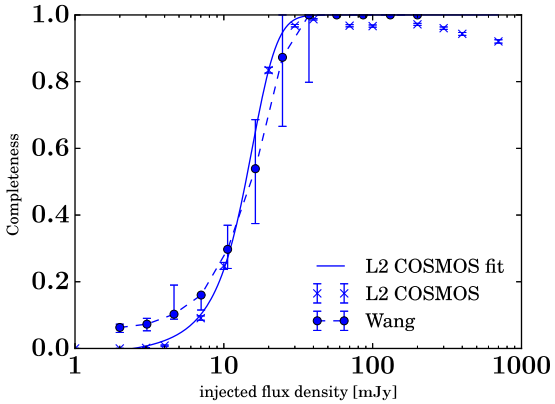

(f) STARFINDER 500μm

Figure 3.12: Comparison of the source injection and full simulation techniques In COSMOS by completeness, broken down by wavelength and extraction algorithm. The different assessment techniques result in a divergence of completeness at low flux.

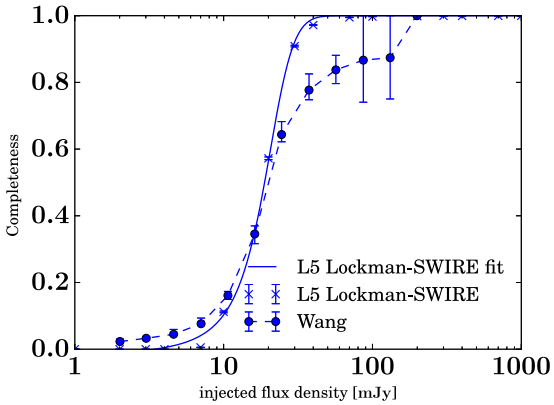

(a) SUSSEXtractor 250μm

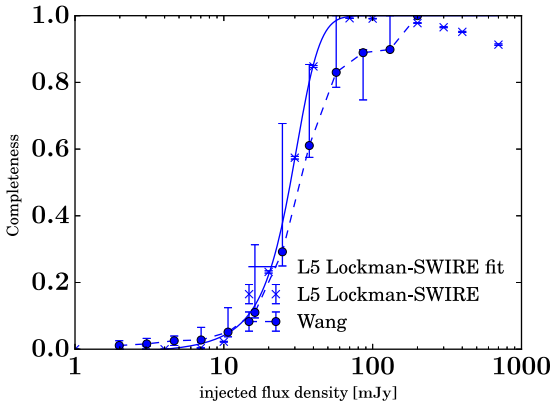

(b) STARFINDER 250μm

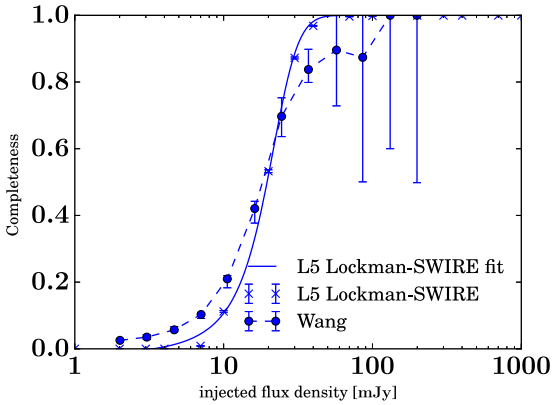

(c) SUSSEXtractor 350μm

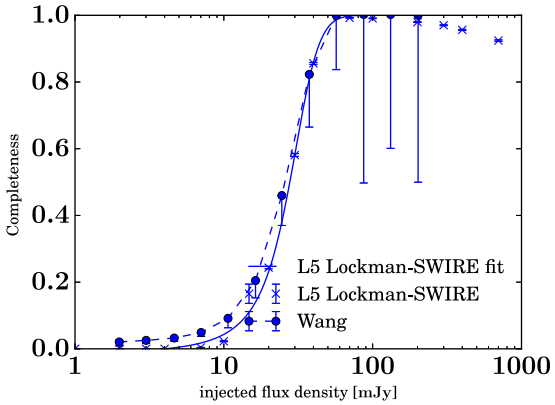

(d) STARFINDER 350μm

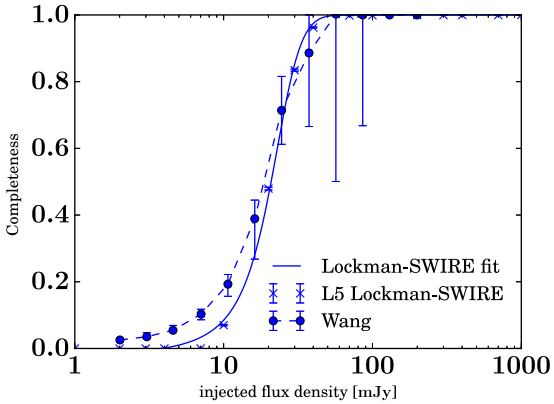

(e) SUSSEXtractor 500μm

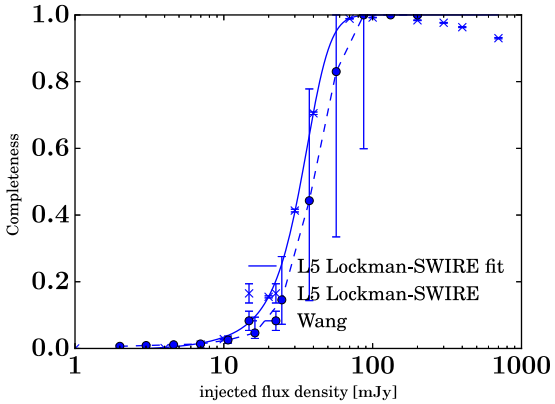

(f) STARFINDER 500μm

Figure 3.13: Comparison of the source injection and full simulation techniques in Lockman-SWIRE by completeness, broken down by wavelength and extraction algorithm. The different assessment techniques result in a divergence of completeness at low flux.

methods appear to differ greatly, the greater uncertainty in the simulation results mean the completenesses could be consistent. These wider error bars are due to the realistic number counts of the truth catalogues are there are not many sources at bright fluxes to calculate the completeness with in a realistic simulation of the data. Thus these two curves agree at bright fluxes, with the injection results arguably more reliable.

The turnover in completeness observed with the STARFINDER source injection maps is not seen in the simulation results. This implies that the drop in completeness at high fluxes with STARFINDER reported in this chapter is a function of the unnaturally bright injected sources in the map and not STARFINDER failing to find any bright sources. Thus STARFINDER does struggle when the background does not fall to a dark sky and the algorithm's ability to perform well is indeed disrupted.

For Lockman-SWIRE there is better agreement due to the shallow nature of the field. Although again the flux at which SUSSEXtractor finds 90% completeness is disputed at 250μm, with Wang et al. (2014) reporting a flux of 100mJy and this work 35mJy. The other points are within 2σ of each other at brighter fluxes. As Lockman-SWIRE is a shallower field, the source injection grid used is spaced at a ninth of the density of the deep fields. Even so, the turnover in completeness is still present.

In both fields there is a discrepancy in the completeness at fainter fluxes which is illustrated in figure 3.14, showing the difference between the input and output fluxes as a fraction of the input flux for COSMOS (the results for Lockman-SWIRE are much the same given the way the data is presented and therefore are not shown). The full simulation method reports extreme over predictions of flux by the algorithms at low flux, whereas this source injection does not show a deviation nearly as bad. This is related to different approaches to source matching. With this particular implementation of source injection, sources are matched if the flux difference is between 50-200%. This gives a hard limit on the difference in flux which is more readily visible at the faint end in previous figures. Wang et al. (2014) however uses a likelihood ratio calculation without hard limits. Also, more than one source can be matched to another. Thus faint sources may be "detected" by the two algorithms in the full simulation case but the flux has been boosted artificially by source confusion.

These two methods are finding two subtly different completeness and accuracy estimations for the images. The source injection method is first assuming a one-to-one ratio with between input and output flux. Therefore the completeness function is describing the probability that a detected source is close in flux value to the true flux, ignoring that the

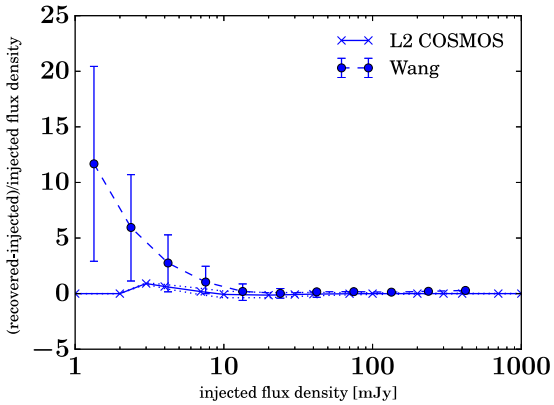

(a) SUSSEXtractor 250μm

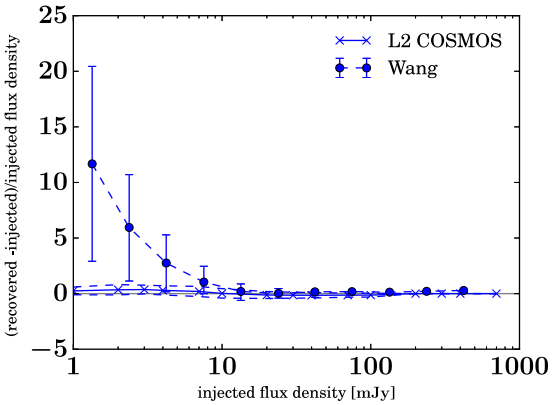

(b) STARFINDER 250μm

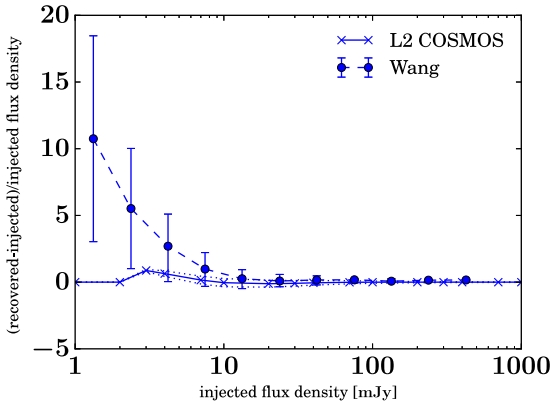

(c) SUSSEXtractor 350μm

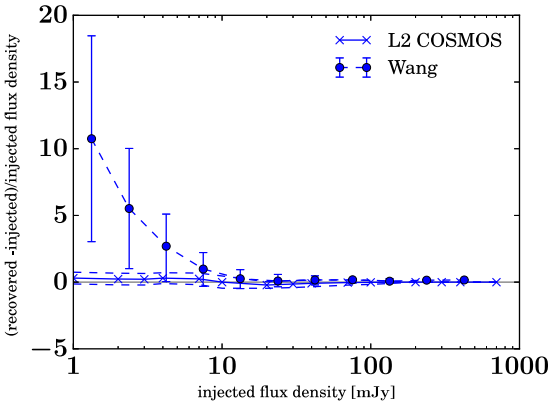

(d) STARFINDER 350μm

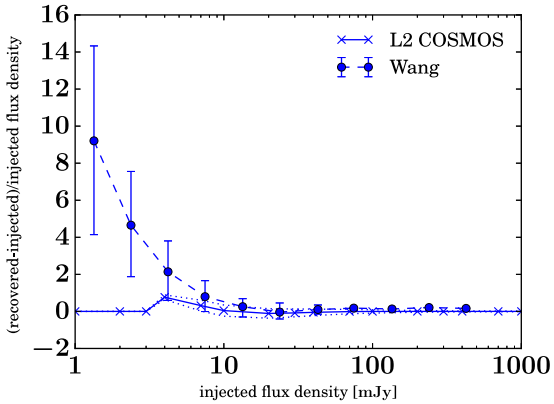

(e) SUSSEXtractor 500μm

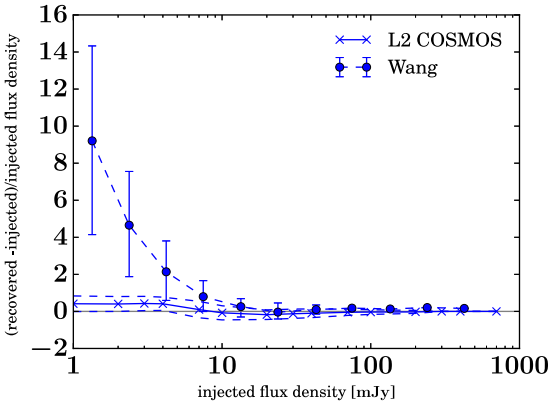

(f) STARFINDER 500μm

Figure 3.14: Comparison of SUSSEXtractor and STARFINDER flux accuracy against Wang et al. (2014) In COSMOS. The matching algorithm in this chapter ensures a stronger flux accuracy, the trade off is a completeness.

flux of the detected source may be boosted due to source blending. The matching used for the full simulations however assumes multiple matches between sources. The reported completeness then is, then, for a given flux, the probability that the flux source will be detected in some fashion whether it is part of a brighter set of blended sources or not. This is what is boosting the completeness and the ratio between input and output flux at low flux.

The suitability of the completeness functions will depend on the use case. If trying to attribute flux in catalogues to sources, the multiple matching technique may be best as this better reflects the all the sources detected in some fashion. If, for example, attempting to correct a measurement of the number counts for incompleteness, the method used for source injection would be the most appropriate. This is because the majority of faint sources have not been detected individually, and therefore this correction would underestimate the number of faint sources at these lower fluxes.

3.6 Investigation of Anomalous *Herschel*-SPIRE Data

All data including fields not catalogued for this thesis were uploaded for public release in 2013. However in early 2015 discrepancies in two catalogues were identified, specifically the noise values calculated for sources in the Böotes and Abell-2390. This section identifies these anomalies, finds their cause and describes the steps taken to rectify the issues. The available catalogues on HeDaM are the updated versions.

3.6.1 Böotes

The 500μm catalogue for "xid250" (DESPHOT photometry calculated with 250μm priors across all three bands) in the Böotes field was noted to have extremely high confusion noise. In other fields, confusion noises were calculated per field and tacked close to the values in Nguyen et al. (2010), in this case 6.8 ± 0.4mJy/beam at 500μm. The value in this field however was found to be 30mJy per source. This, for contrast, is much higher than the 11mJy found in the shallow field HerS, which used a modification of the DESPHOT algorithm to calculate photometry (Viero et al. (2014)).

Upon investigation, the residual map was found to contain a number of extremely negative pixels (figure 3.15) from bright clustered sources. These sources were detected by STARFINDER when it was run on the 350μm and 500μm maps individually and these priors fed into DESPHOT for the single band catalogues. However the prior source positions calculated from the 250μm map appear to be insufficient in this case, with many

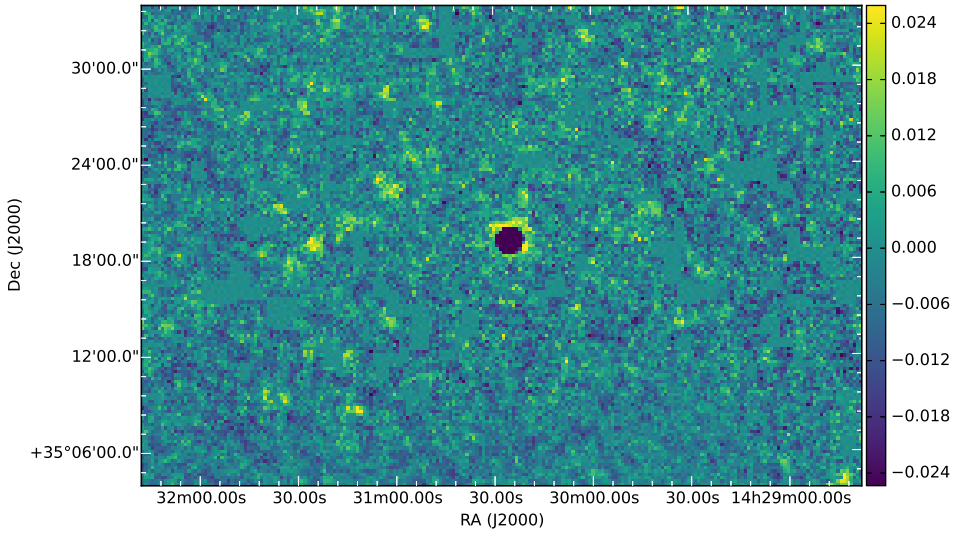

Figure 3.15: The residual map produced by DESPHOT in Böotes in the 500μm band using 250μm priors. The dark central region shows where DESPHOT has overestimated the flux for a number of sources in a bright cluster of sources, causing an extremely negative bowl. The uniform patches of flux are regions with no sources and as such are not taken into account when calculating the confusion noise.

sources unaccounted for. Thus the sources that were detected were over fitted, resulting in an extremely negative set of pixels in the residual map. As source fluxes have not been removed from the residual map, these negative "bright" pixels are skewing the measure of the variance and therefore the confusion noise up.

One solution would be to remove these pixels from the calculation of the confusion noise. This would not be inconsistent with the definition of confusion noise - the measure of the error in flux value when a source is positioned on a background of confused sources. These bright clustered sources represent the tail-end of the flux distribution of sources and so the probability that a randomly positioned source will be positioned amongst these sources is small yet a possibility. In an ideal situation it is right that these sources should be taken into account when calculating the confusion noise. However the overestimation of the flux is extremely unrealistic, a failing of the source extraction algorithm and not related to the population of sources. Therefore, if these pixels are excluded from the variance calculation the measure will be much closer to the true value.

The solution implemented was to "clip" pixels above a certain value. Clipping is considered a robust (yet arguably arbitrary) way of measuring the statistics of data that is Gaussian-like yet skewed, possibly due to contributions from two different populations (background sources and pixels associated with this clustered group of sources). A cut-off

value is applied to the data, discarding in this case pixels above and below a certain value. We clip pixels above and below 20-times the Nguyen confusion noise values, centring the value at the median pixel value. After exclusion this brings the confusion noise measurement down to 6.49mJy/beam which is much more reasonable, consistent with the 500μm Nguyen et al. (2010) result quoted at 6.8 ± 0.4mJy/beam.

3.6.2 Abell-2390

Another catalogue with an atypically high confusion noise value was Abell-2390's 250μm and 350μm SUSSEXtractor catalogue. Abell-2390 is a cluster in the constellation of Pegasus at $z = 0.228$ (Struble & Rood, 1999) that has been shown to exhibit strong gravitational lensing in the optical, will many gravitational arcs created from galaxies between $z = 0.4 - 1.27$ (Bezecourt & Soucail, 1997). Studying these clusters in the far infrared will give clues to the dependence of star formation with environment and very distant, star forming lensed objects could be found in these images. In SUSSEXtractor, the confusion noise calculation uses the matched-filtered image and error map to calculate the variance in the pixels below the median value are found and used as a measure of the total variance in the map. Then the median value of the error map (representing the instrumental noise) is subtracted off in quadrature to find the confusion noise. It is found that the total variance calculation is extremely high, thus there must be an issue in the matched filter maps. To see whether this high total noise was real, a histogram of values in the 250μm, 350μm and 500μm filtered maps and image maps were made, contrasting with two other cluster fields with lower confusion noise in figure 3.16, normalised to the area and width of flux bin. The "total raw noise" is given in the match-filtered image case.

As is shown, the distribution of pixels is much broader in Abell-2390. The median values are also shown as vertical lines and again they're not too dissimilar, also showing that the median is a sensible estimate of an average pixel flux in the matched-filtered beam. Figure 3.17 show the images of the three fields all normalised to the same grey-scale. As is immediately apparent, the field's background fluctuates more than the others due to cirrus contamination. This means that, when placing a source of a given flux in this field, the probability of landing on a bright sources is much higher and therefore remeasuring your flux is more likely to give an incorrect value. Therefore, a higher confusion noise in this field is justified and we can argue no adjustment needs to be made.

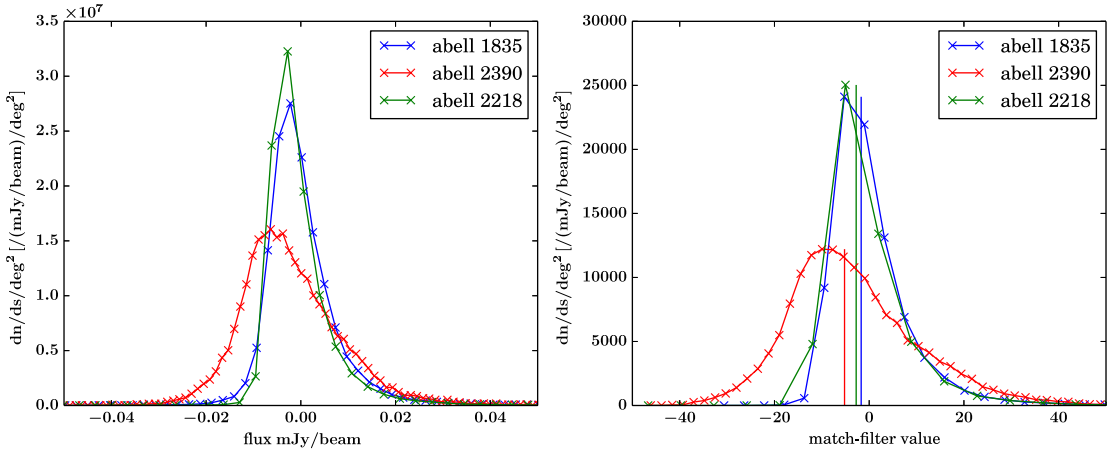

(a) Histogram of pixels fluxes from maps and matched-filtered maps in 250μm

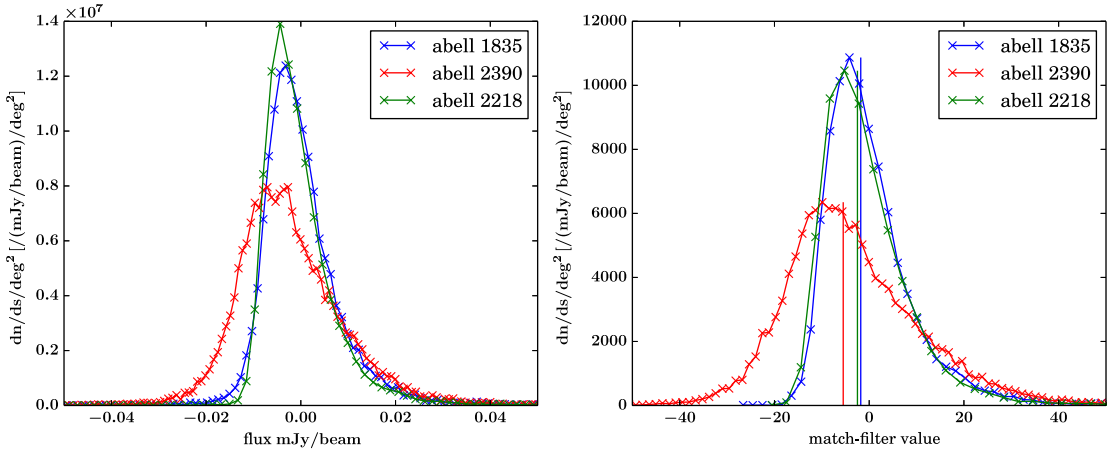

(b) Histogram of pixels fluxes from maps and matched-filtered maps in 350μm

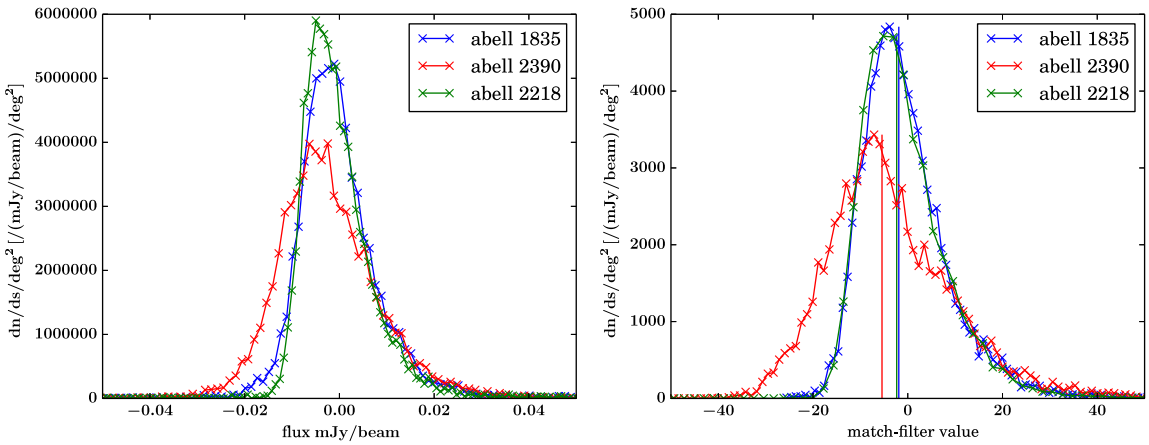

(c) Histogram of pixels fluxes from maps and matched-filtered maps in 500μm

Figure 3.16: Comparision of the pixel fluxes in the maps and match-filtered maps across the SPIRE bands and three cluster fields. The vertical line is the median flux value as calculated in SUSSEXtractor. Abell-2390 has a larger variance in the 250μm and 350μm bands.

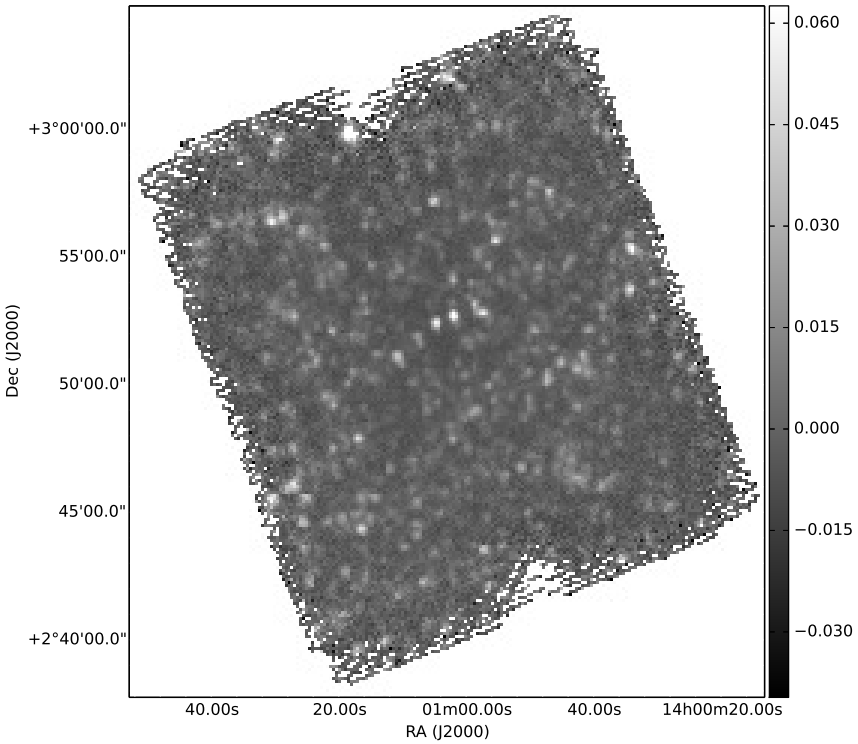

(a) Abell 1835 field at 250μm

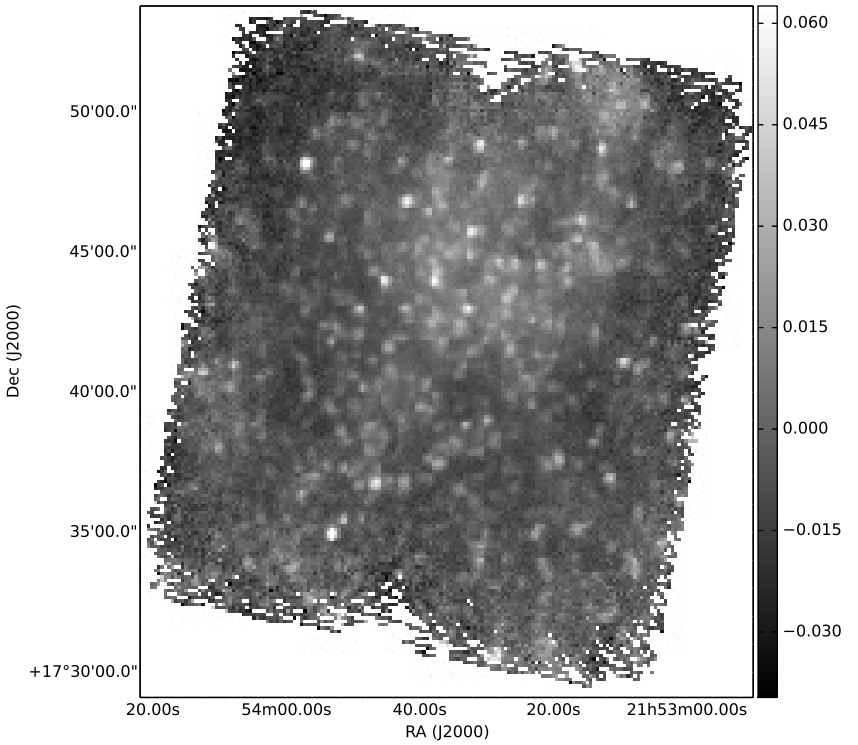

(b) Abell 2390 field at 250μm

Figure 3.17: Comparision of the 250μm maps of two cluster fields. Abell 2390 is clearly less uniform then the other map due to cirrus contamination.

3.7 Conclusions

As an extension of the work conducted in Wang et al. (2014), a full exploration of the effectiveness of the SUSSEXtractor and STARFINDER/DESPHOT algorithms was undertaken. The wide fields of Lockman-SWIRE and XMM-LSS-SWIRE and smaller fields COSMOS and Lockman-North were injected with a grid of sources at a fixed flux from 1 to 4000mJy. The source extraction software was rerun across the maps and the output catalogues matched with the input. The analysis found that SUSSEXtractor was more complete at brighter flux than STARFINDER/DESPHOT for shallower fields, reaching 90% completeness at lower fluxes. The opposite was true in the deeper field COSMOS, as STARFINDER is designed to work especially well in crowded fields.

The flux accuracy of SUSSEXtractor and DESPHOT are also compared, although tenuously as the extremely bright fluxes in the source injected maps cause DESPHOT great difficulty when segmenting the maps, often creating segments far too large. From what can be determined SUSSEXtractor is over predicting fluxes at faint fluxes as sources are confused and DESPHOT is under predicting at all levels due to issues discussed previously.

The completeness and accuracy results are compared to those given in Wang et al. (2014). The method of assessing the accuracy and completeness of the catalogues is different to the one detailed in this chapter, instead using a simulation of the fields in lieu of injecting sources into the map and matching multiple input sources to output sources. Broadly at the bright end the results from the different completeness and accuracy assessments agree which is encouraging, however due to the low number of sources with bright flux within the simulation the tail end of flux estimates and completeness functions are less determined.

For fainter fluxes, this chapter finds in comparison Wang et al. (2014) over reports the completeness. As seen by the extreme flux overestimation at faint fluxes within the paper by at times a factor of five, what constitutes a "match" between input and output catalogue in Wang et al. (2014) is less strict (in this chapter the reported flux must be within 50-200% of they input flux) and multiple sources can be matched to one output source. This explains the increased completeness at low fluxes, and so users of the data must proceed with caution. The analysis performed in this chapter does provide tighter constraints for positional accuracy and completeness than Wang et al. (2014) as there are more bright sources in the injected grid, however the overwhelming flux introduced by these sources broke the DESPHOT algorithm on some segments by creating abnormally large regions, meaning the flux accuracy could not be determined as accurately as one

would hope for DESPHOT.

The different methods of finding the completeness outline subtly different completeness curves. The results from the source injection method have been determined to be a better explanation of the completeness of catalogues on a source-by-source basis for example, correcting for the incompleteness of a catalogue at various flux levels. The completeness curve using multiple input sources could be used to correct the number counts for example if the link between input and output source was preserved. This would be an interesting extension to this method of matching and would ultimately suit the confused *Herschel*-SPIRE maps better.

The confusion noise and instrumental noise of the maps are recalculated for Lockman-SWIRE, XMM-LSS-SWIRE and COSMOS and compared to Nguyen et al. (2010). The values are all bar one reported value within 1 sigma of each other, with the exception 2-sigma away which is reasonable. The maps used in this analysis are updated from the original analysis and so some discrepancy is expected. The confusion noise is calculated as 6.6 ± 0.2 mJy/beam, 7.2 ± 0.2 mJy/beam and 6.8 ± 0.1 mJy/beam, with the instrumental noise as 9.3 ± 0.4 mJy/beam, 9.4 ± 0.5 mJy/beam and 13.3 ± 0.7 mJy/beam for the 250, 350 and 500μm bands respectively. The confusion noise is systematically higher than H-ATLAS results from Rigby et al. (2011), although the method of calculation is calculated on the map with sources subtracted rather than every pixel on the map and thus some difference is expected.

Finally, some discrepancies in the calculation of the confusion noise in individual catalogues are identified and explained. Within the Böotes field, using the STARFINDER catalogue created on the 250μm map to determine the photometry of sources within the 500μm band leaves many bright sources in the 500μm unaccounted for and causing DESPHOT to over fit fluxes, meaning the extremely negative pixels in the residual map are skewing the calculation of the confusion noise. Excluding these bright pixels reduces the confusion noise back to sensible levels. In the Abell-2390 field it was found that cirrus contamination is broadening the distribution of flux within pixels rather than creating a completely separate population of pixels at higher flux, and thus the confusion noise estimate is reliable within the 250μm and 350μm fields. The changes have been carried forward to the released data, available on `http://hedam.lam.fr/HerMES`.

3.8 Further Work

An interesting extension to the DESPHOT pipeline would be try modifying the second pass of the LASSO flux fitting routine. Currently, sources missed by STARFINDER are located in the residual map in the second pass and these sources are given a flux. LASSO will also switch off sources it deems unnecessary for the fit, which could lead to some of the sources detected by STARFINDER given zero flux. This is especially an issue when the prior catalogue has not been developed on the same map as the one the source extraction will be performed on. Weighting by whether the source was in in the original prior would be reasonable, given that the prior catalogue is detected with an algorithm designed for crowded fields and as such should be able to find the majority of the sources within the crowded field, naturally making sources found in the residual map unreliable. Weighting according to the signal to noise of the detected source appears reasonable however this would lead to biases towards high flux source unnecessarily, possibly attributing far too much flux to bright sources. Weighting towards sources with the best correlation between beam and shape of the source in the map seems more reasonable as perfect sources found in the residual map will be preferred over marginally detected sources in the prior catalogue. This will bias selection to high flux sources as brighter sources will generally have a better match to the beam profile as the noise in the map is relatively lower to the flux of the source, but does not strictly bias the selection by flux. Whilst the effect of weighting the sources will have an effect that is as of yet unconstrained, exploring these weighting possibilities and whether there is a significant improvement in the algorithm would be informative.

This improvement could be extended to include prior information on the flux of sources. As DESPHOT uses prior positions from catalogues and HerMES fields have ancillary data across many wavelengths, this is a feasible endeavour. The number counts for each band and the flux of sources at other wavelengths provide a strong constraint on the flux of sources within the *Herschel*-SPIRE maps. This could also be used to deblend fluxes in the map when a catalogue from a better resolved wavelength is used (e.g. the 24μm Spitzer catalogues), or ALMA sources.

This second improvement is currently being undertaken as part of the *Herschel* Extragalactic Legacy Project, HELP, and the first attempt to use simple prior on the number of sources as a function of flux will be published in Hurley et al. (submitted), and has been used to attribute *Herschel*-SPIRE flux to ALMA sources in Bussmann et al. (2015).

Chapter 4

Finding Sources Within HeLMS

The largest and shallowest of the HerMES fields, making up the bottom of the "tiered wedding cake" is HeLMS, the Herschel Large Mode Survey. HeLMS comprises of 270 sq. deg. of sky centred on the celestial equator and is another legacy field, constructed to cover in part the SDSS (Sloan Digital Sky Survey, Alam et al. (2015)) Stripe 82 field. Within the HeLMS region is a plethora of ancillary data across all wavelengths with more observations planned. Both the size and lack of deeper coverage this field pose specific challenges when constructing a catalogue of sources which will be discussed in this chapter, with the final catalogue compared to catalogues from other HerMES fields. The results will be compared to a similarly constructed catalogue of Herschel sources from the HerS field Viero et al. (2014), a 79 sq. deg. field of similar depth. The final HeLMS catalogue has been used in Pitchford & et al. (submitted) as part of a study of the link between the activity of active galactic nuclei and star formation for quasars identified in SDSS. The catalogue itself is available at `hedam.lam.fr/HerMES`.

4.1 HeLMS Observation and Map Generation

The Herschel Large-Mode Survey, or HeLMS, is the largest HerMES field by far. Designed to cover 270 sq.deg. (although covering 300 sq.deg. by pixel count), HeLMS is almost 13 times larger than the level 6 field XMM-LSS-SWIRE, (the largest field released by HerMES in the second data release) and almost three times larger than the area covered by the rest of the HerMES fields combined. The field itself however is shallow and is the only level 7 field in the HerMES "wedding cake" survey design, using the Herschel SPIRE fast-scan observation mode like other shallow level 6 fields but with only two overlapping scans. In contrast to area, the HeLMS observation time totals approximately 100 hours,

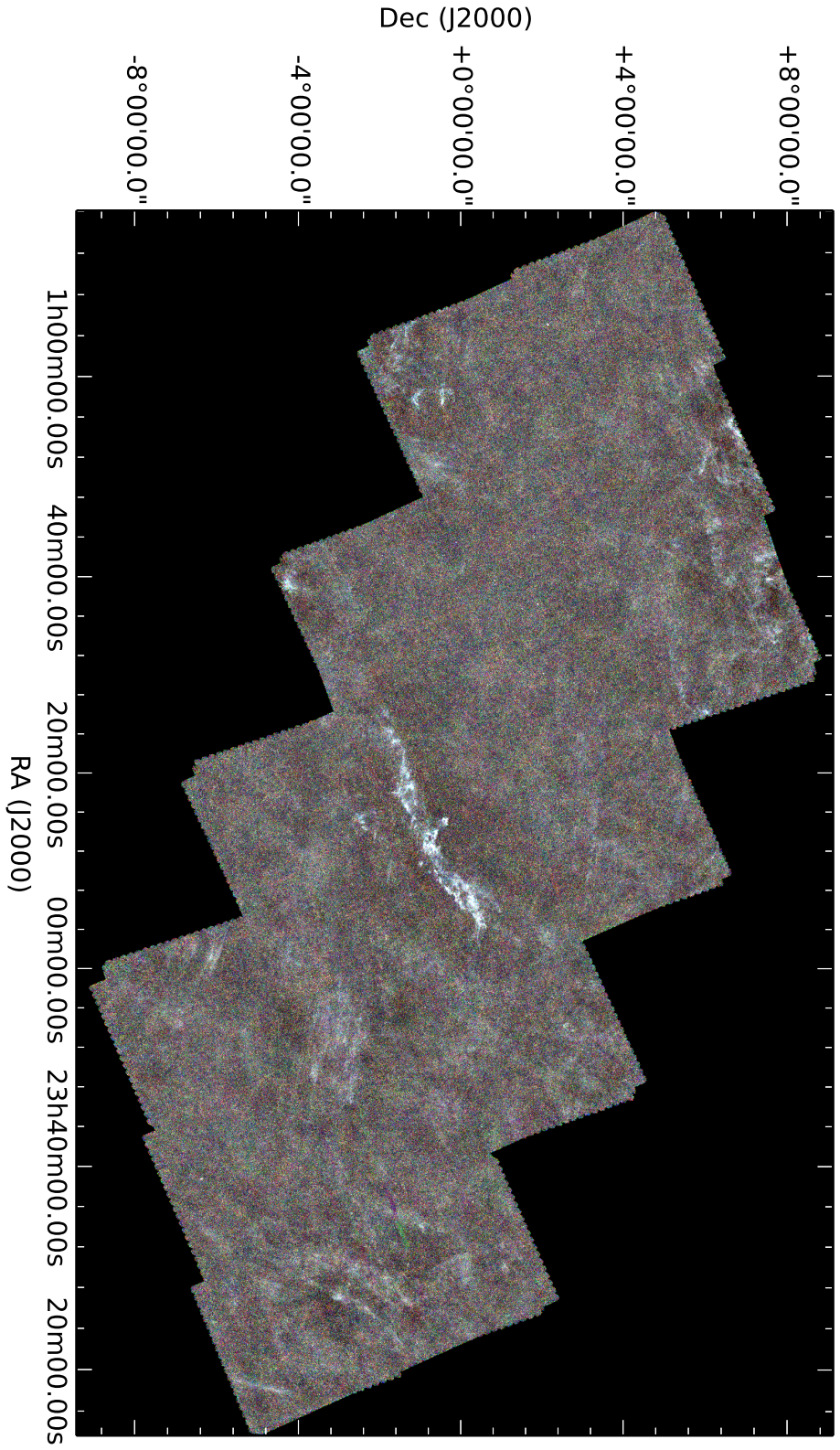

Figure 4.1: RGB representation of the HeLMS field, with 250μm, 350μm and 500μm represented by blue, green and red respectively. Immediately apparent is the size of the field in comparison to other HerMES fields, as is the unavoidable cirrus structure throughout the map.

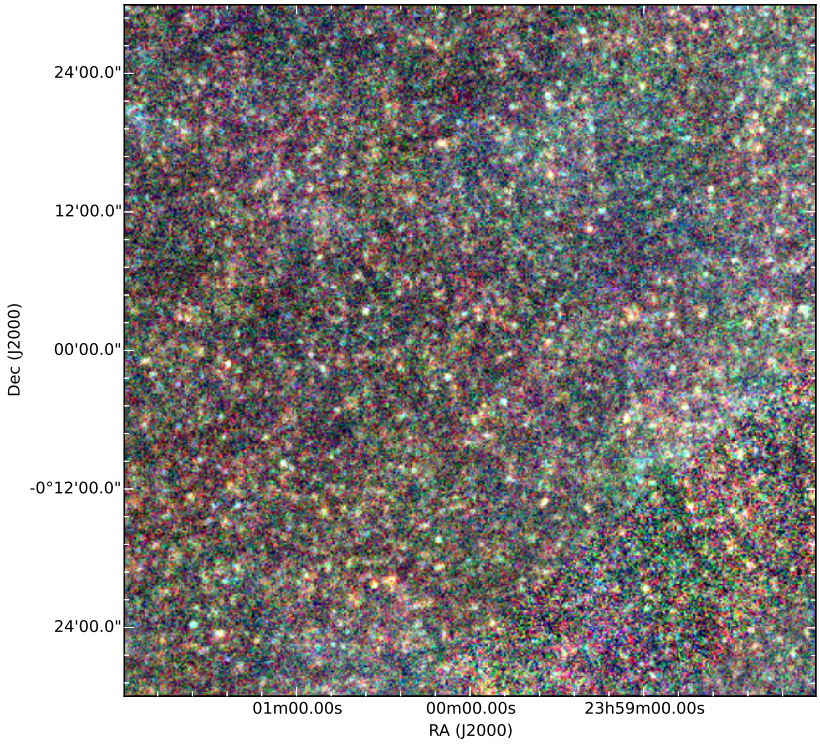

Figure 4.2: A 1 deg^2 cut out of the HeLMS field. Individual sources are visible in the three colour image, however the noise is much higher in this field than in other HerMES fields, posing particular challenges.

which is only twice that of XMM-LSS-SWIRE. There is no complementary PACS data for HeLMS, nor 24μm MIPS catalogues to be used in prior-based in source extraction.

However, there is a wealth of ancillary data: HeLMS was designed to in part cover the SDSS Stripe 82 field, with the HerS field designed to cover the rest. The SDSS telescope covers the $u'g'r'i'z'$ bands, from near-UV to near-infrared. Data release 12, the latest release (Alam et al., 2015) includes additions to photometric data for 500 million objects (stars as well as galaxies) and over 5 million spectra across all SDSS fields. Other survey coverage includes DES (the Dark Energy Survey (The Dark Energy Survey Collaboration, 2005) using the DECam instrument on the Blanco telescope to find supernova in the Stripe 82 region and so will have deeper coverage in the optical and near-infrared. There is further coverage by UKIDSS (UKIRT Infrared Deep Sky Survey, Lawrence et al. (2007)) in the near infrared with the LAS (large area survey) covering 212.5 sq. deg. and a portion Stripe 82. In the mid-infrared WISE (Wide-field Infrared Survey Explorer, Wright et al. (2010)) has full-sky coverage between 3.4 and 22μm and in the radio both the VLA (Very Large Array, e.g Hodge et al. (2011)) and ACT (Atacama Cosmology Telescope, Fowler et al. (2007)) have coverage in the field. Further surveys are being constructed or have recently been created including the VISTA-CFHT Stripe 82 survey (VICS 82, Geach & et al. (submitted)). This survey adds J and Ks band imaging from VISTA's VIRCAM to the i-band imaging of CFHT's (Canada-France-Hawaii Telescope) WIRCAM instrument from the CS82 (Moraes et al., 2014; Erben & et al., submitted) survey. Whilst primarily focussed on coverage for the Stripe 82 field, upcoming surveys like this add to the ever-growing ancillary data within the HeLMS region.

The shallow nature of HeLMS means a majority of the field has been covered by two orthogonal scans only, and a map that is closer to a H-ATLAS field in depth and area than HerMES. HerMES fields have been chosen to avoid contamination from cirrus and the tiling of the scans in the HeLMS field has achieved that to some extent; however, compared to other HerMES fields the amplitude of cirrus in HeLMS is far greater. The observations were processed through the standard Herschel-SPIRE pipeline in HIPE using the SANEPIC algorithm as opposed to the SMAP map-making pipeline.

4.2 First Catalogue Generation with SUSSEXtractor

The established HerMES-SPIRE catalogue pipeline includes blind-source catalogue generation using SUSSEXtractor for each band. Therefore as a first attempt these catalogues were generated using the same parameters as our the HerMES second data release (Wang

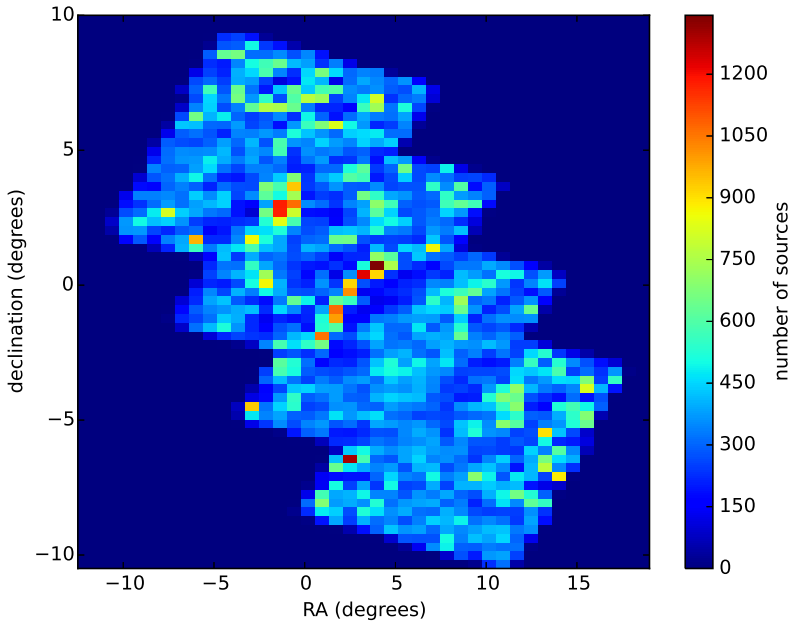

Figure 4.3: Positions of SUSSEXtractor sources in HeLMS as a density plot, resolved to a 0.5^2deg^2 grid. Density appears correlated with cirrus intensity.

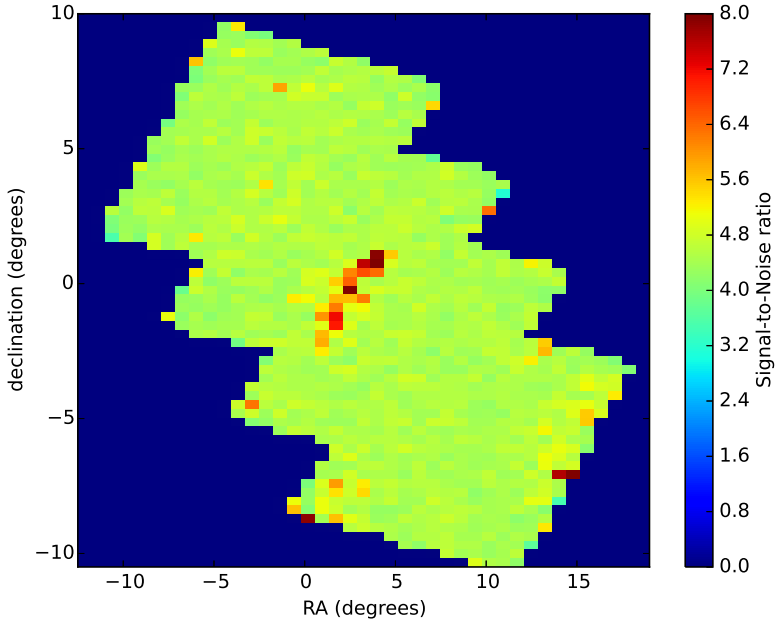

Figure 4.4: Median signal-to-noise ratio of SUSSEXtractor sources in HeLMS binned to 0.5^2deg^2 segments. The high value in the central region implies that the cirrus background is not being taken into account correctly when fitting sources.

et al., 2014) with version 8.3 of HIPE as described in chapter 2. This version of the catalogue was created using the now released version 0.2 maps with the catalogues internally released for the HerMES-ACT collaboration only. These maps are part of HerMES third data release found on HeDaM.

Figure 4.3 shows the density of sources found with SUSSEXtractor gridded to $0.5^2 \mathrm{deg}^2$. Immediately obvious is the correlation between the number of sources found and the intensity of cirrus shown in figure 4.5. Further, figure 4.4 demonstrates a similar correlation between the signal-to-noise ratio of sources and cirrus, that sources lying on strong cirrus regions have, on average, a higher signal-to-noise ratio. These correlations do not reflect the underlying distribution of sources and point to an issue with background estimation in SUSSEXtractor. If the background in the map has been underestimated, the flux assigned to a source will be overestimated as the fitting routine will be forced to fit the beam to a peak much higher then the true value.

The effect of this background underestimation is two-fold. More sources will be found as more pixels will be artificially boosted above the signal-to-noise threshold required for a source detection, thus more pixels will flagged as source candidates. Then as the flux of the source will be brighter due to the background these sources pass the signal to noise cut used to create the catalogue. If the background is significantly brighter and the background flux density fit too low, the fits will have a poor quality value (analogous to χ^2).

4.3 Galactic Cirrus

There is extensive foreground emission from galactic cirrus in HeLMS as can be seen in figure 4.1, far more intense than any other field in the HerMES survey. Cirrus contamination is an unfortunate disadvantage to using large survey fields and this section discusses the nature and subsequent removal of cirrus from the HeLMS images. The structure of cirrus is thought to be similar at all scales, a fractal. This means that cirrus emission has structure at all scales, unlike e.g. zodiacal light that is uniform and can be successfully filtered. If the galactic cirrus in this region was atypical, it may be possible to find a way to remove it, cleaning the maps. This section contains an investigation into the cirrus structure within the HeLMS map to determine whether the cirrus is indeed fractal in nature, even though the region has been selected to avoid extremely bright regions of galactic cirrus. Whilst the results are not used in this thesis to create, for example sim-

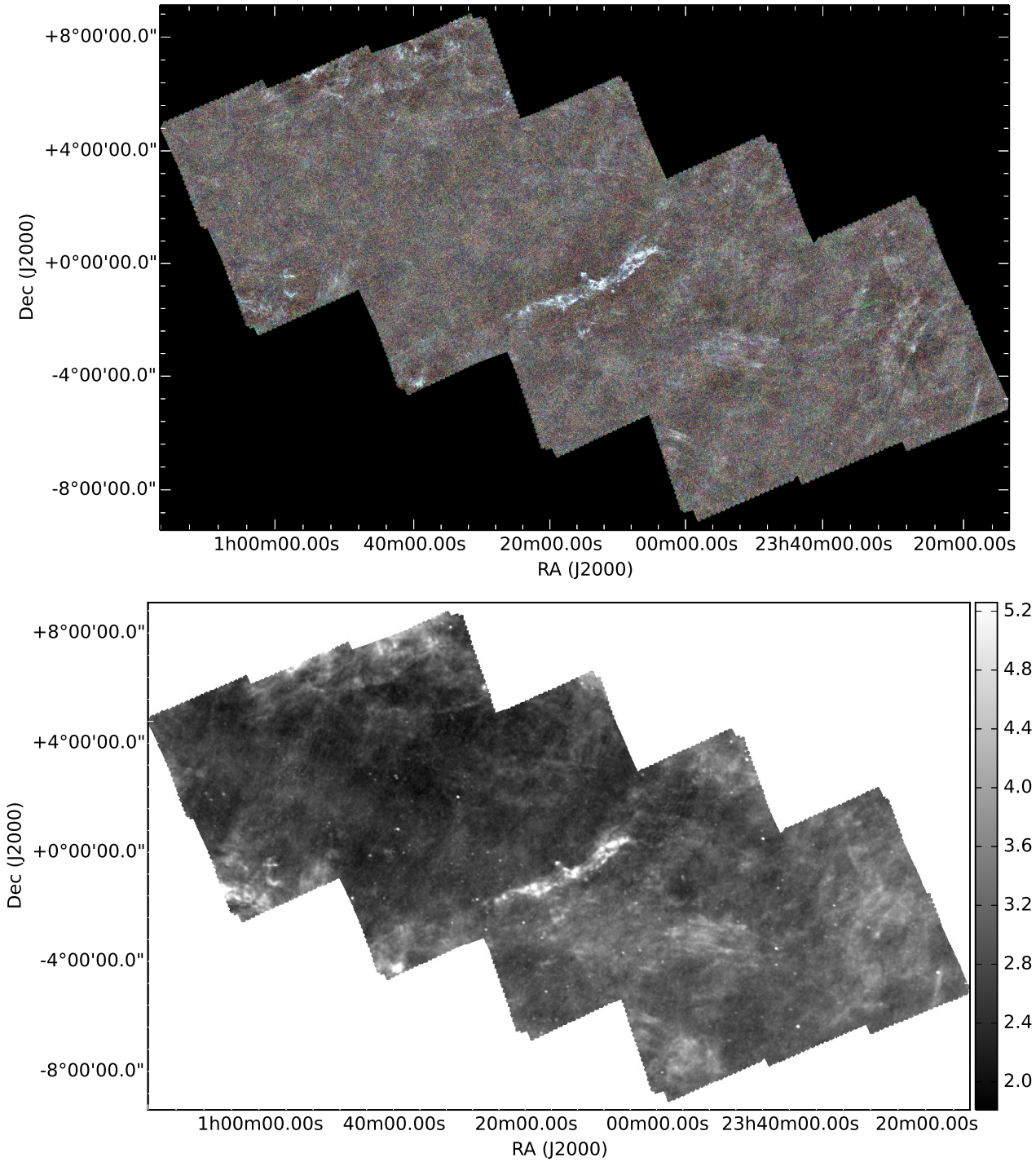

Figure 4.5: A three-colour *Herschel*-SPIRE image (top) against 100μm map (bottom) of the HeLMS field showing the diffuse cirrus structure. The 100μm maps are from IRIS dataset using IRAS images and are shown in MJy. Point-source-like emission is from galaxies or other galactic objects.

ulated cirrus images, it is hoped the results will inform future work into simulations of cirrus within the HerMES or other *Herschel*-SPIRE extragalactic fields.

4.3.1 The Nature of Galactic Cirrus

The long, wispy blue structures in the HeLMS map are far-infrared emission from galactic cirrus. Cirrus structures are structures within our own galaxy made of dust grains. As with dust in other galaxies, this dust has absorbed optical and UV light from stars within the Milky Way and is remitting in the far-infrared. The cirrus is much bluer in comparison to the extragalactic sources of dust emission in the background due to the foreground (i.e. low redshift) nature of the dust, and not because the dust in the Milky Way is at an abnormally high temperature.

The emission of foreground cirrus is best represented at 100μm. Figure 4.5 shows the full sky as mapped by IRAS at 100μm with the HeLMS region overlaid, demonstrating that with respect to the full sky, HeLMS can still be considered a low-cirrus region, with typical maximum surface brightness of cirrus in HeLMS at 5MJy, compared to other studies with a typical maximum double that (Bazell & Desert, 1988). Over the whole sky galactic cirrus is thought to be fractal, following a scale-free power spectra, and, analogously, a correlation between the area and perimeter of regions of bright flux.

4.3.2 Galactic Cirrus as a Fractal

The same cold gas and dust forming stars in other galaxies exists in our own galaxy too, forming stars in regions like the Orion nebula. The dust does not restrict itself to star-forming regions however. Instead it exists as a diffuse structure throughout the Milky Way (and in other galaxies); concentrated, like the stars, along the disk of the galaxy and is broadly less dense away from the disk (at high galactic latitudes). The gas and dust forms what is known as the interstellar medium (ISM) which can be divided into different regions given temperature, density and gas ionisation. The dust within the ISM causes difficulties when observing in the optical causing reddening or attenuation (Trumpler, 1930a) as the dust preferentially scatters light towards the blue end of the spectrum as the dust grains are the same size or smaller as the wavelength of blue light (Trumpler, 1930b).

In the most severe cases, the optical light is blocked entirely, as happens in star-forming regions. This dust causes difficulties at other wavelengths. As the dust absorbs

optical and ultraviolet light, the dust's temperature increases and then the grains emit blackbody radiation peaking in the infrared. This infrared emission is why we can find star formation regions using *Herschel* but conversely a physical process useful to extragalactic astronomers can become a hinderance within our own galaxy.

IRAS (Infrared Astronomical Satellite) observations by Low et al. (1984) found the dust has a filamentary (wispy) structure and coined the name "cirrus" due to the resemblance to cirrus clouds in our own atmosphere. Herschel observations (Miville-Deschênes et al., 2010; André et al., 2010; André, 2013) have shown clumps of star formation in these filamentary structures. Cirrus has temperatures from 15K to 35K, first measured from comparisons between the 60μm and 100μm emission with IRAS (Schlegel et al., 1998). There is also a strong correlation between HI column density and 100μm intensity (Boulanger et al., 1985). Infrared observations then have the opposite problem to optical observations: the cirrus emits infrared light in addition to extragalactic sources, boosting the flux of these distant galaxies. When observed by *Herschel* these galaxies appear bathed in emission and will have a higher observed flux, increasing the likelihood of detection or erroneous detection. With naïve source detection, the density of sources will increase in areas with strong cirrus emission. HerMES survey fields were constructed to avoid strong cirrus emission to avoid contamination, but it cannot be completely avoided. Large survey fields from e.g. H-ATLAS or the HerMES HeLMS field may not have emission from galactic star-forming regions but there is still a relatively strong component present.

Previous work using IRAS images have identified cirrus as having a fractal structure (Bazell & Desert, 1988). Fractals, by definition, are self-similar structures across many scales. Images like the Mandelbrot set (the set of complex numbers c that, under the iteration $z_{n+1} = z_n^2 + c$ with $z_0 = 0$ do not approach infinity) are publicly well-known algorithmically generated fractals. However, fractals are known to appear in nature. Rain clouds in our own atmosphere are known to exhibit fractal behaviour (seminal paper by Lovejoy (1982)) including cirrus clouds, as observed by the METEOSAT-7 satellite by Madhushani & Sonnadara (2012). In astronomy, molecular clouds and the interstellar medium in general have received particular attention (Stutzki et al., 1998; Sánchez et al., 2007). Understanding the nature of the cirrus in HeLMS may allow us to find an appropriate solution to the cirrus contamination in HeLMS that reduces the number of lost sources.

To assess whether the cirrus within the HeLMS field exhibits fractal behaviour, the methods of Lovejoy (1982) and Bazell & Desert (1988) are used and explained below. By

definition, the number of self-similar objects N within a fractal system varies as a function of scale r as

$$N(r) = (r/r_0)^D \tag{4.1}$$

where r/r_0 gives the magnification factor between the two scales and D the dimension of the fractal. The dimension is a measure of complexity in the fractal, giving information as to how the fractal fills the space. Regular 2-D polygons have a fractal dimension of 1, a simple line in two-dimensional space. In contrast, a curve with a dimension of 1.9 would be extremely complicated, filling the space. If considering the area $A \propto (r/r_0)^2$ of a shape varying with perimeter P, for example, this equation can be rearranged as

$$A^{1/2} = KP^{1/D} \tag{4.2}$$

where K is a scaling constant. In the case of circle, $D = 1$ and $K = 1/2\pi^{1/2}$ and a square $D = 1$ and $K = 1/4$. This equation can be further rearranged to give the linear relationship

$$\log P = \frac{D}{2} \log A - D \log K \tag{4.3}$$

.

To calculate the area and perimeter of the cirrus in HeLMS, the 100μm IRIS dust maps were used (Miville-Deschênes & Lagache, 2005). These maps are an improvement on the often used Schlegel et al. (1998) 100μm IRAS dust maps with better zodiacal light modelling, more accurate calibration and improved destriping of the images. The Bazell & Desert (1988) authors used their own zodiacal light subtraction model. The map of cirrus was created by mosaicing IRIS images within and surrounding the HeLMS region to create a rectangular image. HeLMS however is not rectangular, instead a tiling of observations positioned to avoid bright cirrus and so the NaNs surrounding the HeLMS SPIRE image needed to be transferred to the IRAS image. Each 100μm IRAS pixel is 4 by 4 arcmin as opposed to SPIRE's 250μm 6 by 6 arcseconds. An IRAS pixel is masked if over half of the SPIRE 250μm pixel centres within the IRAS 100μm pixel are masked, otherwise the pixel is kept. The IRAS image was not smoothed to 6 by 6 arcseconds as this would be both a very uncertain amount of smoothing to perform, and would affect both the area and perimeter of the cirrus shapes, smoothing out unresolved scales.

The image is thresholded by surface brightness - any pixel below a specified surface brightness is masked and any above or inclusive are set to one. This in effect is a defining a contour on the image. The areas of the image are then divided into separate regions - any two pixels above the threshold surface brightness that have a neighbouring side are

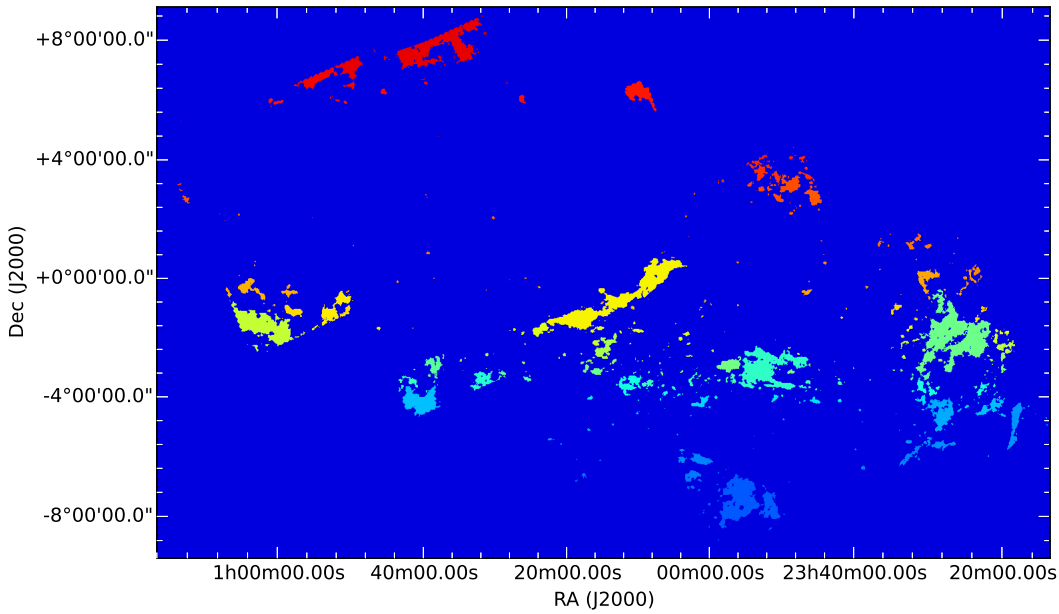

Figure 4.6: Example image showing how cirrus regions are defined. The 100μm map is thresholded at a particular surface brightness (3.5MJy/sr) and pixels with a flux above that level are identified. Neighbouring pixels that meet this threshold are grouped together. Regions on the edge of the map (incomplete) and smaller than thirteen pixels (point sources) are discarded.

considered part of the same region. Note, regions are not considered connected diagonally. Regions on the edge of the image are discarded as the image edge would be a false boundary. Also discarded are any regions with areas less than 13 pixels as these regions correspond to point sources, and are therefore highly unlikely to be from diffuse cirrus structures. Figure 4.6 shows all the regions as different colours generated at a flux of 3.5MJy/sr before any are discarded.

The area is calculated as the number of pixels covered by a region. The perimeter is the number of pixel lengths at the boundary between the region and masked pixels below the threshold. For example, a region 1 pixel in area would have a perimeter of 4 pixel lengths. It is important to note that measuring the perimeter in this manner is only exact for well-aligned, rectangular regions. A circular region or a region that crosses the image diagonally will have an overestimated perimeter as the pixelised boundary "steps" across the image.

Figure 4.7 shows the perimeter as a function of area for one flux threshold of 3.5MJy/sr as a typical example. The fit is an unweighted best χ^2 fit for D and K in equation 4.3, and errors are the sample standard deviations. The fit is very strong across many different

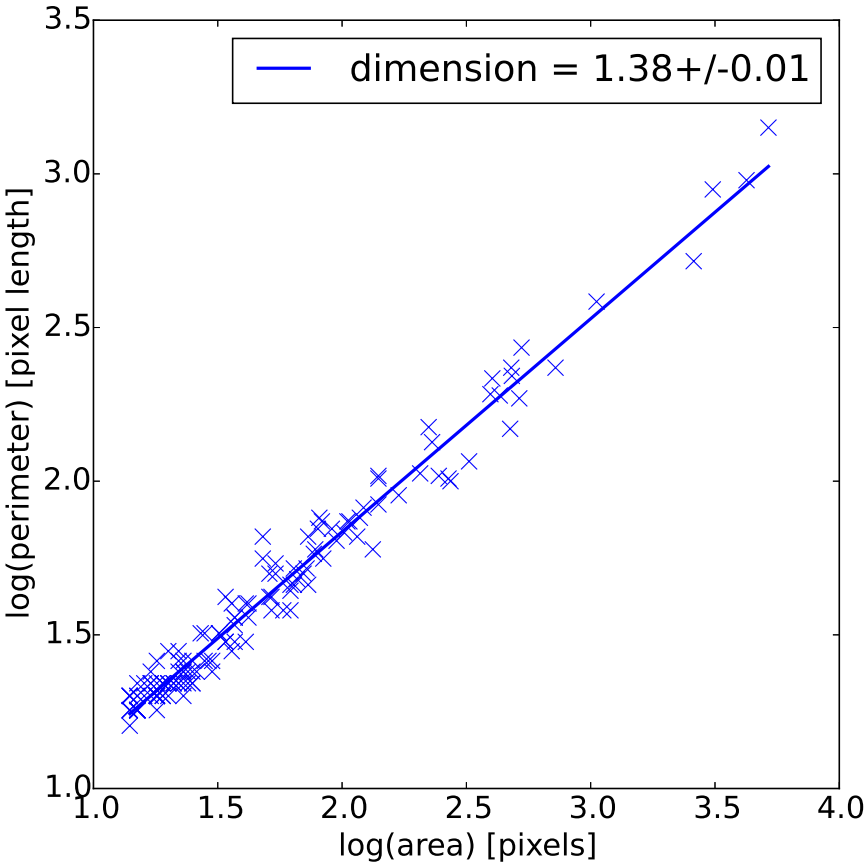

Figure 4.7: Example plot demonstrating the correlation between area and perimeter for the regions identified in figure 4.6. A straight line is fitted in log space and the gradient used to calculate the dimension of the regions.

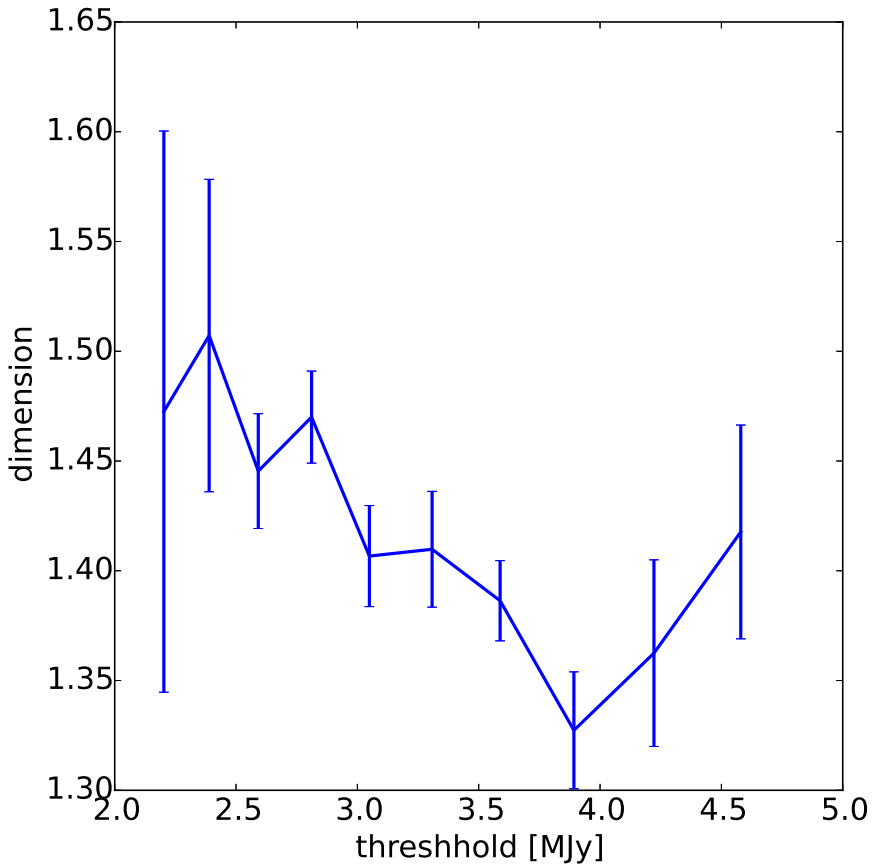

Figure 4.8: Dimension of the cirrus region as a function of flux threshold. HeLMS, like all HerMES fields, was chosen to maximise coverage of ancillary data and minimise cirrus contamination. Thus the cirrus in the region is not very bright and the flux threshold axis does not cover a large range. However, there is definite evolution in the dimension, mirrored in the Bazell & Desert (1988) result.

region sizes, showing that the cirrus at this flux is indeed fractal in nature. All calculated D values are plotted as a function of flux threshold in figure 4.8. Bazell & Desert (1988) note that typical cirrus flux densities range from 1 to 12 MJy/sr. Thankfully the HeLMS field has been carefully selected to not have many cirrus regions above 5 MJy/sr. However, this does not give a large dynamic range to work with when thresholding the image.

Nevertheless, there is definite evolution in the dimension of the cirrus regions in figure 4.8. Given that the dimension of a perimeter in two dimensional space can only vary between 1 and 2 (with 1 a simple shape and tending to 2 as covering the entire area), the variation is quite stark. The downward trend in dimension implies that the complexity of the region decreases with increasing flux density. In other words, very diffuse cirrus has a more complicated structure. The final two points in the distribution show an upward trend again, which could invalidate the downward trend seen. These results do somewhat contract Bazell & Desert (1988) which finds in the same flux density range, find a lower fractal dimension of 1.40 to 1.22, but with a downward trend as these results. As D is a measure of how a structure fills a space, the cirrus in HeLMS could be considered more complex, with more diverging filaments. This would be interesting to investigate further. The other result is that the cirrus *is* fractal due to the strong correlation between area and perimeter.

These results show that it would be possible to simulate a field of cirrus by adhering to a fractal algorithm. To create a simulated map of the sky that includes cirrus, one could use the 100μm maps and scale to the SPIRE wavelengths using a modified blackbody spectral energy distribution with a typical temperature for galactic cirrus. This would add the large-scale fluctuations that are easily visible in the HeLMS image. However, the 100μm map is at a pixel resolution of 4 by 4 arcmin, much larger than the SPIRE beam FWHMs. This means that this approximated cirrus simulation smoothed to SPIRE pixel resolutions would not contain small-scale filamentary structures. This is significant as large-scale fluctuations can be separated from an image consisting mostly of small-scale fluctuations (PSFs), for example with a high pass filter (Viero et al., 2014) or with algorithms like ICA (Independent Component Analysis, Planck Collaboration et al. (2014)). Therefore using a cirrus simulation that is correct only on large scales will lead to an underestimation of the errors on catalogue completeness, source positions and photometry as there will be no residual small-scale cirrus to confuse the source-finder.

However, assuming that the scale-free relationship between area and perimeter remains intact to smaller scales - which is not an unreasonable assumption considering it has been

shown that the relationship is consistent over many decades of area - means the cirrus can be simulated with fractal algorithms to smaller scales. Therefore, a fractal simulation would give a strong handle on the errors associated with cirrus filaments on scales the size of the PSF. This is achievable; simulations of molecular clouds have been created with fractional Brownian motion Bazell & Desert (1988), (a generalised technique for simulating Brownian motion where each timestep is not necessarily independent).

Simulating a field of cirrus and constraining the effect of flux-boosting by small-scale fluctuations will be left for further work due to time constraints. To be consistent with previous work using HerMES source-finding algorithms, an aggressive filtering approach is selected, as used in Viero et al. (2014) for the overlapping HerS field.

4.4 Filtering the Maps and Source Extraction

As seen the cirrus in the map is very strong and unavoidable without attempting to subtract some background or local background. One way to remove large-scale fluctuations is to suppress the large-scale modes in the Fourier transform. The method from Viero et al. (2014) is used. The filter itself is a high-pass filter, the simplest version a filter that sets the amplitude of fluctuations at for large modes to zero and the short modes alone. This filter suppresses scales beyond three times the FWHM of the beam as such:

$$d_f(x,y) = F^{-1}\begin{cases} k \geq 1/(3\times \mathrm{FWHM}), & \hat{f}(l,m) \\ (k < 1/(3\times \mathrm{FWHM}), & \hat{f}(l,m)(3k\times \mathrm{FWHM})^3 \end{cases} \tag{4.4}$$

where FWHM (full-width at half maximum) is in arcminutes, and $k = \sqrt{l^2+m^2}$. d_f is the resultant filtered image, $\hat{f}(l,m)$ is the fourier transformed image. If the k value of a pixel is less or greater than a particular function of the FWHM, the value of the Fourier transform of the image is either preserved or attenuated, then inverse transformed. A length of 3 FWHM is equivalent to $6\sqrt{2\ln 2} \approx 7.065\sigma$, implying the beam will not have been affected to a great extent.

Figure 4.9 shows the original Gaussian fits used for source extraction and the filtered beam when the peak has been scaled to be one, as well as the effect of filtering on the map. The beam has been narrowed and power put into the wings. The beam does now not decrease monotonically as distance from the peak increases. This will cause interference with neighbouring sources, it is possible STARFINDER will struggle to find the close sources in the map and deblend them effectively, if two sources are nearby and their wings interfering, the second fainter source could be flux boosted and STARFINDER could

detect that as an extra source. Further, the wings themselves can be detected as a source (see below).

The full algorithm is as follows. The image maps and Gaussian beams are filtered with the above filter. The image maps are then rescaled to the same value the beams are to reach a value of one, that effectively readjusts the units of the map into Jy/beam again. A further adjustment is applied to the maps to compensate for a discrepancy that found after the maps were first run through the catalogue pipeline.

There is an overlapping region between HeLMS and HerS, and this region was used to check whether the photometric estimates for HeLMS were consistent with HerS. Sources were matched between HeLMS and HerS 250μm maps for 3" or half a pixel. At that distance the sources are guaranteed to be the same source. An offset between fluxes was identified. The adjustment required was calculated from the average scaling needed for sources greater than 100mJy at 250μm and 350μm. These values were 1.048, 1.035 and 1.048 for 250, 350 and 500μm maps respectively, a multiplicative effect applied to each map before source detection and extraction.

The maps are then run through STARFINDER modified to include the filtered beam instead of the Gaussian. STARFINDER is then set to perform one pass finding sources above a signal-to-noise ratio 3 only. These positions are passed to DESPHOT to perform photometry estimates. However, DESPHOT must be modified before proceeding.

4.4.1 DESPHOT Modifications

There are a number of challenged to contend with when dealing with a map the size of HeLMS when using source extraction software that was designed to run on smaller, deeper maps. DESPHOT segments the map along regions of 1-σ pixels to reduce size of the matrix the algorithm needs to invert, there is also a limit on the number of sources per segment to ensure the matrix remains a reasonable size. Further, during the segment calculation, an array the size of the entire map is used as a mask, which again would be memory intensive for a map the size of HeLMS.

When attempting to perform source extraction using the standard DESPHOT algorithm, the maximum segment size was exceeded very quickly. To tackle the first issue, the the same approach is taken as in Viero et al. (2014) by replacing the map segmentation along pixels with a SNR of 1 with a Friends-Of-Friends algorithm, linking sources together with a linking-length of 3'. This is a separation of almost ten FWHMs in beam and so any segment will be very isolated from others.

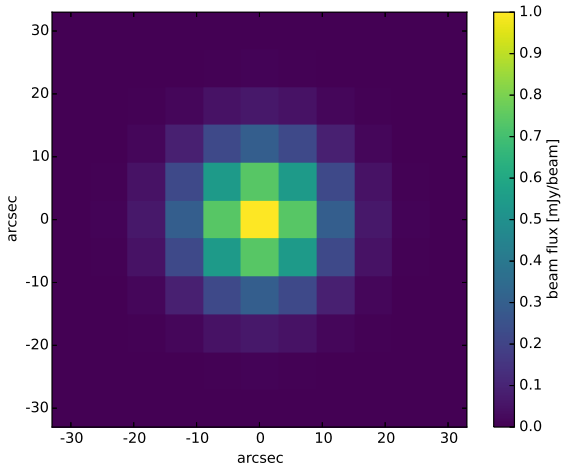

(a) 250μm Gaussian beam

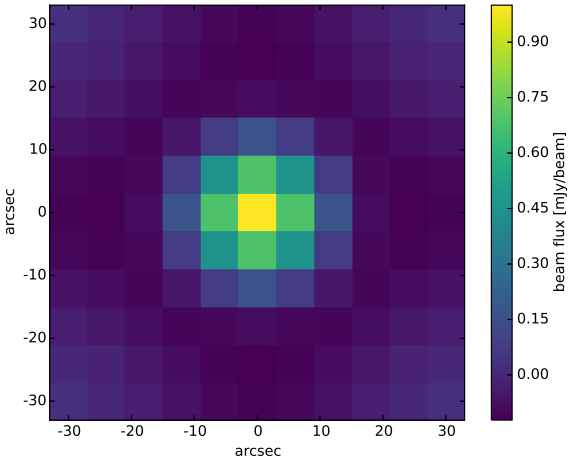

(b) 250μm filtered Gaussian beam

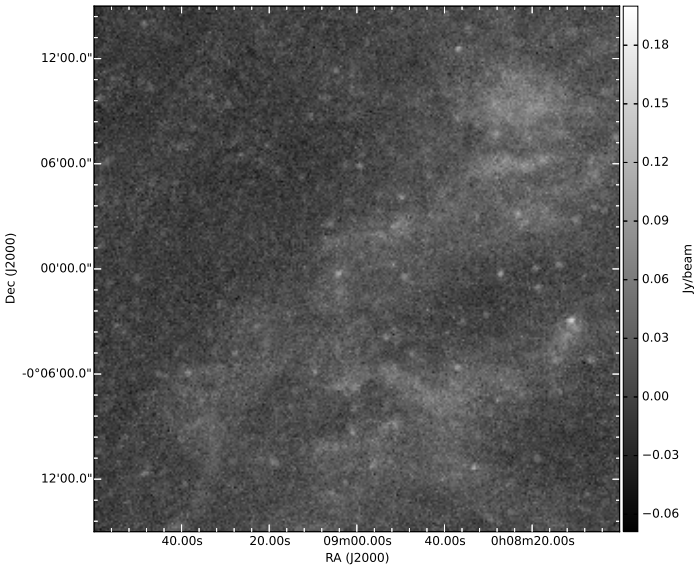

(c) 1 sq.deg. of 250μm HeLMS map

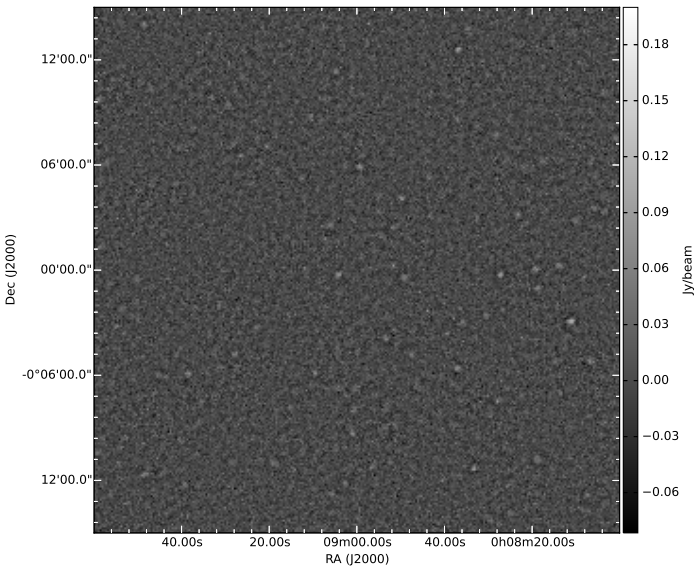

(d) 1 sq.deg. of 250μm filtered HeLMS map

Figure 4.9: The Gaussian fits to the Herschel-SPIRE 250μm beam before (a) and after filtering (b) and the 250μm map before (c) and after (d) filtering.

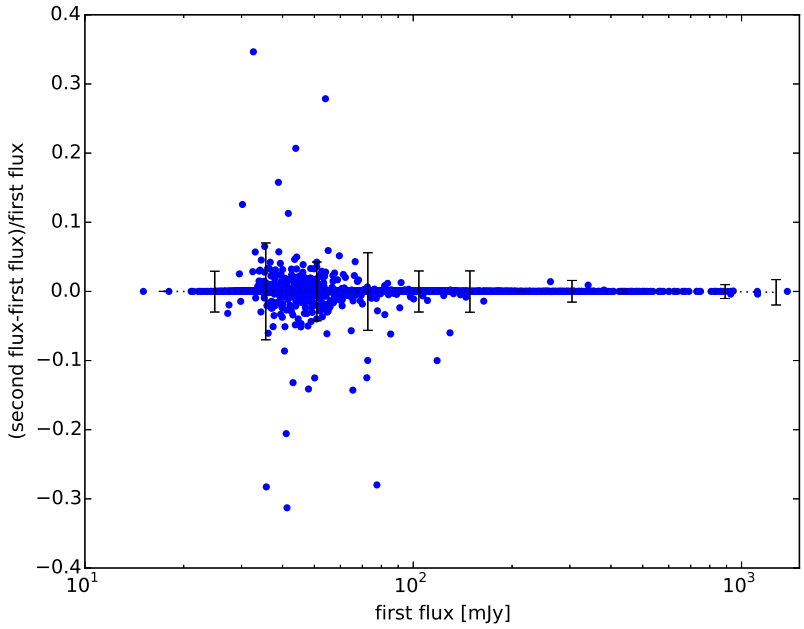

Figure 4.10: Comparison of source fluxes in overlapping HeLMS segments at 250μm created by DESPHOT. Error bars are 10σ values to be visible. With the exception of a few anomalous results from sources on the edge of segments, the fluxes are on average identical, and therefore the map segmentation performed for HeLMS is having little effect or biasing on the fluxes.

To tackle the size of the map, an approach was created especially for HeLMS. The map has been segmented into 118 separate tiles of 4 deg^2 with an overlap with neighbouring tiles of 1 deg. After DESPHOT has been run on these tiles, the resultant catalogues are combined and the duplicated fluxes considered. These fluxes are compared in figure 4.10, reassuringly showing that the determined fluxes are very likely to be identical. In the case of duplicated fluxes we take the flux closest to the centre of the tile (and thus more likely to be on a segment that is truly isolated rather than truncated due to the edge of the tile). For quadruple fluxes we take the flux closest to the mean. In cases where a flux is set to zero as it is on the edge of a segment, that source is ignored and the rest are considered.

The second pass of DESPHOT is not run to find sources in the residual maps. The DESPHOT code uses a Gaussian peak finder (specifically, the IDL algorithm FIND) which cannot take into account a different beam. Given the low exposure in the map, we just use sources from the first pass in this calculation.

The confusion noise and background has been been calculated from the entire map rather than on individual tiles. The total error on each source is given as $\sigma_{\mathrm{T}} = \sqrt{\sigma^2_{\mathrm{conf}} + \sigma^2_{\mathrm{inst}}}$. The confusion noise has been calculated on the residual map by fitting a linear regression on the fluxes as a function of coverage, with the confusion noise the y-intercept as with the standard DESPHOT algorithm. For each band this was calculated as 10.25, 10.36 and 11.38 mJy/beam. These values are higher than the 8mJy/beam quoted for HerS by Viero et al. (2014) and higher than the confusion noise estimates in chapter 3. This is implying that, in the regions in which the confusion noise was calculated (i.e. surrounding detected sources) there are a number of brighter, undetected sources skewing the calculation of the variance in these regions.

4.5 Comparison of SUSSEXtractor and DESPHOT

Figures 4.12 and 4.11 show the new average density and median signal-to-noise values across the HeLMS map created from catalogues from the filtered map. The average density of source across the map has indeed dropped and there is now no correlation between cirrus emission and the number of sources or the signal-to-noise ratio. Whilst it looks from numbers alone the number of detected sources has dropped and the catalogue is less complete, with the lack of correlation between cirrus and sources the DESPHOT catalogue is far better than the previous SUSSEXtractor catalogues. Figure 4.13 demonstrates this difference extremely well, showing the location of sources in the SUSSEXtractor and DESPHOT catalogues, the former catalogues are extremely correlated with the cirrus

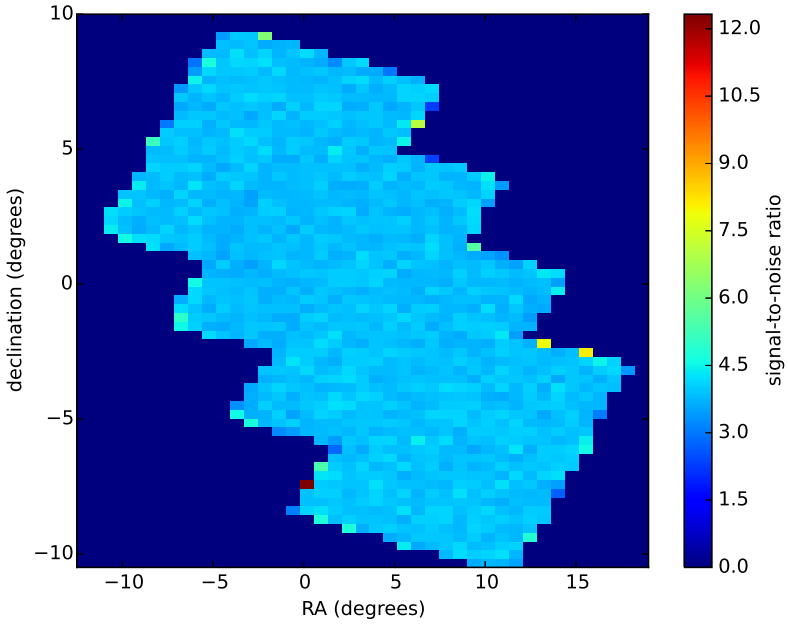

Figure 4.11: Median signal-to-noise ratio of STARFINDER/DESPHOT sources in HeLMS binned to 0.5^2deg^2 segments. The results are uniform across the map (except the edges that have fewer sources) and are therefore now uncorrelated with foreground cirrus.

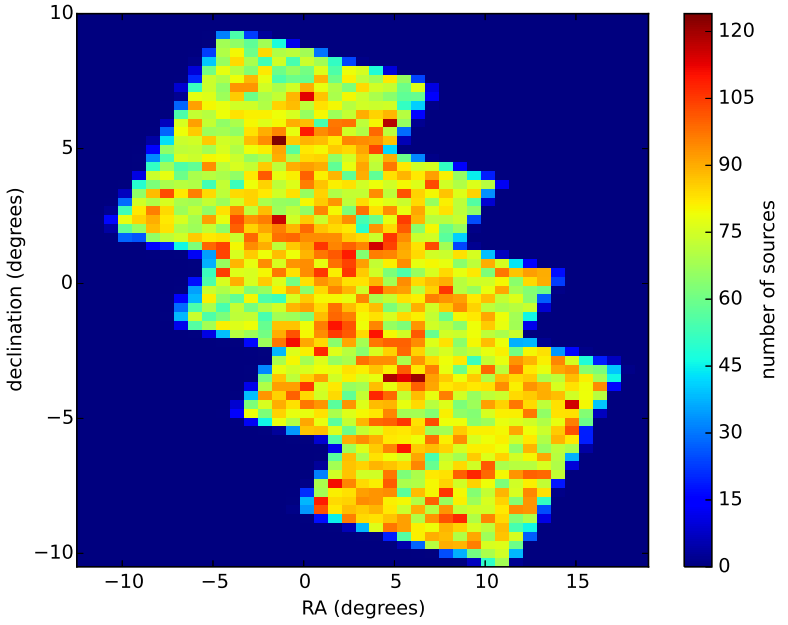

Figure 4.12: Positions of STARFINDER/DESPHOT sources in HeLMS as a density plot, resolved to a 0.5^2deg^2 grid. There are fewer sources found using STARFINDER/DESPHOT, however, the density of sources is not correlated with cirrus as with SUSSEXtractor sources in figure 4.3.

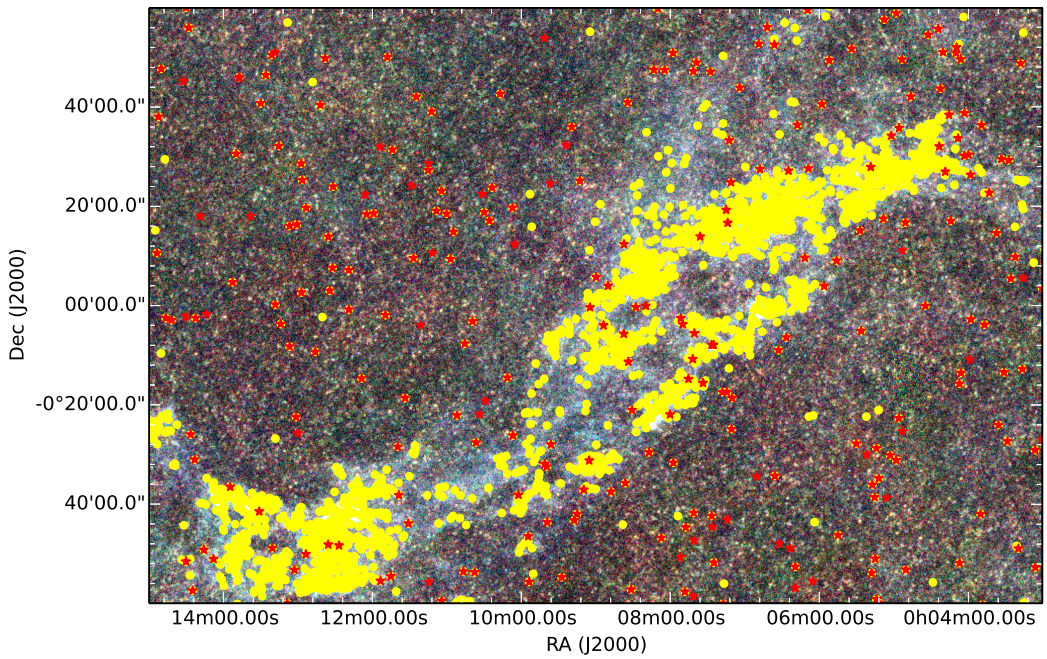

Figure 4.13: Overplotting of the SUSSEXtractor (yellow circles) and DESPHOT (red stars) catalogues over the dense patch of cirrus in the centre of the HeLMS field. SUSSEXtractor was run on the unfiltered map as a first attempt, and the second attempt after filtering with DESPHOT performed much better. Filtering large scale fluctuations out of the image has had the desired effect of reducing the number of spurious sources found in the catalogue. Filtering in Fourier space improve the detection ratio of real to spurious sources in these regions.

structure. Note that high-pass filter has not completely removed the sources within the bright cirrus region as masking these pixels otherwise would. This gives a much more homogenous catalogue without needing to awkwardly segment the map.

4.6 Accuracy and Completeness Estimates

The proportion of recovered sources as well as positional and photometric accuracy needs to be assessed. The small number of scans in HeLMS (2) coupled with the fast-scan nature of the observations and the filtering, the completeness of HeLMS has to be assessed independently. As a first attempt of this assessment and as previously a grid of sources is constructed at a separation of 340.161 arcsec. The lack of integer values for this separation ensures that there is no biasing towards higher completeness with a consistently pixel-centred and radially symmetric beam. The separation distance is also a higher value than in chapter 3 to ensure the Friends-of-Friends segmentation algorithm in DESPHOT does not create large segments spanning the maps. 4560 sources were injected in total, a density of 16.9deg^{-2}. The maps were run through the full filtering and rescaling algorithm, run through STARFINDER, segmented in the same way as the original map and run through DESPHOT. The output catalogues were matched to remove duplicated sources from the overlapping part of the segments. The real HeLMS catalogues were matched to the input grid of sources as in chapter 3 by using a matching radius of 1 FWHM and a flux ratio within 50-200% of the true value. These sources are removed to prevent serendipitous matching skewing the completeness upwards. The matching between input and output catalogues are then performed with the same parameters to create the final matches.

This computation of accuracy and completeness curves is performed three times to identify why there was a systematic difference in the fluxes of HeLMS and HerS sources that needed to be corrected for.

4.6.1 Injecting a Grid of Sources

Figure 4.14 shows the differences in RA and dec between injected and output catalogues. The mean position at all scales is accurate, confirming that STARFINDER, with its modified beam, is not biased in any direction when finding sources. The errors in the position are given as the 1σ standard deviation; 66% of sources are found within one pixel of the true position of the source at fainter fluxes, falling to within 2 arcsec at brighter fluxes.

Figure 4.15 gives the log ratio of injected and output fluxes, showing the fractional effect of over- or underestimating the flux at that particular flux density. The first res-

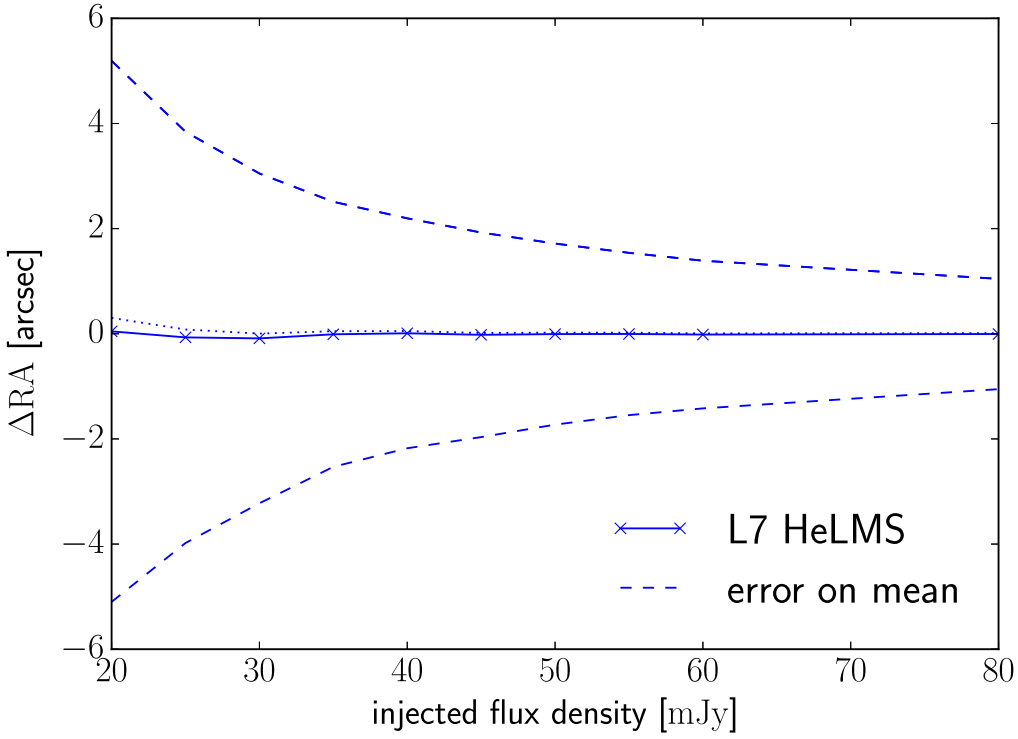

(a) Right Ascension

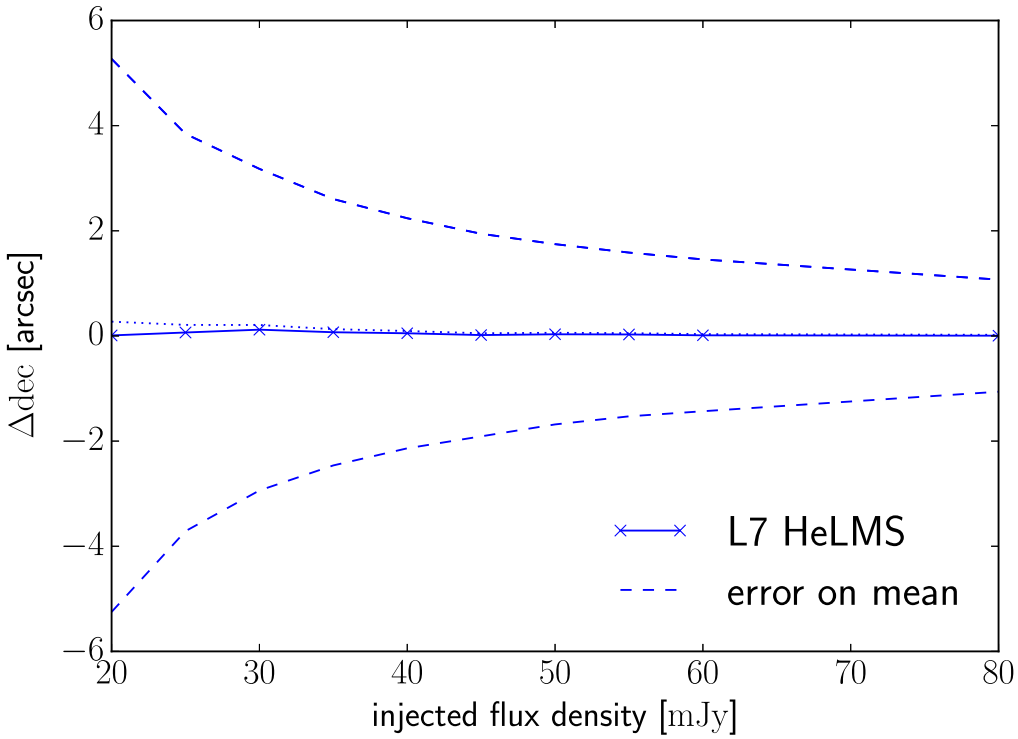

(b) Declination

Figure 4.14: Accuracy in Right Ascension and declination within HeLMS using a grid of injected source catalogues. The dashed line marks the 1σ variation in the value, with the dotted line the error on the mean and is consistent with zero. As expected, accuracy increases as a function of flux.

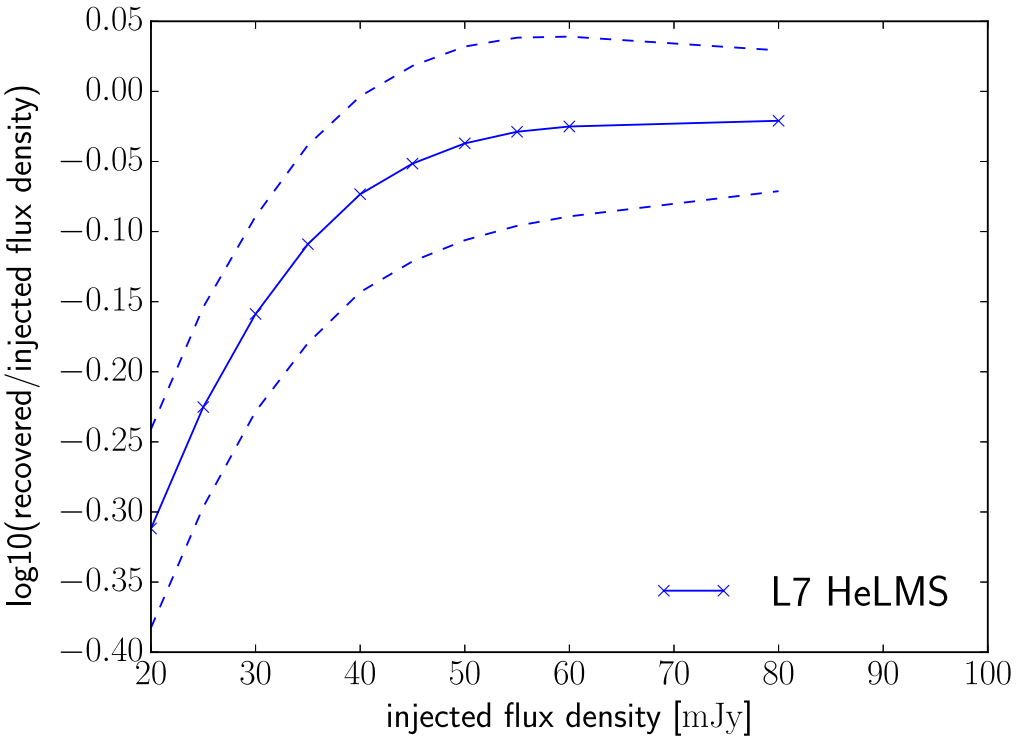

Figure 4.15: Accuracy of flux within HeLMS using injected source catalogues. There is an overestimate of flux at every flux-level, corresponding to a value of 5-15 mJy difference in detection.

ult that stands out is the overestimation of fluxes at low fluxes. This ranges from a 10mJy overestimation for a source flux density of 20mJy (a 50% overestimation) to 5mJy at 100mJy source flux density (5% overestimation). The changing nature of this overestimation suggests that its origin is not (entirely, at least) from a background offset. Further, at an injected source flux of 100mJy for 4560 sources, there has been a total of 1.41×10^{-6}Jy/pix injected into the map at 250μm, translating to a 1.46×10^{-5} Jy/beam increase in flux across every pixel in the map. Therefore the injected sources themselves cannot be causing the flux overestimation.

At low fluxes, the overestimation could be greater due to a compounding number of reasons. Sources are detected in the map with STARFINDER if and only if the signal-to-noise ratio is greater than 3. HeLMS is constructed from fewer scans than other HerMES maps so the noise in each pixel is higher. Therefore a source detected with a flux of, for example, 25mJy in the HerMES map will be at a higher signal to noise value than in HeLMS and less prone to errors in the flux estimate. 25mJy is a low flux in the HeLMS map and it's possible that sources detected at this flux are in truth lower, boosted due to Eddington biasing and thus this is an overestimate.

In section 4.4 fluxes above 100mJy in the catalogue were compared to fluxes in the HerS catalogue to check the calibration of source fluxes. There was an approximate 5%/4%/5% offset between the two sets of sources. When first calculated, this was thought to be due to a implementation difference or error in, for example, the beam used or the effect of the filter applied to the map. When performing estimations of accuracy using source injection, the sources have been added to the map before applying this upwards correction to the flux in the map. If instead the correction was needed due to a difference in map calibration, then injecting sources into the map before applying the correction will effectively change the flux of the injected source, i.e. from 100 to 105mJy. This is tested in the next section by injecting sources after the upwards flux correction has been applied to the map.

Figure 4.16 shows the completeness, i.e. fraction of sources injected into the map that are recovered with source extraction. Unlike the completeness curves produced for the DR2 release, the injected fluxes probe the 20-100mJy range. This is where the transition from 0% to 100% detection is thought to occur with source extraction on these maps, estimated from Viero et al. (2014). The fit was constructed using only results calculated from the 20-60mJy source injection maps. The fraction of sources recovered is the completeness as shown in figure 4.16. As the completeness is a measurement is the probability of recovering a source or not, the system can be modelled as a binomial distribution, with

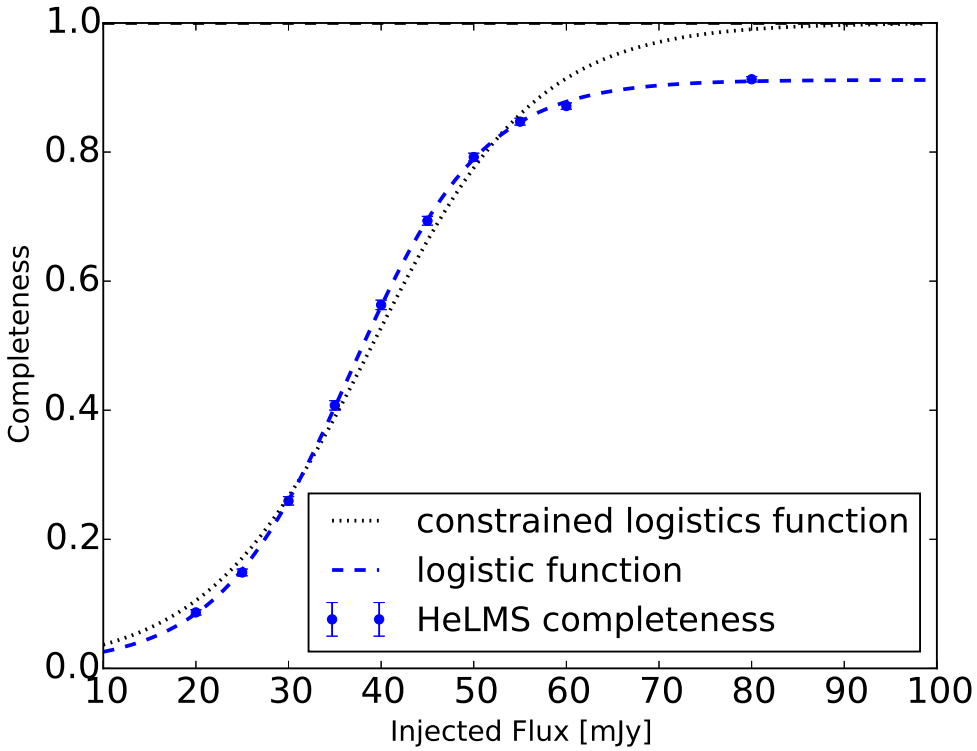

Figure 4.16: Completeness curve parameterised by equation 4.5. The blue dashed line represents the fit when the fits is forced between zero and one, the green solid line when the curve is allowed to freely vary. Fit parameters are given in table 4.1

the variance given as $\sqrt{p(1-p)}$ where p probability of recovering a source or completeness. The completeness can be modelled as a logistics curve:

$$C(S) = B + \frac{A - B}{(1 + e^{(-C(S-S_0))})} \tag{4.5}$$

a smooth curve with a gradient represented by C and S_0 the offset of the curve in relation to the source flux S, B the minimum value and A the peak value. First we fix the peak to $A = 1$ and minimum value $B = 0$ i.e. 100% completeness at higher flux and zero completeness at very low fluxes. The fit is not particularly good, however if A and B are left to vary, the fit is better as seen in figure 4.16, with a peak value of $A = 0.901$. This fit implies a maximum of only 90% of sources at any flux will be recovered in the map. The resultant completeness is alarming. To see whether this was a real trend, 80mJy and 100mJy source injected maps were made and the results overlaid. The results confirm the fit, that the maximum number of sources to be found is only ever ninety percent of the total number of sources.

DESPHOT's LASSO algorithm preferentially turns sources off when a source's flux

gridded, full fit	A	B	C	S_0
gridded, fixed fit	1.0 (fixed)	0.0 (fixed)	0.117 ± 0.010	39.25 ± 0.92
Full fit	0.025 ± 0.005	0.908 ± 0.002	0.139 ± 0.002	36.25 ± 0.12

Table 4.1: The fit parameters for the completeness curve for the grid of injected sources. Letting the minimum and maximum values of the fit vary is a far better fit to the results. Crucially, the completeness does not reach 1.0 at infinity, which would be expected.

does not contribute substantially to reducing the χ^2 fit and therefore those fluxes would be removed from the final catalogue. It is noted in Hurley et al. (submitted) that, for dense prior catalogues, this could lead to many sources with zero flux if a source is on a segment with many other sources or substantially brighter sources. However, in the case of HeLMS, these sources are instead not detected by STARFINDER, with very few sources in the final real catalogue attributed zero flux ($< 0.1\%$). This runs contrary to expectation as at 100mJy sources should typically be at far greater than 3σ signal to noise and therefore detected by STARFINDER. Indeed, the pixels that the sources are on are at a signal to noise ratio greater than three and should pass the first stage of detection in STARFINDER. The hypothesis then is that sources are removed from the potential source candidate list when the correlation between the beam and source in the map is less than 0.5. This is implying that the beam, or the sources, are the wrong shape due to high instrumental noise effects or confusion.

The flux offset will now be explored through testing. To determine whether the injected grid itself is effecting the results (as grids are regular, large structures in the maps and thus could be effected by filtering) sources will be injected randomly to remove that possibility. Then, a comparison between the accuracy and completeness results will be shown, with the flux correction applied before and after the sources are injected into the maps again to see if the flux estimate will be improved.

4.6.2 Randomly Positioned Injected Sources

The grid of sources was chosen as the pattern to inject with to be analogous to the source injection maps in chapter 3. However, a grid of sources is an unnatural structure in the map. Whilst this was not much of a problem in unfiltered maps that were looking for independent sources, after filtering the pixels in the map become correlated. Further, the grid structure means that, in Fourier space, there will be power at scales related to the grid size as the Fourier transform attempts to construct the grid from an addition of

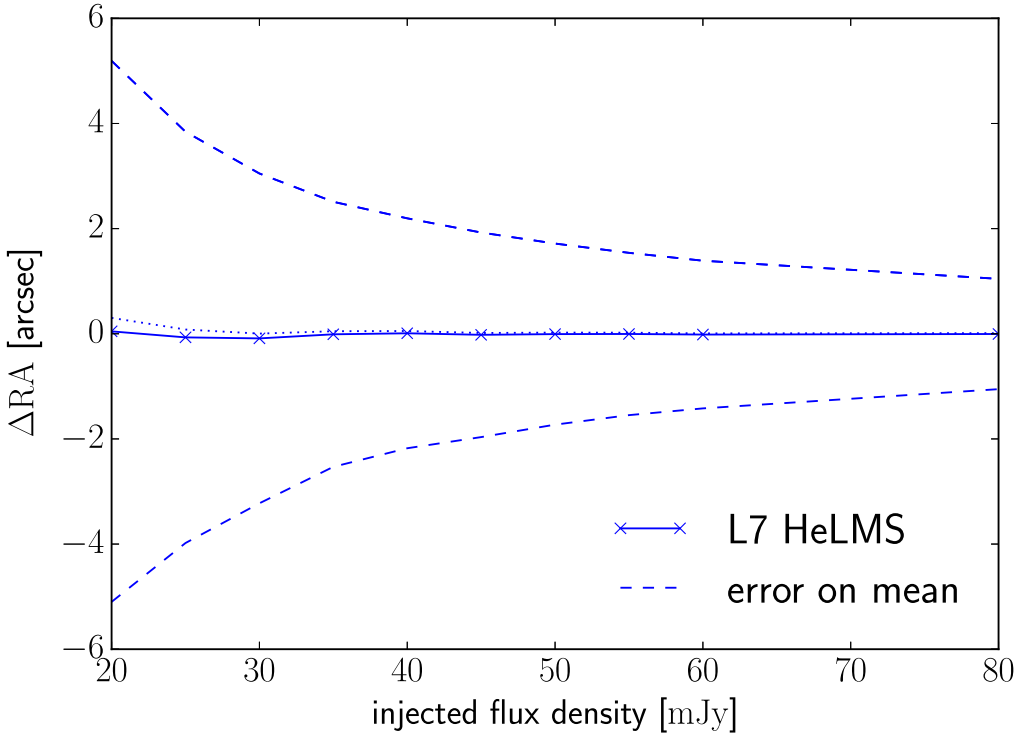

(a) Right Ascension

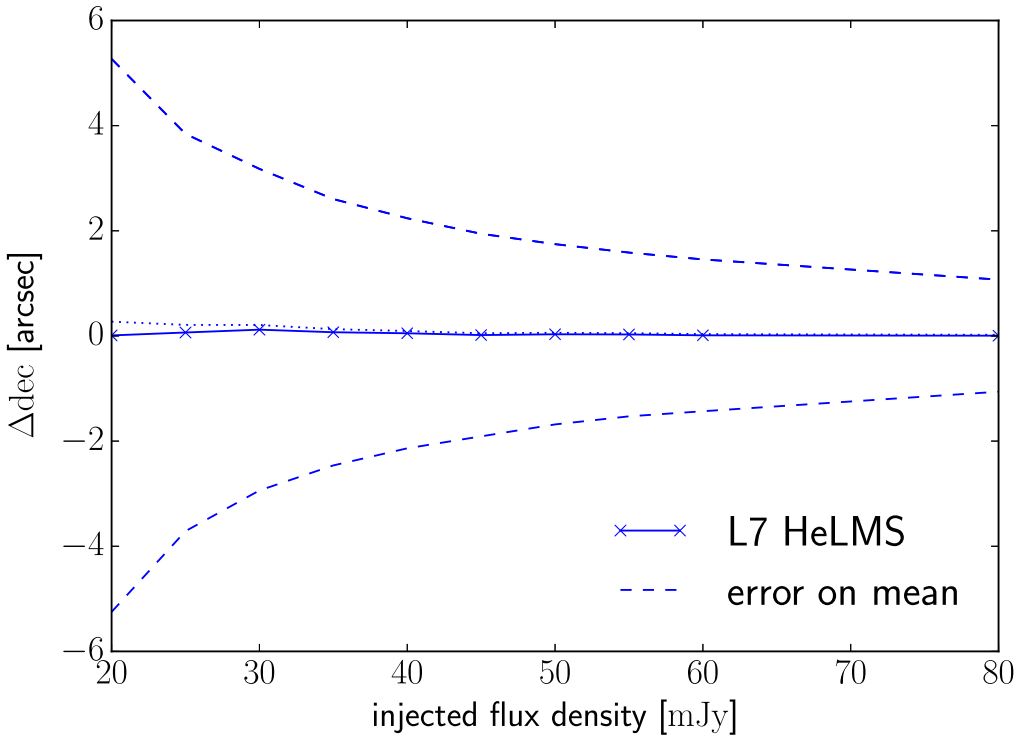

(b) Declination

Figure 4.17: Accuracy in Right Ascension and declination within HeLMS using randomly positioned sources injected after a correction is applied to the map. Accuracy increases as a function of flux.

Fit	A	B	C	S_0
random, calibration first	-0.007 ± 0.024	0.926 ± 0.007	0.139 ± 0.001	36.37 ± 0.64
random, injection first	0.038 ± 0.009	0.929 ± 0.004	0.140 ± 0.004	38.84 ± 0.28

Table 4.2: The fit parameters for the completeness curve for randomly positioned injected sources, placed before and after the calculated calibration for the maps. The completeness is higher than the previous fit to gridded sources, although still not reaching 100% completeness.

sinusoidal waves. Power at these scales are filtered out by the transformation and so the reconstruction of the gridded source will be poorer, leading to a drop in detections.

To test whether the grid is affecting the detection of sources after filtering the analysis is run again, this time with sources positioned randomly. The number of sources is reduced by a factor of four to reduce the chance the random sources will create artificially large segments. In the case of the 250μm injected map this is a change per pixel of 3.123×10^{-6} Jy/beam so should have little effect to the completeness. The positional accuracy is still high and without offsets as shown in figure 4.17.

Figure 4.18 shows the completeness and flux accuracy as for when the grid of sources is injected before (subfigures and and c) and after (b and d) the map calibration has been applied. The completeness is marginally improved by using a random grid as is seen in subfigures b and d in figure 4.18, reaching 92.3% at maximum when the sources are injected before the map correction, the parameters are given in table 4.2, lending weight to the hypothesis that the amplitude of large Fourier modes that made up the grid were being suppressed and effecting the shape of these beams beyond what was expected from an isolated beam.

Subfigure a in figure 4.18 however shows that the photometry estimations are not improved by only randomly distributing the sources. This means filtering the grid of injected sources is not significantly affecting the flux estimates and therefore the issue must be with a map calibration rather than a needed correction due to they implementation of the filtering. Therefore injecting the fluxes after calibrating the map is a better course of action.

Reordering the map calibration and source injection phases of the algorithm and re-running produced subfigures b and d in figure 4.18. Values from the completeness curve fit are in table 4.2. As expected, the completeness curves remains similar, reaching a peak of 93%, and the measure of gradient C is similar. However the point at which the curve

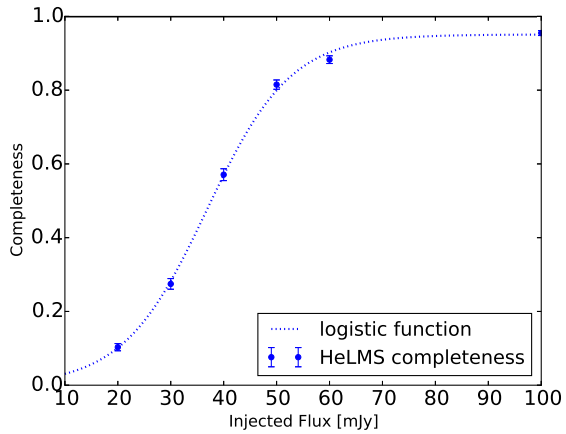

(a) Completeness, source injection first

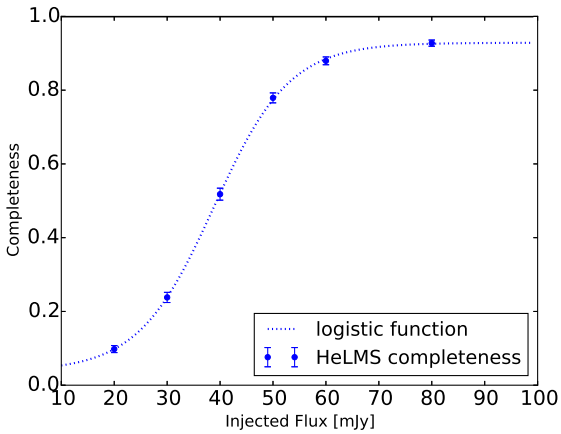

(b) Completeness, calibration first

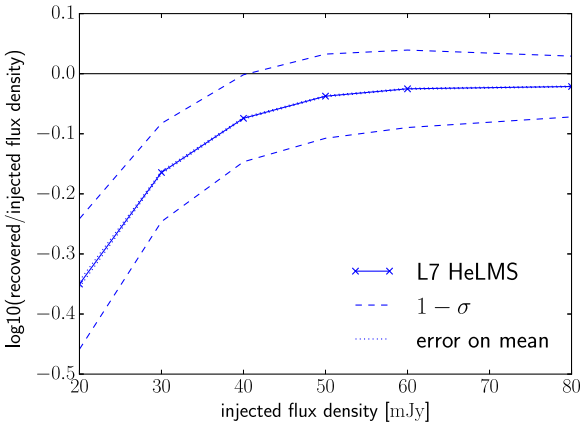

(c) Flux accuracy, source injection first

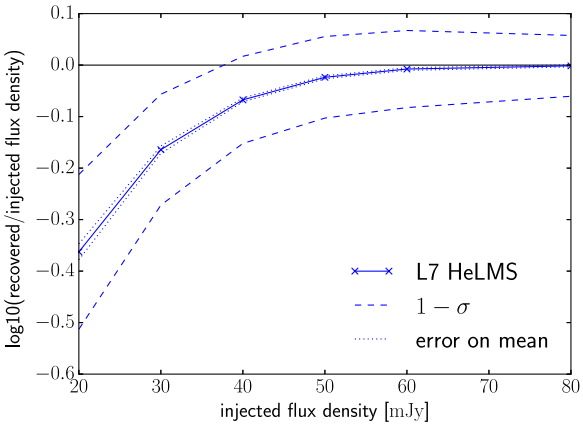

(d) Flux accuracy, calibration first

Figure 4.18: Completeness and flux accuracy within HeLMS using injected source catalogues with randomised positions, placed before (a,c) and after (b,d) the map calibration. There is an overestimate of flux at every flux-level when sources are placed before the map calibration, corresponding to a value of 5-15 mJy difference in detection. Injecting sources after brings these flux values to parity.

reaches 50% completeness moves from 36.4 to 38.8 mJy as the map calibration is now applied before source injection; previously the input fluxes were effectively over reported as the calibration was applied after source injection leading to the appearance that the completeness curve was rising at fainter fluxes.

Comparing to the completeness in Viero et al. (2014), $C = 0.145$ which is marginally steeper than the HeLMS value of $C = 0.140$ (NB, no error bars were given in the paper). The curve is divided over two different regions in HerS, where the overlap of scans in the tiling scheme leads to deeper and shallower areas. S_0 in the deeper region is 30.3mJy and 37.24 mJy in the shallow region. HeLMS appears to match the shallow regions in HerS in catalogue depth, although the fit used for the HerS completeness function has only two degrees of freedom, forcing the fit between 0 and 1 and so these results may not be directly comparable.

The flux accuracy has also changed as seen in subfigure c of figure 4.18, reaching parity at approximately 70mJy in the 250μm band. This value is much higher than seen in chapter 3 due to the fewer numbers of scans used in the HeLMS map, as well as the scans being in fast-scan mode. This is a significant increase on the typical instrumental noise of other HerMES fields. Further, the filtering in the map will effectively add to the uncertainties in the flux as the beam shape has changed.

The catalogue constructed in the HerS field was created in the same way as the HeLMS catalogue. They are also at a similar depth and so one would expect the number counts to be similar. Figure 4.19 shows the raw euclidean normalised number counts from both catalogues compared to the publish results of Clements et al. (2010) in the SDP H-ATLAS field. Completeness and flux boosting corrections derived from simulations are applied to this curve. The paper highlights a rise in number counts from 100mJy to 200mJy, attributed to a population of dusty star-forming galaxies. This upturn is also seen in the HerS catalogue but not in the HeLMS. This is down to two reasons, the difference in completeness between the two curves that causes the discrepancy in each flux bin increasing with flux. The difference at the brightest fluxes could be attributed to both the difference in completeness (estimated at 93% at these fluxes for HeLMS) and over-zealous removal of sources thought to be attributed to the first lobe of the filtered beam of the brightest sources (see section 4.7). Figure 4.20 shows the number counts of the catalogues before these spurious sources are removed. 181 sources and sources associated with 57 extended sources are removed between these two catalogues. However, the majority of the 181 are removed due to association with artefacts in the map. The “true” raw number counts

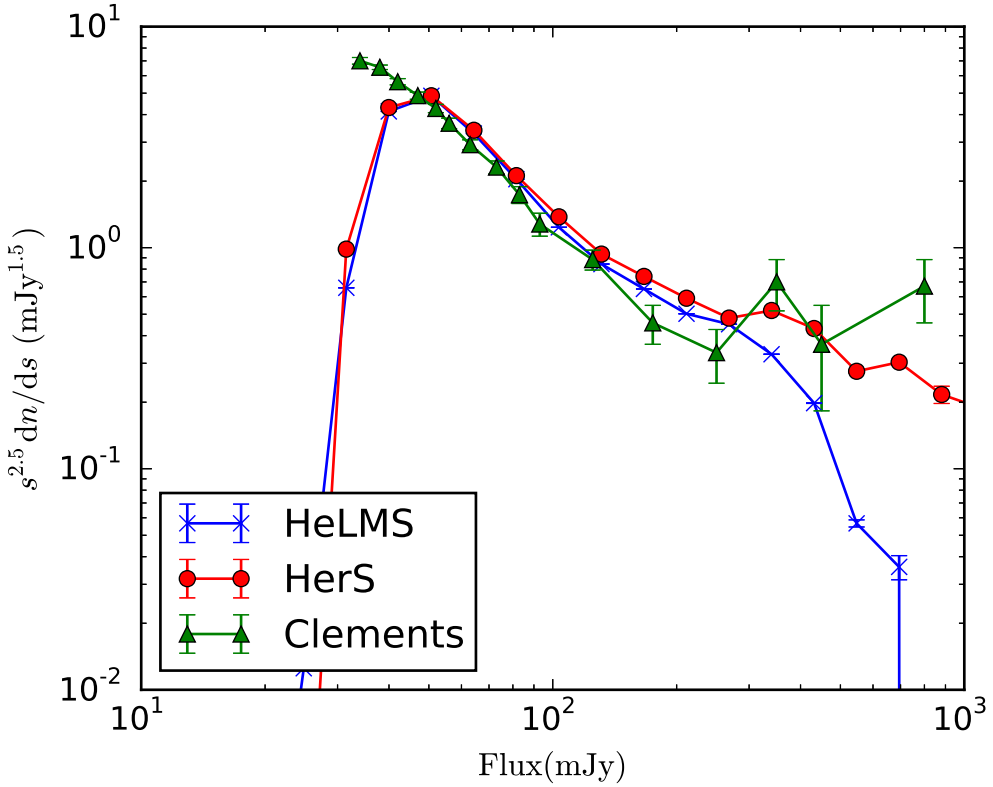

Figure 4.19: The raw number counts at 250μm in the HeLMS and HerS fields. The number counts as calculated on H-ATLAS maps in Clements et al. (2010) are included for reference.

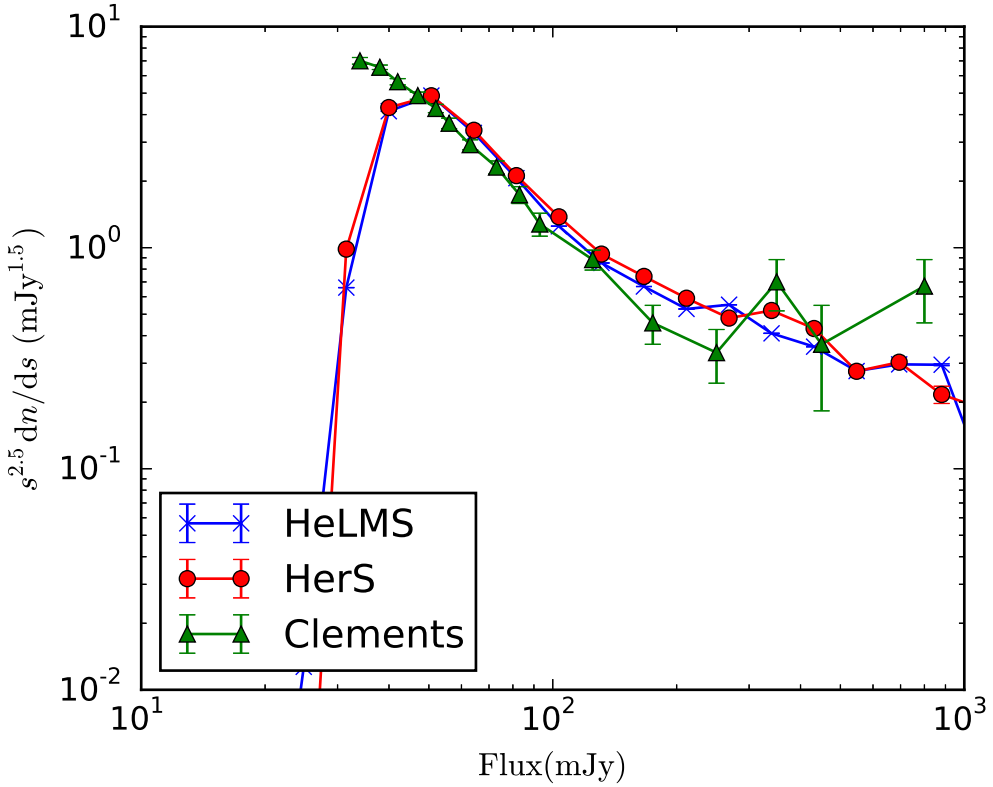

Figure 4.20: The number counts at 250μm in the HeLMS and HerS fields. The HeLMS catalogue has no any extended sources removed. The true raw number counts from this HeLMS catalogue lies somewhere between these values and those in 4.19

from HeLMS therefore lie somewhere between these two curves.

4.6.3 Estimation of Reliability

Reliability is a measure of how likely sources in a catalogue are to be spurious, in other words, noise in the catalogue is able to mimic a source and be detected as such. To mimic a noise map, the jackknifes from Lockman-SWIRE 28 and 28B combination maps are used. These maps are constructed from four scans each in comparison to HeLMS' two, and were observed in fast-scan mode. The "half" jackknives are used, which are jackknifes constructed from half the number of scans (as opposed to e.g. "bolo" that are constructed from different bolometers). These are chosen as the data is split into two in such a way that both jackknives will incorporate the same systematics. The instrumental error in one of these jackknifes is comparable to the instrumental noise in HeLMS. Subtracting the maps should remove the signal and therefore confusion noise from the resulting image (as these are consistent at every pixel unlike the instrumental noise). However there is a nuance in the error propagation. Given the mean difference divided by an arbitrary constant, $R = \frac{A-B}{N}$, the errors propagate as

$$\sigma_R^2 = \frac{\sigma_A^2 + \sigma_B^2}{N^2} \tag{4.6}$$

$\sigma_A == \sigma_B$ therefore for $\sigma_R = \sigma_A$, N must equal $\sqrt{2}$. Both $\frac{A-B}{\sqrt{2}}$ and $\frac{B-A}{\sqrt{2}}$ are calculated. In both cases, 15 sources were found. Given Poisson errors, this leads to 15.0 ± 3.9 sources, or 226.9 ± 58.9 sources in the entire map. This is less than one source per square degree, and should account for 0.25% of sources in the catalogue.

4.7 Extended Sources

Due to the size of the image, one would expect many nearby galaxies to be included in the image. These sources can be a few arcseconds in width so when convolved with the telescope beam the resultant image is not a point source. This can cause problems as a source finder only looking to fit the beam to the map may overfit or fit multiple beams to individual sources. This issue is compounded in HeLMS due to the filtering; for the brightest sources the wings of the beam are bright enough that they can be picked out by STARFINDER as they are above the desired SNR. This leads to a bright central source with a regular pattern of a ring of sources surrounding them. It is possible that these ringed sources could be flagged as lensing candidates with a very naive multiple nearest

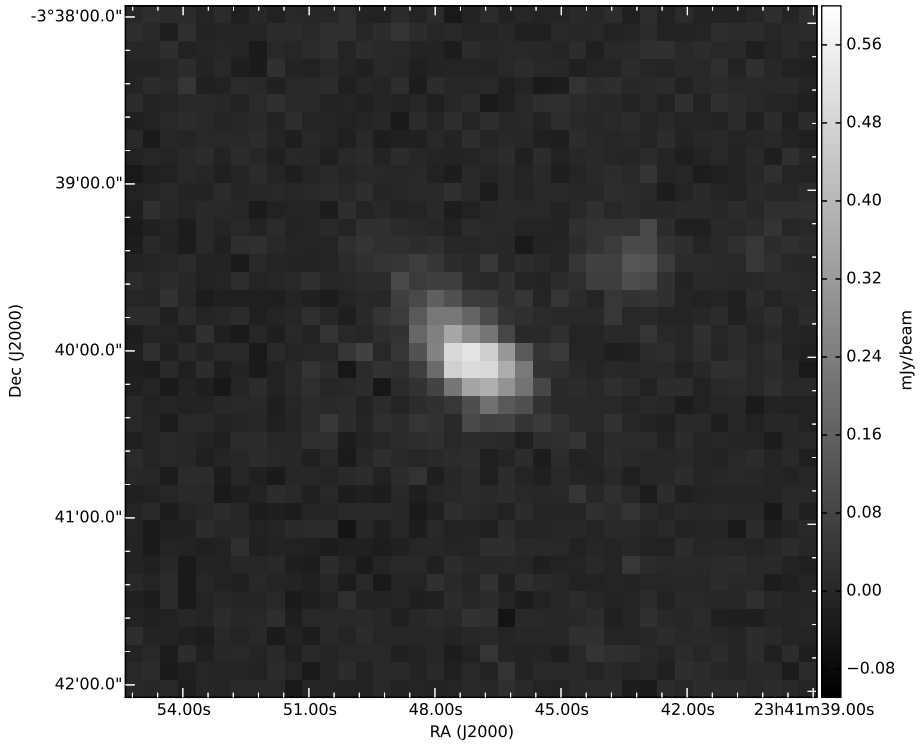

(a) Standard map centred on ARP295A

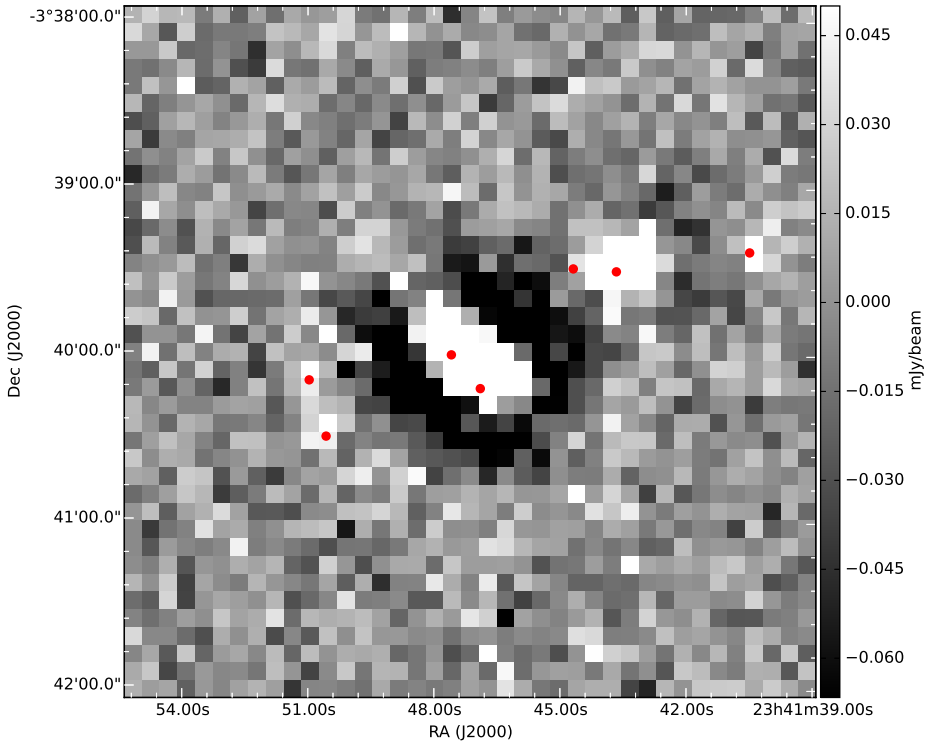

(b) Filtered map centred on ARP295A

Figure 4.21: Extended source ARP295A in the standard and filtered HeLMS maps. Source detections are labelled as red dots.

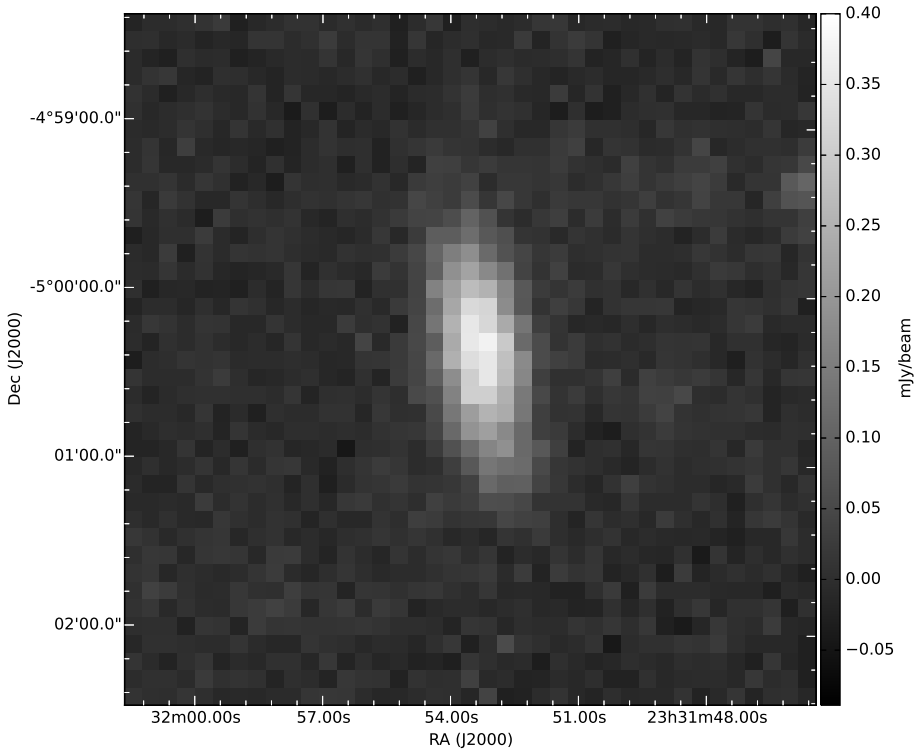

(a) Standard map centred on IC498

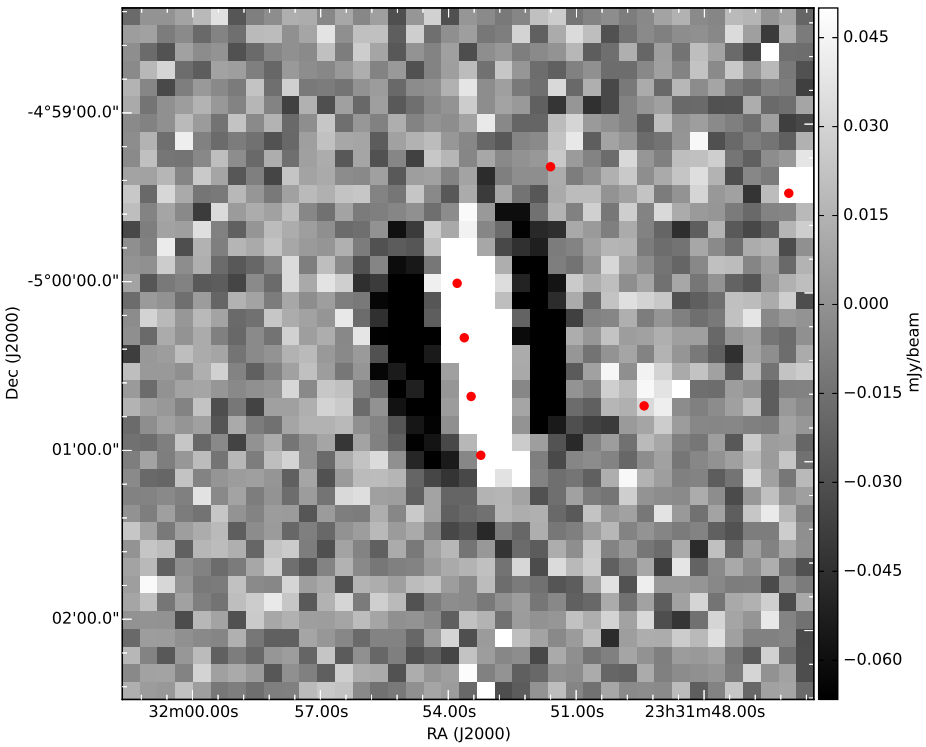

(b) Filtered map centred on IC498

Figure 4.22: Extended source IC498 in the standard and filtered HeLMS maps. Source detections are labelled as red dots.

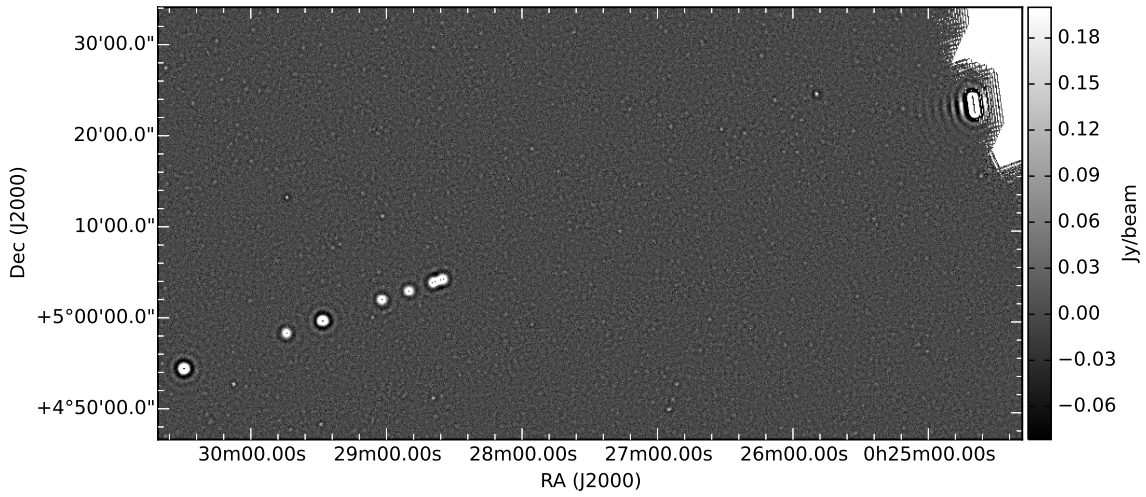

Figure 4.23: A series of artefacts in the filtered image caused by extremely bright pixels in one scan. Filtering correlates pixels across the map causing these anomalous pixels to affect the surrounding pixels in an extreme manner.

neighbour search and therefore these extended sources and their artificial companions must be removed. This process was performed mainly by eye.

Sources within a separation of 30 arcsec or five pixels with another in the 250μm were flagged as extended source candidates. 30 arcsec is less than a separation of two full-width half maximums and so would potentially find sources that have been both broken into multiple candidates or sources from the wings of the beam. Figures 4.21 and 4.22 show nearby galaxies that has been broken into five or more sources. All of the sources corresponding to the extended source were removed.

Approximately 1500 sources were flagged as potential duplicates. Many were flagged unnecessarily but of those that were an issue, these sources were from small errors in the map. A single pixel with a very large positive or negative flux would be easily ignored in a standard map. However due to the filtering in HeLMS the flux from these few pixels was effectively convolved out to other areas of the image. This caused some impossibly bright artefacts in the image. The worst is seen in figure 4.23. This particular artefact has removed a fraction of the sources in that region. In a further run these pixels would be masked before filtering.

Of the 1500 sources checked, 72 were flagged as extended candidates (one from each pair of sources), and their position passed to NED to find candidates. Fifty-seven sources were returned with postage stamps, from a separation distance of < 1 arcsec to degrees. If there was a match, the sources were removed.

A final by-eye check was performed around the edges of the filtered map to find spurious

sources caused by artefacts. In total 181 sources were removed due to artefacts like those in figure 4.23. Sources with a $\chi^2 > 10$ or and SNR < 3 were removed, leaving a catalogue of 92,256 sources. 97% have flux in 350μm, 87% flux in 500μm, 86% in both bands and only 1% have no flux in either 350μm or 500μm.

4.8 Conclusions

This chapter has discussed the HeLMS field, which at 270 sq. deg. is the largest field from the HerMES consortium observed with the *Herschel*-SPIRE instrument. It was also the shallowest, comprising only of two scans in orthogonal directions for each tile. HeLMS encompasses a n array of ancillary data that have associated catalogues and overlaps with another *Herschel*-SPIRE field, the HerS field. Together these fields cover the entire Stripe 82 field in the SDSS survey. It was therefore imperative to produce a catalogue for sources within HeLMS to use in conjunction with ancillary data.

Whilst pipelines for source extraction were in place for smaller, deeper HerMES fields, these techniques had to be adapted for the larger, noisier, cirrus contaminated HeLMS field. A first pass at blind source extraction was performed with the standard HerMES SUSSEXtractor pipeline. It was found that this catalogue had a strong correlation between source density and signal to noise ratio of sources with 100μm flux, with more sources found in regions of strong 100μm emission. This wavelength is the peak wavelength for warmed dust emission, implying contaminating contributions from dust in the 250μm, 350μm and 500μm was a significant issue to overcome in this field.

Galactic cirrus is known to be fractal in nature and thus the cirrus in the HeLMS field could have power at all scales, contaminating the estimates of flux even if the large-scale cirrus structures were removed. It is discussed whether the cirrus within the HeLMS field, selected to be mostly cirrus free and therefore atypical of cirrus across the sky, still exhibits complex structure at all scales. It is found through a study of the area and perimeter of regions of cirrus selected by surface brightness at 100μm that the cirrus within HeLMS, like other more typical cirrus regions is fractal. It is arguable that the dimensionality of the fractals evolves downwards with flux, i.e. brighter cirrus regions are less complex than dimmer regions. This could be indicating an evolution with temperature or with density - one would need information across wavelengths and column densities to be sure, although denser, warmer regions could be collapsing and therefore would be less diffuse. Compared to previous work from Bazell & Desert (1988), the results show the cirrus structures within HeLMS are more complex than a typical region. This would be an interesting

area to explore. These results could inform a future investigation into simulating cirrus to mimic *Herschel*-SPIRE simulations.

To detect and extract sources in the HeLMS field, the methodology of Viero et al. (2014) is followed, using a high-pass filter to remove large-scale emission from the maps. Due to the size of the field and the filtering performed on the maps, the standard HerMES source extraction method had to be modified. Viero et al. (2014) is again followed and the combination of the STARFINDER and DESPHOT algorithms is used with parameters modified from the second data release (chapter 2), outlined in section 4.4. This included a correction applied to the maps to ensure that the fluxes of sources in the overlapping region between HeLMS and HerS matched.

Extended sources (emission from foreground galaxies) are present in the map and must be removed. Finding and removing extended sources issues is compounded by the filter which, for very bright sources, will create a ring of flux around a point-like source from the wings of the beam. This ring can also be detected as sources. Further the detection algorithm will resolve an extended object broken into multiple sources. 57 extended sources were detected with known counterparts, and an additional 181 spurious sources, including sources from artefacts in the map. This removal process may have been overzealous however, with comparisons to the HerS catalogue and Clements et al. (2010) not demonstrating an upturn in the number counts at bright fluxes attributed to luminous and rapidly evolving galaxies at higher redshifts. 92256 sources are found in total. The density and signal to noise ratio of sources through this method was far more uniform and uncorrelated with the HI emission than the SUSSEXtractor catalogue.

The completeness, reliability and accuracy of the catalogue was also assessed. This was achieved in a number of passes to assess the effect of the filter on the maps. The first pass mirrored the source injection technique in chapter 3 by injecting a grid of sources at different flux levels. The completeness was fitted to a logistics curve and was shown to reach a maximum of 90% at 100mJy where all sources should be recovered. Positional accuracy improved as a function of flux. Flux accuracy were overestimated at all fluxes, although significantly more at low flux.

The source injection was run again, this time with sources positioned randomly in the map. It was hypothesised that regular structures of sources in the map created power at large-scale as the Fourier transform attempts to reconstruct the image, large scale modes that the filter will remove. Randomly injecting the sources will reduce this bias. The diagnostics were run again and the completeness marginally improved but was still at

maximum 93%. The flux measurements were still too high.

Finally, the sources were injected after correcting the flux in the maps. The original upward adjustment to the fluxes from matching to the HerS catalogue was assumed to correct for the effects of filtering. However if the injected fluxes are overestimated, this points towards the adjustment correcting for a map calibration error instead. On this pass, the completeness reached the same maximum of 93%, although the flux when 90% completeness is reached has increased to compensate for the previous artificial boosting of sources by the upwards flux correction.

With the diagnostics created the HeLMS results were compared to HerS in Viero et al. (2014) which used the same pipeline. The completeness is different between the two maps, with HerS appearing to be the deeper of the two catalogues. Further, HerS reaches 100% completeness as fluxes greater than 70mJy, whereas HeLMS never reaches 100%.

It was found the lack of completeness is from the STARFINDER end of the pipeline, with DESPHOT associating a flux to each source found with STARFINDER. The sources missed were not correlated with the edge of the maps or with bright or nearby sources. Instead it was hypothesised that the filtering must be having an effect on the shape of the beam significant enough for the correlation between beams to be reduced. This however should also affect the HerS field and does not significantly as the completeness in this field still rises to 100%. Therefore this effect is as of yet unexplained.

In addition, this catalogue has been used in the paper Pitchford & et al. (submitted) along with the HerS catalogue from Viero et al. (2014) and other HerMES fields (Wang et al., 2014) to find a sample of quasars also present in SDSS catalogues. Approximately 500 quasars are identified and their obscured star formation rates calculated. The authors find that, for quasars with very extreme star formation rates, the SFR remains constant with increasing quasar luminosity for quasars with infrared luminosities above $10^{12}L_{\odot}$. This implies that the emission of the galaxies active galactic nuclei is having no effect on the star formation rate of these galaxies.

4.9 Further Work

The final catalogue for the HeLMS field is not complete at high fluxes. One would expect, given sources of a high enough flux, to find all those sources. Therefore the source detection method is lacking in some manner. Given time a full investigation into this should be launched. Parameters to be tested include allowing the signal-to-noise cut of 3 during the STARFINDER portion of the calculation to vary to lower signal-to-noise to find more

sources, change the minimum correlation coefficient or to add in more iterations at a higher signal-to-noise threshold, as at each iteration the beam is refined. Allowing the signal-to-noise ratio to drop below three will add more spurious sources into the prior position catalogue, however the missing sources could be found and passed to DESPHOT where the final signal-to-noise value could be greater than three. Finally, changing the size of the beam image may lead to greater completeness; a smaller number of pixels covering the central region may make it easier to fit the beam to a peak in the map.

Extended sources in HeLMS create an issue as they are normally bright, and therefore the wings of the filtered PSF extend far from the source. Further, the extended source is often broken into multiple sources. Assessing the effectiveness of identifying and removing the source before the filtering takes place would be useful. However this would require elliptical fitting routines to be adapted for regions of high cirrus so doing so may be extremely time intensive for not much increase in sources. However, an automatic, consistent method of flagging possible extended sources would be very useful and would make quantifying systematic uncertainties associated with with extended sources easier to quantify and could bring this catalogue back in line with the HerS catalogue and other H-ATLAS fields.

A further investigation into the errors associated with small scale cirrus fluctuations would also be advantageous to both the catalogue in this field and other Herschel fields with cirrus contamination (e.g. FLS). As has been established in this chapter, the cirrus in this field is complex and fractal in nature. Whilst a simulation of the extragalactic sky can be made and a scaled 100μm or similar map overlaid to represent a cirrus-filled sky, these IRAS images do not have the small-scale structure within them meaning this emission is simple enough to remove. However, with techniques such as Fractional Brownian Motion (Bazell & Desert, 1988) (an algorithm to generate small-scale fluctuations in an image or data cube given information from large-scale fluctuations) the simulations could be very representative of cirrus structure and could be used to assess how cirrus amplitude affects the photometry estimates of catalogued sources.

Improvements could also be made to the source extraction software itself - within the HELP (Herschel Extragalactic Legacy Project) collaboration, prior position *and photometric* information at other wavelengths is being used to estimate the photometry within the SPIRE maps (Hurley et al., submitted). A technique like this could be useful in areas of HeLMS like Stripe 82 which has a wealth of ancillary data to create robust priors for the HeLMS source photometry.

Chapter 5

Principal Component Analysis

In previous chapters we have discussed the generation of catalogues of galaxies from deep and shallow SPIRE maps. Catalogues of objects, especially when matched to other wavelengths, can be used to find interesting individual objects. The downside with SPIRE maps, however, is their confusion - blind source extraction will not find every source in the image and some prior-based source extraction software can misattribute flux or, if the prior is not chosen carefully, some flux will not be found.

In both cases, many sources in the background of the map will be missed completely (as has been seen in previous chapters discussing the catalogues' incompleteness) and so catalogue production is limited in scope.

The maps themselves however contain more information than the catalogue. Whilst it is not possible to resolve the fainter sources, the flux from these sources still contributes to the flux of individual pixels in the map. Statistically therefore we can draw conclusions about fainter galaxies by analysing the maps themselves individually. However, the covariance between maps, how the variations in the maps change related to the other maps, also contains information that can be exploited. This chapter discusses a way to access this covariance information by projecting the *Herschel*-SPIRE maps along a set of orthogonal axes that better captures the covariance information available in the data using Principal Component Analysis. This chapter is motivated with a discussion of probability of deflection analysis, but this projection of data could also be useful for fitting galaxy models.

5.1 The Value of Multi-Dimensional Map Analyses

One way to extract information about galaxies too faint to be found through source detection is with probability of deflection analysis (or P(D)). The method is, in its simplest case, as follows.

A given population of galaxies can be described as a differential number count dN/dS (the number of sources in flux range $S \rightarrow S + dS$), with an intrinsic shape and variance, given in units of solid angle. The galaxy fluxes are distributed on a sky. A telescope will not observe flux from a source as a point on the sky however, the observation will be convolved with the telescope point spread function (PSF), spreading the flux from each source wider than its associated pixel to neighbouring pixels. For a PSF that integrates to one, a histogram of pixel fluxes will not return dN/dS but will be smoothed and pushed to lower fluxes relative to the number counts. The histogram of pixel fluxes will also have a further broadening due to instrumental noise.

The resultant map then is a convolution of the differential number counts placed on the map with the beam and then convolved again with the instrumental noise. This process of moving from source count model to a distribution of pixel fluxes is explained more rigorously in chapter 3 with relation to an analytic definition of the confusion noise in Condon (1974).

As the pixel fluxes are a series of convolutions is therefore possible to use deconvolutions to uncover the underlying number counts. Deconvolutions are inheritently unstable and therefore methods to find number counts will use a simple model, often a power-law (Condon, 1974) or a series of broken power laws (Glenn et al., 2010). The latter authors used Monte-Carlo Markov chains (MCMC) to sample a parameter space for the model's variables, effectively evolving the model forward repeatedly to fit the data. Effectively deconvolving the P(D) can be computationally intensive and so the flux histograms from each band are treated independently to simplify the problem.

We know however that, for the SPIRE bands especially, flux from a particular source is strongly correlated across the bands. This is due to the cool dust modified black-body radiating across these bands. Due to this strong correlation the bands can be said to exhibit strong covariance. Figure 5.1 shows the pixel distributions for each of the three bands in the COSMOS field. The distribution is centred close to zero. The negative tail is due to instrumental noise, and the positive tails a combination of instrumental noise and the brightest sources from the tail end of the number counts. The distribution is therefore a skewed Gaussian. In P(D) analysis, these three distributions are deconvolved

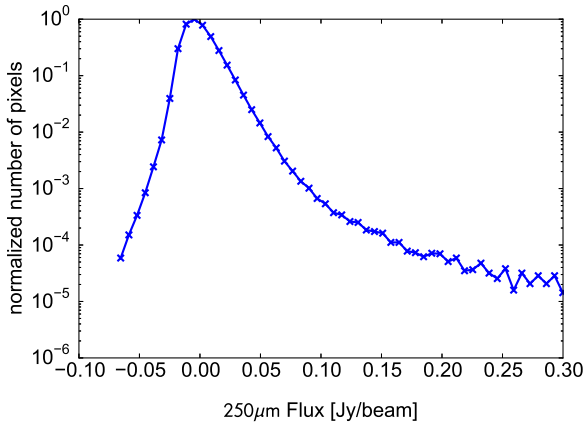

(a) 250μm

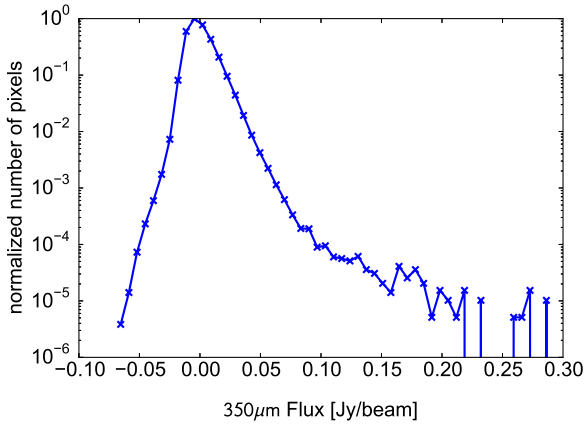

(b) 350μm

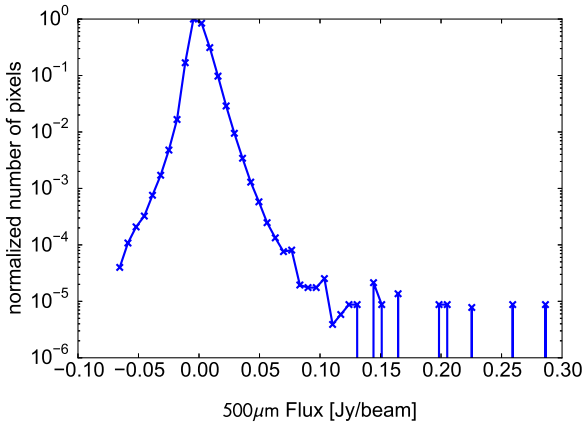

(c) 500μm

Figure 5.1: Pixel fluxes in the COSMOS map. Whilst there is a Gaussian-like nature to the distributions, with one central peak, the distribution is skewed towards brighter flues in all bands due to the source number counts.

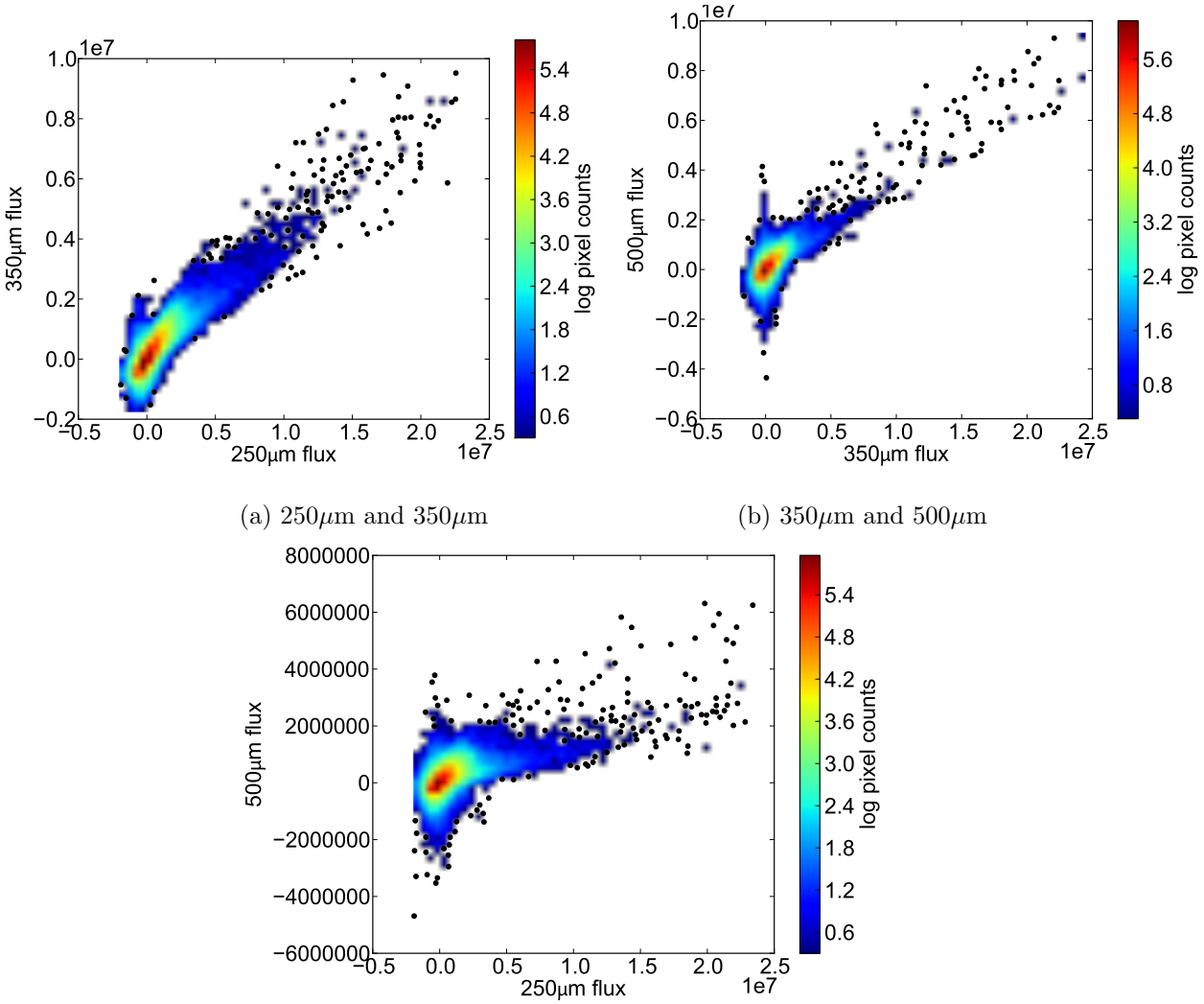

(a) 250μm and 350μm

(b) 350μm and 500μm

(c) 250μm and 500μm

Figure 5.2: Pixel flux against flux in each of the three SPIRE bands representing the 3D pixel flux distribution in COSMOS. The correlation is very strong between all three bands, even present in the 250μm to 500μm plot which would naturally exhibit the least covariance. To make these plots the maps are all resampled and convolved to the same pixel and beam sizes as described below.

separately (or with some model simultaneously fitting all three distributions independently (Glenn et al., 2010)) and a model of number counts found. Figure 5.2 shows the pixel distributions as a density plot, showing 2D projections of the 3D plot of all three SPIRE bands. As expected, the covariance is strong in these bands, especially between the 250μm and 350μm. Further, the covariance is apparent at all fluxes. Note that the density is given as logarithms as most of the fluxes in the map are extremely faint, thus the distribution is extremely clustered close to zero. This additional covariance is missed if treating all three bands independently.

The additional information to be gained when considering multiple dimensional P(D) analysis is clear with the following example in figure 5.3. This toy model is extremely simplistic, using a well resolved image of a "source" when in reality many sources would make up an image. However this particular model is used to make the covariance between images clearer. In this toy model, two distributions of pixels are shown taken from two different images. In the first set of images (a), there is clearly a circular object centred in both images, i.e. a source in both bands represented by images 'top' and 'bottom' with noise. In the second two images (b) however, there is a source in the top image but not in the bottom (the pixels in the bottom image in (a) has been shuffled to create this image). These two sets of images are clearly showing two different distributions.

However, when considering the pixel distribution of the two images (c), the 1D histograms are identical in both sets of images. If one was attempting to determine whether a source existed in both images based on these histograms, a P(D) analysis could imply there is a source in both images. Only when considering the *covariance* between the maps are we able to determine whether there is a source in both top and bottom images or not. The 2-D histograms in (d) show the first set of images in (a) are correlated, whereas the second set of images in (b) are not.

Clearly then, if we extend this simple case to images with many sources, the best way to construct a source model for the SPIRE fluxes is to consider all three bands simultaneously. P(D) analysis across multiple dimensions has not yet been done due to how time-consuming the deconvolution would be, although currently 2 dimensional attempts are being made by Conley & et al. (in prep.). Other studies using one dimensional P(D) analysis like Glenn et al. (2010) do not examine the covariance. The covariance in these analyses is sometimes constrained using a typical spectral energy distribution (SED) for galaxies to enforce covariance.

This chapter discusses the use of an algorithm known as Principal Component Analysis

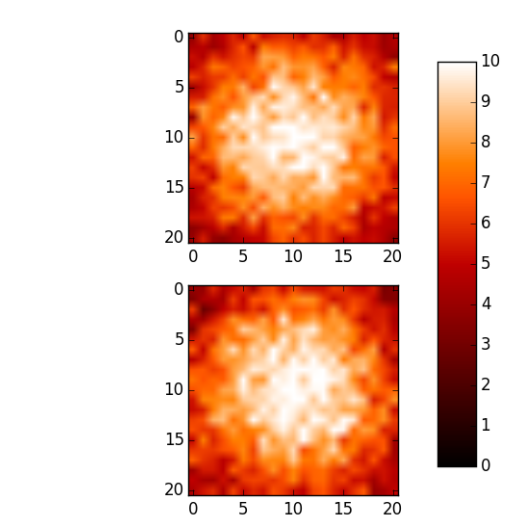

(a) images are correlated

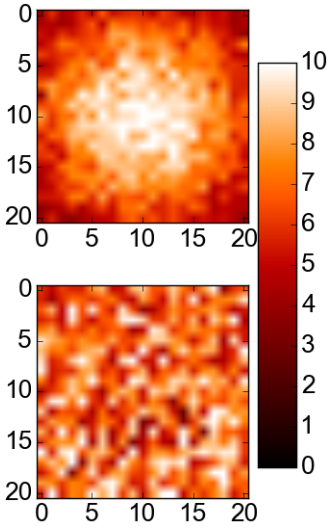

(b) images are uncorrelated

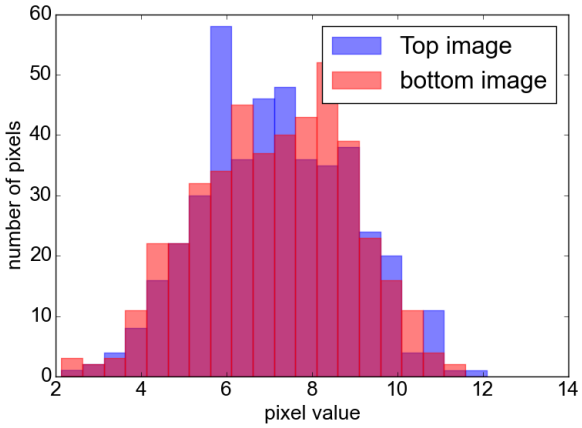

(c) Pixel distributions of x and y are identical

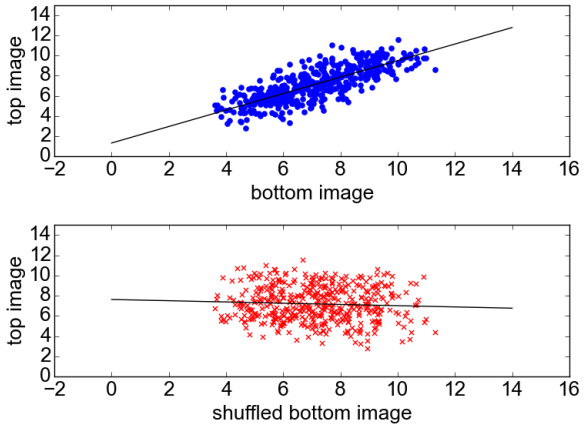

(d) 2D flux distribution shows covariances.

Figure 5.3: An example demonstrating the importance of covariance. Two different sets of images, one with a strong correlation between images (a) and the other not (b), are both shown to have the same pixel distribution (c), with the histogram for 'top' and 'bottom' identical in (a) and (b). By comparing the correlation between the images pixel-by-pixel in (d), the covariance (or lack of) between the images in becomes abundantly clear.

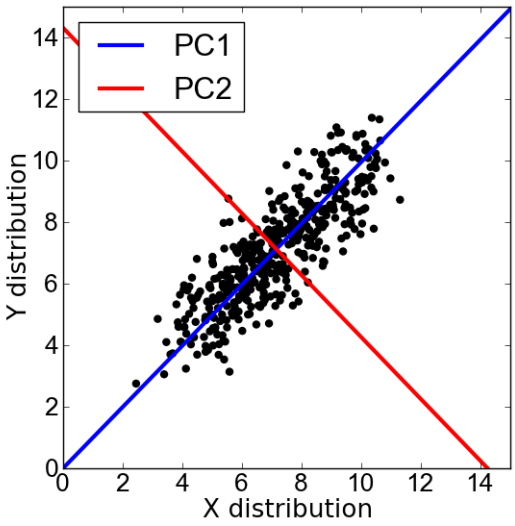

Figure 5.4: A toy model to demonstrate Principal Component Analysis (PCA). The two variables x and y are evidently correlated. The blue line is the line that best captures the covariance of the distribution and is principal component 1 (PC1). The red line is PC2, captures the rest of the covariance and is orthogonal to PC1.

(PCA, Pearson (1901), Jolliffe (2002)) to allow the inclusion of the covariance explicitly between bands whilst keeping the P(D) analysis one-dimensional. Note that this chapter discusses the transformation only and does not perform the full P(D) analysis as this is a proof of concept demonstration.

Figure 5.4 shows a toy model to demonstrate an algorithm known as Principal Component Analysis (PCA). The figure shows the distribution of data with two variables x and y from subfigure (a) in figure 5.3 as as series of points. This plot is similar in appearance to the band-band plots in 5.2 and shows strong covariance between x and y. A model that attempts to fit both x and y independently then will not necessarily capture this covariance. Displaying the data as functions of the two observables x and y may seem like the most natural way to display the data, but it may not be the most informative. Consider this, if one was trying to draw a relationship between the data in 5.4, one might consider a linear fit between x and y as a good way to capture this distribution (represented by the solid blue line). By describing this two-dimensional distribution as a line, we have reduced the dimensionality of the distribution and, if this was a way to describe the distribution of pixel fluxes as in figure 5.2, we would be back to a simpler one-dimensional problem.

Of course, a line does not describe this distribution perfectly. The line was chosen because the total residuals (the sum of the distances from the data-points to the line)

was a minimum (i.e. the χ^2 is smallest), but there is still some deviation away from the line. We have a choice, either to dismiss the residuals as scatter around the line or to parameterise this scatter with another fit. A line orthogonal to the first, centred in the distribution makes most sense, as the data is spread evenly on both sides (red line). By introducing another line we are increasing the dimensionality of the problem back to two dimensions, but this is now not a problem. If we now re-project the data onto these lines now as axes so the axes are a function of x and y, the axes are more complicated, however the data itself looks different. There is now no correlation between axis 1 and 2. This means that any analysis treating the two axes as independent can fully capture the covariance between observables without having to extend to a two dimensional analysis.

This translation and rotation of axes to better capture covariance is therefore intuitive. It is formalised as Principal Component Analysis. Only three observables (corresponding to the three *Herschel*-SPIRE bands) are described in this formalism but PCA is extendible to many dimensions.

Consider a dataset D spanning a three-dimensional space described as

$$D_i(f_{i,250}, f_{i,350}, f_{i,500}) = f_{i,250}\lambda_{250} + f_{i,350}\lambda_{350} + f_{i,500}\lambda_{500} \tag{5.1}$$

where λ_{band} is a basis vector in flux per solid angle units (surface brightness) in that band (e.g Jy/sr), and orthogonal to the others, and $f_{i,band}$ is the flux at pixel i in the map corresponding to that band. NB, it is crucial each map is mean subtracted. This is already the case with *Herschel* maps.

This data has a covariance matrix

$$\Sigma = \begin{pmatrix} \sigma^2_{250} & \mathrm{cov}(\mathrm{f}_{350}, \mathrm{f}_{250}) & \mathrm{cov}(\mathrm{f}_{500}, \mathrm{f}_{250}) \\ \mathrm{cov}(\mathrm{f}_{250}, \mathrm{f}_{350}) & \sigma^2_{350} & \mathrm{cov}(\mathrm{f}_{500}, \mathrm{f}_{350}) \\ \mathrm{cov}(\mathrm{f}_{250}, \mathrm{f}_{350}) & \mathrm{cov}(\mathrm{f}_{350}, \mathrm{f}_{500}) & \sigma^2_{500} \end{pmatrix} \tag{5.2}$$

where σ^2_{band} is the variance of the surface brightness of pixels in that band and $\mathrm{cov}(\mathrm{f_{band}}, \mathrm{f_{band'}})$ is the covariance of the surface brightness between two bands. The variance is defined as

$$\sigma^2_i = \mathrm{E}(\mathrm{f}_\mathrm{i}^2) - (\mathrm{E}(\mathrm{f_i}))^2 \tag{5.3}$$

where $\mathrm{E}(\mathrm{f_i})$ is the expectation value of all the f_i. The covariance is defined as

$$\mathrm{cov(i, j)} = \mathrm{E}[(\mathrm{f_i} - \mathrm{E}(\mathrm{f_i}))(\mathrm{f_j} - \mathrm{E}(\mathrm{f_j}))] \tag{5.4}$$

where f_i and f_j are the vector of surface brightnesses in bands i and j. PCA aims to diagonalise the covariance matrix. This is possible as, by definition, the covariance matrix

is symmetric. The covariance matrix can then be decomposed as

$$\Sigma = W^T \Lambda W \tag{5.5}$$

where W contains the individual eigenvectors as columns (w_1, w_2, w_3) and $\Lambda = \mathrm{diag}(\lambda_1, \lambda_2, \lambda_3)$ represents the eigenvalues. The eigenvectors must be scaled to length one to become unit vectors.

As in the toy model, the first line drawn in figure 5.4 was along the line of greatest variance. This corresponds to the first principal component (PC) w_1. The total variance of the distribution is the sum of the variances along each axis. The eigenvalues of a PC are proportional to the variance of the data along that PC. The explained variance of a PC then w_i is given as $\lambda_i / \sum_j \lambda_j$ i.e. a fraction of the sum of the eigenvalues.

From our toy model, the first PC explains 93% of the variance and the second 7%. This is in contrast to the original distribution that has equal variance in both observables x and y. If the expected variance of the PC is considered negligible (and the variance of the distribution is a complete description of the distribution), then this PC can be ignored and the dimensionality of the data therefore reduced.

This method implicitly assumes that the data is distributed in a Gaussian manner along the PC axes. Results from PCA must be treated with caution for bimodal distributions, heavily skewed distributions or any distribution where the variance is not a complete description of the distribution. There are modifications to PCA that can take into account data with some skew, and one algorithm will be discussed later in the chapter.

5.2 Previous Work Using PCA

Whilst the work presented below is original in the sense that PCA has not been used on Herschel SPIRE maps before, there is a history of using PCA and other component separation techniques within extragalactic astronomy.

Much of the previous work using PCA in astronomy has been used on spectra of galaxies, from full samples of galaxies to sub-sets representing particular populations of galaxies. When the principal components have been found, in some works authors then discuss how to reduce the dimensionality of the data from hundreds of data points in the spectra to a few PCs. For example, using 10 template spectra covering the UV to near-infrared wavelengths (Kinney et al., 1994; Calzetti et al., 1994), Connolly et al. (1995) used PCA to determine only two PCs are needed to represent the data. From there the authors created a classification system to distinguish between elliptical and starburst.

Noting that the distribution of spectra within this two dimensional space followed a line in the subspace, they determined that the galaxy can be described by the angle created when the position of the spectra in the subspace is projected onto the axes. The angle could then be used to classify the galaxy as an elliptical or starburst.This is an extreme example of reducing a multiple dimensional dataset to one dimension to solve a galaxy classification problem.

PCA has also been used on much larger datasets. Bromley et al. (1998) increases the number of spectra analysed to over 26,000 from the Las Campanas Redshift Survey (Shectman et al., 1996; Lin et al., 1996), finding principal components sensitive to morphological type and star formation. They compared their own classification scheme to Connolly et al. (1995) and found their classification scheme more sensitive to the emission and absorption lines.

Building on previous optical classification schemes, Taghizadeh-Popp et al. (2012) used PCA to optically classify SDSS galaxy spectra with only one parameter. The contribution to PCs was projected down into a subspace of PCs physically representing the u-r colour and star formation rate, with individual galaxies lying along an arc in this space. Therefore each galaxy was classified by its position on this arc in a similar manner to the angle used in Connolly et al. (1995).

Classification schemes for galaxies in the optical are well explored, but other work has centred on the infrared to classify star forming galaxies, or to untangle the contribution of many physical processes to the infrared dust emission to better constrain e.g. star formation at these wavelengths.

Wang et al. (2011) ran PCA on 119 Spitzer Infrared Spectrograph (IRS) spectra of ULIRGs (ultra-luminous infrared galaxies) in an attempt to characterise the mid-infrared spectra using all the information available instead of, for example, comparing emission of absorption line strengths as is classically performed to classify and characterise a galaxy, the presence and strength of an AGN, of star formation etc. The study gives physical interpretations to components, with the main component related to the dust temperature, the second related to star formation and the final a correlation of AGN activity and star formation, and concludes that a more holistic approach to classifying ULIRGs would be useful. This study was extended in Hurley et al. (2012b) (software Hurley et al. (2012a)) by finding how many principal components were required to adequately describe the IRS spectra, settling on five, and discussed whether a diagnostic tool can be created with Gaussian mixtures modelling, training the data on the optical classifications of the galaxy's

AGN and finding where in PC space the AGNs reside.

Whilst many PCA analyses have been used to classify or clean galaxy spectra, this is not the only situation in which PCA is useful. Wild et al. (2014) developed a classification system for broad band photometry in the near infrared, using six optical and near infrared filters from Subaru and Spitzer respectively in the UDS field using nearly 40,000 sources. This is closer in nature to the use of PCA discussed in this chapter, using the three broadband SPIRE filters instead of a far-infrared spectrum, although the paper uses sources and not map pixels.

PCA can also be used as a component separation algorithm to remove parts of a spectra that do not arise from the galaxy itself. Wild & Hewett (2005) use PCA to find a component in SDSS spectra corresponding to OH skylines. These skylines were a particular contamination for SDSS spectra, in some cases reducing the signal to noise ratio of spectra by a factor of two. By finding the component related to the OH skylines and subtracting them, the spectra are immediately cleaned.

This component separation use of PCA can be used on the maps themselves. An exploration of the PSF from the WFS (Wild-Field Survey) on the ACS (Advanced Camera for Surveys) instrument onboard the Hubble Space Telescope was conducted in Jee et al. (2007) using PCA, decoupling the spatial and time variance of of the PSF, arising from thermal expansions of the telescope and the camera refocussing. The authors found structures in the PSF beyond the secondary wings of the beam, performing better than previous analyses in this regard. The authors suggest the results could be used for weak-lensing studies, as the beam needs to be known to extremely high precision for these studies. The paper used a beam stacked on many stars, and thus used information directly from the images. However only the PSF is studied and not the map as a whole, unlike the work in this chapter.

Outside of extragalactic astronomy, PCA has been used to find untangle the effect of rotation and precession of proto-stellar jets in Cerqueira et al. (2015) and to isolate and analyse the north-south asymmetry in the atmosphere of Saturn's moon Titan as presented by Karkoschka et al. (2013). MOND (Modified Newtonian Gravity) has also been explored with PCA in Asaba et al. (2013), using PCA to decompose the effects of redshift space distortion and weak lensing on images observed with the future Euclid mission to find any differences to expected observations from general relativity.

Recently, the AMADA software package (de Souza & Ciardi, 2015) has been developed to perform PCA and robust-PCA across catalogues including wavelengths and physical

parameters, recording the results in the form of subspaces, correlation matrices, parameter clustering and other graph-theory staples. The software has been developed from analysis of more general linear modelling performed in de Souza et al. (2015) exploring the relationship between the presence of star formation in mini haloes and the mini halo masses, environment, metallicity and gas fractions in the hydrodynamical simulations of Biffi & Maio (2013) created with GADGET-3 (developed from GADGET-2, Springel (2005)). With software like AMADA now available for astronomers, one would hope PCA and other general linear modelling and component separation techniques will become more popular.

PCA is not the only way to approach component separation of data. Other component separation algorithms include non-negative matrix factorisation, NMF, which can only have positive elements in the principal components. NMF often finds more physically motivated elements than PCA (run on a series of faces, NMF is more likely to pull out individual isolated features as components, for example). NMF was used in Hurley et al. (2014) to find a series of components again for the IRS spectra and applying them to Cornell Atlas of Spitzer/IRS sources (CASSIS) galaxies. The NMF algorithm produced more physical components with an optimal number of seven, including AGN and dust slopes at various temperatures, and pulling out the PAH features as their own component. Using these results the authors derive a classification system based on the relative strengths of components and compare to the commonly used Spoon et al. (2007) diagnostic tool based on the 6.2μm PAH emission feature equivalent width (i.e AGN strength) and the strength of the 9.7μm silicate feature (i.e. dust and therefore star formation), and Armus et al. (2007) comparing again the 6.2μm PAH equivalent width and the ratio of line strengths [OIV]/[NeII]. The authors find their new diagnostic tool to be successful at discriminating between AGN and starburst dominated galaxies and complementary to previous tools.

Whilst NMF is a very useful tool for decomposing spectra PCA was chosen over NMF as this study only uses three wavelengths and thus overcomplicating the analysis at this early stage was seen as unnecessary. Due to the success in the mid-infrared, NMF would be an interesting extension to examine.

5.3 Preprocessing the Maps

Given the three SPIRE maps at 250μm, 350μm and 500μm in a particular HerMES field, we wish to find a coordinate transformation W(250μm,350μm,500μm) such that the covariance between the resultant images is minimised and the variance expressed in the maps

is maximised. In other words, we must perform Principal Component Analysis (PCA) on the maps.

This is not straightforward as the maps have different-sized pixels (6, 25/3,12 arcsec) and beams of different FWHM (18.15, 25.15, 36.3 arcsec). The maps must be at the same pixel size to construct the vector D_i and the same resolution to allow a linear scaling between beams.

The 350μm pixel size does not easily divide into the smallest band, to use these maps either maps of 1/3 arcsec pixel size would have to be constructed which is not feasible, or perform interpolation between pixels which would create strong covariances across pixels in the same map. Instead, pixel sizes of 5,10,15 arcsec were requested for four maps; Nested-Lockman-SWIRE, Nested-CDFS-SWIRE, COSMOS and GOODS-North to cover a variety of depths in singular fields. This allows the calculation of the exact principal components of the maps without worrying about interpolation effects of resizing pixels in the 350μm band. As the flux is being rebinned into different size pixels rather than interpolated, the PCA analysis will be valid on the normal maps.

To put the maps to the same pixel size and resolution they are treated as follows:

- **unit correction:** All maps are transformed to units of Jy/sr, a unit that is not dependent on beam or pixel size.

- **smoothing:** All maps have their NaN values flagged and set to zero. Then each map is iteratively smoothed with a Gaussian beam of 4 pixels (greater than the FWHM of the beam) until the value of the pixels previously flagged as NaNs do not vary more than a specified tolerance limit (1e5 for Jy/sr maps). After each smoothing the flagged pixels are replaced with their smoothed value, and the smoothing run again in this adapted original map. This smoothing is to prevent NaNs, that are by default treated as zero during the convolution, from reducing the total flux in the map during the convolution.

- **convolution:** The 250μm and 350μm maps are convolved to the 500μm resolution. This is achieved using kernels and code from Aniano et al. (2011). These kernels have been created using azimuthally averaged SPIRE beams to transform maps between one beam size to another. These averaged beams are preferred as the orientation of the telescope in any one pixel is unknown. The kernel is gridded to 1 arcsec by 1 arcsec, resampled to the map sizes and normalised to sum to 1 (i.e. area under the kernel is 1), the map is padded with zeros to allow the FFT to be performed faster during the convolution.

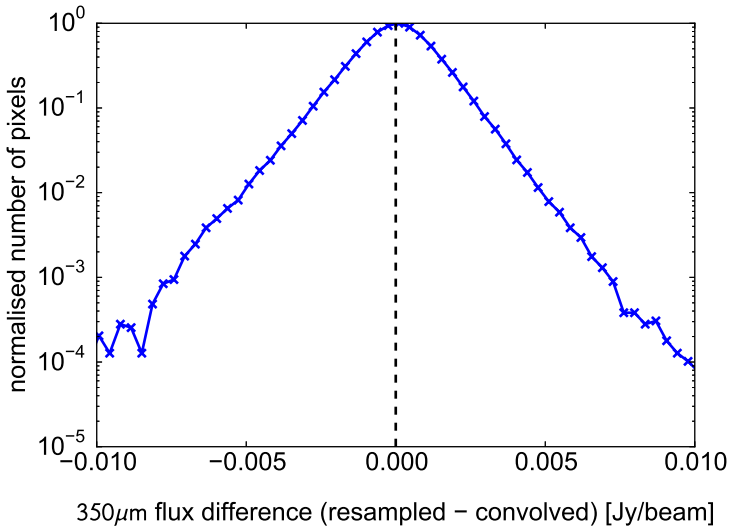

Figure 5.5: Residuals when first resampling or convolving maps as demonstrated on the GOODS-N 350μm map. Resampling first effectively smoothes the 350μm maps. the difference between pixels is negligible and most importantly symmetrical about zero.

- **resampling:** The 350μm and 500μm maps are resampled to the 250μm pixel scale using nearest neighbour resampling. The is effectively splitting the 350μm and 500μm pixels into 4 and 9 separate pixels respectively. Masks representing the location of NaN pixels are resampled in the same way.

- **NaNs replaced** NaN pixels are replaced in the convolved and resampled maps - if one pixel in one map contains a NaN then this is applied to all maps.

One might have some trepidation over which order the convolution and resampling should be performed for the 350um map.

Resampling first would ensure a beam at a finer resolution was used during they convolution and therefore the resultant map was smoother. Convolving first gives the beam a 350μm a "blocky" appearance like the 500μm. However, resampling the maps first introduces covariances between pixels within one map. This presents issues later in this chapter when a different method of finding the principal components is employed, and this will be fully explored. For now, both methods, resampling first and convolving first are performed and the 350μm compared by subtracting the value of the pixels and creating a histogram. Figure 5.5 shows these differences on the GOODS-North map. The 90% of differences between pixels are between ±5mJy/beam difference. More importantly this variance is centred on zero and therefore these differences will not skew any result using the variance of the map.

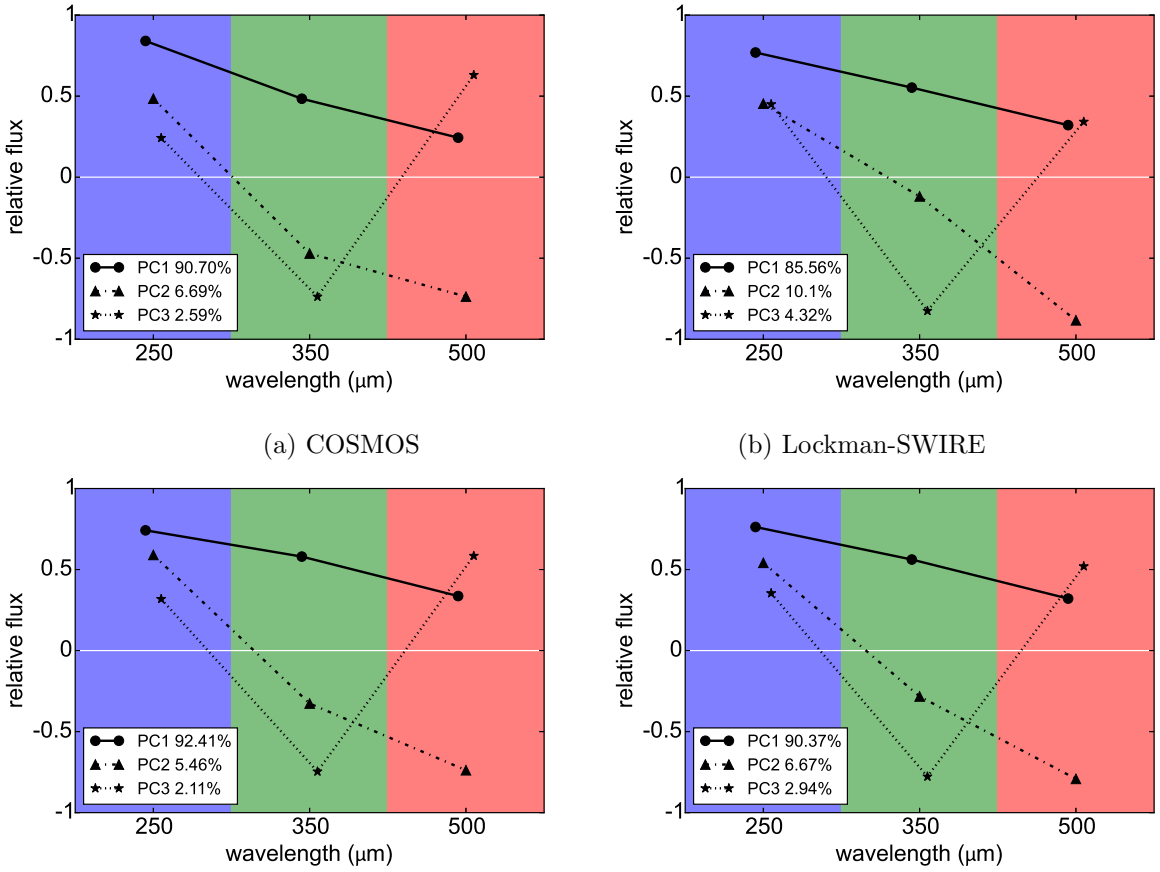

(a) COSMOS

(b) Lockman-SWIRE

(c) GOODS-N

(d) CDFS-SWIRE

Figure 5.6: Principal components for the simplest implementation of PCA. Notice the field-to-field variations and how the deepest fields have the highest explained variance in PC1.

5.4 Simple PCA

Each set of three maps are transformed to one dimensional vectors for each field. Then the PCA algorithm is applied across every set of pixels in the maps. The result is a set of three eigenvectors w_1, w_2, w_3 and eigenvalues, $\lambda_1, \lambda_2, \lambda_3$ and the explained variance calculated. The values from each field are given in table 5.1 and shown in figure 5.6. The general results are first discussed below, and then specific field-to-field results are discussed.

Each field does give different values for the eigenvectors but the broad result of the PCs are the same. w_1 by definition contains the most variance and is positive for each map, i.e. the maps are strongly correlated in the shown proportions. w_2 is showing a component that is positive in the 250μm and negative in the 500μm bands. Finally, the w_3 is correlating the 250μm and 500μm bands and anti-correlating the 350μm band.

These can be interpreted in terms of the shape of spectral energy distributions (SEDs)

field	band	explained variance	contributions 250μm	350μm	500μm
COSMOS	PC1	90.7	0.841	0.484	0.244
	PC2	6.7	0.485	-0.471	-0.7373
	PC3	2.6	0.242	-0.737	0.631
Lockman-SWIRE	PC1	85.6	0.769	0.553	0.321
	PC2	10.1	0.454	-0.119	-0.883
	PC3	4.3	0.450	-0.825	0.342
GOODS-N	PC1	92.4	0.742	0.580	0.336
	PC2	5.5	0.590	-0.327	-0.738
	PC3	2.1	0.318	-0.746	0.585
CDFS-SWIRE	PC1	90.4	0.763	0.562	0.321
	PC2	6.7	0.541	-0.283	-0.792
	PC3	3.0	0.354	-0.777	0.520

Table 5.1: Principal components for the simplest implementation of PCA as shown in figure 5.1. In all fields, over 85% of the variance is explained by the first PC. PCs follow a similar trend in shape.

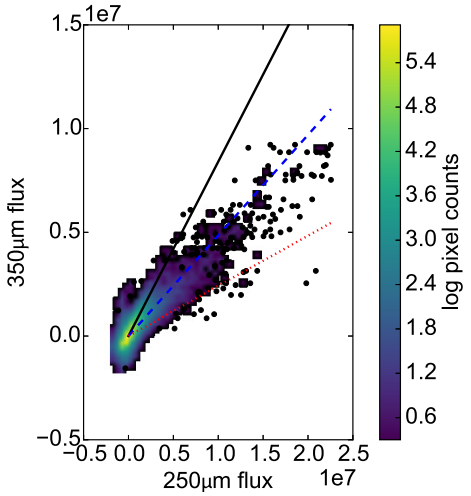

(a) 250μm and 350μm

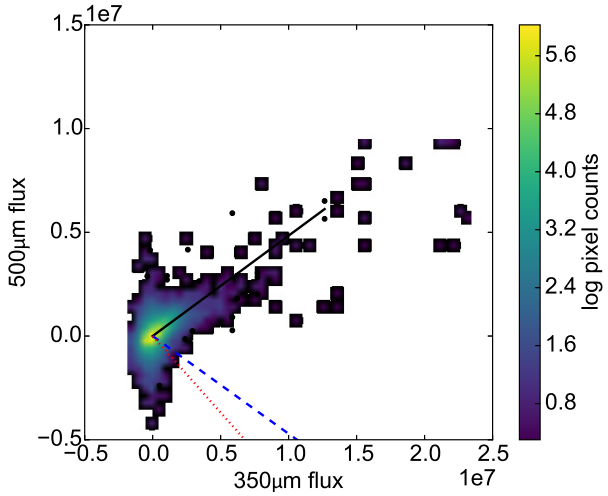

(b) 350μm and 500μm

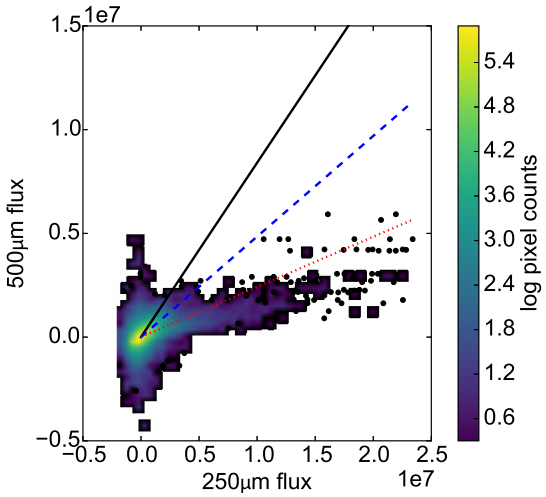

(c) 250μm and 500μm

Figure 5.7: 2D projections of the PCs found when using the simplest PCA on COSMOS fit to the pixel flux distribution.

of galaxies. If we think of the dataset as a collection of SEDs from a variety of galaxies as opposed to a map summing them in a spatial distribution this begins to make sense. w_1 is some form of average SED, representing the curve of the blackbody caused by dust emission in the far-infrared. A positive w_2 value attributed to a source would push the dust peak towards the bluer end and a negative w_2 contribution pushes the peak of the galaxies to the redder end. w_3 is behaving as a broadening, a positive contribution is effectively broadening the 500μm band as the 250μm and 500μm bands are made brighter and the 350μm suppressed, and a negative contribution a narrowing of the peak. The process of redshifting the sources would broaden the overall SED in this manner, as well as translating the dust peak as in w_2.

To interpret these observations as intrinsic properties of galaxies is more tenuous but broadly speaking one would expect a very bright galaxy to have a strong w_1 component and relatively strong (positive or negative) w_2 and w_3 adjustments (although, if w_1 was a perfect descriptor of this galaxy, w_2 and w_3 would not be required). NB w_1 is not finding the luminosity of galaxies as this is requires knowledge of the redshift to find, it is purely related to the intensity.

w_2 and w_3 therefore are more due to the shape of the SED and would therefore encode information on redshift (shifting and stretching the distribution to lower frequencies and reducing the intensity) and the temperature and emissitivty of the SED, setting the peak and width of the SED.

An extremely red object (HFLS3, Riechers (2013) for example) would have some component in w_1 as the source will have some intensity associated to it. This w_1 component will have a positive w_3 component broadening the object and an extremely strong negative component in w_2 to skew the peak of the SED to the red part of the spectrum. A very bright star-forming galaxy at low redshift would have a very bright positive contribution in the w_1 component, have a positive w_2 contribution to make the peak at a bluer wavelength and a slight negative w_3 component to narrow the SED.

Comparing field-to-field results in table 5.1, the first consideration are the differences between the explained variances. In all cases an extremely high explained variance is observed in w_1 (above 85%) implying that the majority of the variance in the maps can be mimicked from fitting to the first principal component. w_3 is between 5% and 2%. If one wanted to reduce the dimensionality of the problem, one could consider ignoring this principal component. However as the variance is not a complete description of the distribution, this particular component is represented strongly by some extreme galaxies

and therefore to fit the entire population correctly the three PCs should be considered.

GOODS-N has the highest explained variance in w_1, and Lockman-SWIRE the lowest. This can be attributed to the size of field; GOODS-N is extremely small and thus the extreme objects are less likely to be sampled in the maps, therefore these sources will not contribute to the variance to make fitting principal components difficult. Essentially the variance is reduced due to cosmic variance. The other explanation is a relative lack of instrumental noise. GOODS-N is a deep map, constructed with many scans. Lockman-SWIRE on the other hand is noisy. Whilst the instrumental noise is independent in each band it does add to the variance and therefore the calculated variance values that are used for each band in the PCA calculation will be greater than the underlying variance of the source population. Following this rule of thumb then one would expect the COSMOS map to have a greater explained variance in w_1 than CDFS-SWIRE, the higher contribution of the 250μm band to w_1 indicates that the population of sources is bluer in COSMOS than other fields. COSMOS however, has very different w_1 values in comparison to other maps. This indicates that the surface brightness of pixels within this map are different from the other fields in some manner and which could be explained by cosmic variance.

Figure 5.7 shows the fit of the COSMOS PCs to the two-dimensional projections of the three-dimensional pixel flux distributions. The black solid line is w_1, the blue dashed w_2 and green dotted w_3. w_1 clearly fits the main correlation between all bands, with w_2 and w_3 providing the widths.

On closer inspection however, the fit for w_1 does not appear to pass through the majority of points, concentrated near the origin. w_1 however does pass through the majority of points when one considers the density of points in this region. This is because the majority of pixels are following a relation between all three bands that is different to the extreme pixels. That same population of pixels is tracked by w_1 when comparing the 350μm and 500μm bands. w_2 and w_3 in 250μm against 350μm especially are tracking the more extreme pixels. Interestingly nothing is directly fitting to the pixels in the 250μm against 500μm plot. This is either because there is a better fit closer to the origin (e.g. w_3 is close to fitting to the correlated pixels), or a projection effect.

The latter explanation is not surprising. Hurley et al. (2012b) briefly discussed the non-Gaussian nature of the spectral data used and whether that would cause issues in the decomposition and in that case it was dismissed. However, galaxy formation is a non-linear process so it stands to reason that finding a set of orthogonal principal components derived from all the data may not accurately represent any part of the galaxy population.

field	band	explained variance (%)	contributions 250μm	350μm	500μm
COSMOS	PC1	89.5	0.750	0.575	0.327
	PC2	6.9	0.527	-0.220	-0.821
	PC3	3.5	0.400	-0.788	0.468
Lockman-SWIRE	PC1	84.5	0.735	0.579	0.354
	PC2	10.8	-0.446	0.019	0.895
	PC3	4.8	-0.511	0.815	-0.272
GOODS-N	PC1	92.9	0.729	0.591	0.345
	PC2	5.0	0.613	-0.340	-0.713
	PC3	2.1	0.304	-0.732	0.610
CDFS-SWIRE	PC1	90.3	0.741	0.580	0.340
	PC2	6.5	0.541	-0.214	-0.814
	PC3	3.2	0.399	-0.7861	0.472

Table 5.2: Principal components when using kappa-sigma clipping to remove pixels, data given in 5.8.

The issue of the skew of the data is explored below to find whether a cleaner approximation to the data using PCA can be found, with the ultimate aim to find the projection of data that can explain the most variance with one or two principal components. A number of other approaches are taken below and the situations when the results would be appropriate to use are discussed.

5.5 The Effect of Clipping Skewed Pixels

As discussed previously, whether the variance and covariance provides a complete description of the distribution of pixels is dependent on the shape of the distribution itself. If the distribution is made from orthogonal Gaussians there is no higher moment to the distribution than the variance. The distribution of pixels in this chapter is a skewed Gaussian however, this means that some of the information is not captured. The simplest form of PCA is not designed for skewed data. The skew is only in one direction in multi-dimensional space PCA can still be performed in some capacity as the PCs can follow the direction of greatest variance, one just has to be careful in the treatment of the data that skews the distribution and the interpretation of the resultant PCs.

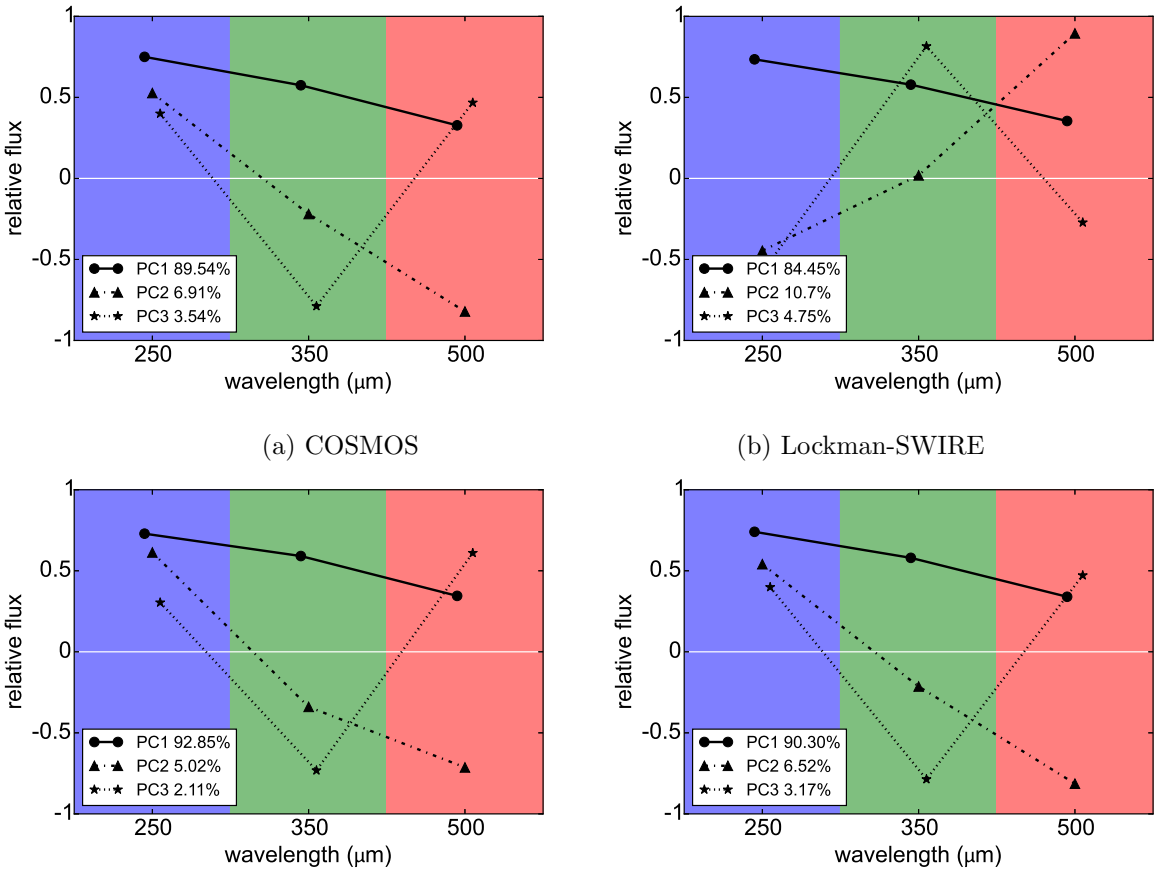

(a) COSMOS

(b) Lockman-SWIRE

(c) GOODS-N

(d) CDFS-SWIRE

Figure 5.8: Principal components when using kappa-sigma clipping at 5σ. Even though some pixels have been excluded, there is not much improvement on the simplest implementation of PCA if at all.

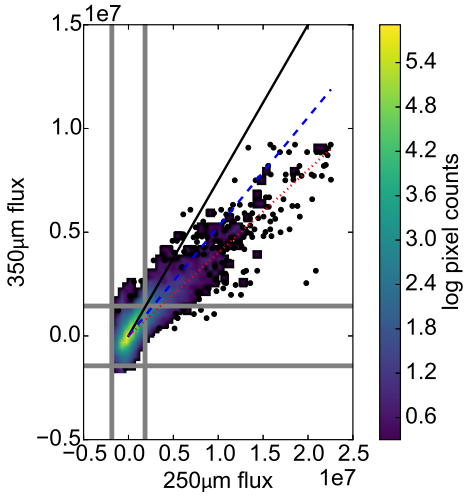

(a) 250μm and 350μm

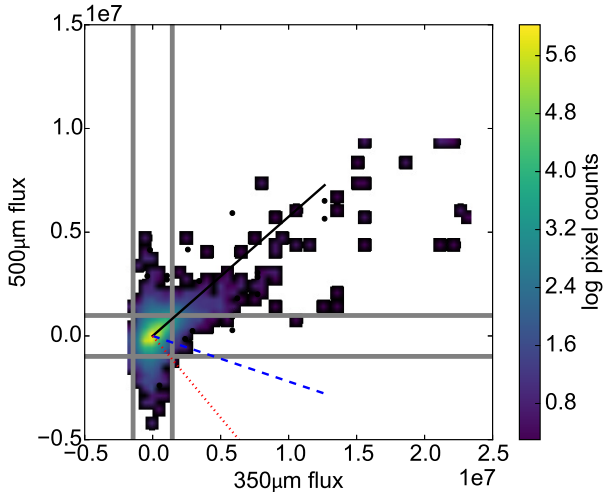

(b) 350μm and 500μm

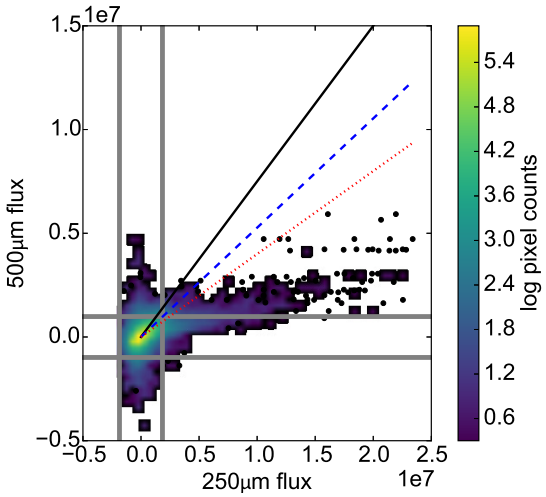

(c) 250μm and 500μm

Figure 5.9: 2D projections of the PCs found when using kappa-sigma clipping COSMOS fit to the pixel flux distribution. Pixels that are not used are outside the 5σ line indicated by the grey lines.

To this end the PCA algorithm was modified to exclude pixels brighter than 5-sigma away from the mean using kappa-sigma clipping simultaneously across the bands. Kappa-sigma clipping (previously described in chapter 2) involves iteratively finding the mean and variance of a distribution and excluding data $\kappa\sigma$ away from the mean of the distribution.

The mean and variance is calculated across all pixels in one band and any pixel 5σ away from the mean value in any band is removed from the distribution of all three. 5σ was chosen as the cut-off value to ensure the majority of pixels were included bar the most extreme values. This excludes extreme pixels that form part of the skewed end of the distribution especially. This calculation is iterated until no more pixels are removed - this take approximately five iterations. In COSMOS <1% of pixels were excluded. The mean for each map was used to recentre maps to zero and the principal components recalculated. Figure 5.8 shows the results, table 5.2 and figure 5.9 projections on COSMOS. Figure 5.8 shows which pixels were discarded from the analysis with grey lines indicating the 5σ thresholds. Note, the w_2 and w_3 PCs for Lockman-SWIRE appear different from the others in table 5.2, although the individual components are just negative compared to the same PCs in other fields. A negative eigenvector is still an eigenvector, and so these PCs are effectively the same just with negative contribution to the PCs.

Sigma-kappa cutting works very well to exclude, as shown in chapter 2, a small populations of pixels in a bimodal distribution. However, when the pixels are from the same slightly skewed distribution the effect of sigma-kappa cutting is very arbitrary. Further, running this in multiple dimensions leads to these very sharp cuts in the distribution as shown by the grey lines in figure 5.8. As <1% of pixels have been removed in each case, the effect on the calculated PCA values is not very great even though the most extreme pixels have been removed. Specifically, comparing the tabulated results in 5.1 and 5.2, the greatest effect has been on the value of the elements in COSMOS w_1, reducing the 250μm contribution by 10% and bringing the values into line with the other fields. Comparing the other results, the explained variances remain similar, only changing by a fraction of a percent and elements of the PCs changing by only a few percent at most. This demonstrates that these extreme pixels, bright as they are (and therefore any fitting procedure would be drawn to them) are not necessarily leading the variance measurement and therefore calculation of PCs.

The cuts applied to the data are very ad-hoc, with the cuts as functions of the original basis vectors of the distribution rather than a function of the distribution for example. This means that the shape of the distribution is far from Gaussian in appearance. Due

to this sigma-kappa cutting is therefore not an ideal way to removed skewed pixels within the distribution. A more consistent method would be preferred.

Such an algorithm exists. The Robust Principal Component Analysis with Adjusted Outlyingness (ROBPCA-AO) works with skewed Gaussian-like data. By using this method it is hoped that the explained variance in w_1 will also increase in each field, with the hope of reducing the contribution of w_3 in particular to the distribution to possibly reduce the dimensionality of the data.

5.6 Robust Principal Component Analysis

As implied, Principal Component Analysis reprojects data on the eigenvectors on the covariance matrix. For the covariance matrix to be a complete description of the distribution, the data should be distributed as a symmetrical multidimensional Gaussian in some frame of reference. As we have shown, the data does not conform to this distribution, with many more bright pixels from bright galaxies than faint ones. In similar cases, an attempt to transform the data can be made; representing the data in log-space would reduce the skewed nature of the data considerably, however many of the pixels are negative (the mean of *Herschel* maps is zero as there has been no definitive background measurement made) and so an artificial background would have to be added to make all the pixels positive. At this point, any data transformation would make the interpretation of the resultant principal components and the reprojection of the data unintuitive.

The ROBPCA-AO algorithm (Robust Principal Component Analysis with Adjusted Outlyingness, Hubert et al. (2009)) instead calculates the covariances between datasets by finding and excluding the contributions of outlying data in a more robust fashion than sigma clipping. We outline below the crucial steps in the ROBPCA algorithm from Hubert & Rousseeuw (2005) and the modifications made for ROBPCA-AO, but refer the reader to the relevant papers for a more in-depth discussion.

- **Choose the coverage,** α: The number of datapoints to be included in the calculation is set by α. This in turn sets $h = \alpha n$ rounded down (where n is in this case the number of pixels in one map) to give an absolute value for the number of pixels to include in the calculation. The default value of $\alpha = 0.75$ is kept for this study.

- **Calculate the (Adjusted) Outlyingness, mean and covariance matrix**: This is given as

$$\mathrm{outl}(x_i, X) = \sup_{v \in B} \frac{|x_i' - m(x_j' v)|}{s(x_j' v)} \tag{5.6}$$

where x_i represents the surface brightness of a pixel in band i in pixel number X, m is the Minimum Covariance Determinant (MCD) estimator of location and s is the estimator of scale, and B is a set of 250 directions in the data drawn between two randomly selected data points. The MCD estimator attempts to find h observations from the total n that, together, have the smallest determinant in the calculation of the covariance matrix. The MCD estimate of location is the average of this subset of points and the estimate of scatter or scale is the covariance matrix. The determinant is a measure of the "volume" of the data, representing the scatter in the dataset. Therefore, MCD chooses h number of points with the smallest "volume" and thus eliminating outlying points. The function "sup" is the supremum, the least value that is greater than or equal to all the data within (related to, but not the equivalent of, the maximum value).

The *adjusted* outlyingness calculated in Hubert et al. (2009) instead uses median and interquartile range values rather than MCD estimators with means, the full calculation being

$$AO_i = \max v \in B \frac{|x_i'v - \mathrm{med}(x_j'v)|}{(c_2(v) - \mathrm{med}(x_j'v))I[x_i'v > \mathrm{med}(x_j'v)] + (\mathrm{med}(x_j'v) - c_1(v))I[x_i'v < \mathrm{med}(x_j'v)]} \tag{5.7}$$

with c_1 the smallest observation which is greater than $Q_1 - 1.5e^{-4MC}IQR$, with Q_1 the first quartile, IQR the interquartile range and MC the medcouple, and c_2 the largest observation which is smaller than $Q_3 - 1.5e^{-3MC}IQR$. The medcouple is a robust measure of skewness that is calculated from the median difference from the left and right halves of a distribution rather than the third moment of the data distribution. The specific calculation of these values is noted for completeness of explanation rather than full understanding being required by the reader, more important to note is the adjusted outlyingness calculation is able to identify outliers in extremely skewed distributions by relying on median values and interquartile ranges of data. This technique can handle data skewed in many directions and so bodes well for the *Herschel*-SPIRE data. More directions are included in B to compensate for skewed data, although this increases the computational time.

- **Compute robust centre and covariance matrix in this new subspace**: The selected h pixel sets are then run again through the MCD estimators to find the principal components. When using the adjusted outlyingness calculations, the mean

and covariance matrix is computed from the h points with the lowest adjusted outlyingness.

NB there are extra steps that can be taken to reduce the dimensionality of the data within the algorithm itself. However, this step has not been taken in this investigation as reducing the dimensionality may not be appropriate.

The above algorithms come packaged as Matlab code. The only modification made to the code was to lift the limit on the number of data points to use in the calculation. Originally the algorithm forced a limit of $n = 5e4$ data points. This corresponds to a square of side length 223 pixels or 18.6 arcmin. This is not a very large region and as such could suffer from cosmic variance. Selecting the data points randomly is a better idea, although again one would wish to sample the largest number of pixels possible. The limit is adjusted to 1e6 pixels and the pixels are selected randomly from the data. This means all of GOODS-N is included and a randomly selected subsample of pixels (39.0%, 15.1% and 9.86%) from COSMOS, CDFS-SWIRE and Lockman-SWIRE. This random selection was performed many times as a check on Lockman-SWIRE and the PCs were found change in values $< 0.1\%$. This extremely stable value of the components can be attributed to the size of the PSF; the flux from one source is spread over many pixels, and so a random selection of pixels of this size is bound to use a pixel influenced by each source.

Further, with only 75% of pixels being used to calculate the PCs, pixels belong to the more extreme objects will be excluded in favour of pixels closer the origin regardless, where the distribution of pixels is already better sampled.

The selected pixels are run through the ROBPCA-AO algorithm and the PCs are calculated and projected onto the data in figure 5.11. From figure 5.10 and table 5.3 the appearance of the principal components has not changed substantially even though many pixels have been discarded, but the explained variance captured has; in all cases the variance captured by w_1 has increased marginally (1.5-3%) and the contribution to w_2 and w_3 dropped. Whilst clipping the data achieved the same effect of removing outlying sources, the far more robust calculation with ROBPCA-AO has made an improvement on the explained variances.

In all cases the explained variance in w_1 has increased by a few percentage points, transferred from mostly w_2. COSMOS now has a higher explained variance then CDFS-SWIRE in w_1. The values of w_1 are now more in line with the rest of the results. As this was not the case with the implementation of the simplest version of PCA which included

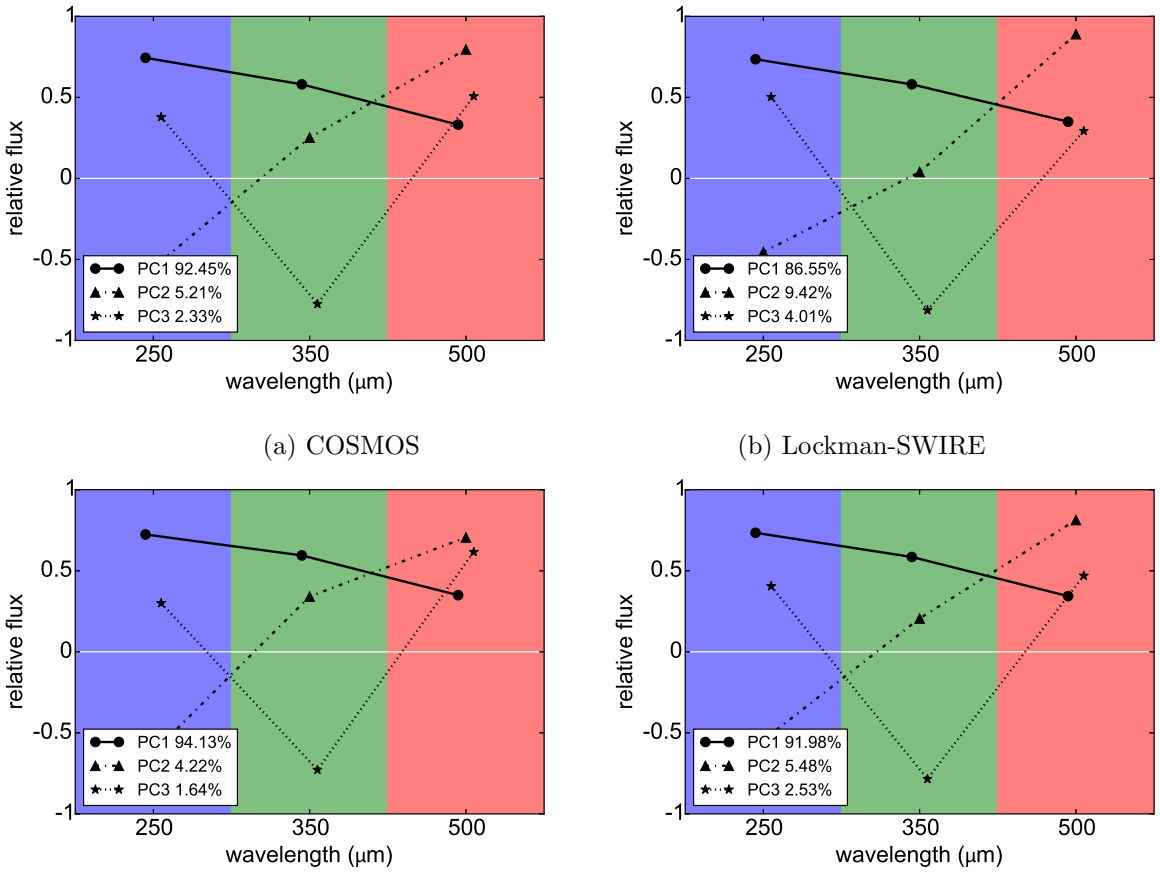

(a) COSMOS

(b) Lockman-SWIRE

(c) GOODS-N

(d) CDFS-SWIRE

Figure 5.10: Principal components when using ROBPCA-AO. Only 75% of pixels are used to calculate the variance of this data. The explained variance is higher in PC1 compared to simplest implementation of PCA.

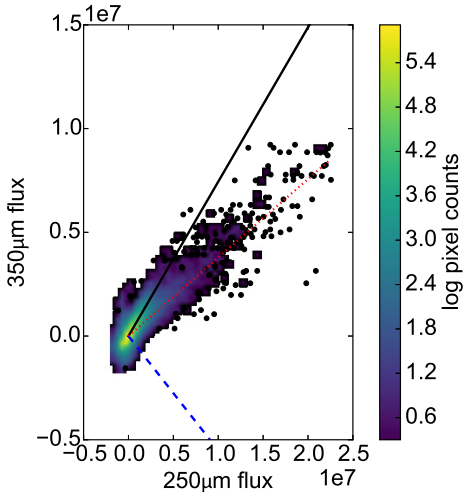

(a) 250μm and 350μm

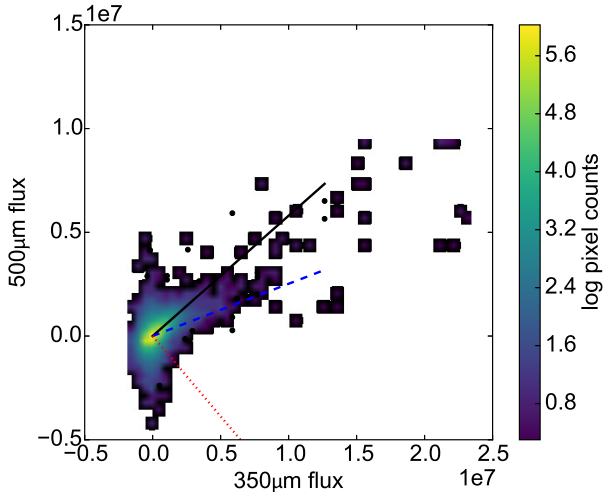

(b) 350μm and 500μm

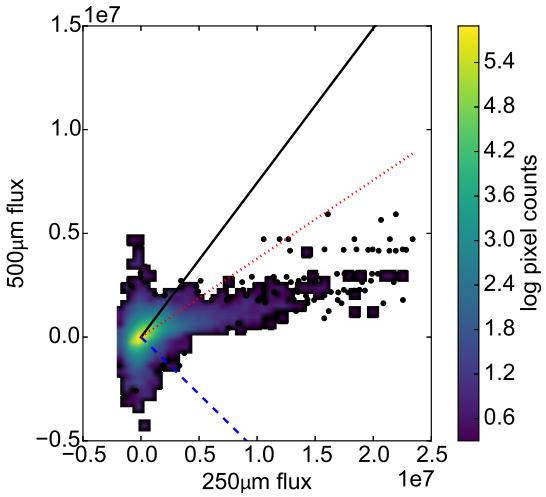

(c) 250μm and 500μm

Figure 5.11: 2D projections of the PCs found when using ROBPCA-AO in COSMOS and the fit to the pixel flux distribution. The fit is much better to the densest part of the

field	band	explained variance (%)	contributions 250μm	350μm	500μm
COSMOS	PC1	92.5	0.744	0.580	0.331
	PC2	5.2	-0.551	0.252	0.796
	PC3	2.3	0.378	-0.774	0.507
Lockman-SWIRE	PC1	86.6	0.735	0.580	0.350
	PC2	9.4	-0.455	0.039	0.890
	PC3	4.09	0.502	-0.813	0.293
GOODS-N	PC1	94.1	0.724	0.595	0.349
	PC2	4.2	-0.621	0.342	0.706
	PC3	1.6	0.301	-0.728	0.616
CDFS-SWIRE	PC1	92.0	0.734	0.585	0.343
	PC2	5.5	-0.544	0.206	0.813
	PC3	2.5	0.405	-0.784	0.470

Table 5.3: Principal components when using ROBPCA-AO to remove pixels, data given in 5.10

all the pixels, the change then could be attributed to cosmic variance. As the brightest pixels - pixels containing flux that is more likely to belong to nearby objects - have been removed, the remaining pixels must belong to the background of sources. These sources are less susceptible to the effects cosmic variance due to their distance as at higher redshifts more sources are contained within one solid angle.

Figure 5.12 shows the flux distribution for pixels in COSMOS, this time for the three principal components (compare with 5.1 for the original distribution) for all pixels, not just the 75% used in the calculation. Each histogram has been normalised to one to aid comparisons of the variance of the distribution by eye. The contribution in w_2 has been reversed so the skew is in the same direction as the other PCs, the direction of each PC can be reversed without any loss in meaning as it is a vector. Immediately obvious is the variance of the three distributions, the first principal component w_1 is far broader as indicated by the explained variance by the algorithms. Thus, most of the variance has indeed been transferred to w_1. However, as the explained variance of w_1 is around 20 times that of w_3 one would expect the width of the distribution in w_1 to be approximately 4.6 times wider than w_3. This would be the case if the data was represented by perfect Gaussians. As it stands, the skewed distribution remains in w_2 and w_3, implying that the

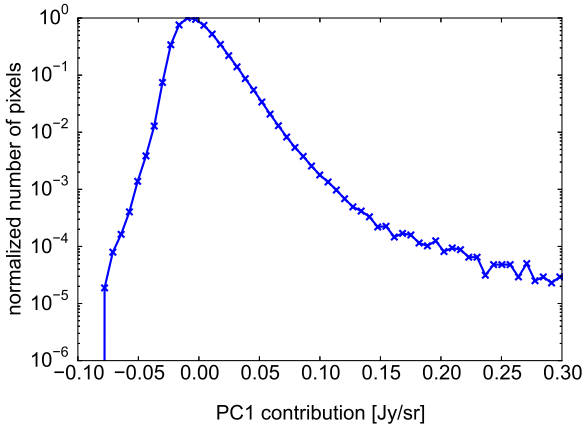

(a) 250μm and 350μm

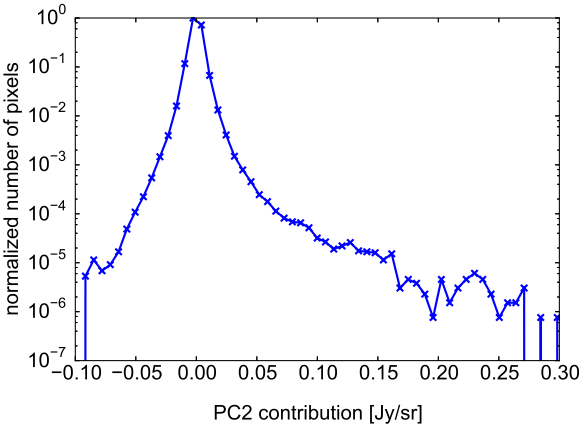

(b) 350μm and 500μm

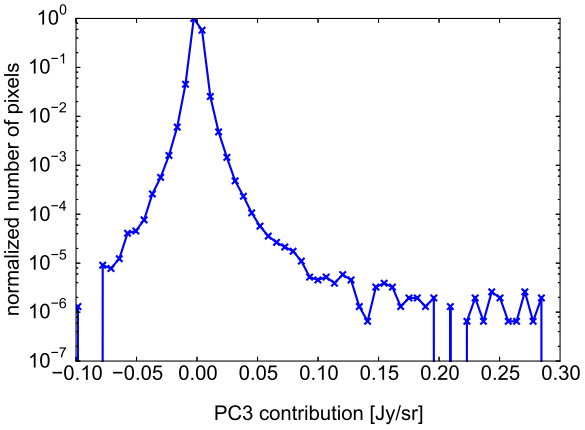

(c) 250μm and 500μm

Figure 5.12: 1D pixel distribution reprojected down onto the PCs found when using ROBPCA-AO in COSMOS.

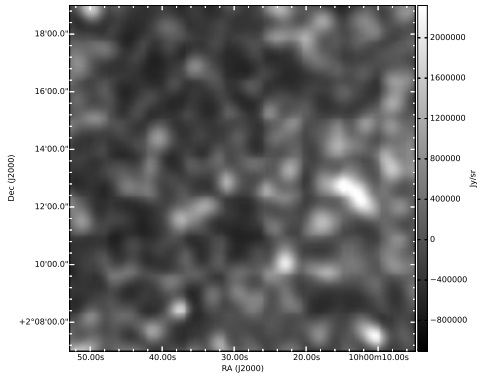

(a) 250μm

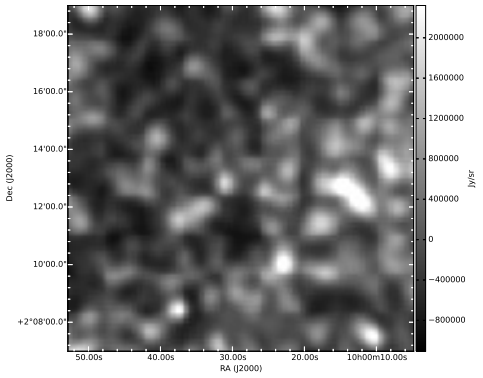

(b) PC1

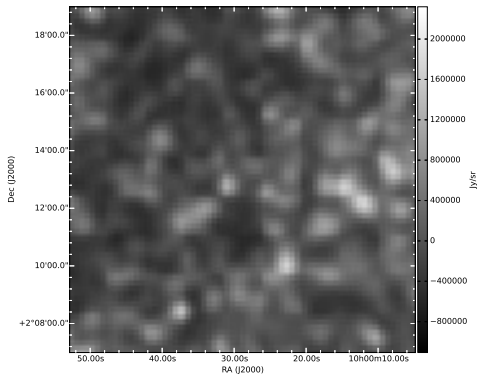

(c) 350μm

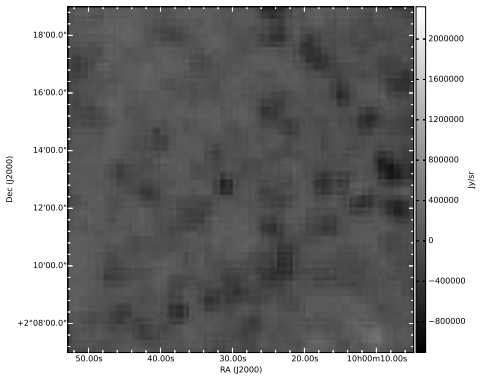

(d) PC2

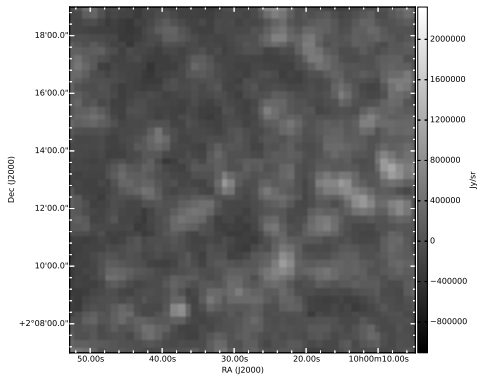

(e) 500μm

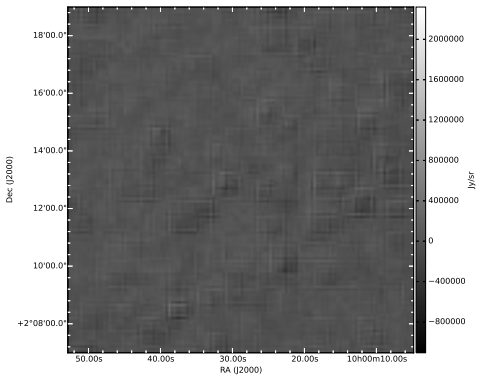

(f) PC3

Figure 5.13: The original and reprojected maps in COSMOS with ROBPCA-AO. The same few sources are shown in each image, however the scaling of the map has been fixed to show how the variance is moved from one PC to another.

skew was in multiple dimensions and not just one direction. Nevertheless, the dynamic range of w_2 and w_3 is far smaller than w_1 implying that, whilst one would not want to ignore the third principal component to reduce the dimensionality of the problem, fitting to the distribution represented in w_1 first would be preferable.

Figure 5.13 demonstrates the change in dynamic range after applying the PCA transformation. On the left are the 250μm, 350μm and 500μm stamps all fixed to the same flux range - 500μm is less bright than the 250μm band in general. On thought is the w_1, w_2 and w_3 show a considerable difference in that the bulk of the dynamic range is indeed in w_1. w_2 and w_3 both have positive and negative contraptions but the range of values is far smaller than in w_1, and many sources in w_1 are without a counterpart in w_2 and w_3. One can therefore clearly see the use of PCA; whilst the flux-flux distributions show there are many different populations of high-flux pixels that PCA is not fitting to and thus reducing the dimensionality may not be preferable, one can treat these PCs reasonably independently.

5.7 Confusion Noise Covariance Matrix

The ROBPCA-AO algorithm has provided a more stable and robust measure of the principal components by removing the contribution of the very bright sources to the calculation of variance. However, the principal components are calculated on each field and are therefore specific to the exact noise properties and size of each field. There was definite evolution of the explained variance of the principal components with depth of field, implying that instrumental noise is creating some variance. To use PCA on Herschel data for further analysis with this method, one would then argue that principal components for each field would have to be provided as each field has different noise properties. This would therefore not extend to fields outside the four used here. Ideally, a universal set would be constructed that is independent of noise, and this is attempted below, using the confusion noise estimation method in Nguyen et al. (2010) which was first seen in chapter 2 and is reviewed and extended here.

Each map can be constructed as:

$$d_i = f_i + n_i \tag{5.8}$$

where d_i is a pixel i in the map, f_i the true flux of the sky at that position and n_i instrumental noise, a noise value which, in the SPIRE maps, is drawn from a Gaussian distribution and has dependence on the exposure time of the pixel. Flux from correlated

1/f noise is considered removed from the timelines before the map is constructed. The variance in the map is therefore characterised as

$$\sigma^2_{T,i} = \sigma^2_{conf} + \sigma^2_{inst}/t_i \tag{5.9}$$

where $\sigma^2_{T,i}$ is the total variance at pixel i, σ^2_{inst} the variance associated with the Gaussian from which the instrumental noise is drawn from (here on referred to as the instrumental noise), t_i the exposure time and σ^2_{conf} the intrinsic variance associated with the flux of the sky (here on referred to as the confusion noise). Again note that this confusion noise has a different method of calculation from the values calculated in the constructed HerMES catalogues.

In noisy fields like Lockman-SWIRE, the variance of the maps, whether clipping the bright fluxes or not, is greater than GOODS-N. This is because the average integration time at each pixel is lower and therefore the instrumental noise greater. It stands to reason that, at infinite integration time, the contribution to the noise from instrumental noise will be zero, and therefore any variation in the map will be from confusion noise alone. Thus it would be preferable to perform PCA by populating the covariance matrix with variances and covariances representing the sky alone.

The underlying confusion noise can be found in the maps by binning pixels according to integration time, finding the variance of these pixels, σ^2_T and fitting a straight line against $1/t$. The gradient will be the instrumental noise and the y-intercept the confusion noise as shown in chapter 3. This gives the values for the leading diagonal of the covariance matrix. The off-diagonal terms are simply the covariance of the maps, as the instrumental noise is independent in each band (as explained in chapter 2) and thus exhibits no covariance.

The Lockman-SWIRE maps are used for this study. Both COSMOS and GOODS-N maps are too small CDFS-SWIRE and consistent in coverage to bin pixels by coverage. The maps are converted to Jy/beam values using the sr/beam value for the 500μm beam as all maps have been converted up to this beam size.

5.7.1 Finding Variances and Covariances

The method of finding the confusion noise is not as simple for the maps used in PCA however, as these maps have been convolved and resampled. Therefore the expression for the error given above will have to be modified. There is an intuitive sense to this. The flux in the map at a pixel is an average of many time samples, sample numbers (or exposure times) are given in the coverage map. But by convolving the map with a kernel, the number of samples in each bin has been effectively changed, and binning the map

by exposure time without considering the convolution will only give approximate results. Further, resampling the maps to smaller pixels in the case of the 350μm and 500μm leads to correlations in the map.

The 250μm and 350μm maps have been convolved with the beam as

$$M_{new} = P * M_{old} \tag{5.10}$$

where M_{old} is the map before convolution, M_{new} the map after convolution and P the convolution kernel. One can treat the pixels in the map as uncorrelated, which is a reasonable assumption as correlated $1/f$ noise has been removed. In this case, the propagation of the error associated with each map pixel can be expressed as

$$\sigma^2_{Mnew,j} = \sum_i (p_i)^2 \, \sigma^2_{Mold,i} \tag{5.11}$$

where p_i refers to the value of the convolution kernel at position i. $\sigma^2_{Mold,i}$, the error associated with the original map pixel at position i can be expanded as above to be a function of the confusion noise, instrumental noise and exposure time t to yield

$$\sigma^2_{Mnew,j} = \sum_i (p_i^2)(\sigma^2_{conf} + \sigma^2_{inst}/t_i) \tag{5.12}$$

which rearranges to

$$\sigma^2_{Mnew,j} = \sigma^2_{conf} \sum_i (p_i^2) + \sigma^2_{inst} \left(\sum_i (p_i^2)/t_i \right) \tag{5.13}$$

and can be rewritten to be explicit as

$$\sigma^2_{Mnew,j} = \sigma^2_{conf} \sum_i (p_i^2) + \sigma^2_{inst} (P^2 * 1/T) \tag{5.14}$$

where T is the exposure map. Effectively, the total variance of the convolved map changes as a function of exposure time, but not completely dependant on the value of the exposure at that one pixel, instead changing as a sum of all the pixel exposures. Now, to fit a straight line to the variances the abscissus will be the convolution of the kernel squared with one over the exposure map, the gradient the instrumental noise squared (σ^2_{inst}) and the y-intercept the confusion noise times the sum of the kernel squared ($\sigma^2_{conf} \sum_i (p_i^2)$). NB, the intrinsic variance of the map and therefore what we want to use for principal component analysis is now $\sigma^2_{conf} \sum_i (p_i^2)$, with σ_{conf} the confusion noise from the unconvolved map.

Equation 5.14 is the modified version of the Nguyen analysis use to find the new confusion noise after applying a kernel to change the beam size. It will be used for the 250μm and 350μm maps. The 500μm map has only been resampled by dividing the pixels into nine separate pixels values and coverage associated to the pixels are identical.

The above analysis highlights why, in the case of 350μm maps, the map has been convolved before resampling. We have assumed the pixels are uncorrelated when formulating the covariance.

If the resampling had occurred before convolution, pixels in the 350μm map that have been split into four separate pixels are completely correlated with each other. Otherwise, the pixels are independent. As there would be correlations within the map before convolving, the total error would be calculated as

$$\sigma^2_{Mnew,j} = \sum_i \sum_k (p_i p_k)\sigma_{Mold,i}\sigma_{Mold,k}\rho_{ik} \tag{5.15}$$

where ρ_{ik} is the correlation between pixels i and k. In the case of no correlation with any other pixels, this reduces down to equation 5.14. Expanding out ρ_{ik} for cases of these neighbouring pixels, this calculation becomes

$$\sigma^2_{Mnew,j} = \sum_i (p_i(p_{i_1} + p_{i_2} + p_{i_3}))\sigma^2_{Mold,i} \tag{5.16}$$

where p_i is the value of the kernel at pixel i and p_{i_n} is the value of the neighbouring three pixels, what these values are depends on i. The $\sigma^2_{Mold,i}$ value appears again as the correlation between pixel i and k is one, so the total errors will be identical. This expands and rearranges to

$$\sigma^2_{Mnew,j} = \sigma^2_{conf} \sum_i (p_i(p_{i_1} + p_{i_2} + p_{i_3})) + \sigma^2_{inst} \sum_i (p_i(p_{i_1} + p_{i_2} + p_{i_3})/t_i) \tag{5.17}$$

Again, the y-intercept will be the original confusion noise multiplied by some function of the convolution kernels and the gradient the instrumental noise, with the abscissia values some modified convolution of the exposure map.

However, it is easy to see why this calculation will be non-trivial. For every pixel j in the new map, the convolution will have to be calculated by recentring the convolution kernel over j, finding which three pixels correlate with pixel i and summing and multiplying the weights. This is a high-order N calculation, i.e. it does not scale well with size as opposed to the fast-fourier transform convolutions used previously. One way around this could be to create four convolved maps using the original maps, with the kernel modified to be the sum of weights dependent on which of the four pixels are centred, and use those maps to calculate the final convolution. However this would not be so simple to replicate. Resampling the maps first would prevent the resultant maps appearing "blocky" in the 350μm band, but not improve the accuracy the of the result a great deal; recall figure 5.5 showing the difference in the fluxes of the maps when convolving first or second to show how much would be gained.

As the instrumental noise is independent in all three bands and the correlated $1/f$ noise has been removed by the map-maker, the covariance between maps is already at the intrinsic covariance of the population of sources within the map and therefore calculating the covariances between maps is relatively trivial. Every pixel in a map is paired with its counterpart in the other map and the covariance is calculated on all maps simultaneously as

$$\mathrm{cov}_{A,B} = \frac{1}{N}\sum_{i}^{N}[(m_{Ai} - \bar{m}_A)(m_{Bi} - \bar{m}_B)] \tag{5.18}$$

where $\bar{m}_A$ is the mean value of the flux in map A.

In this case the calculation is made only on the Lockman-SWIRE map. These maps are nested and therefore contain a larger range of coverage in pixels than e.g. COSMOS. It is also the largest field and so per bin will have more pixels to estimate the variance in. A measurement is only used if more than 10 pixels were in the bin. Running the algorithm and populating the covariance matrix gives

$$\begin{pmatrix} \sigma^2_{250} & \mathrm{cov}(\mathrm{f}_{350},\mathrm{f}_{250}) & \mathrm{cov}(\mathrm{f}_{500},\mathrm{f}_{250}) \\ \mathrm{cov}(\mathrm{f}_{250},\mathrm{f}_{350}) & \sigma^2_{350} & \mathrm{cov}(\mathrm{f}_{500},\mathrm{f}_{350}) \\ \mathrm{cov}(\mathrm{f}_{250},\mathrm{f}_{350}) & \mathrm{cov}(\mathrm{f}_{350},\mathrm{f}_{500}) & \sigma^2_{500} \end{pmatrix} = \begin{pmatrix} 15.62^2 & 166.0 & 95.39 \\ 166.0 & 11.52^2 & 71.71 \\ 95.39 & 71.716 & 6.700^2 \end{pmatrix} \tag{5.19}$$

As the diagonal values are consistent with a measurement of the confusion noise, naïvely one would believe these results are somewhat comparable with the published Nguyen et al. (2010) results and the unpublished results from chapter 3. Indeed, there has been no change in resolution (only pixel size through resampling) in the 500μm map. The value calculated here is 6.70mJy/beam which is consistent with Nguyen et al. (2010)'s value of 6.8$\pm$0.4 mJy/beam. For the other bands however, the area of the beam has been changed and so a direct comparison is not possible. Converting the area of the beam from the area at 250 or 350μm to the 500μm beam would seem to correct for this. However, as the beam size has changed, the number of confused sources has also changed. Thus a unit conversion to directly compare the values calculated here and in chapter 3 would also require a correction related to the number counts to be folded in. With a larger beam, the confusion noise is expected to increase which is the case.

Another minor effect that would increase the variance in this calculation would be related to the convolution kernel. Whilst the convolution kernel has been created using the real *Herschel*-SPIRE beams, they have been radially averaged. Thus the kernel, if broken into a two-stage deconvolution with the old beam and then convolution with the new beam, will be twice exacerbating the difference between the beam in the map and the

field	band	explained variance	contributions 250μm	350μm	500μm
Lockman-SWIRE	PC1	95.4	0.769	0.556	0.317
	PC2	3.3	0.636	-0.719	-0.280
	PC3	1.3	-0.072	-0.417	0.906

Table 5.4: Principal components when using the confusion noise estimates only, figures shown in figure 5.14

radially averaged beam. Thus the beam in the convolved maps is not the 500μm beam exactly but an approximation. However this would be a secondary effect to the change caused by the act of convolution of the maps.

The off-diagonal elements of the matrix is the covariance. The covariance is related to a measure of correlation between the two variables A and B as cov $=$ corr$\sigma_{\rm A}\sigma_{\rm B}$. Specifically this is the Pearson's product moment correlation coefficient. Anti-correlation results in -1, 0 is no correlation and 1 completely correlated. This can be used to describe the correlation between the bands. For 250-350μm this is 0.92, 250-500μm is 0.91 and 350-500μm 0.93. The results from this analysis still hold that the data is highly correlated as expected.

This covariance matrix is then decomposed into eigenvectors and eigenvalues to find the PCs and explained variances.

The explained variance of the data calculated using only the confusion noise is very different to other approaches, now w_1 has an explained variance of over 95%, almost 10% higher than the values calculated with ROBPCA-AO (table 5.4). w_3 has been reduced to 1.3%, showing the transfer of variance into w_1. This is encouraging as it shows removing the effect of instrumental noise and effectively reducing the variance measures on the leading diagonal of the covariance matrix has a beneficial effect to the analysis. The shape of w_2 and w_3 have changed, both now showing a skew effect. Applying a positive w_2 contribution will both broaden the SED and push the peak to bluer fluxes. A positive w_3 value will again broaden the SED but push the peak to redder fluxes. These two PCs fulfil the same functions as PCs calculated with previous algorithms, just in a different manner, with w_1 remaining an average-like SED. The projections onto the 2D flux distributions in 5.14 show that, whilst the explained variances are smaller in w_2 and w_3 even in the Lockman-SWIRE field, the PCs are not cleanly fitting distributions at the brightest fluxes and for the brightest sources. This projection of data has not replaced the importance of considering higher moments of the distribution when fitting models for example.

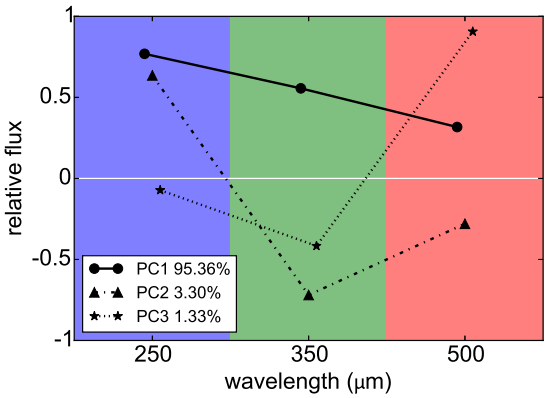

(a) Lockman-SWIRE

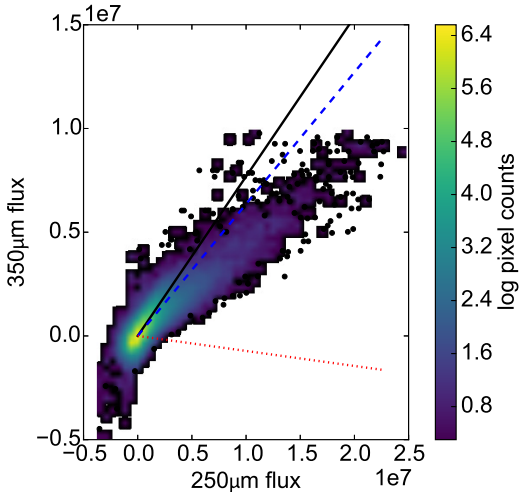

(b) 250μm and 350μm

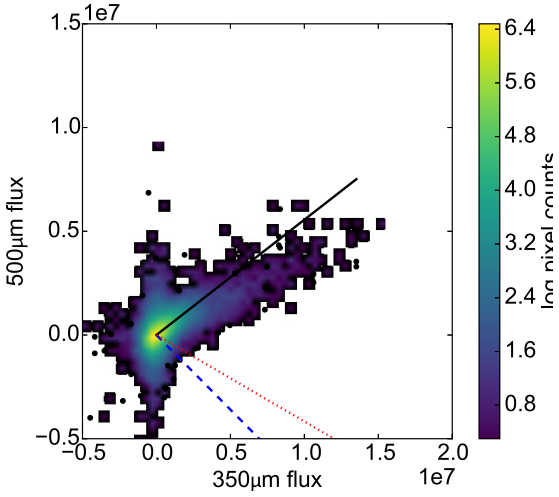

(c) 350μm and 500μm

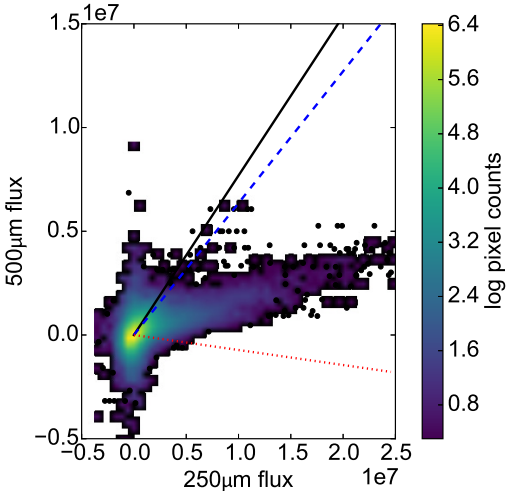

(d) 250μm and 500μm

Figure 5.14: 2D projections of the PCs found when using ROBPCA-AO in Lockman-SWIRE and the fit to the pixel flux distribution. The fit is much better to the densest part of the distribution.

Whilst the PCs calculated with only the confusion noise may be closer to describing the true values of the population by removing the instrumental noise, comparing these results to, for example, observed data means the effect of the instrumental noise would have to be added back in. This particular result is useful to fit population models to, for example, as these will have no instrumental noise added. Also note that this reproduction, explaining most of the variance in one component, still requires the variance from the two other dimensions to be taken into account. This new projection of data is an additional tool to help capture covariance in data, rather than a replacement to the fits to the traditional one-dimensional P(D).

5.8 Conclusions

This chapter has presented original work exploring covariance between the *Herschel*-SPIRE maps. It is well understood that at the far-infrared wavelengths observed by the *Herschel*-SPIRE instrument (bands centred at the 250μm, 350μm and 500μm wavelengths) the emission from galaxies is dominated by modified blackbody-like emission from cool dust, dust warmed due to obscured star formation. Many galaxies have emission at far-infrared wavelengths. As such, there is extremely strong covariance between the bands and this strong covariance had the potential to be exploited.

In previous studies in the UV to mid-infrared, correlations between data points in spectra were exploited (e.g. emission lines arising from the same physical processes in galaxies) to decompose spectra into components that can be linearly summed. This led to the creation of spectral components representing emission arising from different physical processes in galaxies such as AGN activity and star formation. Thus the contribution of each process across the entire spectrum of a galaxy (rather than comparisons from emission lines or individual photometric bands) can be assessed.

In the simplest case this decomposition can be achieved with principal component analysis (PCA), where the covariance matrix of N spectra with M data points is created and diagonalised by finding the eigenvectors (principal components) and eigenvalues of the matrix. This process creates vectors in M dimensional space along which the variance of the data has been maximised. The spectra can often be reconstructed to a high accuracy with less than M principal components and thus the dimensionality of the problem can be reduced. Galaxies can also be classified with discriminators constructed using the contribution of a galaxy to each principal component. The vast majority of astronomical science performed with PCA uses galaxy spectra with some noted exceptions.

This work instead takes a different approach, motivated by the lack of a multi-dimensional P(D) (probability of deflection) analysis. Source detection software is unable to find every source in an image and so, to understand the population of galaxies below the confusion limit one must analyse the maps directly. By iteratively convolving a model for source number counts with the PSF and a noise model, and fitting the result to the number of pixels in a map at a particular surface brightness, one can determine parameters for source count models below the confusion limit of the maps. Currently, P(D) analysis treats each individual map independently, the only covariance between the bands guaranteed if fitting a model involving an SED template typical of SEDs within the *Herschel*-SPIRE bands. By exploring the use of PCA on the map pixels directly, it was hoped that the principal components found would appear independent, capture the majority of the covariance in one principal component which would maybe allow for a reduction in the dimensionality of a P(D) analysis.

Four maps were used; COSMOS and GOODS-N as they are smaller and deeper and the nested Lockman-SWIRE and CDFS-SWIRE maps released in DR2 as there is a variety of depths in the fields. The maps were convolved with kernels to bring the beam size in each map to the larger 36.3 arcsec 500μm beam to achieve consistency. The maps were then resampled to the smallest 6 arcsec pixel width of the 250μm map.

For the first pass, the simplest implementation of PCA was used, using all the pixels to construct a set of PCs for each map. In each case, the first principal component w_1 has a variance of over 84%. The largest field, Lockman-SWIRE had the smallest explained variance in w_1 due relatively noisy nature of the observation. GOODS-N had the highest explained variance of 92% in w_1. This field is the deepest and also the smallest, with almost four times the number of scans and therefore includes almost half the instrumental noise of COSMOS. The relative lack of instrumental noise and lack of extreme objects due to the small size of the field (cosmic variance effect) gives a less skewed multidimensional flux distribution for PCA to find PCs for and therefore the explained variance in w_1 is the highest. When projected onto the 3D flux distribution however, the PCs do not seem to follow the trend of the brightest pixels, instead fitting to the majority of pixels at fainter fluxes. This implies, as is already known, that there are multiple populations of sources, with the brighter, possibly foreground, objects separate to the sources making up the cosmic infrared background.

The skewed flux distribution in each band was also considered. The skew arises as there is only positive flux in the map and there are more fainter sources than brighter ones.

Pixels associated to bright sources contribute to the tail of the flux distributions. PCA assumes data represents a multidimensional Gaussian. Kappa-sigma clipping (iteratively removing pixels beyond $\kappa\sigma$ away from the mean distribution) in an attempt to crudely remove outlying pixels was attempted. In this case $\kappa = 5$ and approximately 1% of pixels were removed in each band. However the cuts on the flux distribution was indeed crude and the PCA algorithm performed as well or worse than the original PCA algorithm, as measured by the percentage of explained variance captured by w_1. Whilst unsuccessful, this prompted a search for a more intelligent approach for flagging outlying pixels in the flux distribution.

The Robust-PCA with Adjusted Outlyingness (ROBPCA-AO) algorithm is an adapted PCA algorithm that can identify outliers and manage skewed data. The algorithm selects a subset of pixels to perform PCA on, but unlike kappa-sigma clipping selects these pixels based on their distance away from vectors projected through the data, as opposed to the original basis vectors. The vectors are chosen using median values, interquartile ranges and robust measures of the skew of the data instead of assuming that the mean and variance fully describes the distribution as in the original PCA algorithm. Even with an extremely aggressive cut removing 25% of the outlying pixels, the calculated PCs are similar in shape to the PCs calculated with the unmodified PCA algorithm. However, the explained variance indicates that a higher proportion of variance has been captured by w_1, with a maximum of 94% of the variance explained in w_1 for GOODS-N and less than 2% in w_3.

As in other PCA studies, the PCs can be interpreted physically. As w_1 shows a correlation across all three bands, the contribution to this PC gives the intensity of the source (the combination of luminosity and redshift) and can be considered some type of 'averaged' SED. w_2, dependent on the sign of the contribution, pushes the peak of the SED to bluer or redder fluxes, giving a strong indication of redshift or dust temperature. w_3 is correlated in the 250μm and 500μm, and again dependent on the sign of the contribution can either be effectively stretching or narrowing the SED. A stretched SED will be a cooler temperature or higher redshift. Whilst all the components are degenerate with redshift and so physical parameters of the galaxy like dust temperature or luminosity have not been decoupled, it is apparent that the variance in contributions of the first component is driven more by the source intensity than the contributions at each individual wavelength.

As the found PCs and explained variances depend on the depth of the fields, a final attempt to find the underlying PCs of the field was performed by removing the contribution

of instrumental noise. As the total noise in the surface brightness of pixels within a map is the sum in quadrature of the confusion noise and instrumental noise, one can calculate the confusion noise as in chapter 3 and using those values in the covariance matrix instead of the total variance. This only affected the leading diagonals of the covariance matrices as the instrumental noise is not correlated across bands. This regression performed on the Lockman-SWIRE map only (as this map had the required depth of field) found 95% of the variance could be explained by one PC, compared with 84% on the first attempt.

Projecting the data onto the 3D flux distribution shows the PCs have not captured the variance of the brightest fluxes and therefore the PCs are not truly independent. The third component then, whilst calculated as capturing 1% of the variance, would still be important to any fitting routine. Thus PCA does not strictly reduce the dimensionality of, for example, any P(D) analysis one would wish to perform on the *Herschel*-SPIRE bands. However the analysis is valuable. There is strong covariance between the bands to exploit and, performing this transformation to run P(D) and fitting these PCs, in addition to the bands in isolation, will provide constraints on the model without necessarily having to make restrictive assumptions on galaxy SEDs. As the PCs are connected to physical attributes of sources, any deviation of a simulation from the fit to e.g. the w_1 contributions would imply an issue with the assumed infrared luminosity function used in modelling. Therefore considering even only the first principal component along with the other wavelengths will provide a wealth of information. For specific simulations or observations of particular fields and include instrumental noise effects, the results from the ROBPCA-AO analysis would be the most representative results to fit to.

5.9 Further Work

Independent component analysis, or ICA, (Herault & Jutten, 1987; Comon, 1994), is similar to PCA in that it can be used to reduce the dimensionality of data. However the first principal component is constructed to be independent of any other vectors (as opposed to finding the vector that would capture the greatest variance), with all proceeding vectors orthogonal to the first. ICA has been used in a proof of concept for blind source identification in Li et al. (2001), decoupling background sources of flux from the wanted foreground in Hubble Space Telescope images and decomposing sources into independent physical contributions. In chapter 4 ICA was suggested as method to untangle the contribution of the foreground cirrus emission as in Planck Collaboration et al. (2014). Whilst source extraction was not performed in this chapter, using a technique such as ICA could be useful

for removing cirrus emission and simultaneously finding sources in confused regimes. This is a potential area to explore to extend this proof of concept analysis.

A natural extension would be to include the *Herschel*-PACS bands to this analysis, as some correlation between bands should exist at all levels. In the preliminary testing phases these bands were included. However they were ruled out in this proof of concept as all the maps would need to be resampled to 2 arcsec and convolved up to 36.3 arcsec, losing much of the fidelity of the PACS maps. There was still extremely strong correlation between the three SPIRE bands and correlation between the PACS bands, although not much between the two instruments. This could be due to different systematic observing effects from the two instruments and greater contamination from cirrus. The inclusion of the PACS bands would be good to explore when using other techniques such as ICA for component separation or considering the creation of broadband eigen spectra like those in created in Wild et al. (2014).

Chapter 6

Quantifying Discrepancies Between the HerMES and H-ATLAS Data Reduction Methods and Angular Correlation Functions

In chapter 2 conflicting results between HerMES and H-ATLAS, two *Herschel* legacy surveys, were highlighted. Specifically, the angular correlation function which gives the strength of galaxy clustering was shown to be positive in HerMES results (Cooray et al., 2010) and consistent with zero in H-ATLAS (Maddox et al., 2010) at 250μm. This is significant as the clustering strength of bright galaxies in the infrared can be used to infer the masses of the dark matter haloes star-forming galaxies typically belong to. As the data used by both collaborations originates from the the same telescope, the inconsistency between these results can arise either from the data reduction pipelines used by each team or the calculation of the clustering measurement. A second result using HerMES data from Mitchell-Wynne et al. (2012) shows a lower clustering strength than previously detected with Cooray et al. (2010). However, this follow-up study does not correct for sources blended or missing from the catalogue at small angular scales.

This chapter presents the ongoing work to untangle these discrepancies. To begin with, the H-ATLAS map and catalogue production pipeline is outlined and contrasted with HerMES. Two datasets have been given to both teams to reduce, and the results

from the COSMOS field data are compared and discussed within this chapter. This work is part of the HELP (*Herschel* Extragalactic Legacy Project) collaboration, where H-ATLAS and HerMES data will both be used. This work will decide whether data needs to be re-reduced through one pipeline only, or whether data products are currently similar enough to proceed.

Further, the background to the angular correlation function measurement is given, and the angular correlation function is re-calculated using one of the fields used in Cooray et al. (2010). The first attempt at correcting the correlation function at small scales is presented, using a full simulated map with realistic number counts. The corrections for SUSSEXtractor generated catalogues are given. The next steps to take in this work in regards to improvements that can be made are also outlined.

6.1 HELP and H-ATLAS

The *Herschel* Extragalactic Legacy Project (HELP) is a European-funded, 4-year project is provide homogenised datasets from many wavelengths across a wide number of legacy fields. *Herschel* data will form the heart of the release, with the catalogues from other wavelengths acting as prior information in the source extraction in the low resolution *Herschel* images (Hurley et al., submitted). HELP will provide tools for astronomers to calculate metadata such as selection functions, completeness curves and transparently calculated errors to allow astronomers to draw informed conclusions from the data.

Herschel data will be an integral part of the dataset provided by HELP and will be obtained from multiple collaborations. Homogeneity is therefore paramount. Data and data reduction methods from two *Herschel* collaborations will be considered. University of Sussex and Cardiff University, involved with HerMES and H-ATLAS respectively, are both core member Universities in the HELP project and are therefore primed to (re)reduce the Herschel data archive.

H-ATLAS (Eales et al., 2010a) was a survey designed for large, shallow fields to find rarer, bright extragalactic sources and events. As such, the maps and catalogues have been processed in different ways to account for this difference in scale. A like-for-like comparison is needed to assess which of the HerMES and H-ATLAS teams' data reduction pipeline and source extraction software will be the best for HELP's purposes, or whether there is very little difference in the reduction and HELP can proceed without any re-reduction needed.

To test the suitability of both pipelines, two different fields, one originating from each collaboration, are chosen and re-reduced. COSMOS is a HerMES field, < 3 sq. deg. and considered deep, at the centre dominated by confusion noise. GAMA15 is a H-ATLAS field chosen to overlap with the GAMA team's field of the same name. It is approximately 56 sq. deg. in size. From H-ATLAS the GAMA15 map was chosen to be included in HELP for its ancillary data from the SLOAN foundation 2.5m telescope as part of the GAMA survey. It is on par with the HerS field in size and similar in construction; both are shallow-field surveys with overlapping tiled scans.

6.2 H-ATLAS Map Reduction

H-ATLAS's map-making process is similar to HerMES, although subtle differences are present. H-ATLAS also utilise the Herschel Interactive Processing Environment (HIPE) to construct level-1 time-ordered data (TODs) from 0.5 data products as follows. Glitches on individual detectors are flagged with the sigma-kappa deglitcher. Glitches are replaced with white noise as opposed to HerMES' masking, although the glitched regions are eventually removed from the H-ATLAS data. The use of white noise is to allow filtering and other fitting to occur without bias. DC offsets (jumps in signal that decorrelate bolometer temperatures from thermistors) are found by eye and corrected at the timeline level by shifting the data in the timeline by a value estimated by the data. The electronic and bolometric cross-talk matrices are applied as in HerMES. Timelines for individual scans are stitched together to create long timelines for each observation, again like HerMES data.

To create the level 1 data products, the next step is to remove correlated noise from the TODs. The data for each detector is the sum of signal from sources, from uncorrelated Gaussian-like noise and correlated $1/f$ noise across detectors as

$$d_i(t) = A_{ip} S_p + n_i(t) + \alpha_i C(t) \tag{6.1}$$

where i represents a detector, p a pixel, S_p the contribution to each pixel by the flux of the source, n_i the instrumental/Gaussian noise, $C(t)$ the correlated $1/f$ noise, $A_{ip}(t)$ the pointing matrix mapping between the contribution of each detector to each pixel and α_i is a constant scaling factor for each detector, similar to the gain in the HerMES processing. The signal from each bolometer is plotted against the thermistor signal. The thermistor is then fitted with a fifth-order polynomial, and this is subtracted off. A low-pass filter at 20mHz (which removes signal from Fourier modes with frequency above 20mHz) effectively

smooths the response. The fifth-order polynomial is then added back to the signal. This initial subtraction was performed to preserve the gradient of the signal - Fourier methods often attempt to fit to zero at the start and end of the signal whereas the temperature drift modelled by the thermistor will increase across the data rather than reducing to zero. Then the filtered signal from the thermistor $C(t)$ times by α is subtracted from the timeline.

The instrumental noise n(t) is calculated next. The timelines are binned into maps and the flux at each pixel value calculated. The noise in the map drops by $\sqrt{n}$ where n is the number of samples in the map. The map is turned back into a timeline and the new timeline subtracted from the old. This re-production effectively averages over the samples in each pixel and thus reduces the noise in this reproduced timeline, and thus the subtraction removes the signal from sources the timeline. This gives an estimate of the noise for each bolometer. The residual timelines are Fourier filtered, the power spectrum found and fitted to $1/f$ noise model

$$P(f) = \omega_0^2 \left[\left(\frac{f_0}{f} \right) + 1 \right] \tag{6.2}$$

where ω_0 is a measure of white noise and f_0 the knee. f_0 is found to be below 4mHz - this is a crucial value as this corresponds to scales above 4.2deg at a scan rate of 60 arcsec s^{-1}, which is the size of the survey field and speed of the fast-scan rate respectively. Scales above this value are unconstrained by the data and can therefore be removed with filtering.

Using these results, the timelines are high-pass filtered above 4mHz. The PSF is not affected significantly. This filtered TOD corresponds to a level-1 data product.

To create maps from the TODs, individual samples are binned according to the pixelisation process and averaged. The maps are binned using HIPE's naive map-maker at pixel sizes of 6, 8 and 12 arcsec. Pixels without samples are flagged and have no flux value. In HerMES, median pixel values are used in the map-making process rather than the mean. In terms of pixel size, only the 350μm map differs to HerMES value which is 25/3 arcsec.

For the data comparison H-ATLAS made the maps to HerMES pixel sizes. Instrumental noise in the map is calculated from jackknife maps by splitting the data by scan, subtracting and then measuring the resulting variance in flux. In the SDP-phase this was given as 29.6, 31 and 36mJy/sample$^{0.5}$, consistent with the timeline values.

The astrometry of the map is calculated and corrected using SDSS DR7 r-band sources. A cross correlation between the catalogues (as described below) and SDSS image provides

a distribution of offsets in x and y. The peak of the distribution of errors is taken to be the map offset, which is typically less than 2 arcseconds. In contrast HerMES stacks on Spitzer 24μm catalogues to find the astrometry offset as these are available in HerMES fields.

6.3 H-ATLAS Catalogue Production

Catalogues were generated used MADX, Multi-band Algorithm for source eXtraction (Rigby et al., 2011). The official paper detailing MADX has not been published although we summarise the algorithm to date here.

First a local background is calculated and subtracted. The background must be local as strong cirrus contamination exists in the H-ATLAS fields. The image is divided into 30×30 pixel blocks and a histogram generated for the flux of each pixel. Each block is assigned the peak value of the histogram and a bi-cubic interpolator is run across this larger grid, and interpolated back down to the original image size. This estimated background is subtracted off the map. This is in contrast to the global background fit of DESPHOT used in low-cirrus fields.

The maps are then convolved with a matched-filter, in this case the PSF for each band with every pixel weighted with the inverse variance estimated from the noise map. This is similar in method to SUSSEXtractor. The 350μm and 500μm maps are interpolated to the grid-resolution of the 250μm. Only the 250μm map is used to find sources in the catalogues considered here, although MADX can use all three bands simultaneously to find sources. Peaks of SNR$>$ 2.5 are located and ranked by descending SNR. Considering one source at a time, Gaussians are fit to the peak to provide a positional estimate at the sub pixel level. Given these positions, a bi-cubic interpolation on the filtered maps provides flux estimates for the sources. Each source is then subtracted from the map to ensure any flux blending does not effect other estimates. A cut on the resultant catalogue is made at 5σ.

6.4 Comparisons of COSMOS Data

To quantify the difference between the HerMES and H-ATLAS data products, the same telescope data will be given to both collaborations to reduce. Note, the H-ATLAS COSMOS maps have had the astrometry corrected using using the MIPS 24μm catalogue available in this field as opposed to the standard SDSS catalogues used. The maps and

catalogues will then be compared and the differences discussed.

The results presented in this section are the comparison between COSMOS maps. The maps are compared through stacking on known sources and an elliptical Gaussian beam with a parameter for the rotation and background is fitted to each stack and the residual found. The simplified Gaussian beam used for source extraction is also fitted and discussed. The catalogues compared are the MADX and STARFINDER/DESPHOT xid250 catalogues. Both these algorithms use positional priors generation on the 250μm map to inform the source extraction process, and prior-based source extraction is the type of algorithm the HELP collaboration is developing. The catalogues were produced on the HerMES reduced maps only as the HerMES pipeline was constructed specifically for smaller fields like COSMOS. Producing catalogues on the same map ensures that any differences between the catalogues is a result of the source detection and extraction software and not from the map-making pipelines.

6.4.1 Comparison of Maps with Stacking

Stacking is a process that typically uses positions of galaxies from other, relatively better resolved wavelengths to average together flux from sources that would not otherwise be detected in the data of interest. The method involves cutting out a stamp in the map surrounding the position of a source for a number of sources and averaging the stamps pixel by pixel. Stacking on a carefully selected population of sources can provide information about the average value of sources, such as the flux. There is a benefit in map-based approaches like stacking over comparing detected sources in catalogues. If the population of sources is at an extremely low flux and thus undetectable amongst the noise, the resultant stack will show a signal in the shape of the beam at the centre of the image with the surrounding objects in individual stamps smoothed out in the stack.

Formally, stacking involves creating an averaged stack of cutouts $p(x, y)$ shape $S \times S$ where S belongs to the odd integers and $-(S-1)/2 \leq i, j \leq (S-1)/2$

$$p(x,y) = \frac{1}{N'_{xy}} \sum_{k}^{N} d(i_k - x, j_k - y) \tag{6.3}$$

where N is the total number of sources k, i_k, j_k are the positions in the image of the source and N'_{xy} is the total number of non-zero contributions to the stack at position x, y. The unbiased variance estimator is given as

$$\sigma_p^2(x,y) = \frac{N'_{xy} \sum_k^N d(i_k - x, j_j - y)^2 - (\sum_k^N d(i_k - x, j_k - y))^2}{N'^2_{xy} - N'_{xy}} \tag{6.4}$$

There is a caveat when stacking on confusion-limited maps like Herschel-SPIRE maps. Fluxes from nearest-neighbours will contaminate the stack, adding flux to the central beam and raising the background from a zero flux. This particular problem has been addressed with the SIMSTACK method which reduces or removes this contamination (Viero et al., 2013). This contamination is not a problem for this particular comparison, however, as this comparison is quantifying relative differences between the stacks on the two maps. This means that any bias within the object selected to stack on will be consistent within the maps. Further, contamination from neighbouring sources will again be consistent.

For the purposes of this comparison, the stacking will be conducted with a 24μm catalogue from Sanders et al. (2007) in the COSMOS field. It is known that there is a strong correlation between 24μm sources and far infrared sources, implying that sources at an e.g. low flux in the 24μm will also be low flux in the 250μm (Elbaz et al., 2010). To prevent the few brightest sources from dominating the stack but not every pixel in the map contributing to the stack due to the density of sources, lower and upper flux limits are applied. Sources between 0.25 and 1mJy in the 24μm are used.

This particular upper limit has been chosen because both map pipelines include some form of Fourier filtering. As such it is possible that extended sources will appear different in stamps which could affect the resulting stacks and conclusions drawn about point sources. As these extended sources are typically bright, an upper limit on the fluxes was included.

In figure 6.1 the stack has been performed on both the HerMES and H-ATLAS reduced COSMOS maps. The maps were resampled with a nearest neighbour algorithm to 1arcsec, effectively dividing each pixel up into e.g 36 separate pixels for the 250μm. This allows the position of the 24μm sources to be more accurately stacked. Therefore the comparison will be more sensitive to broadening of the beam due to the different map-making processes rather than broadening due to misalignments of the beam centres. This is a legitimate way to stack sources as the position of the 24μm sources selected have an average uncertainty of < 1 arcsec (Levenson et al., 2010).

6.4.2 Fitting a 2D Gaussian

For the first comparison, an elliptical Gaussian was fit, minimising the χ^2 fit to the stacks. The *Herschel*-SPIRE beams are known to be radially asymmetrical (Griffin et al., 2010) and so fitting this particular general function will demonstrate whether there are directional dependent differences in the resultant stacked beam. The elliptical Gaussian is

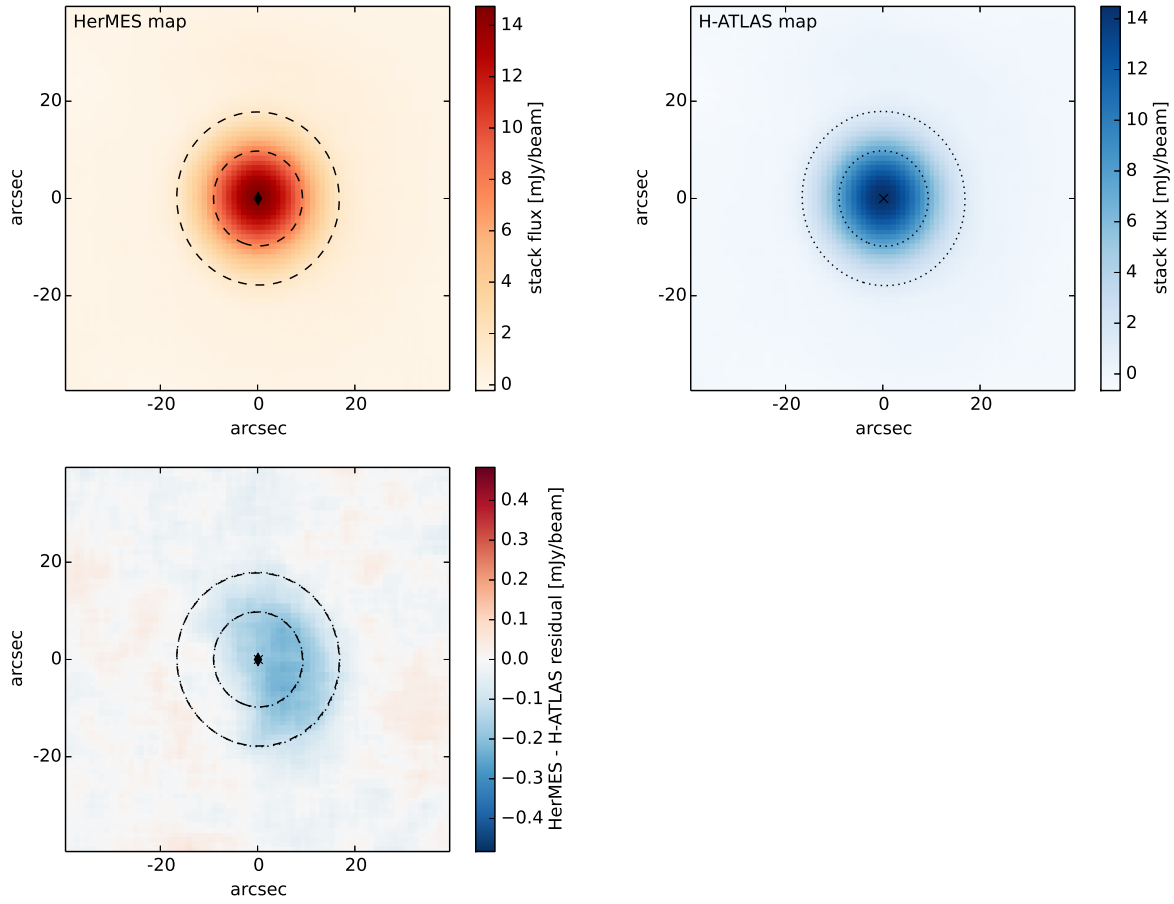

Figure 6.1: A comparison of the COSMOS 250μm maps from HerMES and H-ATLAS using stacking. In each case an elliptical Gaussian is fitted and the centre, where the fit is 0.5 and 0.1 times the peak is shown in subfigures a and b. Subfigure c overlays the fits and shows the residual between both stacks.

defined as

$$f(x,y) = A\exp(-\{\alpha(x-x_0)^2 + \beta(x-x0)(y-y0) + \gamma(y-y_0)^2\}) + B \tag{6.5}$$

parameterised by amplitude A, offset from the centre of the stack in x and y (x_0 and y_0). $\alpha, \beta\,\gamma$ are defined as

$$\alpha = (\frac{\cos^2(\theta)}{2\sigma_x^2} + \frac{\sin^2(\theta)}{2\sigma_y^2}) \tag{6.6}$$

$$\beta = (\frac{\sin(2\theta)}{2\sigma_x^2} - \frac{\sin(2\theta)}{2\sigma_y^2}) \tag{6.7}$$

$$\gamma = (\frac{\sin^2(\theta)}{2\sigma_x^2} + \frac{\cos^2(\theta)}{2\sigma_y^2}) \tag{6.8}$$

the width of the Gaussian (σ_x and σ_y) and rotation (θ) and a background component B.

In figure 6.1 and table 6.1 we see that the 2D Gaussian fits of the maps (characterised in the figure by lines at $0.5A$ (the FWHM) and $0.1A$ are extremely similar. Subplot

parameter	250μm		350μm	
	HerMES	H-ATLAS	HerMES	H-ATLAS
A [mJy/beam]	14.716 ± 0.016	14.893 ± 0.016	10.72 ± 0.008	10.767 ± 0.009
x_0 [arcsec]	0.086 ± 0.008	0.167 ± 0.009	0.728 ± 0.008	0.772 ± 0.008
y_0 [arcsec]	-0.004 ± 0.009	-0.005 ± 0.009	0.607 ± 0.009	0.59 ± 0.009
σ_x [arcsec]	7.766 ± 0.009	7.78 ± 0.009	10.529 ± 0.009	11.22 ± 0.01
σ_y [arcsec]	8.289 ± 0.009	8.352 ± 0.01	11.229 ± 0.01	10.519 ± 0.009
θ [deg]	5.704 ± 0.675	8.078 ± 0.623	-10.087 ± 0.498	-9.333 ± 0.505
B [mJy/beam]	0.186 ± 0.002	-0.23 ± 0.002	0.178 ± 0.002	-0.201 ± 0.002
	500μm			
	HerMES	H-ATLAS		
A [mJy/beam]	5.923 ± 0.007	5.747 ± 0.003		
x_0 [arcsec]	0.128 ± 0.019	0.191 ± 0.009		
y_0 [arcsec]	0.744 ± 0.018	0.722 ± 0.01		
σ_x [arcsec]	15.61 ± 0.027	15.268 ± 0.013		
σ_y [arcsec]	16.248 ± 0.026	16.902 ± 0.014		
θ [deg]	43.807 ± 0.986	8.440 ± 0.238		
B [mJy/beam]	0.094 ± 0.004	-0.198 ± 0.002		

Table 6.1: Parameters for the elliptical Gaussian fits for all three SPIRE bands. The 250μm plots are shown in figure 6.1.

c shows the residual map and overlays the fits. By eye there is no difference. There is a consistent central offset and similar rotation in both cases. However, we can see the H-ATLAS stack peaks at a higher value, 14.89 ± 0.02mJy as opposed to HerMES 14.72 ± 0.02mJy, an increase of 1.1% that is not accounted for in the errors. The σ_x and σ_y values however are different, with the H-ATLAS beam being marginally broader in the 250μm by a fraction of an arcsec, although comparing these values is difficult due to the inclusion of the rotation parameter and as such the σ_x and σ_y direction aren't aligned with x_0 and y_0. The rotation parameter fitted at 500μm is extremely different, comparing 44 deg. and 8 deg. for HerMES and H-ATLAS respectively. In this case the fitted beams are extremely rotationally offset.

There is a greater difference in the fitted backgrounds, 0.416, 0.379, 0.292 mJy/beam at 250μm, 350μm and 500μm respectively, with the H-ATLAS values consistently below that of the HerMES maps. As the background in this case is fitted across the entire stamp, this value gives information on the effect of map-making on the large-scale fluctuations across the map. All *Herschel*-SPIRE maps are created to average to a surface brightness of zero as at the time of the pipeline development there was no known absolute background (this could now be calculated with observations from the *Planck* satellite). As the background in the HerMES map is positive and therefore areas of the map not include must be on average negative to balance this, this implies the HerMES beam has marginally brighter wings that have not been as affected by filtering. This is visible in the residual map as the surface brightness at larger distances from the source centre is skewed positive to the HerMES map.

A slight offset in the x direction exists in the 250μm, although this is 0.08 of an arcsec, which amounts to 1.3% of a pixel at 250μm so the effect is not significant. In the residual of the stacks, subfigure c in 6.1, the fitted backgrounds have also been subtracted to 'zero' the residuals. The slight offset in x is now apparent as the residual shows an excess of surface brightness in the H-ATLAS stamp in one direction. This is maximally at 0.28mJy, less than 2% of the peak flux.

Is a 1.1% difference in the fitted beam, or a 2% difference in the residuals of the maps significant? For studies performing map-based analyses then any systematic differences between the two datasets will be significant. A power spectrum analysis would show at which scales the filtering of the maps has had the greatest impact, although this study is left to further work due to time constraints. For catalogue-based studies, an assessment of the PSF used for source detection and extraction will be more informative and will show

whether the systematic differences in the maps determined above are significant.

6.4.3 Fitting the Source Detection Gaussian

Whilst a 2D Gaussian is an easily parameterisable fit to a stack of *Herschel*-SPIRE sources, and the fit above does show that the beam is not radially symmetric, it is not feasible to perform source-finding on the Herschel-SPIRE maps using this beam. To do so would require information on the orientation of the telescope for each data sample. To this end source detection uses an approximated radially symmetric beam defined as

$$f(x,y) = A\exp\left\{-\left(\frac{(x-x_0)^2+(y-y_0)^2}{2\sigma^2}\right)\right\} + B \tag{6.9}$$

with x_0 and $y = 0$ again the offsets from the central pixel, σ parameterising the width of the beam and B as the background. This is effectively the same equation as equation 6.5 with $\sigma_x = \sigma_y$ which makes the rotational component of the equation irrelevant.

As we want to demonstrate how well the source-finding beam fits, we fix σ to FWHM$/2\sqrt{2\ln 2}$, where the FWHM is 18.15, 25.15 and 36.3 arcsec for 250μm, 350um and 500μm respectively.

Figure 6.2 shows the resultant fits, with the values in table 6.2. Again we see the same marked differences in the value of B as with the 2D Gaussian fit with the HerMES values more positive than the H-ATLAS values, demonstrating the background is important to fit during source extraction if both HerMES and H-ATLAS maps are to be used. The peak of the fits, A, is again higher in the H-ATLAS maps, 15.21 ± 0.02 to 15.45 ± 0.02 at 250μm, a 1.6% increase in the flux from HerMES to H-ATLAS sources. There is a marginal difference in the positional offset in the x_0 direction again in the 250μm and 500μm maps, approximately 0.08 and 0.05 arcsec respectively, Again this is 1% of a pixel and thus at the *Herschel*-SPIRE resolution is minimal.

Of greater interest are subfigures d and e in figure 6.2, showing the subtraction of the fits from the maps, i.e. what would remain when subtracting sources from the map to create a residual map. As a fraction of the fitted peaks A, the centre of the peak is overestimated by 5.1% and 5.3% for HerMES and H-ATLAS respectively. The first wing of the beam as compared to $0.3A$, the contour where peak of the wing resides, shows the fit is underestimated by 13% and 14%. Both these values are calculated on the 250μm map. These differences arise from two effects; the shape of the beam used for source detection and extraction not fitting the stacked beam exactly, as well as correlation between the sample of sources used to stack. These differences mean however that the difference

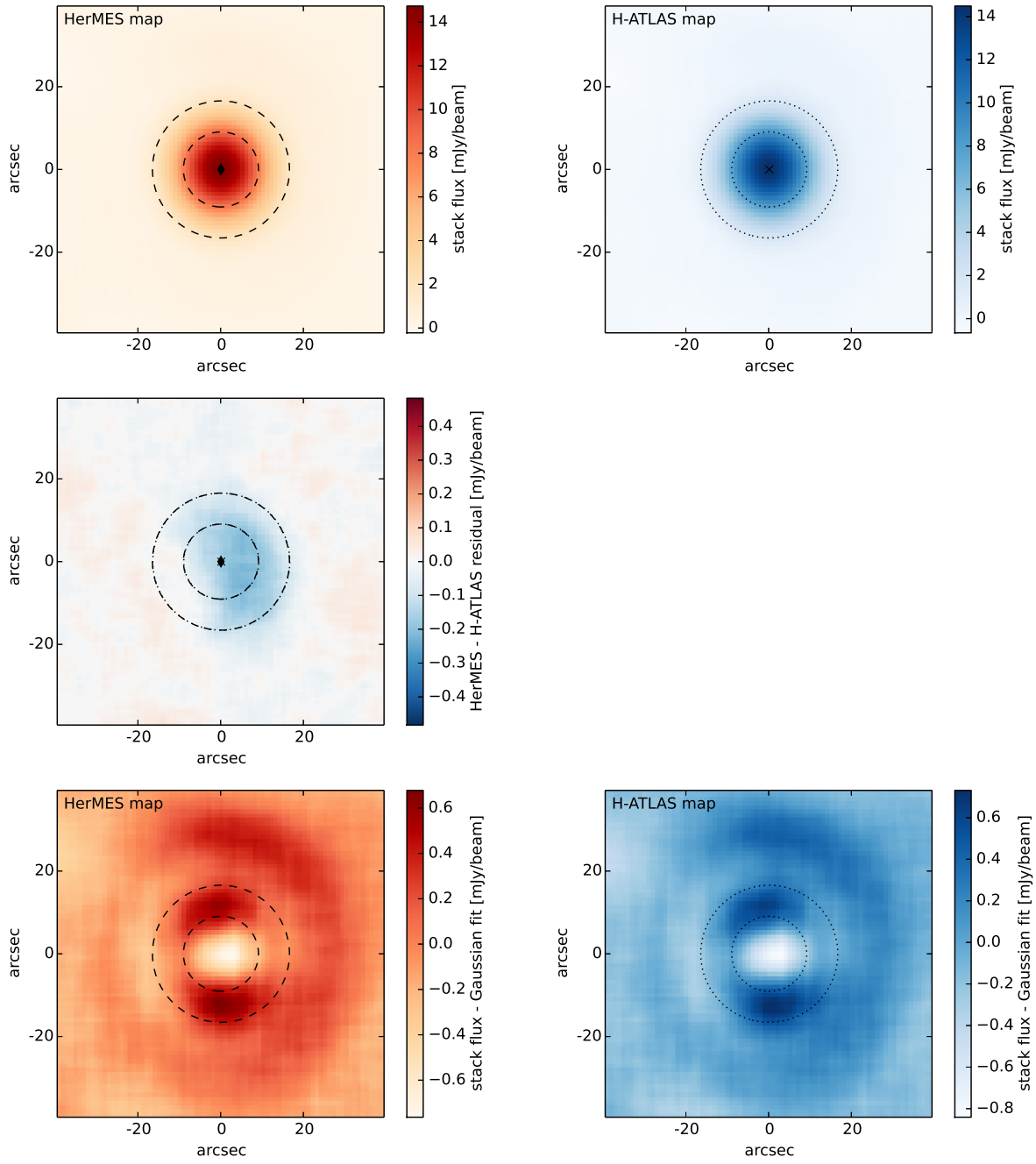

Figure 6.2: A comparison of the COSMOS 250μm maps from HerMES and H-ATLAS using stacking. The Gaussian PSF used for source detection is fitted and the centre and where the fit is 0.5 and 0.1 times the peak is shown in subfigures a and b. Subfigure c overlays the fits and shows the residual between both stacks. Subfigures d and e show the residual between the fitted Gaussian and the stacks.

parameter	250μm		350μm	
	HerMES	H-ATLAS	HerMES	H-ATLAS
A [mJy/beam]	15.211 ± 0.016	15.45 ± 0.017	11.149 ± 0.017	11.166 ± 0.017
x_0 [arcsec]	0.076 ± 0.011	0.156 ± 0.011	1.41 ± 0.023	1.455 ± 0.022
y_0 [arcsec]	0.001 ± 0.011	0.001 ± 0.011	1.266 ± 0.023	1.25 ± 0.022
B [mJy/beam]	0.23 ± 0.003	-0.18 ± 0.003	0.046 ± 0.002	-0.322 ± 0.002
	500μm			
	HerMES	H-ATLAS		
A [mJy/beam]	5.983 ± 0.006	5.793 ± 0.007		
x_0 [arcsec]	0.113 ± 0.017	0.188 ± 0.018		
y_0 [arcsec]	0.748 ± 0.017	0.725 ± 0.018		
B [mJy/beam]	0.168 ± 0.002	-0.106 ± 0.002		

Table 6.2: Parameters for the Gaussian PSF fits for all three SPIRE bands. The 250μm plots are shown in figure 6.2.

between the shape of the signal in the map and the PSF used for source extraction is far greater than the difference between the maps themselves. However, this is before one considers the effect of correlation between sources, e.g. by using simultaneous fitting to obtain photometry of sources, or simultaneously stacking sources with SIMSTACK, which can explain some of the flux in the residual maps. Of primary concern for studies using catalogues therefore is the residual between the map and PSF used as opposed to the difference between the beams in the map from each team's data.

The particular source detection and extraction algorithms used however will have very different systematic errors associated with them, and it is suspected that these differences will be greater than those between maps processed with pipelines.

6.5 Comparing Catalogues

Whilst the maps have their differences, many astronomers will use only catalogues generated by the two teams. For this comparison we use HerMES's STARFINDER/DESPHOT photometry pipeline with 250μm priors, officially designated as xid250 catalogues. H-ATLAS's catalogue production uses MADX with sources detected at 250μm as priors. As COSMOS was originally designed as a HerMES field, all catalogue production has been performed on the HerMES-COSMOS map only.

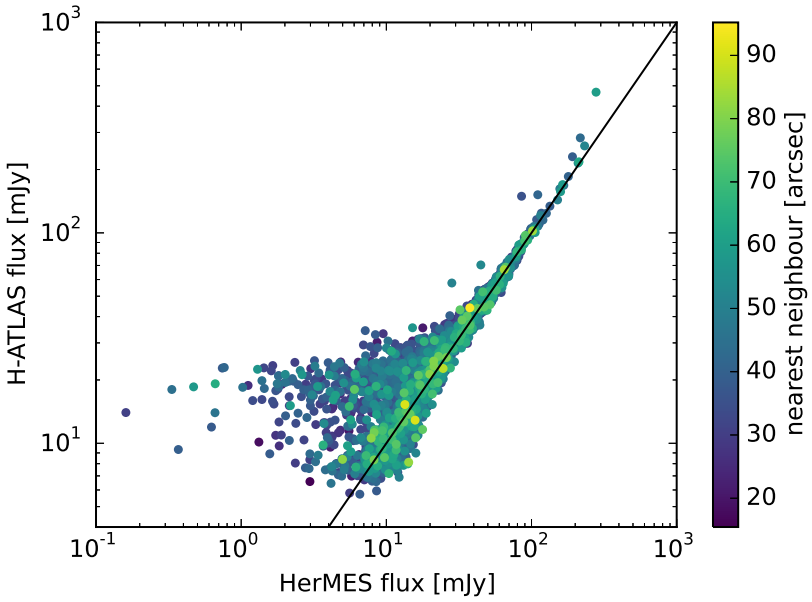

Figure 6.3: HerMES and H-ATLAS COSMOS catalogues compared by flux. The colour axis indicates the distance to nearest neighbour in the H-ATLAS catalogue. There is an obvious trend reflecting figure 6.5 showing H-ATLAS over-estimates the flux of a source when sources are closer together.

6.5.1 Matching the Catalogues

For comparison, all sources in the 250μm catalogues are matched to 2 arcseconds (a third of a pixel at 250μm). From 14038 and 9501 sources in the output catalogue for HerMES and H-ATLAS respectively, 2746 matches are found. To understand differences between the extracted sources, the environment of the sources in the map must be assessed. To this end, each matched source is compared to the full catalogue it originated from and the distance to nearest neighbour is recorded in arcseconds. This value acts as a proxy for the density of environment of the source.

Plotting flux against flux (figure 6.3) shows that whilst there is generally good agreement with the flux of sources, H-ATLAS does over-estimate fluxes when compared to HerMES fluxes estimation methods. Given that HerMES's catalogue production pipeline was designed to deblend sources in deep maps, it's possible that flux from neighbouring, undetected sources has contaminated fluxes in the H-ATLAS catalogues.

Figure 6.4 shows the distance to nearest neighbour in the catalogues for HerMES and H-ATLAS. The distance to nearest neighbour appears to be consistent, with both HerMES and H-ATLAS attributing flux to sources at similar separations beyond the FWHM of the beam, with a slight tendency of HerMES sources to be found closer together than those

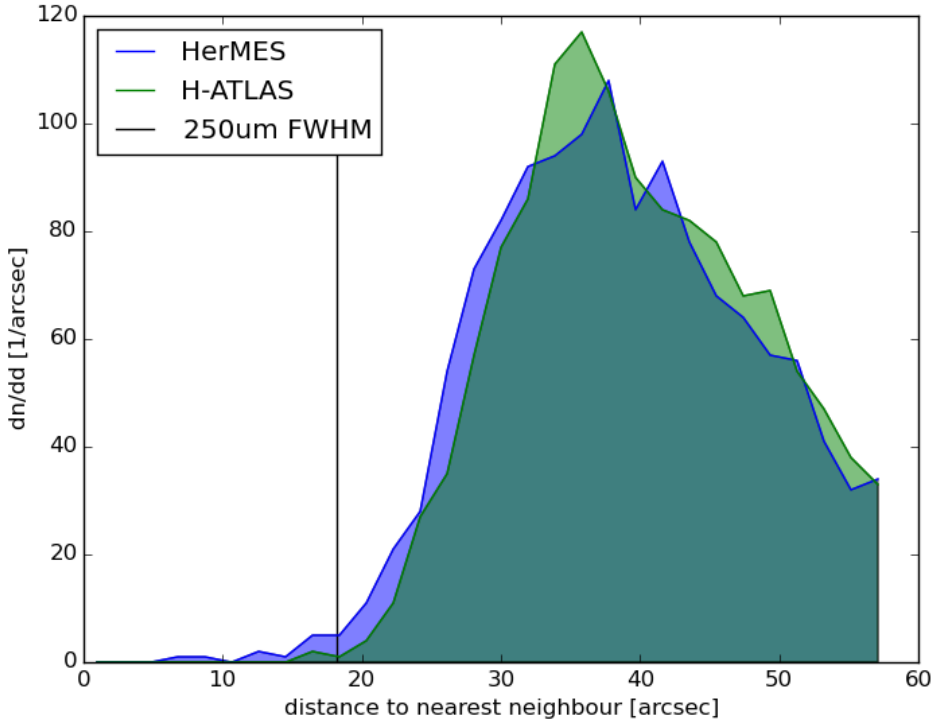

Figure 6.4: The distance to the nearest source in HerMES and H-ATLAS catalogues. The HerMES catalogues are more likely to contain sources closer together, although the difference is marginal.

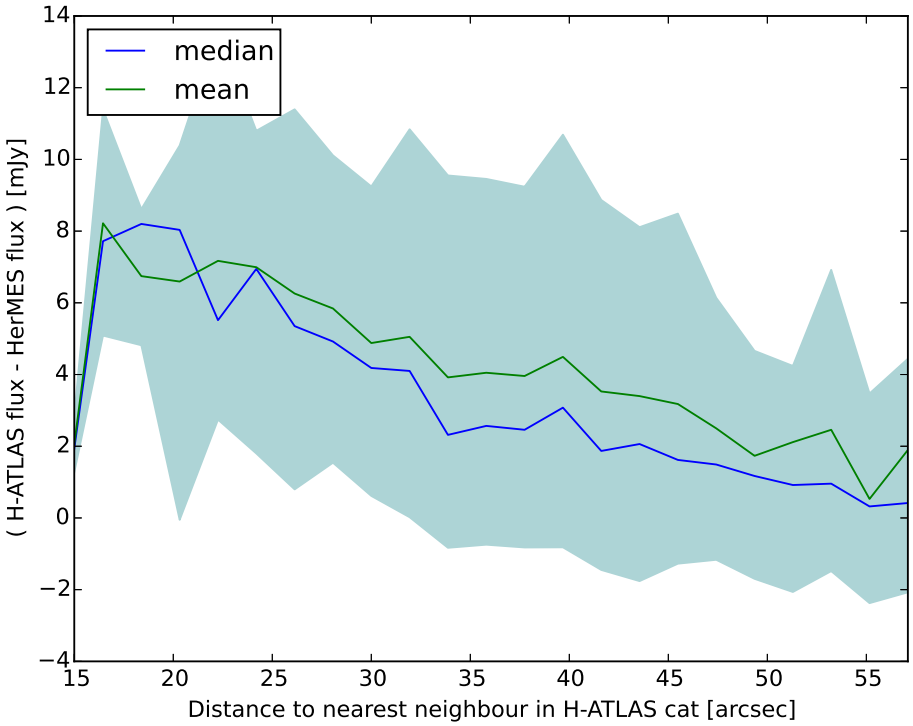

Figure 6.5: The overestimation of source flux in H-ATLAS as a function of distance to nearest neighbour. Both the mean, median and 16th and 84th (central 68%) percentiles are shown. Fluxes are not on average overestimated compared to the HerMES catalogue at a source separation of one arc minute.

from H-ATLAS. It is also very unlikely for sources to be found within a FWHM of another source, showing a limit to the deblending abilities of both pipelines.

To understand whether there is a systematic effect on the estimation of flux as a function of distance to nearest neighbour, sources are binned by this distance calculated from the H-ATLAS catalogues as shown in figure 6.5. The difference between the flux as determined by MADX and DESPHOT is shown. Plotted in addition are the median and 16th and 84th percentiles (central 68% of distribution) of the distribution, given because the distribution of flux differences is non-Gaussian. The mean is plotted to show that the difference between median and mean is minimal. There is a definite trend between the difference in flux with distance to nearest neighbour, with H-ATLAS highly over-estimating fluxes at small separations. At 15 arcsec, a separation of approximately 1FWHM the over-estimation is 8mJy, falling to zero at 1 arcmin, at 3.3 FWHM separation.

Figure 6.3 displays this distance information as the colour of the points. Whilst the true distribution of sources in this flux-flux space is not entirely dependent on distance to

nearest neighbour, the trend is clearly visible, with sources close to the equality line more likely to correspond to greater separations. This shows H-ATLAS is not de-blending fluxes correctly in deep maps like COSMOS. However, MADX was not designed to find sources in very deep maps. The shallower H-ATLAS maps contain much more instrumental noise and therefore the density of sources detected drops. Therefore the average separation between sources increases and this over-estimation of flux is less likely to be an issue. SUSSEXtractor uses a similar source detection technique with a matched-filter, although the convolution kernel used in SUSSEXtractor is far narrower to compensate for this confusion. If MADX was to be adapted for use in these deep maps, this is the part of the algorithm that would need modification.

6.6 Recommendations for the HELP project

From the analysis on the COSMOS map, subtle differences have already been shown highlighting the differences between the HerMES and H-ATLAS pipelines. As seen from stacking the maps themselves, the fluxes can be seen to have an approximately 1% discrepancy between the analysis through fitting Gaussians to the peak of the stacks. The background itself differs by a fraction of a mJy, depending on the study using the maps this value could be significant and so keeping note of these differences is recommended. The discrepancy between the PSF used for source extraction and the maps themselves is approximately 5%, similar to the value noted in Griffin et al. (2010) and is greater than the difference between the two maps. For studies conducting source extraction then, the discrepancy between the PSF used for source extraction and the map is a more important to take into account than the systematic differences between the maps. Based on the COSMOS field, the deep maps at least do not need to be rerun, only the systematic differences highlighted above need to be taken into account.

There are fundamental differences between the catalogue creation pipelines MADX and STARFINDER/DESPHOT. The main difference in performance is the overestimation of the flux by MADX as a function of source separation as determined in the COSMOS field. COSMOS however is a deep map with the noise dominated by confusion noise and therefore blended sources. The source detection algorithms are able to find sources within these confused regions, but only DESPHOT, using simultaneous fitting for the fluxes, is able to avoid being affected by the source blending. HELP is planning to use a Bayesian simultaneous fitting technique to find fluxes in the maps called XID (Hurley et al., submitted), and the current comparison is demonstrating that this is a good direction in

which to proceed.

To further this investigation of the map and catalogue based approaches, the GAMA15 field, the wide, shallow field that MADX has been optimised on, would need to be investigated. This is left for further work due to time constraints.

The difference in performance between source extraction pipelines may go some way to explain the differences in the angular clustering result found by both collaborations. To ascertain what differences need to be explained, the angular clustering analysis will need to be recreated to rule out any systematic effects due to the methodology used by both collaborations.

6.7 The Clustering of Galaxies

With gravitational collapse of baryonic onto dark matter, galaxies in the Universe will not be distributed randomly across the sky, instead broadly tracing the underlying dark matter distribution. Understanding the distribution of galaxies can shed light on the underlying cosmology of the Universe and can be used to calculate the typical masses of the dark matter haloes a particular population of galaxies reside in. The density of galaxies point-to-point across the sky is one discriminator, but the description can extend to higher moments of this distribution. In this section the second moment is discussed in the form of the angular 2-point correlation function and previous results for infrared galaxy populations given. This correlation function is calculated with catalogues in the Lockman-SWIRE field found with SUSSEXtractor. Attempts are made to correct this function for both the limited size of the field at large scales and for source blending at small scales. The individual corrections are discussed and improvements suggested. This result is compared to recent HerMES and H-ATLAS results to reconcile the conflict between the collaborations. The continuing work is then outlined.

6.7.1 Definition of the 2-point Angular Correlation Function

In this subsection the angular correction function is defined and the link between the three dimensional and 2D dimensional description outlined. the connection between these correlation functions and physical attributes of the Universe is also given, although this is for context as these values are not calculated.

The second moment of the galaxy distribution function is defined as the probability P of finding a neighbouring galaxy within a volume V. For a Universe with galaxies

distributed randomly, this is defined as

$$\delta P = n\delta V \tag{6.10}$$

where n is the mean number density of galaxies. In the non-homogenous case (i.e. galaxies are distributed with clustering and voids), this is generalised to

$$\delta P = n(1 + \xi(r))\delta V \tag{6.11}$$

with $\xi(r)$ representing the clustering between two objects distance r apart. Constraints exist for ξ; $\xi \geq -1$ to ensure positive probability and $\xi \to 0$ as $r \to 0$ as at small scales the generalised density should tend to the mean density n. Due to assumptions of isotropy, r in this case is not a vector; a general description of galaxy clustering across the Universe should obey the isotropy condition of the cosmological principle. The *joint* probability of finding two galaxies separated by distance r is then given as

$$\delta P(r) = n^2(1 + \xi(r))\delta V_1 \delta V_2 \tag{6.12}$$

Whilst the 2-point correlation function $\xi(r)$ provides three-dimensional information about the nature of galaxy clustering and therefore is the most powerful discrimination tool between models of galaxy clustering, as the current data stands this is not directly calculable with HerMES data. To find the three-dimensional, real space correlation function, accurate redshifts are required for each galaxy in the sample. Whilst ancillary data with redshifts have been matched to sources within the HerMES catalogues, and photometric redshifts can be calculated (Clements et al., 2014) the high degree of confusion between HerMES sources makes any calculation of redshift, and therefore $\xi(r)$ tenuous at best at this stage.

Reducing the spatial 2-point correlation function $\xi(r)$ to the angular 2-point correlation function $\omega(\theta)$, a function of separation on the sky θ can provide constraints to clustering models as no radial distance information is required. $\omega(\theta)$ is the projection of $\xi(r)$ on the sky. Equation 6.12 can be rewritten for the angular case as

$$\delta P(\theta) = n^2(1 + \omega(\theta))\delta\Omega_1 \delta\Omega_2 \tag{6.13}$$

with $\delta\Omega$ as the infinitesimal solid angle and n now the surface density.

6.7.2 Estimators of $\omega(\theta)$

Estimating $\omega(\theta)$ can be achieved by estimating the ratio of probabilities of finding sources at angular separation θ (Davis & Peebles, 1983). One can calculate the total number

of sources within angular separation $\theta + \delta\theta$ for each galaxy. This pair counting can be performed for each galaxy to record all *unique* pairs and summed over all galaxies. This measurement, referred to in the literature as dd or the unnormalised "data-data" pair count is then normalised by the number of possible unique pairs,

$$DD(\theta) = \frac{dd(\theta)}{N_d(N_d - 1)} \tag{6.14}$$

with N_d the total number of sources with the catalogue. This value must then be compared to what is expected from a Poisson-like distribution of sources, as naturally the number of expected pairs found would increase with separation θ. Naively, the number of expected pair counts at separation $\theta + \delta\theta$ would be $2\pi n\theta\delta\theta$, with n_r the density of random sources. However, the sky is not infinite in size, especially considering the finite size of the map, and so this value must be calculated to take this into account. A catalogue of points are placed randomly within the map. The random catalogue must have a much higher number density of sources than the data catalogue, allowing the estimate of RR(θ) to be unhindered by shot noise. RR is calculated as

$$RR(\theta) = \frac{rr(\theta)}{N_r(N_r - 1)} \tag{6.15}$$

The ratio of the two values (with the number of pair counts acting as a proxy to the number densities n_d and n_r) gives

$$\omega(\theta) = \frac{DD}{RR} - 1 \tag{6.16}$$

This measurement is not quite analogous to the probability in equation 6.13 as DD is measuring the probability of finding a neighbouring galaxy within separation θ *from another galaxy*. Therefore this value is biased. To be truly analogous, the $\omega(\theta)$ measure must be calculated from a random position. A better approximation can be given by replacing RR with DR, a function of the total number of unique counts *between* the data and random catalogue expressed as

$$DR(\theta) = dr(\theta)/N_r N_d \tag{6.17}$$

where $dr(\theta)$ the unnormalised pair counts between the data and random catalogue. $\omega(\theta)$ is then given as (Davis & Peebles (1983))

$$\omega(\theta) = \frac{DD}{DR} - 1 \tag{6.18}$$

effectively the ratio of the two different probabilities of finding sources at a separation of θ.

This is not however the best estimator to use. Landy & Szalay (1993) discuss the mean and variance calculations of both equations 6.16 and 6.18. They found that, due to correlations between quantities, the variance in the measurements is greater than the shot noise generated by the sizes of the data and random catalogues. Instead they construct a new estimator that has approximately Poisson variance, given as

$$\omega(\theta) = (DD - 2DR + RR)/RR \tag{6.19}$$

With this estimation the error in each bin can be expressed with Poisson noise (Baugh & Efstathiou, 1994; Hewett, 1982) as

$$\delta\omega(\theta) = \sqrt{\frac{1+\omega(\theta)}{\langle DD\rangle}}. \tag{6.20}$$

These errors can be directly compared to bootstrapped sampling of the data (Ling et al., 1986).

From the late sixties and through the seventies, measurements of angular clustering (Totsuji & Kihara, 1969; Peebles, 1974) have shown a power law-like measurement for $\omega(\theta)$ given as

$$\omega(\theta) = A_\omega \theta^{1-\gamma} \tag{6.21}$$

with $\gamma \approx 1.8$ across a variety of scales. This is significant as the measurement lends credence to the assumption that the Universe is homogeneous. The amplitude or strength of clustering, A_ω, provides information on the relative strengths of clustering for different populations; the larger the value of A_ω the stronger the clustering.

6.7.3 Incorporating Evolution with Redshift

Whilst the correlation function $\xi(r)$ cannot be directly calculated without redshifts for each source, the parameters of the angular correlation function A_ω and γ can be used to calculate the typical clustering scale r_0. In the case of small angles the spatial correlation function and redshift evolution can be uncoupled and approximated as power-laws, with $\xi(r)$ becoming

$$\xi(r,z) = \left(\frac{r}{r_0}\right)^{-\gamma} (1+z)^{-(3+\epsilon)} \tag{6.22}$$

with r_0 specifying the clustering amplitude; the smaller the distance r_0 the stronger the clustering; physically this is the comoving correlation length at $z = 0$. ϵ parameterises the evolution, $\epsilon = 0$ reduces the evolution to the expansion of space only with clustered regions remaining fixed, and $\epsilon = 3 - \gamma$ implies clustering scales expand along with the

expansion of space (i.e. everything moves further apart withe the Hubble flow) (Mo et al., 2010).

Whilst lack of spectroscopic information for HerMES sources makes a *direct* calculation of $\xi(r)$ impossible, Limber's equation (Limber, 1953) uses a specified redshift distribution and $\xi(r)$ to calculate an integrated $\omega(\theta)$ along line of sight. Inverting the equation will provide an estimate for r_0. Limber's equation simplified for small angular scales (i.e. small fields) and using equation 6.21 (Phillipps et al., 1978) is

$$A_\omega = C r_0^\gamma \frac{\int D_\theta^{1-\gamma} g^{-1}(z)(1+z)^{-(3+\epsilon}(\mathrm{dN/dz})^2\,\mathrm{dz}}{[\int \mathrm{dN/dz})]\mathrm{dz}]^2} \tag{6.23}$$

where dN/dz is the redshift distribution, C is the function

$$C = \pi^{1/2}\frac{\Gamma[(\gamma-1)/2]}{\Gamma(\gamma/2)} \tag{6.24}$$

D_θ is the angular diameter distance and g(z) relates the scale factor to the comoving distance as

$$g(z) = \frac{c}{H_0}\left[(1+z)^2(1+\Omega_0 z)^{1/2}\right]^{-1} \tag{6.25}$$

Given these equations it is possible to calculate the typical galaxy separation r_0 using the measured angular correlation function. Limber's equation is not calculated on the results presented in this ongoing chapter, but in future this equation could be used in conjunction with redshift distributions calculated with HerMES or H-ATLAS (Béthermin et al., 2012; Burgarella et al., 2013; Eales et al., 2010b). However, the preference for interpreting the angular correlation function is by using a technique called halo modelling (section 6.7.4) as this also recovers physical attributes of the dark matter haloes sources reside in.

6.7.4 The Link Between Galaxies and Dark Matter

Galaxies do not directly trace the underlying dark matter distribution. Baryonic matter interacts more than just gravitationally (as cold dark matter is currently modelled to) and so any purely gravitational collapse will be hindered by pressure interactions, feedback forces within galaxies, radiation pressures, interaction with and decays of nuclei; effectively these are results of electromagnetic, weak and strong forces. Kaiser (1984) demonstrate the density contrast of matter to galaxies can be expressed as

$$\left(\frac{\delta\rho}{\bar{\rho}}\right)_{\mathrm{mat}} = b\left(\frac{\delta\rho}{\bar{\rho}}\right)_{\mathrm{gal}} \tag{6.26}$$

where $\bar{\rho}$ is the mean, smoothed density over a large scale. This absolute bias b is shown to relate to the correlation function $\xi(r)$ as

$$b = \sqrt{\frac{\xi_{\rm mat}}{\xi_{\rm gal}}} \tag{6.27}$$

the square root of the ratio between the correlation functions. The bias between different galaxy populations for example is referred to as the relative bias.

This particular calculation is folded into halo modelling, where the 1-halo and 2-halo terms of the distribution of sources are modelled against the correlation function (or the corresponding power spectrum in Fourier space). The 1-halo term characterises the clustering of central dark matter halos and the surrounding sub halos. These sub halos could be accreted onto the central halo, and are at a lower mass than the central halo. 2-halo clustering refers to the strength of central to central halo clustering, i.e. the clustering between larger structures in the Universe. The measured correlation functions can be used to measure the clustering of dark matter halos through calculations of the bias and halo modelling. Halo modelling is also able to break down the power-law nature of the observed clustering distributions into the 1-halo and 2-halo components. Halo modelling and the calculation of the bias is not performed on the results below but would be a desired extension to the work to update the results in Cooray et al. (2010).

6.7.5 Previous Results

In this section previous results are outlined. This is not an exhaustive list of infrared correlation function calculations but gives scope to previous work performed. Clustering of galaxies in the infrared has a long history of study, and angular correlation analyses have found largely consistent results. Early in modern infrared astronomy, studies with subsets of IRAS galaxies found angular correlation functions in the form $\omega(\theta) = (\frac{\theta}{\theta_0})^{1-\gamma}$ with $\gamma = 1.7$ for galaxies at 60μm at high and low galactic latitude (Rowan-Robinson & Needham, 1986). The clustering of infrared galaxies in relation to optical galaxies was also found; Babul & Postman (1990) determined the clustering of IRAS sources was identical to late-type optical galaxies with $\gamma \approx 1.8$. Lahav et al. (1990) compared the strength of clustering between infrared and optical sources (comparing the bias b) and find a range of values $b_{opt}/b_{IR} \approx 1.0 - 2.0$.

With this difference in clustering strength between optical and infrared sources, it was hypothesised that the infrared emission was not tracing stellar mass directly but obscured star formation only. Further measurements of the angular clustering function have been

made on small scales with ISO (Infrared Space Observatory); Gonzalez-Solares et al. (2004) analysed 4 sq. deg. in the ELAIS S1 (Oliver et al., 2000) region, with 462 sources at 15μm and $\gamma = 2.04 \pm 0.18$. With deeper Spitzer imaging, Oliver et al. (2004) find on a total of 2 sq. deg. a consistent value of $\gamma = 2.03 \pm 0.10$ for sources at 3.6μm. In Gonzalez-Solares et al. (2004) this calculation is taken further, inverting Limber's equation using an estimated median redshift to parameterise a redshift distribution function to find a three dimensional clustering value of $r_0 = 4.4 \pm 0.1 h^{-1}$ Mpc.

Populations of infrared galaxies are also studied. Farrah et al. (2006) select a sample of ultra-luminous infrared galaxies (ULIRGs) between redshifts $1.5 < z < 2$ and $2 < z < 3$, finding $r_0 = 14.40 \pm 1.99 h^{-1}$ Mpc and $r_0 = 9.40 \pm 2.24 h^{-1}$ Mpc respectively, an extremely strong clustering bias indicating ULIRGs are in very dense environments and residing in the most massive halos. At 24μm, recent results are born out, showing galaxies with high infrared flux lie in progressively more massive halos; Gilli & Daddi (2007) finding $r_0 = 4.1 \pm 0.4 h^{-1}$ Mpc and $\gamma = 1.5 \pm 0.1$.

BLAST, the Balloon-borne Large Aperture Sub-millimetre Telescope was originally developed as a pathfinder mission for the Herschel-SPIRE instrument, with wavelengths 250μm, 350μm and 500μm. Whilst source clustering wasn't performed, a power-spectrum analysis of the maps was performed in Viero et al. (2009) and the results interpreted back to real-space, finding a correlation length $r_0 = 4.9 \pm 0.7 h^{-1}$ Mpc, $r_0 = 5.0 \pm 0.7 h^{-1}$ Mpc and $r_0 = 5.2 \pm 0.7 h^{-1}$ Mpc for the three bands respectively. The selection criteria for the power spectra analysis is harder to translate back into real-space, but the study itself was attempting to quantify the clustering of the far-infrared background rather than just easily resolvable galaxies and found a small clustering scale, implying that sources making up the cosmic infrared background were covering a wide range of redshifts and were not all belonging to a strongly clustered population e.g. ULIRGs.

Finally, there has also been work exploring the data obtained from the Herschel Space Observatory. The earliest results were from Cooray et al. (2010) from HerMES, finding clustering of resolved sources $r_0 = 4.5 \pm 0.5$Mpc at 250μm and $r_0 = 6.3 \pm 0.7$Mpc at 500μm, and the correlation function was resolved well enough to fit a halo-model to the results, resolving the correlation functions in to 1-halo and 2-halo contributions. The halo model indicates that the minimum halo mass for the clustered sources is $(5 \pm 4) \times 10^{12} \mathrm{M}_{\odot}$. This deconstruction of the correlation function was also performed by Amblard et al. (2011) in the frequency domain also on science demonstration data, finding a minimum halo mass an order of magnitude below the Cooray et al. (2010) results. Viero et al. (2012) ran a

similar analysis on data from HerMES' first data release and find a minimum halo mass even lower by an order of magnitude. However the authors note that the power spectra is dominated by sources sub 5mJy in flux whereas the Cooray et al. (2010) sources had a minimum flux of 30mJy, thus biasing those results to higher masses. Finally, Mitchell-Wynne et al. (2012) find a correlation function in the 250μm that is weaker than Cooray et al. (2010). The halo modelling performed is however in agreement with the Amblard et al. (2011) result.

The H-ATLAS team also published results parameterising the clustering on their science demonstration data. Maddox et al. (2010) fold in the redshift distribution from Amblard et al. (2011) and find a clustering measurement of $7 - 11h^{-1}$ Mpc dependent on which value of γ used for the 350μm and 500μm band only; they find a clustering measurement consistent with zero in the 250μm, finding 30% of sources with $z < 1$ (Smith et al., 2012b) and thus a weaker clustering signal.

6.7.6 The Discrepancy at *Herschel*-SPIRE wavelengths

The majority of results within the infrared have been consistent with previous studies. An issue of contention arises however when considering the results of Cooray et al. (2010) and Maddox et al. (2010), with the former finding a strong clustering signal in the 250μm band and the latter either a negative clustering or a result consistent with zero. The H-ATLAS fields are wider, shallower and have greater cirrus contamination and as such are filtered before source extraction. This filtering could affect the efficacy of source extraction. The inconsistency could also arise due to the systematic differences in the catalogue production pipelines.

Previous studies have been consistent in finding clustering rather than under densities of sources in the infrared, implying that the H-ATLAS results are under estimating the clustering of 250μm sources. The HerMES 250μm result is also contrary to received wisdom however; the amplitude of clustering is much stronger than in the 350μm and 500μm bands. As the majority of bright 250μm sources should be at a lower redshift, the clustering amplitude should be weaker in this band. HerMES find the stronger amplitude in both Lockman-SWIRE and FLS fields which lends weight to the result, but it is surprising. By reproducing the HerMES results, these Cooray et al. (2010) results can be checked.

6.8 Calculating $\omega(\theta)$

6.8.1 Calculating the Raw $\omega(\theta)$ Values

To resolve this issue we take the updated HerMES catalogues from SUSSEXtractor for the Lockman-SWIRE field and rerun the clustering study. The study is run on AORs 34 and 40 with catalogues created as part of the first data release. There was the option to use the catalogues created as part of the second data release in chapter 2 or to use the nested fields combining AORS 28+28B, however these were nested fields with a variety of depths and therefore the clustering measurement would not be as uniform as a shallow, flat field. The same cuts at 30mJy were used; as shown in chapter 3 the catalogue can be considered complete and the flux boosting minimal at this flux.

A set of 500 random catalogues of 100,000 sources were generated within the field footprint for each band, a number density ten times greater than the data to reduce shot noise. The data was also bootstrapped to create 100 measurements of the data-data (DD) pair count. This gives 500,000 separate measurements of the 2-point angular clustering function.

The distances calculated were Euclidean distances, transforming the coordinates from ra and dec to x and y image coordinates. For this relatively small field (as opposed to spanning hundreds of sq. deg.) this was deemed sufficient. Counts were binned into a histogram of 1 arcsec separation and then rebinned into log-spaced bins of 0.3 to 30 arcmin to cover a wide range of separations for plotting.

To speed up the pair counting process, nearest neighbour queries on kd-trees were used. A kd-tree separates data into 'leaves', blocks of data in multidimensional space (in this case, x and y). When the tree is queried with a position and a maximum separation, the tree immediately discards leaves that are too far from the queried point, significantly reducing the number of distances to calculate.

The initial results, the raw angular correlation functions for each *Herschel*-SPIRE band are shown in figure 6.8. To be compared to other results however, the raw $w(\theta)$ must be corrected for effects at small scales with the transfer function (subsection 6.8.2) and at large scales with the integral constraint (section 6.8.3).

6.8.2 Calculating the Transfer Function

At small separations source blending may make identifying sources extremely difficult or sources below the flux cut may be boosted above it. As established from chapter 3, sources

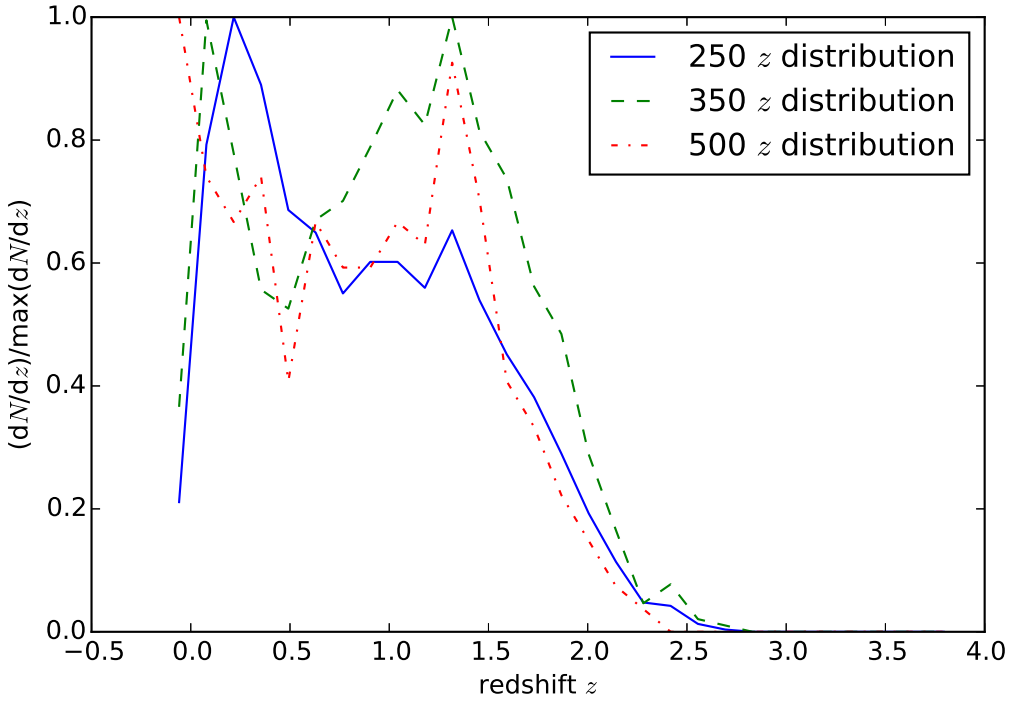

Figure 6.6: The redshift distribution of simulated sources in the 250, 350 and 500μm bands. The sources selected are above 30mJy in flux, and in each case the distribution has been normalised to peak at 1. The 250μm redshift distribution contains bluer and therefore lower redshift galaxies. The clustering of these galaxies would therefore constraining the transfer function using these sources would be difficult. The 350μm is used for all three transfer functions.

can be missed or boosted at low fluxes. This could cause the angular correlation function to be over- or under-estimated at small angular separations. This can be corrected for by finding the ratio between the true clustering in the sky and the observed clustering from the catalogues. This ratio, and the correction applied to the observed clustering to recover the truth, is known as the transfer function. To that end, a realistic simulation of the sky from Lacey (2015) (created to mimic a H-ATLAS field) is adopted and modified for this purpose. A semi-analytic model instead of a simple distribution of points on the sky is used to ensure that the correction for deblending as accurate as possible. The cross-over between halo models of one and two halo clustering as fitted by Cooray et al. (2010) are sensitive to small scales. SAMs can replicate the one and two halo distributions unlike a distribution of points conforming to only a power-law fit.

The simulation used is a variant of the GALFORM semi-analytic model (SAM, (Lacey, 2015; Cowley et al., 2015)). A suite of physical processes are modelled and iteratively

matched to empirical data to find the best-fit parameters for these models. These models are used in conjunction with the merger trees of dark matter halos constructed from the Millennium simulation (Springel et al., 2005). Physical properties and observables of the galaxies the dark matter halos should contain are then catalogued along with the halo position. By projecting a cone through the simulated cosmological volume over different time-steps in the Millennium simulation, a projection of this simulation as an image of the sky can be made. This structure is called a lightcone. Different lightcones can be made with the same cosmological simulation by changing the direction of the projection through the simulation. The Lacey (2015) simulation was chosen above other GALFORM models as it can reproduce a range of observations across many wavelengths and combines a number of different physical models used in previous GALFORM SAMs.

As detailed in chapter 2, simulated maps can be created with catalogue positions and fluxes, resolving creating the sky to a 2 arcsec grid, convolving with the appropriate telescope beam and running this map through the SMAP simulator to produce simulations of the observation with appropriate noise levels. As the aim of the simulation is to calculate how $\omega(\theta)$ changes as an input and output after source extraction, the simulation does not need to be completely accurate, only representative of the clustering an number counts. The clustering in the 250μm band is expected to be weak and so finding the ratio between $\omega(\theta)_{in}$ and $\omega(\theta)_{out}$ above the shot noise may be difficult. The redshift distribution of sources at fluxes about 30mJy is determined in figure 6.6. As the 350μm sources are at a more distant mean redshift, the clustering will appear stronger in this band. Therefore, the 350μm catalogue is used for the simulation of all three bands. Fortuitously, this choice allows a direct comparison of the effect of the blending caused by the beam size on the measurement of $\omega(\theta)$ across all three bands.

A number of simulated images constructed from lightcones would be required to form an accurate estimate of the input and observed clustering strengths and thus form an averaged transfer function. Unfortunately only one lightcone (covering 15 sq. deg.) was made available. The dimensions were too small to simulate Lockman-SWIRE. By using a smaller field however, and centring the field footprint over different regions in the simulated sky, this would effectively create many simulated maps. The largest and shallowest field that would fit into this lightcone was FLS at 6 sq. deg. Five realisations of the FLS field are made by centring the field footprint in different regions of the Lacey (2015) lightcone. Due to the relative small size of the circular lightcone compared to the field, these observations experience significant overlap. However, as not exactly the same parts

of the lightcone are sampled in each realisation, there will be a different clustering strength in each region and so the measurements can be considered independent. Each realisation of the map is subdivided into four regions of approximately equal area to increase the number of measurements of the transfer function. The transfer function has been shown to only have an effect at < 10 arcmin scales (Cooray et al., 2010) or < 3 arcmin scales (Mitchell-Wynne et al., 2012). Therefore subdividing the region was deemed an acceptable way to create more realisations. Whilst the ratio of input to output $\omega(\theta)$ would allow one transfer function to be calculated, the values that govern the shape of $\omega(\theta)$ are DD and DR. Therefore constraining the effect of observation on these pair counts would more accurately pinpoint what is changing between the input and observed correlation functions. Therefore a separate transfer function is calculated for both of them.

Subfigure a in figure 6.7 show the ratio between DD_{in} and DD_{out} for the SUSSEXtractor pipeline, and subfigure b the analogous ratios between DR_{in} and DR_{out} for the four cut outs from one realisation. SUSSEXtractor shows a lot of variation at small projected angles for DD_{in}/DD_{out}, especially below 2 arcmin. The DR ratio is far smaller than the DD ratio as the pair counts are dominated by the random catalogue in this case. It is important to stress that this is a first attempt at a correction; larger simulated maps or many more realisations would be appropriate to calculate these values far more robustly. The correlated fluctuations in the ratio of the different realisations are most likely down to the repeated nature of the simulations used. One would expect, on average, the ratios to be smooth, showing a converging or diminishing to 1 ratio at the largest separations. Instead the ratio fluctuates. This indicates that there is an excessive or insufficient number of pair counts at this particular separation, possibly due to a denser than average number of sources in that region, some of which will be lost in the confusion. To wash this effect out in the averaging of the ratios, a greater number of simulated light cones would need to be used (i.e.) a different projection through the Millennium simulation with the same model applied. With this need for improvement in mind, the analysis proceeds to see what effect the transfer function has at all scales to determine whether the number of simulations used needs to increase dramatically, or whether this approximate set of transfer functions can be incorporated into the rest of the analysis as a first attempt.

Subfigures c and d of figure 6.7 show the averaged values over the five realisations and the error on the mean for the SUSSEXtractor transfer function. As these values are ratios, the average in log-space is taken. In the case of both the DD and DR corrections, the transfer functions are not very smooth due to the small number (20) of realisations used

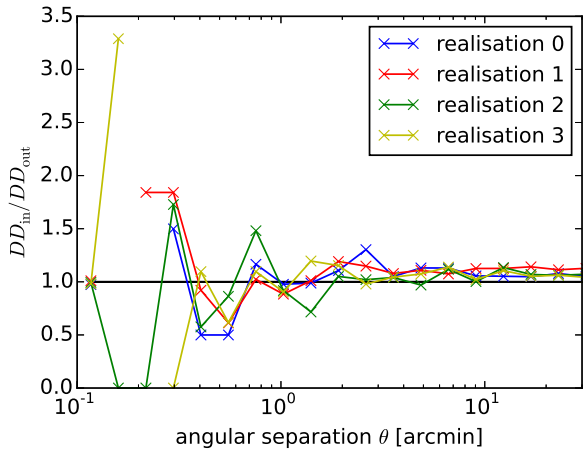

(a) Ratio $DD_{\rm in}/DD_{\rm out}$ at 250μm

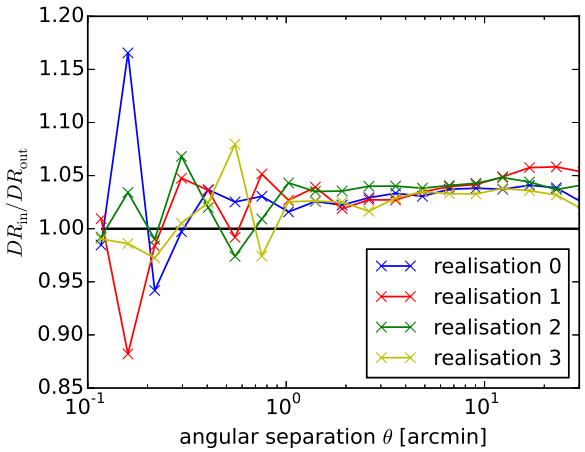

(b) Ratio $DR_{\rm in}/DR_{\rm out}$ at 250μm

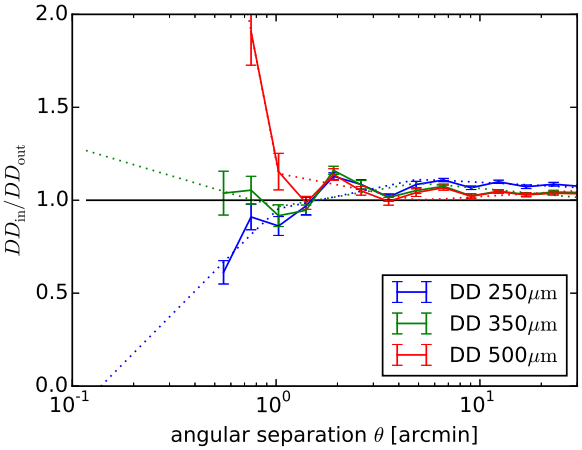

(c) Transfer function for DD for all bands

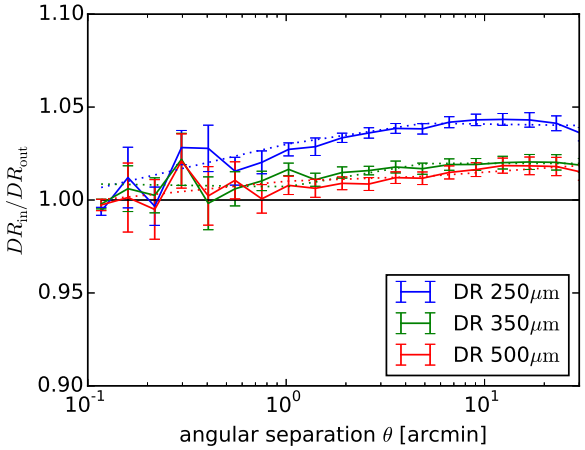

(d) Transfer function for DR for all bands

Figure 6.7: The ratio between input and output DDs and DR. The results from each cutout and realisation are averaged and the ratio is fitted by linear splines in log10(θ) space, with knots at 1 and 5 arcsec. There is a strong deviation at angular separations less than 1 arcmin, due to the effect of source blending.

to construct it. As an attempt to smooth the transfer function to ensure the corrected $\omega(\theta)$ is somewhat continuous, two linear splines are fitted in semi-log space for each band with a knot at 1 and 5 arcmin and are shown on the figures.

As all the simulated maps were created with exactly the same sky (only at different beam resolutions) the differences between the calculated transfer functions at 250, 350 and 500μm must be due to the size of the beam and instrumental noises. On smaller scales than 1 arcmin, there is a strong deviation between the bands even though the same maps at different resolutions are used. At 500μm the pair counts are severely under-estimated (factor of 0.5 at 0.4 arcmin); sources are extremely confused and so at very small scales the number of pair counts reduced. In the 250μm map finding sources is not as significant an issue as flux boosting caused by Eddington biasing, particularly a problem in dense, clustered regions (factor of 1.5 at 1 arcmin). More sources are detected above a flux cut in these regions and thus the number of pair counts are over-reported at these smaller scales. In contrast, DR shows the pair counts are underestimated by a maximum of 4.5% in the 250μm but at angular separations of 10 arcmin.

From these results it is apparent that the transfer function applies at all scales from these simulations, a constant factor of a few percent in DR and changing for DD. This is in contrast to Cooray et al. (2010), reporting that the transfer function only applied at scales $<$ 10arcmin. These results imply that the true clustering strength is greater at large scales than is reported by raw $\omega(\theta)$ calculation. This is not due to the so-called integral constraint that corrects for the finite size of the field as the simulated catalogues cover the same area as the real catalogues. As these result are unexpected, a more rigorous calculation of the transfer function using a larger number of simulated images would be beneficial.

The transfer functions are applied to the raw calculations of $\omega(\theta)$ in figure 6.8. It is applied to every DD and DR measurement before calculating $\omega(\theta)$. Whilst the correlation function of the 500μm sources has indeed been increased at small scales, the effect at other wavelengths is not as expected. At 250μm the correlation function has been suppressed so much there is a definite turnover. At 350μm the correlation function now flattens off. Whilst it is possible that these corrected correlation functions are correct, the unexpected behaviour of the transfer functions (e.g. the ratio of pair counts not being smooth across all scales) is implying these results are not to be trusted at this stage. Instead the analysis proceeds with only the integral constraint applied to the correlation function.

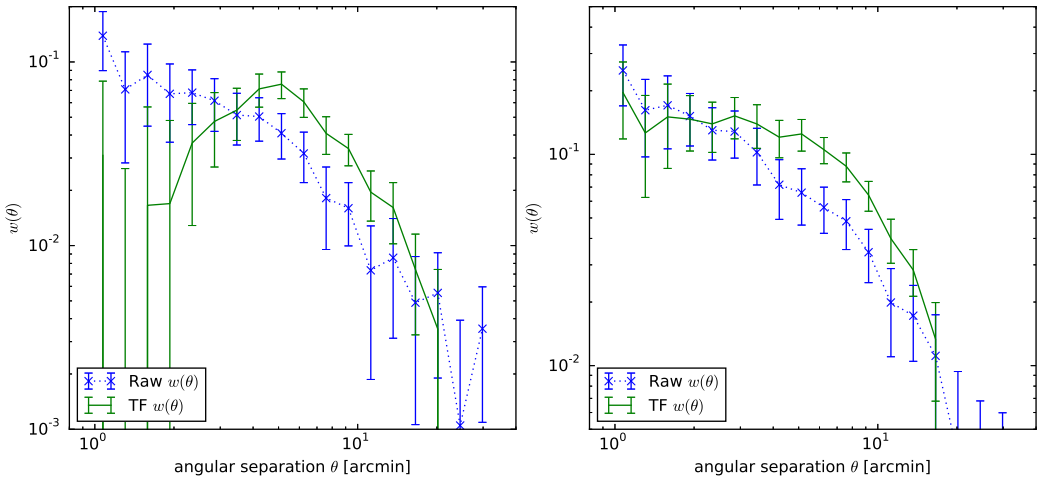

(a) 250μm

(b) 350μm

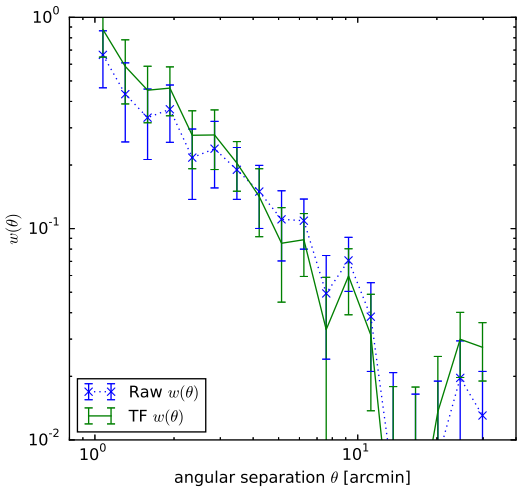

(c) 500μm

Figure 6.8: The estimated transfer function corrections are applied to the raw angular correlation functions plotted with errors on the mean values. Plots for all three *Herschel*-SPIRE bands are shown. The corrections are applied to every DD and DR measurement before averaging and calculating $\omega(\theta)$. Even with relatively small corrections at large θ, the difference between the raw and corrected $\omega(\theta)$ values is large. Due to the size of these corrections and the small number of simulations the transfer function was derived on these results are not carried forward.

band	Int. Constraint	A	γ	$A_{\gamma=1.8}$	$A_{\mathrm{Maddox},\gamma=1.8}$
250μm	0.0227	0.194 ± 0.034	1.920 ± 0.074	0.145 ± 0.008	-0.00
350μm	0.0238	0.303 ± 0.030	1.755 ± 0.038	0.339 ± 0.009	0.11
500μm	0.0218	0.649 ± 0.196	1.966 ± 0.119	0.438 ± 0.038	0.51

Table 6.3: The integral constraint calculated for band, as well as the parameters for the power-law fits. The Maddox et al. (2010) values for A when $\gamma = 1.8$ are also given.

6.8.3 Calculation of the Integral Constraint

If the transfer function application was successful, the next stage at recovering the true value of $\omega(\theta)$ would be to calculate and apply the integral constraint. In this case, the integral constraint is calculated and applied to the raw $\omega(\theta)$. The integral constraint corrects for the underestimate of the mean galaxy density calculated in $\omega(\theta)$ due to finite size of the field examined. This in turn means $\omega(\theta)$ at large scales relative to the size of the field has been underestimated. Therefore there is an additive correction to make to $\omega(\theta)$. The integral constraint is calculated as in Roche & Eales (1999) by fitting a modified power law to the raw $\omega(\theta)$ as

$$\omega(\theta)_{\mathrm{raw}} = A(\theta^{1-\gamma} - C) \tag{6.28}$$

where A is the amplitude of clustering as usual and C is

$$C = \frac{\sum_j N_{rr}(\theta_j)\theta^{1-\gamma}}{N_{rr}(\theta_j)} \tag{6.29}$$

with the integral constraint itself being AC. This value is added to every $\omega(\theta)$ and as it is additive it will have the greatest effect at large scales where the clustering power is weaker, effectively making the angular clustering function shallower. The calculated values of the integral constraint are given in table 6.3, and are approximately 0.02. The corrections are therefore extremely significant (equal to $\omega(\theta)$) on scales of $> 7, 13, 20$ arcmin for 250, 350 and 500μm respectively. Subfigures a, c and e show the effect of applying the integral constraints onto the raw measurements. The change in power of the correlation function is apparent at all wavelengths but is most apparent at the largest scales as expected.

6.8.4 $\omega(\theta)$ Against Published *Herschel*-SPIRE Results

Figure 6.9 shows the raw $\omega(\theta)$ calculation against the 'final' preliminarily corrected value with the integral constraint applied, against previous published results for all three *Herschel*-SPIRE wavelengths. The fits shown in subfigures b d and f of this figure also include

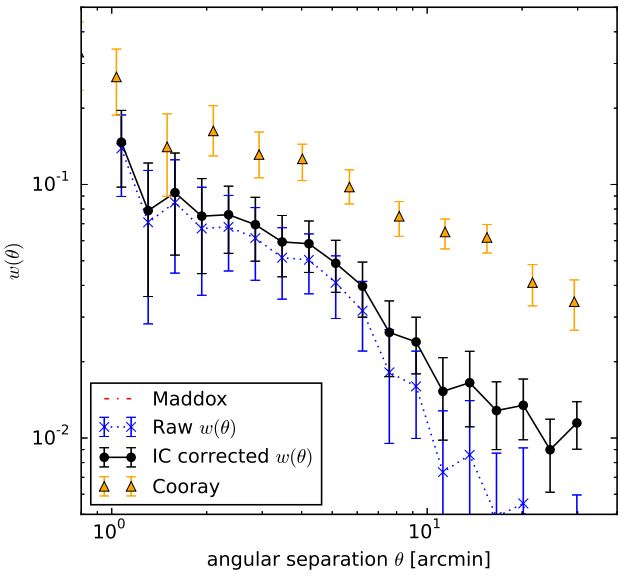

(a) 250μm

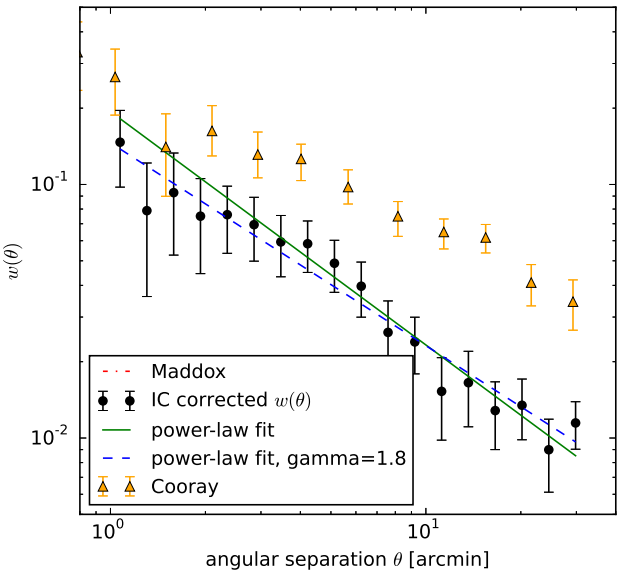

(b) 250μm

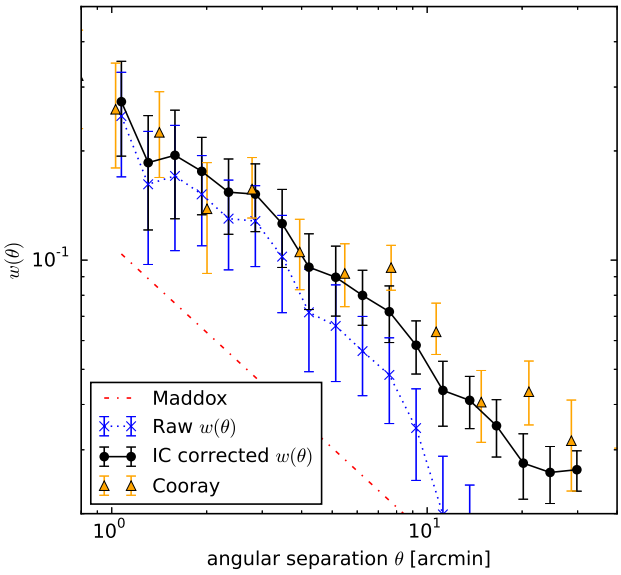

(c) 350μm

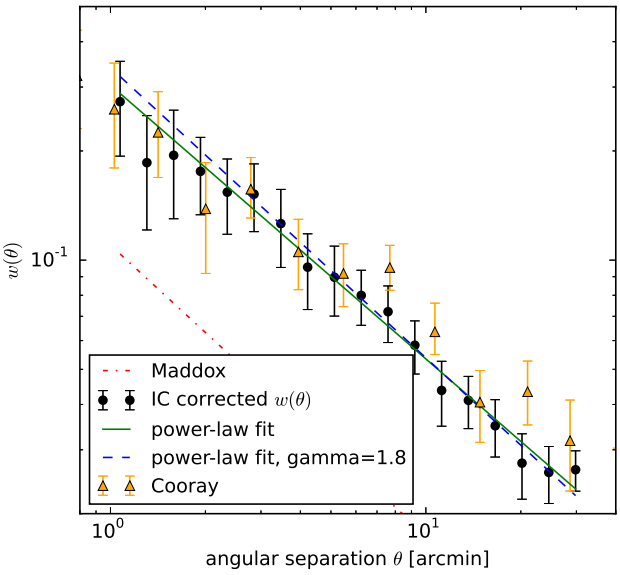

(d) 350μm

Figure 6.9: (Continued overleaf)

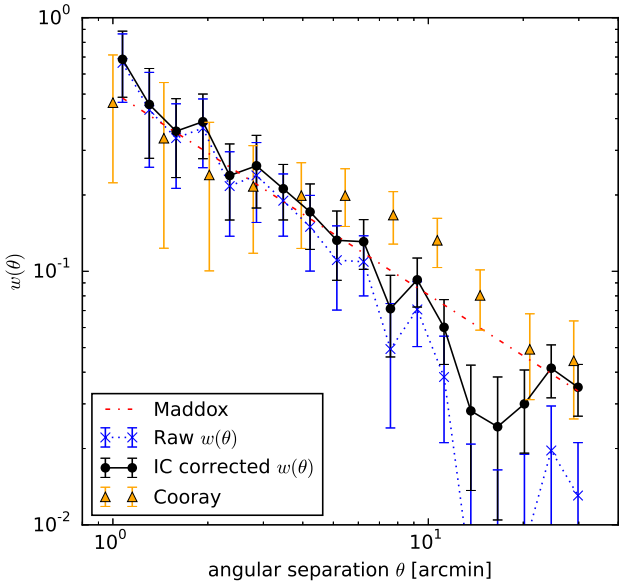

(e) 500μm

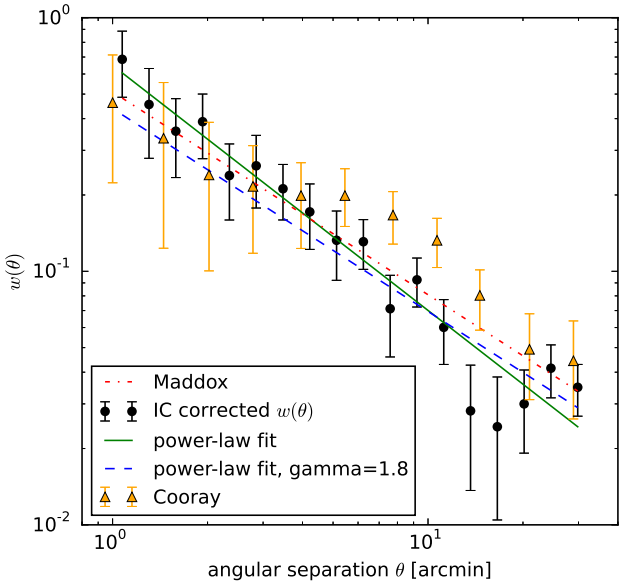

(f) 500μm

Figure 6.9: Preliminary angular correlation function results as determined from the updated Lockman-SWIRE field across all three bands for sources of minimum 30mJy flux. Subfigures a, c and e show the effect of applying the integral constraints onto the raw measurements. The two power-law fits are shown against Cooray et al. (2010) and Maddox et al. (2010) results in subfigures b, d and f. The data is split over two subfigures for clarity. Note, the Maddox et al. (2010) results at 250μm are not visible as the result is consistent with zero.

power-law fits of the data with equation 6.21, with γ allowed to vary and with γ fixed to 1.8, a value consistent with previous studies. These fits are only performed at $\theta > 3$ arcmin to prevent the under or over-estimation of the clustering strength at small angular separations effecting the fit. The results are tabulated in table 6.3.

At 250μm the Maddox et al. (2010) power law fit is not present as the result is consistent with zero. The individual data points from the Cooray et al. (2010) results for Lockman-SWIRE (albeit from the Science Demonstration Phase as opposed to the DR1 dataset) are plotted with error bars. These values are significantly higher than the results calculated in this chapter. Thus the reported difference in angular clustering by Mitchell-Wynne et al. (2012) bear out, that the clustering strength at 250μm is over reported by Cooray et al. (2010). This is significant as comparing the strength of angular clustering A calculated at all wavelengths, the 250μm clustering is weaker than the 350μm which is in turn weaker than the 500μm result. This follows previous results that angular clustering measurements performed on a population of sources at higher redshift (redder sources in *Herschel*-SPIRE data) should appear more strongly clustered.

At 350μm the results from this chapter do agree with the values from Cooray et al. (2010). However these results do not agree with the 350μm results in Maddox et al. (2010), a clustering strength of 0.339 compared to 0.11. This is significant as this shows the clustering strength of these sources are stronger and therefore these sources can be associated to higher mass haloes (Cooray & Sheth, 2002). At 250μm $\gamma = 1.92$ when γ was a free parameter, compared with $\gamma = 1.76$ at 350μm, both values are between 1-2σ away from the expected result of $\gamma = 1.8$. Cooray et al. (2010) claim $\omega(\theta)$ result is well-resolved enough to calculate the 1-halo and 2-halo terms which do not directly sum to a power-law result. If the one and two-halo terms are resolvable in the results calculated in this chapter, the power-law fit could have been biased by this deviation away from a power law. Ideally in future, these results will be analysed with halo modelling techniques to recover physical parameters about the dark matter halos hosting the galaxies forming the angular correlation function.

The results at 500μm are more reassuring. There looks to be better agreement from all three calculations. The strength of clustering could also be considered in agreement with the Maddox et al. (2010) results within 2σ or better, as the error on the published results are not given. At large angular separations there is a drop in the measured correlation function that is not present in the previous published Lockman-SWIRE results in Cooray et al. (2010). This could be field specific. Jacknifing the catalogues by area and calculating

$w(\theta)$ for other fields could determine whether these results are field specific i.e. cosmic variance.

6.9 Conclusions and Further Work

The work in this chapter is very much an ongoing process. However the results so far are summarised and the next step to improve and extend these results are outlined within this final section.

The HELP collaboration will be homogenising data from many different wavelengths from a variety of collaborations. The *Herschel*-SPIRE data will form the core of this data and will use fields from the HerMES and H-ATLAS consortiums. The map creation and catalogue pipelines from these teams were developed independently. To determine whether the data reduction needed to be reproduced by one team only or whether the data products were similar enough to proceed, the same data is reduced by both teams. The results from COSMOS are given in this chapter, and a more detailed assessment given in section 6.6. From a stacking analysis, elliptical Gaussians and the PSF used for source detection are fitted to determine the shape of the beam. An approximately 1% difference is found in the peak fitted to the maps at 250μm. Backgrounds fitted to the stack differ by a fraction of a mJy indicating that large-scale fluctuations in the map may differ due to the different filtering used. The residuals of the fitted beam used for source detection shows up to a 5% difference at the peak of the beams.

These results show that, other than a small systematic difference in the maps there is very little difference between the maps and, keeping the differences in mind, both pipelines can be used concurrently rather than one team needing to re-reduce all the data. To extend this, the differences at large scales could be sought using the differences between the power spectra. This should highlight at which scales the effect of filtering is greatest. The wider map reduced by both teams, GAMA15, also needs to be analysed in the same way. This will highlight the different ways the teams deal with artefacts like extended cirrus emission.

Catalogues from MADX and STARFINDER/DESPHOT are both created on the same (HerMES reduced) COSMOS map. MADX appears to overestimate the fluxes of sources, this overestimation is a function of source separation in these deep maps. At separations of > 1 arcmin, the difference between the catalogues is minimal. MADX was designed to work on the large, shallow maps like GAMA15 rather than COSMOS, therefore that matched filter used for these deeper maps map not be optimal (c.f. SUSSEXtractor's modified Gaussian beam as a matched filter). The difference between the two catalogues

created on GAMA15 would be an interesting addition. The HELP project is moving to using simultaneous source fitting to find sources in the *Herschel*-SPIRE data with XID (Hurley et al., submitted) which, from the results shown here, would be the best course of action to prevent this flux overestimation.

At the current stage of this analysis, no difference has been found that can conclusively explain the different angular clustering ($\omega(\theta)$)results between Cooray et al. (2010) and Maddox et al. (2010), which differ significantly at the 250μm and 350μm wavelengths. However a recalculation, as a first step, of the HerMES results will provide an updated HerMES measurement of the angular clustering function to compare to the Maddox et al. (2010) results.

The measured or raw $\omega(\theta)$ result will differ from the true function due to the restricted size of the map at large angular source separations and at small scales due to the source detection algorithm's inability to distinguish highly-blended sources.

An attempt was made to calculate the transfer function, this small-scale correction, using simulated images. The difference between the pair counts as a function of θ can be compared for the sources input into the simulation and those observed to find the correction needed to be applied to recover the true $\omega(\theta)$. This calculation was preliminary and appeared to be unsuccessful, with the calculated transfer function over-correcting particularly at 250μm and applying at unexpected angular separations. If these transfer functions are correct, the repercussions would be an even stronger clustering strength of sources at 250μm and 500μm, with a turnover in clustering at small angular separations in the 250μm indicating an under density of star forming galaxies in the highest mass dark matter halos. To improve this work a larger although as of yet unconstrained number of lightcones would need to be produced to find this transfer function to a reasonable degree of accuracy.

As a preliminary comparison the integral constraint, a correction that mostly affects large scales, is calculated for the $\omega(\theta)$ for each band at scales > 3 arcmin (to reduce inaccuracies in the calculation due to the uncorrected small-scale correlation function). The constant is added across all scales and these results compared to results from Cooray et al. (2010) and Maddox et al. (2010). At 250μm there is no agreement with either published result, with the Cooray et al. (2010) result over-estimating the clustering strength and Maddox et al. (2010) finding no strength at all. These results do however qualitatively agree with results from Mitchell-Wynne et al. (2012) that find some clustering strength but also weaker clustering than Cooray et al. (2010). At 350μm these results agree with

Cooray et al. (2010) with Maddox et al. (2010) again under-estimating the correlation and at 500μm there is agreement with all results.

The HerMES estimation of the correlation function has been updated in this chapter, with the estimate of the strength of the 250μm results revised downwards. However, to understand why the H-ATLAS result deviates from these results the correlation function will need to be estimated using the MADX catalogues on GAMA15, and then to be extremely robust the DESPHOT catalogue generated on GAMA15 to compare the differences. If these correlation function can be found this acts as an update to they *Herschel*-SPIRE correlation function at different scales and the difference between the data reduction pipelines for both teams will be quantified and ready to use for the HELP collaboration.

Chapter 7

Overall Conclusions

The formation and growth of galaxies through the formation of stars is an ongoing area of research in astrophysics. Understanding how galaxies build up their stellar mass is one particular problem under investigation. Emission from galaxies in the far-infrared is known to be strongly correlated with obscured star formation and makes up a significant fraction of the cosmic infrared background. Therefore observations of these wavelengths can provide valuable insight into the star formation history of galaxies across cosmic time.

The *Herschel* Space Observatory, observing in the far infrared, locates galaxies forming stars across the peak of cosmic star formation. Tracing this crucial transition in galaxy evolution will assist in constraining a variety of models, from simulations of the large-scale structure of the Universe to understanding processes behind star formation within giant molecular clouds.

The *Herschel* Multi-tiered Extragalactic Survey (HerMES) was the survey with the largest guaranteed time on *Herschel*. HerMES focussed on a wide-range of extragalactic legacy fields of different sizes and depths. The collaboration produced a wealth of scientific results from data products primarily consisting of maps and catalogues constructed from observations taken with the *Herschel*-PACS and *Herschel*-SPIRE instruments. Observations of distant galaxies in the far-infrared suffer substantially from source confusion. Infrared emission from galaxies is so ubiquitous and the resolution of *Herschel* data is such that the signal from neighbouring galaxies on the sky blends together, becoming confused. Finding individual sources and accurately reporting the flux is not simple. To this end, HerMES have produced two source detection and extraction pipelines, the blind source extraction algorithm SUSSEXtractor, and the combination of source detection algorithm STARFINDER with prior-driven source extraction algorithm DESPHOT, developed especially to work with confused regions of the sky.

This thesis covers the production of additional galaxy catalogues using these algorithms for two fields as part of HerMES' second data release, which contributed to the companion paper Wang et al. (2014). These catalogues were directly compared to discuss differences between the source extraction and detection capabilities of the two algorithms; finding that at lower fluxes SUSSEXtractor relatively overestimates fluxes of sources compared to DESPHOT. These results were expanded on using the more objective comparison of source injection, which gave the completeness as well as the absolute positional and flux accuracy for both algorithms. The analysis found that deeper fields were complete at lower fluxes, and that DESPHOT and SUSSEXtractor were more complete in the deeper and shallower fields respectively. The results also confirmed SUSSEXtractor was indeed over-estimating flux at the lowest fluxes. This analysis was contrasted with previous work assessing the completeness and accuracy of these catalogues in Wang et al. (2014) which matched multiple input sources to one output source using a full simulated map. In particular the work in this thesis provides tighter completeness constraints at bright fluxes than given in Wang et al. (2014) and the completeness functions provide a more traditional correction that can be used for e.g. the calculation of the number counts.

This thesis also includes the first publicly available source catalogue for the HeLMS field, the largest field observed in HerMES. This particular field is larger than all the other HerMES fields combined, is the shallowest and is affected by infrared emission from the interstellar medium, galactic cirrus. Cirrus is typically known to be a fractal, with self-similar structure at all scales. However, the shape of the HeLMS field was chosen to exclude regions of bright cirrus contamination and therefore the cirrus in the field is atypical. Work conducted within this thesis showed that the cirrus in HeLMS was indeed fractal. However, interestingly, the cirrus in HeLMS had a higher fractal dimension than typical cirrus shown in previous studies. This analysis could have repercussions for future simulation of cirrus within low cirrus regions. Catalogues were generated with a modified version of DESPHOT adapted for a field this large, with the large-scale effect of cirrus removed with a high-pass filter. The completeness and accuracy of the modified algorithm was assessed with source injection, finding a peak completeness of 93% across the map, indicating that future work could improve these catalogues.

Galaxy catalogues are extremely valuable resources used to understand galaxy evolution. However HerMES catalogues are naturally incomplete at low fluxes as unresolved sources still remain in the images. Therefore the maps themselves contain more information than the catalogues alone and analyses conducted on the maps can produce statistical

results. One such analysis is probability of deflection (P(D)) analysis which uses the distribution of the number of pixels as a function of surface brightness to calculate galaxy number counts. The maps from each wavelength are treated separately however, which means the strong correlation between source fluxes across the *Herschel*-SPIRE wavelengths is completely ignored. Work in chapter 5 tackled this problem by finding a new set of basis vectors for source fluxes to be mapped to using Principal Component Analysis (PCA). PCA finds the linear combination of the original basis vectors that best captures the variance of the multi-dimensional distribution along one axis. Different methods are assessed to remove the skewing effect of the brightest pixels on the found principal components, with the Robust PCA with Adjusted Outylingness algorithm found to be the optimal algorithm for finding principal components of skewed distributions. A further method is also developed. By removing the variance caused by the instrumental noise from the covariance matrix, the principal components were fit to the confusion noise, and therefore fit the underlying distribution of galaxies only. This particular method was able to capture 95% of the variance in one principal component only. These results have applications in, for example, P(D) analysis, allowing the covariance between wavelengths to be preserved even if the principal components are fit to separately.

A new collaboration, the *Herschel* Extragalactic Legacy Project (HELP) will be using *Herschel* observations from both HerMES and the H-ATLAS collaboration, as well as available ancillary data to create homogenous, multi-wavelength data products. As a result these data products will be extremely valuable to the community. Chapter 6 takes the maps and catalogues from both collaborations and compared them, finding that the catalogues in particular are not consistent and thus one source extraction method will have to be selected to reduce the data with.

This comparison and resulting discussion led into a discussion on discrepant science results between the HerMES and H-ATLAS collaborations, namely the angular correlation functions produced by Cooray et al. (2010) and Maddox et al. (2010). This is a measure of the clustering strength of galaxies as a function of separation distance and provides constraints on large-scale structure. Chapter 6 includes a preliminary recalculation of the HerMES angular correlation function across the *Herschel*-SPIRE wavelengths and finds agreement with both studies at 500μm, Cooray et al. (2010) only 350μm (with the Maddox et al. (2010) result indicating weaker clustering) and no agreement at 250μm. These are preliminary results as the transfer function, the correction to apply on small scales to compensate for undetected sources due small separations, was not well-constrained

by the few simulated images used and thus a full halo modelling analysis could not be performed. Future work using the homogenised catalogues developed for HELP, as well as improvements in the calculation of the transfer function, will be able to better constrain the angular correlation function for both HerMES and H-ATLAS datasets, and untangle the discrepancy found in Cooray et al. (2010) and Maddox et al. (2010).

Bibliography

Ade, P. A. R., Pisano, G., Tucker, C., & Weaver, S. 2006, in Society of Photo-Optical Instrumentation Engineers (SPIE) Conference Series, Vol. 6275, Society of Photo-Optical Instrumentation Engineers (SPIE) Conference Series, 0 21

Alam, S., Albareti, F. D., Allende Prieto, C., et al. 2015, The Eleventh and Twelfth Data Releases of the Sloan Digital Sky Survey: Final Data from SDSS-III, ApJS, 219, 12 5, 102, 105

Amblard, A., Cooray, A., Serra, P., et al. 2011, Submillimetre galaxies reside in dark matter haloes with masses greater than 3×10^{11} solar masses, Nature, 470, 510 209, 210

André, P. 2013, The Herschel View of Star Formation, ArXiv e-prints, arXiv:1309.7762 110

André, P., Men'shchikov, A., Bontemps, S., et al. 2010, From filamentary clouds to prestellar cores to the stellar IMF: Initial highlights from the Herschel Gould Belt Survey, A&A, 518, L102 110

Aniano, G., Draine, B. T., Gordon, K. D., & Sandstrom, K. 2011, Common-Resolution Convolution Kernels for Space- and Ground-Based Telescopes, PASP, 123, 1218 155

Armus, L., Charmandaris, V., Bernard-Salas, J., et al. 2007, Observations of Ultraluminous Infrared Galaxies with the Infrared Spectrograph on the Spitzer Space Telescope. II. The IRAS Bright Galaxy Sample, ApJ, 656, 148 154

Asaba, S., Hikage, C., Koyama, K., et al. 2013, Principal component analysis of modified gravity using weak lensing and peculiar velocity measurements, JCAP, 8, 29 153

Astropy Collaboration, Robitaille, T. P., Tollerud, E. J., et al. 2013, Astropy: A community Python package for astronomy, A&A, 558, A33 v

Babul, A., & Postman, M. 1990, IRAS galaxies and the large-scale structure in the CfA slice, ApJ, 359, 280 208

Baines, K. H., Yanamandra-Fisher, P. A., Momary, T. W., et al. 2013, The temporal evolution of the July 2009 Jupiter impact cloud, Planet. Space Sci., 77, 25 17

Barger, A. J., Cowie, L. L., Steffen, A. T., et al. 2001, Submillimeter Properties of the 1 Ms Chandra Deep Field-North X-Ray Sample, ApJ, 560, L23 9

Baugh, C. M., & Efstathiou, G. 1994, A Comparison of the Evolution of Density Fields in Perturbation Theory and Numerical Simulations - Part One - Nonlinear Evolution of the Power Spectrum, MNRAS, 270, 183 206

Bazell, D., & Desert, F. X. 1988, Fractal structure of interstellar cirrus, ApJ, 333, 353 109, 110, 111, 114, 115, 116, 139, 142

Beichmann, C. A. 1985, Infrared Astronomical Satellite (IRAS) catalogs and atlases. Explanatory supplement (ESO) 22

Bertin, E., & Arnouts, S. 1996, SExtractor: Software for source extraction., A&AS, 117, 393 22

Béthermin, M., Dole, H., Lagache, G., Le Borgne, D., & Penin, A. 2011, Modeling the evolution of infrared galaxies: a parametric backward evolution model, A&A, 529, A4 87

Béthermin, M., Le Floc'h, E., Ilbert, O., et al. 2012, HerMES: deep number counts at 250 μm, 350 μm and 500 μm in the COSMOS and GOODS-N fields and the build-up of the cosmic infrared background, A&A, 542, A58 29, 57, 59, 207

Bezecourt, J., & Soucail, G. 1997, Redshift survey of gravitational arclets in Abell 2390., A&A, 317, 661 96

Biffi, V., & Maio, U. 2013, Statistical properties of mass, star formation, chemical content and rotational patterns in early z>9 structures, MNRAS, 436, 1621 154

Boch, T., & Fernique, P. 2014, in Astronomical Society of the Pacific Conference Series, Vol. 485, Astronomical Data Analysis Software and Systems XXIII, ed. N. Manset & P. Forshay, 277 v

Bonnarel, F., Fernique, P., Bienaymé, O., et al. 2000, The ALADIN interactive sky atlas. A reference tool for identification of astronomical sources, A&AS, 143, 33 v

Bonnor, W. B. 1956, Boyle's Law and gravitational instability, MNRAS, 116, 351 7

Boulanger, F., Baud, B., & van Albada, G. D. 1985, Warm dust in the neutral interstellar medium, A&A, 144, L9 110

Bouwens, R. J., Illingworth, G. D., Oesch, P. A., et al. 2012, UV-continuum Slopes at z = 4-7 from the HUDF09+ERS+CANDELS Observations: Discovery of a Well-defined UV Color-Magnitude Relationship for z>=4 Star-forming Galaxies, ApJ, 754, 83 9

Bower, R. G., Benson, A. J., Malbon, R., et al. 2006, Breaking the hierarchy of galaxy formation, MNRAS, 370, 645 6

Bromley, B. C., Press, W. H., Lin, H., & Kirshner, R. P. 1998, Spectral Classification and Luminosity Function of Galaxies in the Las Campanas Redshift Survey, ApJ, 505, 25 152

Burgarella, D., Buat, V., Gruppioni, C., et al. 2013, Herschel PEP/HerMES: the redshift evolution ($0 \leq z \leq 4$) of dust attenuation and of the total (UV+IR) star formation rate density, A&A, 554, A70 9, 10, 207

Bussmann, R. S., Riechers, D., Fialkov, A., et al. 2015, HerMES: ALMA Imaging of Herschel-selected Dusty Star-forming Galaxies, ArXiv e-prints, arXiv:1504.05256 73, 101

Calzetti, D., Kinney, A. L., & Storchi-Bergmann, T. 1994, Dust extinction of the stellar continua in starburst galaxies: The ultraviolet and optical extinction law, ApJ, 429, 582 151

Cerqueira, A. H., Reyes-Iturbide, J., De Colle, F., & Vasconcelos, M. J. 2015, Principal Component Analysis of Computed Emission Lines from Protostellar Jets, AJ, 150, 45 153

Chapin, E. L., Chapman, S. C., Coppin, K. E., et al. 2011, A joint analysis of BLAST 250-500 μm and LABOCA 870 μm observations in the Extended Chandra Deep Field-South, MNRAS, 411, 505 19, 88, 89

Chary, R., & Elbaz, D. 2001, Interpreting the Cosmic Infrared Background: Constraints on the Evolution of the Dust-enshrouded Star Formation Rate, ApJ, 556, 562 9

Clements, D. L., Bendo, G., Pearson, C., et al. 2011, The AKARI Deep Field-South: Spitzer 24- and 70-μm observations, catalogues and counts, MNRAS, 411, 373 19

Clements, D. L., Rigby, E., Maddox, S., et al. 2010, Herschel-ATLAS: Extragalactic number counts from 250 to 500 microns, A&A, 518, L8 83, 87, 132, 133, 140

Clements, D. L., Braglia, F. G., Hyde, A. K., et al. 2014, Herschel Multitiered Extragalactic Survey: clusters of dusty galaxies uncovered by Herschel and Planck, MNRAS, 439, 1193 204

Comon, P. 1994, Independent Component Analysis - A New Concept?, Signal Processing, 36, 287 184

Condon, J. J. 1974, Confusion and Flux-Density Error Distributions, ApJ, 188, 279 53, 82, 84, 144

Conley, A., & et al. in prep., in prep. 147

Connolly, A. J., Szalay, A. S., Bershady, M. A., Kinney, A. L., & Calzetti, D. 1995, Spectral Classification of Galaxies: an Orthogonal Approach, AJ, 110, 1071 151, 152

Cooray, A., & Sheth, R. 2002, Halo models of large scale structure, Phys. Rep., 372, 1 221

Cooray, A., Amblard, A., Wang, L., et al. 2010, HerMES: Halo occupation number and bias properties of dusty galaxies from angular clustering measurements, A&A, 518, L22 30, 31, 186, 187, 208, 209, 210, 212, 214, 216, 220, 221, 223, 224, 227, 228

Cooray, A., Calanog, J., Wardlow, J. L., et al. 2014, HerMES: The Rest-frame UV Emission and a Lensing Model for the z = 6.34 Luminous Dusty Starburst Galaxy HFLS3, ApJ, 790, 40 31

Cowley, W. I., Lacey, C. G., Baugh, C. M., & Cole, S. 2015, Simulated observations of sub-millimetre galaxies: the impact of single-dish resolution and field variance, MNRAS, 446, 1784 212

Croton, D. J., Springel, V., White, S. D. M., et al. 2006, The many lives of active galactic nuclei: cooling flows, black holes and the luminosities and colours of galaxies, MNRAS, 365, 11 6

Dahlen, T., Mobasher, B., Dickinson, M., et al. 2007, Evolution of the Luminosity Function, Star Formation Rate, Morphology, and Size of Star-forming Galaxies Selected at Rest-Frame 1500 and 2800 Å, ApJ, 654, 172 9

Davis, M., & Peebles, P. J. E. 1983, A survey of galaxy redshifts. V - The two-point position and velocity correlations, ApJ, 267, 465 204, 205

de Graauw, T., Helmich, F. P., Phillips, T. G., et al. 2010, The Herschel-Heterodyne Instrument for the Far-Infrared (HIFI), A&A, 518, L6 20

De Lucia, G., Springel, V., White, S. D. M., Croton, D., & Kauffmann, G. 2006, The formation history of elliptical galaxies, MNRAS, 366, 499 6

de Souza, R. S., & Ciardi, B. 2015, AMADA-Analysis of multidimensional astronomical datasets, Astronomy and Computing, 12, 100 153

de Souza, R. S., Cameron, E., Killedar, M., et al. 2015, The overlooked potential of Generalized Linear Models in astronomy, I: Binomial regression, Astronomy and Computing, 12, 21 154

Devlin, M. J., Ade, P. A. R., Aretxaga, I., et al. 2009, Over half of the far-infrared background light comes from galaxies at z>=1.2, Nature, 458, 737 19, 23

Doi, Y., Komugi, S., Kawada, M., et al. 2012, Akari Far-Infrared All-Sky Survey Maps, Publication of Korean Astronomical Society, 27, 111 19

Dowell, C. D., Conley, A., Glenn, J., et al. 2014, HerMES: Candidate High-redshift Galaxies Discovered with Herschel/SPIRE, ApJ, 780, 75 31

Driver, S. P., Wright, A. H., Andrews, S. K., et al. 2016, Galaxy And Mass Assembly (GAMA): Panchromatic Data Release (far-UV-far-IR) and the low-z energy budget, MNRAS, 455, 3911 11

Eales, S., Dunne, L., Clements, D., et al. 2010a, The Herschel ATLAS, PASP, 122, 499 30, 187

Eales, S. A., Raymond, G., Roseboom, I. G., et al. 2010b, First results from HerMES on the evolution of the submillimetre luminosity function, A&A, 518, L23 30, 207

Efstathiou, A., Oliver, S., Rowan-Robinson, M., et al. 2000, The European Large Area ISO Survey - III. 90-μm extragalactic source counts, MNRAS, 319, 1169 18

Einasto, J., Klypin, A. A., Saar, E., & Shandarin, S. F. 1984, Structure of superclusters and supercluster formation. III Quantitative study of the local supercluster, MNRAS, 206, 529 6

Elbaz, D., Hwang, H. S., Magnelli, B., et al. 2010, Herschel unveils a puzzling uniformity of distant dusty galaxies, A&A, 518, L29 30, 74, 192

Erben, T., & et al. submitted, submitted 105

Fadda, D., Flores, H., Hasinger, G., et al. 2002, The AGN contribution to mid-infrared surveys. X-ray counterparts of the mid-IR sources in the Lockman Hole and HDF-N, A&A, 383, 838 9

Farrah, D., Lonsdale, C. J., Borys, C., et al. 2006, The Spatial Clustering of Ultraluminous Infrared Galaxies over 1.5 <z<3, ApJ, 641, L17 209

Fowler, J. W., Niemack, M. D., Dicker, S. R., et al. 2007, Optical design of the Atacama Cosmology Telescope and the Millimeter Bolometric Array Camera, Appl. Opt., 46, 3444 105

Geach, J. E., & et al. submitted, submitted 105

Geach, J. E., Chapin, E. L., Coppin, K. E. K., et al. 2013, The SCUBA-2 Cosmology Legacy Survey: blank-field number counts of 450-μm-selected galaxies and their contribution to the cosmic infrared background, MNRAS, 432, 53 17, 23

Gilli, R., & Daddi, E. 2007, in Astronomical Society of the Pacific Conference Series, Vol. 380, Deepest Astronomical Surveys, ed. J. Afonso, H. C. Ferguson, B. Mobasher, & R. Norris, 409 209

Glass, I. S. 1999, Handbook of Infrared Astronomy, ed. R. Ellis, J. Huchra, S. Kahn, G. Rieke, & P. B. Stetson (Cambridge University Press) 15

Glenn, J., Conley, A., Béthermin, M., et al. 2010, HerMES: deep galaxy number counts from a P(D) fluctuation analysis of SPIRE Science Demonstration Phase observations, MNRAS, 409, 109 30, 53, 57, 59, 60, 83, 84, 87, 144, 147

Gonzalez-Solares, E. A., Oliver, S., Gruppioni, C., et al. 2004, Large-scale structure in the ELAIS S1 Survey, MNRAS, 352, 44 209

Griffin, M. J., Abergel, A., Abreu, A., et al. 2010, The Herschel-SPIRE instrument and its in-flight performance, A&A, 518, L3 20, 192, 202

Griffin, M. J., North, C. E., Schulz, B., et al. 2013, Flux calibration of broad-band far-infrared and submillimetre photometric instruments: theory and application to Herschel-SPIRE, MNRAS, 434, 992 33, 38

Gruppioni, C., Pozzi, F., Rodighiero, G., et al. 2013, The Herschel PEP/HerMES luminosity function - I. Probing the evolution of PACS selected Galaxies to z=4, MNRAS, 432, 23 30

Héraudeau, P., Oliver, S., del Burgo, C., et al. 2004, The European Large Area ISO Survey - VIII. 90-μm final analysis and source counts, MNRAS, 354, 924 22

Herault, J., & Jutten, C. 1987, in AIP Conference Proceedings 151 on Neural Networks for Computing (Woodbury, NY, USA: American Institute of Physics Inc.), 206–211 184

Hewett, P. C. 1982, The estimation of galaxy angular correlation functions, MNRAS, 201, 867 206

Hodge, J. A., Becker, R. H., White, R. L., Richards, G. T., & Zeimann, G. R. 2011, High-resolution Very Large Array Imaging of Sloan Digital Sky Survey Stripe 82 at 1.4 GHz, AJ, 142, 3 105

Hogerheijde, M. R., Bergin, E. A., Brinch, C., et al. 2011, Detection of the Water Reservoir in a Forming Planetary System, Science, 334, 338 20

Holland, W. S., Bintley, D., Chapin, E. L., et al. 2013, SCUBA-2: the 10 000 pixel bolometer camera on the James Clerk Maxwell Telescope, MNRAS, 430, 2513 17

Holwerda, B. W. 2005, Source Extractor for Dummies v5, ArXiv Astrophysics e-prints, astro-ph/0512139 23

Hopkins, A. M., & Beacom, J. F. 2006, On the Normalization of the Cosmic Star Formation History, ApJ, 651, 142 11

Hopkins, A. M., Miller, C. J., Connolly, A. J., et al. 2002, A New Source Detection Algorithm Using the False-Discovery Rate, AJ, 123, 1086 23

Houck, J. R., Schneider, D. P., Danielson, G. E., et al. 1985, Unidentified IRAS sources - Ultrahigh-luminosity galaxies, ApJ, 290, L5 18

Huang, J.-S., Rigopoulou, D., Magdis, G., et al. 2014, HerMES: Spectral Energy Distributions of Submillimeter Galaxies at z>4, ApJ, 784, 52 30

Hubert, M., & Rousseeuw, P. 2005, ROBPCA: A New Approach to Robust Principal Component Analysis, Technometrics, 47, 64 166

Hubert, M., Rousseeuw, P., & Verdonck, T. 2009, Robust PCA for skewed data and its outlier map, Computational statistics & data analysis, 53, 2264 166, 167

Hurley, P. D., Oliver, S., Farrah, D., Lebouteiller, V., & Spoon, H. W. W. 2014, Learning the fundamental mid-infrared spectral components of galaxies with non-negative matrix factorization, MNRAS, 437, 241 154

Hurley, P. D., Oliver, S., Farrah, D., Wang, L., & Efstathiou, A. 2012a, PCA: Principal Component Analysis for spectra modeling, Astrophysics Source Code Library, ascl:1207.012 152

—. 2012b, Principal component analysis and radiative transfer modelling of Spitzer Infrared Spectrograph spectra of ultraluminous infrared galaxies, MNRAS, 424, 2069 152, 161

Hurley, P. D., Oliver, S. J., Betancourt, M., et al. submitted, submitted 101, 128, 142, 187, 202, 223

Inoue, Y., Inoue, S., Kobayashi, M. A. R., et al. 2013, Extragalactic Background Light from Hierarchical Galaxy Formation: Gamma-Ray Attenuation up to the Epoch of Cosmic Reionization and the First Stars, ApJ, 768, 197 13

Ishihara, D., Onaka, T., Kataza, H., et al. 2010, The AKARI/IRC mid-infrared all-sky survey, A&A, 514, A1 19

Jee, M. J., Blakeslee, J. P., Sirianni, M., et al. 2007, Principal Component Analysis of the Time- and Position-dependent Point-Spread Function of the Advanced Camera for Surveys, PASP, 119, 1403 153

Johansson, D., Sigurdarson, H., & Horellou, C. 2011, A LABOCA survey of submillimeter galaxies behind galaxy clusters, A&A, 527, A117 73, 83

Jolliffe, I. 2002, Principal Component Analysis (New York: Springer) 149

Kaiser, N. 1984, On the spatial correlations of Abell clusters, ApJ, 284, L9 30, 207

Karkoschka, E., Griffith, C., & See, C. 2013, in AAS/Division for Planetary Sciences Meeting Abstracts, Vol. 45, AAS/Division for Planetary Sciences Meeting Abstracts, 305.05 153

Kennicutt, Jr., R. C. 1998, The Global Schmidt Law in Star-forming Galaxies, ApJ, 498, 541 8

Kessler, M. F., Steinz, J. A., Anderegg, M. E., et al. 1996, The Infrared Space Observatory (ISO) mission., A&A, 315, L27 18

Kinney, A. L., Calzetti, D., Bica, E., & Storchi-Bergmann, T. 1994, The Reddening law outside the local group galaxies: The case of NGC 7552 and NGC 5236, ApJ, 429, 172 151

Kostiuk, T., Fast, K., Livengood, T. A., et al. 1997, Ethane abundance on Titan, Planet. Space Sci., 45, 931 17

Lacey, C. 2015, in prep. 212, 213

Lagache, G., Dole, H., & Puget, J.-L. 2003, Modelling infrared galaxy evolution using a phenomenological approach, MNRAS, 338, 555 27

Lagache, G., Dole, H., Puget, J.-L., et al. 2004, Polycyclic Aromatic Hydrocarbon Contribution to the Infrared Output Energy of the Universe at z=2, ApJS, 154, 112 87

Lahav, O., Nemiroff, R. J., & Piran, T. 1990, Relative bias parameters from angular correlations of optical and IRAS galaxies, ApJ, 350, 119 208

Landy, S. D., & Szalay, A. S. 1993, Bias and variance of angular correlation functions, ApJ, 412, 64 206

Lari, C., Pozzi, F., Gruppioni, C., et al. 2001, A new method for ISOCAM data reduction - I. Application to the European Large Area ISO Survey Southern Field: method and results, MNRAS, 325, 1173 23

Lawrence, A., Warren, S. J., Almaini, O., et al. 2007, The UKIRT Infrared Deep Sky Survey (UKIDSS), MNRAS, 379, 1599 17, 105

Lebofsky, L. A., Sykes, M. V., Tedesco, E. F., et al. 1986, A refined 'standard' thermal model for asteroids based on observations of 1 Ceres and 2 Pallas, Icarus, 68, 239 83

Leinert, C., Bowyer, S., Haikala, L. K., et al. 1998, The 1997 reference of diffuse night sky brightness, A&AS, 127, 1 14

Levenson, L., Marsden, G., Zemcov, M., et al. 2010, HerMES: SPIRE Science Demonstration Phase maps, MNRAS, 409, 83 32, 34, 37, 192

Li, C., Kong, X., & Cheng, F. 2001, The application of principal components analysis to astrophysics, Progress in Astronomy, 19, 9 184

Lilly, S. J., Le Fevre, O., Hammer, F., & Crampton, D. 1996, The Canada-France Redshift Survey: The Luminosity Density and Star Formation History of the Universe to Z approximately 1, ApJ, 460, L1 9

Limber, D. N. 1953, The Analysis of Counts of the Extragalactic Nebulae in Terms of a Fluctuating Density Field., ApJ, 117, 134 207

Lin, H., Kirshner, R. P., Shectman, S. A., et al. 1996, The Power Spectrum of Galaxy Clustering in the Las Campanas Redshift Survey, ApJ, 471, 617 152

Ling, E. N., Barrow, J. D., & Frenk, C. S. 1986, Uncertainties in the cluster-cluster correlation function, MNRAS, 223, 21P 206

Lonsdale, C., Polletta, M. d. C., Surace, J., et al. 2004, First Insights into the Spitzer Wide-Area Infrared Extragalactic Legacy Survey (SWIRE) Galaxy Populations, ApJS, 154, 54 22

Lonsdale, C. J., Smith, H. E., Rowan-Robinson, M., et al. 2003, SWIRE: The SIRTF Wide-Area Infrared Extragalactic Survey, PASP, 115, 897 18

Lonsdale Persson, C. J., & Helou, G. 1987, On the origin of the 40-120 micron emission of galaxy disks A comparison with H-alpha fluxes, ApJ, 314, 513 9

Lovejoy, S. 1982, Area-Perimeter Relation for Rain and Cloud Areas, Science, 216, 185 110

Low, F. J., Young, E., Beintema, D. A., et al. 1984, Infrared cirrus - New components of the extended infrared emission, ApJ, 278, L19 18, 84, 110

Lutz, D., Poglitsch, A., Altieri, B., et al. 2011, PACS Evolutionary Probe (PEP) - A Herschel key program, A&A, 532, A90 20, 30

Madau, P., & Dickinson, M. 2014, Cosmic Star-Formation History, ARA&A, 52, 415 11

Madau, P., Ferguson, H. C., Dickinson, M. E., et al. 1996, High-redshift galaxies in the Hubble Deep Field: colour selection and star formation history to z=4, MNRAS, 283, 1388 9

Maddox, S. J., Dunne, L., Rigby, E., et al. 2010, Herschel ATLAS: The angular correlation function of submillimetre galaxies at high and low redshift, A&A, 1005.2406 30, 186, 210, 218, 220, 221, 223, 224, 227, 228

Madhushani, K. N. R. A. K., & Sonnadara, D. U. J. 2012, Fractal Analysis of Cloud Shapes, Proceedings of the Technical Sessions, 28, 59 110

Magnelli, B., Elbaz, D., Chary, R. R., et al. 2011, Evolution of the dusty infrared luminosity function from z = 0 to z = 2.3 using observations from Spitzer, A&A, 528, A35 9

Matsuhara, H., Wada, T., Matsuura, S., et al. 2006, Deep Extragalactic Surveys around the Ecliptic Poles with AKARI (ASTRO-F), PASJ, 58, 673 19

Mitchell-Wynne, K., Cooray, A., Gong, Y., et al. 2012, HerMES: A Statistical Measurement of the Redshift Distribution of Herschel-SPIRE Sources Using the Cross-correlation Technique, ApJ, 753, 23 30, 186, 210, 214, 221, 223

Miville-Deschênes, M.-A., & Lagache, G. 2005, IRIS: A New Generation of IRAS Maps, ApJS, 157, 302 111

Miville-Deschênes, M.-A., Martin, P. G., Abergel, A., et al. 2010, Herschel-SPIRE observations of the Polaris flare: Structure of the diffuse interstellar medium at the sub-parsec scale, A&A, 518, L104 110

Mo, H., van den Bosch, F. C., & White, S. 2010, Galaxy Formation and Evolution (Cambridge University Press) 7, 207

Moraes, B., Kneib, J.-P., Leauthaud, A., et al. 2014, in Revista Mexicana de Astronomia y Astrofisica Conference Series, Vol. 44, Revista Mexicana de Astronomia y Astrofisica Conference Series, 202–203 105

Moshir, M., Kopman, G., & Conrow, T. A. O. 1992, IRAS Faint Source Survey, Explanatory supplement version 2 (ESO) 22

Murakami, H., Baba, H., Barthel, P., et al. 2007, The Infrared Astronomical Mission AKARI, PASJ, 59, 369 19

Neugebauer, G., & Leighton, R. B. 1969, Two-micron sky survey. A preliminary catalogue (NASA) 16

Neugebauer, G., Soifer, B. T., Beichman, C. A., et al. 1984a, Early results from the Infrared Astronomical Satellite, Science, 224, 14 15, 18

Neugebauer, G., Habing, H. J., van Duinen, R., et al. 1984b, The Infrared Astronomical Satellite (IRAS) mission, ApJ, 278, L1 17

Nguyen, H. T., Schulz, B., Levenson, L., et al. 2010, HerMES: The SPIRE confusion limit, A&A, 518, L5 29, 84, 86, 87, 94, 96, 100, 174, 178

Oliver, S., Rowan-Robinson, M., Alexander, D. M., et al. 2000, The European Large Area ISO Survey - I. Goals, definition and observations, MNRAS, 316, 749 18, 209

Oliver, S., Waddington, I., Gonzalez-Solares, E., et al. 2004, Angular Clustering of Galaxies at 3.6 Microns from the Spitzer Wide-area Infrared Extragalactic (SWIRE) Survey, ApJS, 154, 30 209

Oliver, S. J., Wang, L., Smith, A. J., et al. 2010, HerMES: SPIRE galaxy number counts at 250, 350, and 500 μm, A&A, 518, L21 83

Oliver, S. J., Bock, J., Altieri, B., et al. 2012, The Herschel Multi-tiered Extragalactic Survey: HerMES, MNRAS, 424, 1614 26

Ott, S. 2010, in Astronomical Society of the Pacific Conference Series, Vol. 434, Astronomical Data Analysis Software and Systems XIX, ed. Y. Mizumoto, K.-I. Morita, & M. Ohishi, 139 32, 83

Pascale, E., Ade, P. A. R., Bock, J. J., et al. 2008, The Balloon-borne Large Aperture Submillimeter Telescope: BLAST, ApJ, 681, 400 19

Patanchon, G., Ade, P. A. R., Bock, J. J., et al. 2008, SANEPIC: A Mapmaking Method for Time Stream Data from Large Arrays, ApJ, 681, 708 35

Pearson, K. 1901, On lines and Planes of Closest Fit to Systems of Points in Space, Philosophical Magazine, 2, 559 149

Peebles, P. J. E. 1974, The Gravitational-Instability Picture and the Nature of the Distribution of Galaxies, ApJ, 189, L51 206

Penteado, P. F., Griffith, C. A., Greathouse, T. K., & de Bergh, C. 2005, Measurements of CH_3D and CH_4 in Titan from Infrared Spectroscopy, ApJ, 629, L53 17

Phillipps, S., Fong, R., Fall, R. S. E. S. M., & MacGillivray, H. T. 1978, Correlation analysis deep galaxy samples - 1. Techniques with applications to a two-colour sample, MNRAS, 182, 673 207

Pilbratt, G. L., Riedinger, J. R., Passvogel, T., et al. 2010, Herschel Space Observatory. An ESA facility for far-infrared and submillimetre astronomy, A&A, 518, L1 19

Pitchford, K., & et al. submitted, submitted 102, 141

Planck Collaboration. 2015, Planck 2015 results. XIII. Cosmological parameters, ArXiv e-prints, arXiv:1502.01589 6

Planck Collaboration, Ade, P. A. R., Aghanim, N., et al. 2014, Planck 2013 results. XII. Diffuse component separation, A&A, 571, A12 12, 115, 184

Poglitsch, A., Waelkens, C., Geis, N., et al. 2010, The Photodetector Array Camera and Spectrometer (PACS) on the Herschel Space Observatory, A&A, 518, L2 20

Price, S. D. 1977, in Bulletin of the American Astronomical Society, Vol. 9, Bulletin of the American Astronomical Society, 430 16

Price, S. D., Murdock, T. L., Shivanandan, K., & Bowers, P. F. 1983, The brighter 94 micron sources observed by the far-infrared sky survey experiment, ApJ, 275, 125 16

Price, S. D., & Walker, R. G. 1976, The AFGL four color infrared sky survey: Catalog of observations at 4.2, 11.0, 19.8 and 27.4 micrometers, Tech. rep., NASA 16

Richards, F. J. 1959, A Flexible Growth Function for Empirical Use, J. Exp. Bot., 10, 290 65

Riechers, D. A. 2013, Astronomy: New distance record for galaxies, Nature, 502, 459 31, 160

Riess, A. G., Filippenko, A. V., Challis, P., et al. 1998, Observational Evidence from Supernovae for an Accelerating Universe and a Cosmological Constant, AJ, 116, 1009 4

Rigby, E. E., Maddox, S. J., Dunne, L., et al. 2011, Herschel-ATLAS: first data release of the Science Demonstration Phase source catalogues, MNRAS, 415, 2336 86, 100, 190

Roche, N., & Eales, S. A. 1999, The angular correlation function and hierarchical moments of approximately 70000 faint galaxies to R=23.5, MNRAS, 307, 703 218

Rodríguez-Ardila, A., & Viegas, S. M. 2003, Hidden starbursts in Seyfert 1 galaxies, MNRAS, 340, L33 17

Rowan-Robinson, M., & Needham, G. 1986, The two-dimensional covariance function for IRAS sources, MNRAS, 222, 611 208

Rowan-Robinson, M., Roseboom, I. G., Vaccari, M., et al. 2010, Cold dust and young starbursts: spectral energy distributions of Herschel SPIRE sources from the HerMES survey, MNRAS, 409, 2 30

Rowan-Robinson, M., Wang, L., Wardlow, J., et al. 2014, Detailed modelling of a large sample of Herschel sources in the Lockman Hole: identification of cold dust and of lensing candidates through their anomalous SEDs, MNRAS, 445, 3848 31

Salim, S., Dickinson, M., Michael Rich, R., et al. 2009, Mid-IR Luminosities and UV/Optical Star Formation Rates at z<1.4, ApJ, 700, 161 9

Sánchez, N., Alfaro, E. J., & Pérez, E. 2007, Fractal Dimension of Interstellar Clouds: Opacity and Noise Effects, ApJ, 656, 222 110

Sanders, D. B., Salvato, M., Aussel, H., et al. 2007, S-COSMOS: The Spitzer Legacy Survey of the Hubble Space Telescope ACS 2 deg^2 COSMOS Field I: Survey Strategy and First Analysis, ApJS, 172, 86 192

Schlegel, D. J., Finkbeiner, D. P., & Davis, M. 1998, Maps of Dust Infrared Emission for Use in Estimation of Reddening and Cosmic Microwave Background Radiation Foregrounds, ApJ, 500, 525 110, 111

Serjeant, S., Oliver, S., Rowan-Robinson, M., et al. 2000, The European Large Area ISO Survey - II. Mid-infrared extragalactic source counts, MNRAS, 316, 768 18

Serjeant, S., Dunlop, J. S., Mann, R. G., et al. 2003, Submillimetre observations of the Hubble Deep Field and Flanking Fields, MNRAS, 344, 887 42

Serjeant, S., Carramiñana, A., Gonzáles-Solares, E., et al. 2004, The European Large Area ISO Survey - IX. The 90-μm luminosity function from the Final Analysis sample, MNRAS, 355, 813 18

Shang, C., Haiman, Z., Knox, L., & Oh, S. P. 2012, Improved models for cosmic infrared background anisotropies: new constraints on the infrared galaxy population, MNRAS, 421, 2832 53

Shectman, S. A., Landy, S. D., Oemler, A., et al. 1996, The Las Campanas Redshift Survey, ApJ, 470, 172 152

Shupe, D. L., Rowan-Robinson, M., Lonsdale, C. J., et al. 2008, Galaxy Counts at 24 μm in the SWIRE Fields, AJ, 135, 1050 22

Siringo, G., Kreysa, E., Kovács, A., et al. 2009, The Large APEX BOlometer CAmera LABOCA, A&A, 497, 945 17

Skrutskie, M. F., Cutri, R. M., Stiening, R., et al. 2006, The Two Micron All Sky Survey (2MASS), AJ, 131, 1163 17

Smith, A. J., Wang, L., Oliver, S. J., et al. 2012a, HerMES: point source catalogues from deep Herschel-SPIRE observations, MNRAS, 419, 377 45, 63, 65, 68

Smith, D. J. B., Dunne, L., da Cunha, E., et al. 2012b, Herschel-ATLAS: multi-wavelength SEDs and physical properties of 250 μm selected galaxies at z<0.5, MNRAS, 427, 703 210

Sodroski, T. J., Odegard, N., Arendt, R. G., et al. 1997, A Three-dimensional Decomposition of the Infrared Emission from Dust in the Milky Way, ApJ, 480, 173 9

Soifer, B. T., Rowan-Robinson, M., Houck, J. R., et al. 1984, Infrared galaxies in the IRAS minisurvey, ApJ, 278, L71 18

Spoon, H. W. W., Marshall, J. A., Houck, J. R., et al. 2007, Mid-Infrared Galaxy Classification Based on Silicate Obscuration and PAH Equivalent Width, ApJ, 654, L49 154

Springel, V. 2005, The cosmological simulation code GADGET-2, MNRAS, 364, 1105 6, 154

Springel, V., White, S. D. M., Jenkins, A., et al. 2005, Simulations of the formation, evolution and clustering of galaxies and quasars, Nature, 435, 629 6, 213

Stetson, P. B. 1987, DAOPHOT - A computer program for crowded-field stellar photometry, PASP, 99, 191 45

Struble, M. F., & Rood, H. J. 1999, A Compilation of Redshifts and Velocity Dispersions for ACO Clusters, ApJS, 125, 35 96

Stutzki, J., Bensch, F., Heithausen, A., Ossenkopf, V., & Zielinsky, M. 1998, On the fractal structure of molecular clouds, A&A, 336, 697 110

Swinyard, B. M., Ade, P., Baluteau, J.-P., et al. 2010, In-flight calibration of the Herschel-SPIRE instrument, A&A, 518, L4 85

Sykes, M. V. 1988, IRAS observations of extended zodiacal structures, ApJ, 334, L55 15, 18

Szalay, A. S., Connolly, A. J., & Szokoly, G. P. 1999, Simultaneous Multicolor Detection of Faint Galaxies in the Hubble Deep Field, AJ, 117, 68 23

Taghizadeh-Popp, M., Heinis, S., & Szalay, A. S. 2012, Single Parameter Galaxy Classification: The Principal Curve through the Multi-dimensional Space of Galaxy Properties, ApJ, 755, 143 152

Taylor, M. B. 2005, in Astronomical Society of the Pacific Conference Series, Vol. 347, Astronomical Data Analysis Software and Systems XIV, ed. P. Shopbell, M. Britton, & R. Ebert, 29 v

Ter Braak, C. J., Boer, M. P., Totir, L. R., et al. 2010, Identity-by-descent matrix decomposition using latent ancestral allele models, Genetics, 185, 1045 44

The Dark Energy Survey Collaboration. 2005, The Dark Energy Survey, ArXiv Astrophysics e-prints, astro-ph/0510346 105

Tibshirani, R. 1996, Regression shrinkage and selectin via the lasso, J. Royal. Statist. Soc B, 58, 267 44

Totsuji, H., & Kihara, T. 1969, The Correlation Function for the Distribution of Galaxies, PASJ, 21, 221 206

Trumpler, R. J. 1930a, Absorption of Light in the Galactic System, PASP, 42, 214 109

—. 1930b, Spectrophotometric Measures of Interstellar Light Absorption, PASP, 42, 267 109

Vaccari, M., Marchetti, L., Franceschini, A., et al. 2010, The HerMES SPIRE submillimeter local luminosity function, A&A, 518, L20 30

Valiante, E., Ade, P. A. R., Bock, J. J., et al. 2010, BLAST Observations of the South Ecliptic Pole Field: Number Counts and Source Catalogs, ApJS, 191, 222 19

Valtchanov, I. 2014, The Spectral and Photometric Imaging Receiver (SPIRE) Handbook, Ivan Valtchanov 14, 21, 32, 84

Viero, M. P., Ade, P. A. R., Bock, J. J., et al. 2009, BLAST: Correlations in the Cosmic Far-Infrared Background at 250, 350, and 500 μm Reveal Clustering of Star-forming Galaxies, ApJ, 707, 1766 209

Viero, M. P., Moncelsi, L., Mentuch, E., et al. 2012, Measuring star formation in high-z massive galaxies: a mid-infrared to submillimetre study of the GOODS NICMOS Survey sample, MNRAS, 421, 2161 209

Viero, M. P., Moncelsi, L., Quadri, R. F., et al. 2013, HerMES: The Contribution to the Cosmic Infrared Background from Galaxies Selected by Mass and Redshift, ApJ, 779, 32 30, 32, 53, 57, 192

Viero, M. P., Asboth, V., Roseboom, I. G., et al. 2014, The Herschel Stripe 82 Survey (HerS): Maps and Early Catalog, ApJS, 210, 22 65, 94, 102, 115, 116, 117, 120, 126, 132, 140, 141

Walker, R. G. 1975, AFCRL infrared sky survey. Volume 1: Catalog of observations at 4, 11, and 20 microns, Tech. rep., NASA 16

Wang, L., Farrah, D., Connolly, B., et al. 2011, Principal component analysis of the Spitzer IRS spectra of ultraluminous infrared galaxies, MNRAS, 411, 1809 152

Wang, L., Viero, M., Clarke, C., et al. 2014, HerMES: point source catalogues from Herschel-SPIRE observations II, MNRAS, 444, 2870 24, 26, 31, 61, 62, 63, 65, 87, 92, 93, 99, 105, 141, 226

Wardlow, J. L., Cooray, A., De Bernardis, F., et al. 2013, HerMES: Candidate Gravitationally Lensed Galaxies and Lensing Statistics at Submillimeter Wavelengths, ApJ, 762, 59 31

Weiß, A., Kovács, A., Coppin, K., et al. 2009, The Large Apex Bolometer Camera Survey of the Extended Chandra Deep Field South, ApJ, 707, 1201 23

Werner, M. W., Roellig, T. L., Low, F. J., et al. 2004, The Spitzer Space Telescope Mission, ApJS, 154, 1 18

Wild, V., & Hewett, P. C. 2005, Peering through the OH forest: a new technique to remove residual sky features from Sloan Digital Sky Survey spectra, MNRAS, 358, 1083 153

Wild, V., Almaini, O., Cirasuolo, M., et al. 2014, A new method for classifying galaxy SEDs from multiwavelength photometry, MNRAS, 440, 1880 153, 185

Wilkins, S. M., Gonzalez-Perez, V., Lacey, C. G., & Baugh, C. M. 2012, The accuracy of the UV continuum as an indicator of the star formation rate in galaxies, MNRAS, 427, 1490 8

Wright, E. L., Eisenhardt, P. R. M., Mainzer, A. K., et al. 2010, The Wide-field Infrared Survey Explorer (WISE): Mission Description and Initial On-orbit Performance, AJ, 140, 1868 19, 105

Zuckerman, B., & Evans, II, N. J. 1974, Models of massive molecular clouds, ApJ, 192, L149 8